

UNIVERSITÀ  
DEGLI STUDI  
DI PADOVA

Sede Amministrativa: Università degli Studi di Padova

Centro Interdipartimentale di Studi e Attività Spaziali CISAS “G. Colombo”

---

SCUOLA DI DOTTORATO DI RICERCA IN: SCIENZE TECNOLOGIE E MISURE SPAZIALI  
INDIRIZZO: MISURE MECCANICHE PER L'INGEGNERIA E LO SPAZIO  
CICLO XXV

TITOLO TESI

**ANALYSIS OF PROPELLANTLESS TETHERED SYSTEM FOR  
THE DE-ORBITING OF SATELLITES AT END OF LIFE**

**Direttore della Scuola:** Ch.mo Prof. GIANPIERO NALETTO

**Coordinatore d'indirizzo:** Ch.mo Prof. STEFANO DEBEI

**Supervisore:** Ch.mo Prof. ENRICO LORENZINI

**Co-Supervisore:** Dr. CLAUDIO BOMBARDELLI

**Dottorando:** DENIS ZANUTTO



# Contents

<b>Nomenclature</b>	<b>vii</b>
<b>Conferences/Papers/Reports</b>	<b>ix</b>
<b>Sommario</b>	<b>III</b>
<b>1 Introduction</b>	<b>1</b>
1.1 Electrodynami c Tethers and Applications . . . . .	2
1.2 Space Debris . . . . .	4
1.3 BETs Project . . . . .	5
1.3.1 BETs Team and Work Packages . . . . .	6
1.3.2 CISAS . . . . .	8
<b>2 Mathematical Models</b>	<b>11</b>
2.1 Dumbbell Model . . . . .	11
2.1.1 References Frames . . . . .	11
2.1.2 Description of the Model . . . . .	13
2.1.3 Orbital Motion . . . . .	14
2.1.4 Attitude Motion . . . . .	17
2.2 Flexible Tether . . . . .	19
2.2.1 Tension Along the Tether . . . . .	19
2.2.2 Massless Tether . . . . .	19
2.2.3 Massive Inextensible Tether . . . . .	20
2.2.4 Massive Extensible Tether . . . . .	29
2.2.5 Lump Masses Model . . . . .	29
2.2.6 Normal Modes . . . . .	33
<b>3 Earth's Environment</b>	<b>37</b>
3.1 Ionosphere . . . . .	37
3.2 Magnetic Field . . . . .	39
3.2.1 Dipolar Magnetic Field . . . . .	39
3.2.2 Eccentric Dipolar Magnetic Field . . . . .	40
3.2.3 International Geomagnetic Reference Field . . . . .	41
3.3 Atmosphere . . . . .	41
3.4 Gravitational Field . . . . .	42

---

<b>4 Electrodynamic Bare Tethers</b>	<b>45</b>
4.1 Electric Current Profile . . . . .	46
4.1.1 Electric Circuit Equations . . . . .	47
4.1.2 Nondimensional Electric Circuit Equations . . . . .	50
4.1.3 Resolution Algorithms . . . . .	51
4.2 Energetic Considerations . . . . .	56
<b>5 EDT Dynamics</b>	<b>59</b>
5.1 Spectral Analysis of a Rigid Dumbbell Tethered System . . . . .	59
5.1.1 Spectral analysis with different magnetic fields . . . . .	59
5.2 Shape Modes of a Flexible Tethered System . . . . .	62
5.2.1 Eigen-Frequencies . . . . .	63
5.2.2 Taut wire . . . . .	64
5.2.3 Inert Tethered Satellite . . . . .	65
5.2.4 Simulations . . . . .	71
<b>6 Deorbiting Performance</b>	<b>81</b>
6.1 Perpendicular Component of the Magnetic Field . . . . .	83
6.2 Reentry Time . . . . .	85
<b>7 Control Techniques</b>	<b>89</b>
7.1 Uncontrolled EDT Dynamics . . . . .	89
7.2 Summary About Techniques Proposed in the Past . . . . .	91
7.2.1 Self-Balanced EDT . . . . .	92
7.2.2 Periodic Orbits . . . . .	92
7.2.3 Electric Current Control . . . . .	95
7.3 Control Techniques Proposed for The BETs Project . . . . .	100
7.3.1 Results With Dumbbell Model . . . . .	101
7.3.2 Results With Inextensible Flexible Wire Model . . . . .	102
7.3.3 Results With Extensible Flexible Wire Model . . . . .	112
<b>8 Deployment Strategies</b>	<b>129</b>
8.1 Deployment strategies . . . . .	129
8.2 Past Flight Experience . . . . .	131
8.3 Deployment study plan . . . . .	132
8.4 Deployer . . . . .	135
8.4.1 Concept1 . . . . .	135
8.4.2 Concept2 . . . . .	136
8.4.3 Concept3 . . . . .	136
8.4.4 Concept4 . . . . .	137
8.4.5 Concept5 . . . . .	138
8.4.6 Concept6 . . . . .	138
8.4.7 Concept7 . . . . .	139
8.4.8 Comparison . . . . .	140
8.4.9 Enginnering Model . . . . .	141
8.5 Deployment Equations . . . . .	142
8.6 Optimal Profile . . . . .	145

---

## *CONTENTS*

---

8.6.1 Optimization . . . . .	146
8.6.2 Results . . . . .	149
8.7 Control-Brake Strategy . . . . .	159
<b>9 Conclusion</b>	<b>169</b>



# Nomenclature

$a$	=	albedo coefficient
$A$	=	cross section area [ $\text{m}^2$ ]
$A$	=	viscous coefficient of the tether [kg/s]
$\vec{B}$	=	Earth's magnetic field [T]
$\vec{E}$	=	motional electric field [V/m]
$E_t$	=	motional electric field projected along the tether [V/m]
$E_Y$	=	Young module of the tether [V/m]
$\vec{F}_a$	=	aerodynamic force [N]
$\vec{F}_{el}$	=	electrodynamic force [N]
$\vec{F}_{gr}$	=	gravitational attraction [N]
$\hat{h}$	=	orbital angular momentum unit vector [m]
$h$	=	thickness of the tether [m]
$h_{ij}$	=	$h$ -coefficients of magnetic potential spherical expansion
$G$	=	system centre of mass
$G_{xyz}$	=	orbital reference frame
$G_{x_B y_B z_B}$	=	body reference frame
$g_{ij}$	=	$g$ -coefficients of magnetic potential spherical expansion
$k$	=	damping coefficient
$I$	=	electrical current along the tether [A]
$I_{av}$	=	average electric current [A]
$I_{sh}$	=	short circuit current [A]
$I_s$	=	satellite inertia momentum [ $\text{kg}^*\text{m}^2$ ]
$l_m$	=	lump mass
$J_s$	=	solar flux [W/m <sup>2</sup> ]
$L$	=	tether length [m]
$m$	=	mass of whole system [kg]
$m_B$	=	tip mass [kg]
$m_{sat}$	=	mass of the satellite [kg]
$O_{X_I Y_I Z_I}$	=	inertial reference frame
$O_{x_E y_E z_E}$	=	geocentric reference frame
$p$	=	perimeter of the tether [m]
$\vec{r}$	=	orbital position w.r.t. inertial frame [km]
$R$	=	electrical resistance of the tether [ $\Omega$ ]
$R_E$	=	Earth equatorial radius [km]
$t$	=	time [s]
$T_E$	=	temperature of the Earth [K]
$\hat{u}$	=	unit vector along the tether

$\vec{v}$	=	orbital velocity w.r.t. inertial frame [km/s]
$\vec{v}_{rel}$	=	relative orbital velocity w.r.t. ionospheric plasma [km/s]
$w$	=	width of the tether [m]
$\vec{x}_B$	=	eccentric dipole magnetic field offset [km]
$\vec{Y}$	=	tension force along the tether [N]
$\alpha_m$	=	Earth's magnetic dipole longitude [rad]
$\alpha_s$	=	absorption coefficient in the visible range
$\alpha_T$	=	thermal expansion coefficient [1/K]
$\beta_m$	=	Earth's magnetic dipole co-latitude [rad]
$\varepsilon_s$	=	electrodynamic interaction parameter
$\varepsilon_s$	=	absorption coefficient in the infrared range
$\mu_m$	=	Earth's magnetic dipole magnitude [T]
$\mu_E$	=	Earth's gravitational mass parameter [km <sup>3</sup> /s <sup>2</sup> ]
$\omega_{orb}$	=	orbital angular velocity [rad/s]
$\omega_E$	=	Earth's rotational velocity [rad/s]
$\sigma$	=	electrical conductivity [1/(Ω s)]
$\theta$	=	in-plane attitude angle [rad]
$\varphi$	=	out-of-plane attitude angle [rad]
$\dot{\theta}$	=	in-plane attitude angle velocity [rad/s]
$\dot{\varphi}$	=	out-of-plane attitude angle velocity [rad/s]

# Conferences/Papers/Reports

1. Lorenzini, E. C., Curreli, D., Zanutto, D., “Exploration of the Galilean Moons using Electrodynamic Tethers for Propellantless Maneuvers and Self-Powering”, Proceedings IAU Symposium, No. 269, 2010
2. Zanutto, D., Curreli D., Lorenzini, E. C., “Stability of Electrodynamic Tethers in a Three-Body System”, Journal of Guidance, Dynamics and Control, Vol. 34, No. 5, pp. 1441-1456, September-October 2011.
3. J. R. Sanmartin, S. B. Khan, C. Bombardelli, E. C. Lorenzini, G. Colombatti, D. Zanutto et al., “Propellantless Deorbiting of Space Debris by Bare Electrodynamics Tethers”, 62<sup>nd</sup> International Astronautical Congress, Cape Town, SA, October 2011.
4. Zanutto, D., Lorenzini, E. C., Colombatti G., “Electrodynamic Tethers for Deorbiting Maneuvers”, The International Conference of the European Aerospace Societies, Venice, 24-28 October 2011.
5. Zanutto, D., Lorenzini, E. C., Mantellato, R., Colombatti G., Sanchez, A., “Orbital Debris Mitigation Through Deorbiting With Passive Electrodynamic Drag”, 63<sup>rd</sup> International Astronautical Congress, Naples, 1-5 October 2012.
6. J. R. Sanmartin, S. B. Khan, C. Bombardelli, E. C. Lorenzini, G. Colombatti, D. Zanutto et al., “An Universal System to De-Orbit Satellites at the End of Life”, Journal of Space Technology and Science, Japanese Rocket Society, Vol. 26, No. 1, pp. 21-32, 2012.
7. Bombardelli C., Zanutto D., Lorenzini, E. C., “Deorbiting Performance of Bare Electrodynamic Tethers in Inclined Orbits”, Journal of Guidance, Dynamics and Control, (accepted and to be published).
8. Reports for the FP7 project “BETs: The Bare Electrodynamic Tethers Project”.







*Come faceva a sapere se il potere  
del Partito sarebbe durato per sempre?*

*Quasi a fornigli una risposta,  
gli tornarono alla mente i tre slogan  
sulla facciata del Ministero della Verità:*

*GUERRA È PACE  
LIBERTÀ È SCHIAVITÙ  
L'IGNORANZA È FORZA*

*Prese dalla tasca una moneta  
da venticinque centesimi.  
Anche qui, in caratteri chiari e netti,  
erano incisi gli stessi slogan.  
Sul rovescio, la testa del Grande Fratello,  
i cui occhi anche qui parevano seguirvi.*

George Orwell, 1984



## Abstract

The increase of orbital debris and the consequent proliferation of smaller objects through fragmentation is driving the need for mitigation strategies that address this issue at its roots. The present guidelines for mitigation point out the need to deorbit new satellites injected into low Earth orbit (LEO) within a 25-year time. The issue is then how to deorbit the satellite with an efficient system that does not impair drastically the propellant budget of the satellite and, consequently, reduces its operating life. In this contest a passive system, which makes use of an electrodynamics tether to deorbit a satellite through Lorentz forces, has been investigated. The system collects electrons from the ionosphere at its anodic end (the conductive tether itself left bare) and emits electrons through a plasma contactor at the cathodic end. The current that circulates in the tether produces the Lorentz drag force through the interaction with the Earth's magnetic field. Power can also be tapped from the tether for running the cathode and other ancillary on-board equipment. The deorbiting system will be carried by the satellite itself at launch and it will be deployed from the satellite at the end of its life. From that moment onward the system operates passively without requiring any intervention from the satellite itself.

This thesis summarizes the results of the analysis carried out to show the deorbiting performance of the system starting from different orbital scenarios and for satellite configurations, and describing the tethered system by means of different mathematical models in order to include the lateral flexibility and increase the accuracy of the results, which can be easily scaled. Moreover high-fidelity and latest environmental routines has been used for magnetic field, ionospheric density, atmospheric density and a  $4 \times 4$  gravity field model, since the environment is very important for describing appropriately each external interaction, in particular the electrodynamic one. The electric properties of the wire depends on its temperature, which is computed dynamically by a thermal model that considers all the major input fluxes and the heat emitted by the tether itself. At last the electric current along the rope is constantly evaluated during the reentry, since large variations happens passing from sunlight to shadow regions, and vice-versa.

Without any control the system goes rapidly into instability, because the electrodynamic torque pumps continuously energy into the system enlarging the libration of the tether. So ad hoc strategies must be thought and included. In the past several techniques have been proposed, but with a lot of assumptions and limitations. In this work a new concept has been implemented, mounting in the satellite at the basis of the tether a damping mechanism for dissipating the energy associated with the lateral motion.

At last the whole deployment of a tape tether has been analyzed. Several configurations have been studied, and the tradeoff analysis concluded that a non-motorized reeling deployer is well suited for a 1-3 cm wide tape like the tapes. Optimal reference profiles have been evaluated for two class of tether (3 and 5km), and are then used to regulate the brake mechanism mounted on the deployer itself to control the deployment. Different conditions have been analyzed to demonstrate the capabilities of the control law to provide a successful deployment in the presence of various errors.

# Sommario

Dall'inizio dell'esplorazione spaziale i satelliti a filo hanno catturato l'interesse di molto scienziati in virtù delle loro numerose applicazioni. Tale tecnologia fù inizialmente proposta da M. Grossi e G. Colombo negli anni 70 ed è formata principalmente da tre elementi: il satellite che contiene il filo, prima che venga dispiegato e tutti i componenti elettrici e meccanici per il suo corretto funzionamento; il filo che collega il satellite alla massa posta all'altra estremità, generalmente lungo alcuni km e caratterizzato da una sezione molto sottile; e la massa d'estremità: una volta rilasciata dallo spacecraft fornisce la tensione dovuta al gradiente di gravità necessaria a disegnare il filo e stabilizzarlo durante l'intera operazione. Tali sistemi sono dispositivi molto utili, che possono essere impiegati come, ad esempio, sonde atmosferiche, laboratori di microgravità, space elevator, osservatori per la regione interna della magnetosfera di Giove, oppure utilizzati per eseguire trasferimenti orbitali o manovre di cattura per l'esplorazioni di pianeti.

Negli ultimi cinquant'anni un gran numero di satelliti sono stati lanciati in orbite basse (LEO), a una quota compresa approssimativamente tra 200 e 2000km sopra la superficie terrestre. Questa regione dello spazio è di notevole interesse per diversi motivi (scientifici, militari, commerciali, meteorologici, osservazione, ...), dunque molto popolata. Per garantire la sopravvivenza dei satelliti operativi diventa necessario provvedere manovre di rientro al termine della missione, in modo da evitare la proliferazione di detriti spaziali, che attualmente sono già molto intensi e rappresentano una grave minaccia. Tali detriti (di origine umana) sono costituiti principalmente da stadi di lanciatori, satelliti spenti o parte di essi, frammenti generati da collisioni ed esplosioni, ed espongono lo spacecraft a rischio di impatto iperveloce ( $v_{sat} \approx 7\text{km/s}$  a 1500km d'altezza), provocando danni ai diversi sottosistemi e al payload, o addirittura il fallimento dell'intera missione. Esistono diverse possibilità per compiere tale manovra, ad esempio mediante motori liquidi o elettrici. In entrambi i casi, già per satelliti di medie dimensioni, la massa aggiuntiva richiesta per l'operazione di rientro diventa non trascurabile e, anzi, rappresenta un forte vincolo in fase di progettazione. Un sistema vantaggioso, senza consumo di carburante e a massa aggiuntiva ridotta è l'utilizzo del tether eletrodinamico: il campo elettromotore indotto dal moto del satellite che taglia costantemente le linee di campo magnetico permette il flusso di elettroni, collezionati dalla ionosfera, lungo un circuito elettrico che comprende il tether e si chiude nella stessa ionosfera. L'interazione tra gli elettroni in movimento e il campo magnetico genera forze di Lorentz distribuite lungo tutto il filo, che frenano il moto del satellite e ne abbassano continuamente l'orbita fino a portarlo al rientro atmosferico. Diverse missioni a filo hanno volato nel passato per verificare l'efficienza, e studiare la dinamica e le tecniche di dispiegamento, così da ottenere importanti informazioni sul suo funzionamento. Nel 1992 venne lanciato il TSS-1, un programma spaziale sviluppato in collaborazione tra ASI e NASA e montato a bordo dello Shuttle STS-46. Fù un'importante missione per indagare la dinamica del filo, testarne il dispiegamento usando un meccanismo attivo motorizzato, e meglio esplorare l'ambiente spaziale. Per tale motivo un filo di 20km era stato montato a bordo, ma a causa di problemi tecnici il deployment si interruppe dopo solo 260m. L'anno dopo l'esperimento PMG venne lanciato per

testare l'efficienza di un catodo cavo nel fornire una corrente elettrica bipolare tra lo spacecraft a la ionosfera. Successivamente nel 1993-94 le missioni SEDS 1-2, progettate e sviluppate dal Marshall Space Flight Center, dimostrarono con successo la possibilità di deploiare (in maniera passiva) un piccolo payload usando un filo di 20km. Nel 1996, TSS-1R montò a bordo dello shuttle Columbia STS-75 un filo elettrodinamico (EDT), ossia un sistema in grado di collezionare elettroni dalla ionosfera. In tale occasione l'obiettivo principale dell'esperimento era dimostrare alcune importanti applicazioni del sistema a filo, e in particolare lo studio della fisica del plasma, la misura del campo elettromotore e della distribuzione delle cariche elettriche attorno al filo, e dunque dell'intensità della corrente che scorre lungo esso. Fù nuovamente utilizzato un filo di 20km, che venne dispiegato con successo, ma la missione fallì dopo un'ora a causa di un arco elettrico. Ad ogni modo i dati collezionati fino a tale momento e trasmessi a Terra furono molto utili per comprendere meglio la natura delle particelle cariche presenti nella ionosfera e come avviene il processo di collezione degli elettroni. Nello stesso anno l'esperimento TiPS della US Naval Research Laboratory fù messo in orbita. Formato da due payload connessi da un filo lungo 4km, fornì ulteriori informazioni sulla dinamica del sistema e sul rischio di danno dovuto ad impatti iperveloci dei detriti spaziali. Nel 1997 la missione YES dell'ESA venne lanciata in GTO con a bordo un filo di 35km. Pianificata per deorbitare una sonda sfruttando il  $\Delta V$  fornito dal moto di librazione, in realtà il filo non fù dispiegato per questioni di sicurezza. Più recentemente, nel 2007, altre due missioni furono lanciate in orbita: MAST per meglio studiare la sopravvivenza del filo all'ambiente spaziale e YES2, un'altro esperimento per studenti sponsorizzato nuovamente dall'ESA. Il deployment di MAST si interruppe dopo un solo km, mentre YES2 deploì con successo 32km di filo per far poi rientrare la capsula posta all'altra estremità del cavo. Purtroppo problemi con il sistema di comunicazione montato sulla capsula non ne permisero il recupero, però i dati forniti dalla telemetria del satellite durante il deployment permisero di concludere che l'operazione si completò con successo e la capsula rientrò come previsto. Infine nel 2010 la missione T-REX a bordo del sounding rocket S-520-25 venne lanciata raggiungendo la sua massima altezza di circa 300km. Lo scopo era di condurre alcuni esperimenti sul filo elettrodinamico immerso nella ionosfera e controllare l'assetto di un robot usando un filo soggetto a condizioni di micro-gravità. Il filo, a forma di nastro e lungo 300m, fù dispiegato usando una nuova strategia, simile alla tecnica degli origami.

Quando parliamo di satelliti a filo (per operazioni di rientro) in termini di prestazioni i principali obiettivi sono: analizzare e simulare la dinamica orbitale di un sistema per condizioni operative realistiche in modo da ottimizzare il deorbiting di un EDT per differenti configurazioni ed orbite. Infatti le prestazioni di tale sistema dipendono fortemente dai parametri orbitali, quale inclinazione, semiasse maggiore ed eccentricità. Il campo elettromotore è funzione del campo magnetico (in termini di modulo e direzione), che decresce con il cubo dell'altezza dell'orbita, mentre la corrente che fluisce lungo il filo lo è anche della densità elettronica della ionosfera e ciò limita l'utilizzo del tether a quote non troppo elevate. La lunghezza del cavo, l'inerzia del satellite e la sua massa complessiva sono importanti per quanto concerne la stabilità in termini di moto in piano e fuori piano (gli angoli sono valutati dalla verticale locale rispetto al piano orbitale). Infatti le forze di Lorentz generano coppie elettrodinamiche che tendono a destabilizzare l'assetto del satellite, mentre il gradiente gravitazionale genera delle coppie che cercano di riallineare il filo lungo la verticale locale. Lungo orbite ellittiche le variazioni di velocità angolare contribuiscono a portare il sistema in instabilità causando ampie rotazioni.

Per studiare il sistema EDT in modo esaustivo è necessario implementare un simulatore che in-

clude tutti gli aspetti fondamentali della dinamica del tether, come ad esempio l'incurvamento del filo e la sua risposta elastica, il modello di collezione degli elettroni, e il modello termico tenendo conto di tutti i principali flussi che colpiscono la superficie del filo. Un'analisi dettagliata delle sue prestazioni necessita di modelli ambientali accurati, infatti il campo magnetico dipolare e il campo gravitazionale generato da una massa sferica uniformemente distribuita sono troppo approssimativi e adatti solo per uno studio preliminare. Proprio per questo motivo il simulatore deve comprendere un modello di campo magnetico IGRF2010, uno di densità ionosferica IRI-2007, uno di densità atmosferica NRLMSISE-2000 e infine uno di campo gravitazionale almeno 4x4, che permettano di descrivere un comportamento del satellite molto più vicino a quello reale, di quanto non si possa fare con modelli ambientali semplificati.

L'equazione di bilancio termico fornisce le temperature di diversi punti del tether computando tutti i flussi: illuminazione solare, radiazione infrarossa terrestre, albedo, perdite ohmiche del filo, impatto degli elettroni collezionati, emissività infrarossa del filo. Il calcolo della temperatura è importante dal momento che la resistenza di ogni punto del cavo, e di conseguenza il profilo di corrente lungo il tether, dipende da essa. Infine il simulatore deve essere relativamente veloce in termini computazionali, in modo da esaminare un elevato numero di configurazioni di satellite che siano rappresentative di una larga classe di spacecraft generalmente presenti in LEO, tether e orbite, così da mettere in evidenza profili di missione che permettano un rientro controllato in tempi ragionevoli. Proprio per questo motivo si è scelto di scrivere il codice in Fortran, uno dei linguaggi di programmazione di riferimento in campo scientifico.

Il simulatore deve indagare, tramite analisi e simulazioni, la dinamica di un tether flessibile soggetto alle perturbazioni ambientali (principalmente interazione elettrodinamica e attrito atmosferico a basse quote) per stimare i limiti operativi e derivare adeguate leggi di controllo. L'EDT è continuamente soggetto a diverse forze e coppie ambientali che ne modificano la dinamica orbitale e l'assetto. Ad alte quote le più importanti sono rappresentate da quelle del gradiente di gravità, che lo mantengono teso ed allineato con la verticale locale, e quelle elettrodinamiche, che agendo in direzione trasversale all'asse principale del filo tendono ad incurvarlo e farlo librare con oscillazioni sempre più ampie all'aumentare dell'interazione con l'ambiente fino a portarlo ad instabilità e dunque a rapide rotazioni. A basse quote diventano predominanti le azioni aerodinamiche, infatti, sotto i 150km la densità atmosferica è sufficientemente alta per frenare il satellite e abbassarne rapidamente l'orbita, destabilizzando l'assetto del filo. Dunque, se non controllato, il tether non può sopravvivere se non per breve tempo o lunghezze del cavo molto ridotte, ma che significano bassi livelli di corrente e implicano lunghi tempi di rientro. L'obiettivo è, dunque, innanzitutto caratterizzare la dinamica del tether e la sua dipendenza dai parametri del sistema, in modo da derivare delle opportune strategie di controllo che mantengano l'orientamento del filo stabile, lungo la verticale locale, e forniscano allo stesso tempo un rapido deorbiting.

La tesi è composta da sette capitoli in cui vengono descritti i principali modelli matematici utilizzati, il comportamento del filo, le prestazioni e le tecniche di controllo, mentre l'ultimo capitolo è dedicato al deployment di un tape tether. Infatti tale geometria garantisce migliori prestazioni rispetto al caso circolare, in quanto aumenta l'area di collezione a parità di quella trasversale.

**Modelli matematici:** in letteratura esistono diversi modelli per descrivere la dinamica di un satellite a filo. In particolare possiamo dividerli in fili rigidi e flessibili. Nel primo caso l'intero sistema è schematizzato come un corpo rigido, generalmente chiamato modello *dumbbell*, mentre

nel secondo è possibile entrare un po' più nel dettaglio includendo la dinamica laterale.

Il modello *dumbbell* è molto utile per ottenere rapide informazioni sulle prestazioni di rientro e identificare scenari operativi d'interesse. Invece il filo flessibile fornisce una descrizione dettagliata della dinamica d'assetto, studiando anche l'incurvamento del filo quando perturbato dalle forze esterne.

Nel modello *dumbbell* il tether è un sottile elemento rigido di massa  $m_t$  e lunghezza  $L$ , che connette le due masse d'estremità  $m_{sat}$  e  $m_B$ . Il sistema non ammette alcuna deformazione e ignora tutti i fenomeni elastici. La semplicità del modello permette di studiare il sistema dinamico usando un approccio analitico, e derivare le equazioni del moto, che sono facilmente implementabili. La traiettoria seguita dal satellite dipende da tutte le forze agenti su di esso e lungo il filo. I contributi sono diversi, e i principali, come già anticipato prima, sono l'attrazione gravitazionale, l'interazione elettrodinamica e il drag atmosferico. Allo stesso modo l'assetto, governato dal momento angolare  $\vec{H}$ , varia a causa della coppia del gradiente gravitazionale, e quelle elettrodinamiche e aerodinamiche. Questo approccio permette di investigare le principali instabilità dovute alla geometria del sistema, eliminando però quelle legate alla flessibilità del tetheder.

Nel passato diversi metodi per modellare la flessibilità del tether sono stati adottati, e possono essere suddivisi in continui e discreti. Il primo approccio diventa molto complesso e oneroso quando anche le forze elettrodinamiche agiscono sul satellite, perché funzione di vari parametri quali la temperatura, la posizione, la forma e la deformazione istantanea del filo. Quindi questo metodo porta a molti problemi numerici quando si vuole simulare la dinamica del tether per un elevato numero di modi. Per risolvere il moto dell'intero sistema, evitando troppe complicazioni matematiche, bisogna passare al caso discreto, che si può implementare seguendo due strade. La prima considera il filo come inestensibile e lo divide in  $n$  barre rigide, mentre la seconda è più precisa e valuta anche la deformazione assiale discretizzandolo con una serie di masse concentrate collegate da molle e smorzatori. In entrambi i casi, la soluzione diventa sempre più precisa aumentando il numero di elementi utilizzati, ma ciò significa che il tempo di calcolo necessario per la soluzione cresce rapidamente. Quindi il numero di elementi deve essere un buon compromesso tra un'accurata descrizione del moto reale e la minimizzazione del tempo di integrazione senza perdita di informazioni fondamentali su aspetti critici del sistema.

**Modelli ambientali:** le prestazioni del tether elettrodinamico dipendono da diversi parametri, come la quota orbitale, l'inclinazione, l'intensità del campo magnetico e la densità elettronica. Lo studio della dinamica del satellite necessita di modelli ambientali di riferimento che approssimano la vera natura dell'atmosfera terrestre, il campo magnetico e l'attrazione gravitazionale. In letteratura esistono diversi modelli, alcuni più accurati e altri più semplici e veloci da implementare. In questo lavoro si vuole simulare il comportamento di un satellite a filo in dettaglio, quindi sono adottati i modelli più accurati presenti al giorno d'oggi in letteratura, come IRJ2007, IGRF2010, NRLMSISE-2000 e un campo gravitazionale almeno  $4 \times 4$ .

La ionosfera è una regione dell'alta atmosfera caratterizzata da un'alta concentrazione di elettroni liberi, e si estende da circa 50 km a 1500 km sopra la terra. La densità elettronica  $N_e$  varia da  $10^7$  particelle per  $m^3$  a 50 km ad un massimo di  $10^{12}$  particelle per  $m^3$  a 250-300 km, e poi decresce all'aumentare della quota, diventando trascurabile (per il nostro scopo) sopra i 1500km. La ionosfera si forma quando le radiazioni elettromagnetiche e particelle ad alta contenuto energetico provenienti dal sole e dallo spazio ionizzano le molecole d'aria creando

del plasma nell'atmosfera.

In prima approssimazione il campo magnetico può essere descritto come un dipolo inclinato con poli ribaltati rispetto a quelli terrestri, ma lavorando con maggior precisione esso è definito come il gradiente di una funzione potenziale  $V_B$ , generalmente espressa come espansione in armoniche sferiche, secondo gli sviluppi di Legendre. Tale espansione in serie tiene conto di tutte le anomalie delle linee di campo, come ad esempio quella del Sud Atlantico.

L'atmosfera è uno strato di gas, la cui temperatura media alla superficie è di 14-15°C, che circonda il pianeta ed è trattenuto dalla gravità terrestre. In questo lavoro il modello NRLMSISE-00 è stato adottato per valutarne la densità, e fornisce la temperatura e la composizione dell'aria dalla superficie sino alla termosfera.

Il nostro pianeta non è un corpo perfettamente sferico, e neanche la massa è omogeneamente distribuita. Infatti ci sono montagne, zone di pianura, deserti, oceani, e anche sotto la superficie la densità cambia muovendosi verso il nucleo. Quindi, al fine di tener conto di tutti questi effetti, il campo gravitazionale terrestre può essere espressa mediante espansione in armoniche sferiche, in modo analogo a quanto fatto per il campo magnetico.

**Modello di collezione degli elettroni:** i fili elettrodinamici sono sistemi utili per estrarre energia elettrica a spese del plasmasfera di un pianeta. L'alta densità di elettroni e il forte campo magnetico permette di collezionare una considerevole quantità di elettroni e far fluire una corrente di qualche Ampere lungo il filo. Dal punto di vista elettrico il sistema è costituito da un cavo sottile conduttore collegato al satellite, un anodo dato dalla porzione di filo (nudo) dove la differenza di potenziale tra esso e la plasmasfera è positiva, e infine un catodo che espelle gli elettroni nella ionosfera, tramite la quale il circuito si chiude.

L'ipotesi principale fatta in questa tesi, e in generale per ogni lavoro su tether elettrodinamici nudi, è nel processo di collezione, che è supposto avvenire in regime *Orbital Motion Limited* (OML), ottimale per le sonde cilindriche [85]. In effetti data la disparità tra le dimensioni longitudinali e trasversali, ogni punto del filo raccoglie elettroni come se appartenesse ad un cilindro uniforme polarizzato.

Il calcolo del profilo di corrente lungo tutto il filo rappresenta un problema al contorno, e necessita la risoluzione dell'equazioni differenziali (fornite dal regime OML) fino a soddisfare la chiusura del circuito. Un modo semplice per risolvere il problema consiste nella determinazione del profilo di corrente lungo tutto il tether variando le condizioni iniziali della caduta di potenziale all'anodo  $\Delta V_A$  fino a garantire quella al catodo  $\Delta V_C$ . Anche se particolarmente lento, l'algoritmo di bisezione può essere utilizzato per modificare il valore iniziale di  $\Delta V_A$  e arrivare alla soluzione, ma richiede la soluzione delle equazioni differenziali ad ogni interazione. In letteratura ci sono altre tecniche migliori per risolvere il problema: il metodo asintotico [9] e quello semi-analitico [52] [83]. Anche se raggiungono la soluzione in due modi differenti, si basano sulla stessa idea: invece di calcolare l'intero profilo ad ogni iterazione, viene prima risolta un'equazione fortemente non-lineare per trovare la posizione dove il potenziale tra filo e plasmasfera si annulla, e quindi determinato il set di equazioni differenziali, un'unica volta. Questi metodi sono molto efficienti, e permettono di risparmiare molto tempo computazionale limitando il numero di operazioni richieste.

**Dinamica del satellite a filo:** è stata studiata in dettaglio sia per cavi rigidi che flessibili. Utilizzando il modello *dumbbell* è stata eseguita un'analisi spettrale per indagare le principali frequenze che influenzano il moto del satellite. In particolare la trasformata di Fourier ha permesso di evidenziare quali sono i contenuti in frequenza, dovuti alle forze esterne, che più

incidono nel moto d'assetto del tether.

Successivamente mediante l'approccio a masse concentrate le caratteristiche principali dei modi vibrazionali laterali sono state analizzate, mettendo in risalto che nel caso di filo perturbato dalla forzante elettrodinamica solo le prime frequenze vengono eccitate, mentre quelle superiori hanno un contenuto di energia molto più basso, che cala all'aumentare della frequenza. Per questo motivo un numero limitato di nodi, ad esempio 5, è più che sufficiente per descrivere in maniera accurata la dinamica del filo.

**Prestazioni di deorbiting:** durante le prime analisi preliminari può essere molto utile avere alcune espressioni, anche semplificate, che forniscono informazioni rapide per comprendere la dipendenza delle prestazioni dalla configurazione del sistema (massa, dimensioni del filo,...) e dalla scelta dell'orbita (altezza iniziale e inclinazione). Per questo motivo il seguente capitolo è dedicato alla descrizione di un algoritmo utilizzato per ricavare delle equazioni analitiche per valutare il tempo di rientro richiesto. Il modello ottenuto si basa su tre ipotesi principali: stabilizzazione tramite gradiente gravitazionale (filo sempre allineato lungo la verticale locale), orbite LEO circolari e inclinate, corrente elettrica media uguale a quella di corto circuito.

Lavorando in modo più generale possibile, il modello è stato costruito partendo direttamente dalla espressione dell'espansione in serie del campo magnetico, fermandola a diversi ordini in modo da osservare la variazione in accuratezza.

In operazioni con satelliti a filo la componente principale è quella perpendicolare all'orbita. Tramite software matematici, le equazioni sono state opportunamente manipolate in modo da ottenere tale espressione, e integrarla lungo l'orbita. Semplici formule del tempo di rientro sono state così ottenute, che possono essere facilmente scritte in maniera ricorsiva all'aumentare dell'ordine usato per approssimare il campo magnetico.

**Strategie di controllo:** i sistemi EDT sono estremamente instabili a causa della forza di Lorentz che pompa continuamente energia sul sistema ampliando sia la librazione in piano che quella fuori piano. Se non controllato con una strategia adeguata, il filo non riesce a mantenersi vicino alla verticale locale, e la librazione si trasforma rapidamente in una rotazione. Quindi tecniche di controllo sono necessarie per fornire le condizioni ottimali per un decadimento orbitale rapido e completo.

I parametri chiave d'instabilità possono essere raggruppati in quattro categorie principali: le dimensioni del filo, la distribuzione di massa del satellite, i parametri orbitali e ambientali. Il primo gruppo include la lunghezza, lo spessore e la larghezza del cavo, il secondo comprende la distribuzione satellitare di massa, il terzo riguarda l'inclinazione orbitale e l'altitudine, mentre l'ultimo concerne l'indice di attività solare, e dunque la densità degli elettroni nella ionosfera. Infatti se una delle tre dimensioni del filo si allunga, anche la corrente media che fluisce lungo esso aumenta, intensificando la forza di Lorentz; se il rapporto di massa tra satellite e massa d'estremità diventa più grande allora il baricentro tende ad allontanarsi dal centro di pressione del carico elettrodinamico, incrementando così la coppia; l'inclinazione orbitale ha un effetto destabilizzante come spiegato da Peláez e Lorenzini in [70], mentre l'altitudine aumenta il tempo di rientro e il rischio di impatto dovuto ai detriti spaziali; infine i periodi di intensa attività solare aumentano la densità di elettroni nella ionosfera, e quindi nel filo può scorrere una corrente elettrica molto più alta.

In passato diverse tecniche sono state studiate per il modello *dumbbell*, e riguardano principalmente la condizione di auto-bilanciamento, il controllo della corrente o, sotto ipotesi molto restrittive, sulla possibilità di inserire la dinamica librazionale lungo un profilo periodico. La

prima tecnica si prefigge di eliminare la coppia elettrodinamica mediante una precisa scelta di ogni componente del sistema. Invece la strategia delle orbite periodiche tenta di inserire il moto accoppiato in piano e fuori piano in una traiettoria chiusa nello spazio delle fasi, in modo tale che l'energia totale accumulata dopo una oscillazione completa è nulla. Infine la tecnica del controllo in corrente apre e chiude il circuito in funzione della dinamica di librazione. Quando l'energia associata con l'oscillazione del filo supera una soglia prefissata l'algoritmo di controllo permette il circolo di corrente elettrica solo quando la forza di Lorentz è opposta alla librazione.

Mentre il terzo concetto è più realistico e facile da ottenere, gli altri due sono limitati dalle assunzioni che è necessario fare, in particolare le orbite periodiche esistono solo in casi ideali e richiedono la ripetizione delle medesime condizioni ambientali. In realtà anche il controllo in corrente ha delle limitazioni, dovute principalmente al rischio di archi elettrici nella fase di apertura e chiusura del circuito.

Una nuova soluzione promettente è stata proposta: un meccanismo di smorzamento viene introdotto nel sistema per dissipare l'energia in eccesso pompata dalle forze elettrodinamiche e aerodinamiche. Lo smorzatore, collocato tra il satellite e il tether, è tale da mantenere il sistema stabile attorno alla posizione di equilibrio istantaneo, che è una funzione della posizione orbitale e della configurazione del sistema, durante tutta la manovra di decadimento e garantire tempi di rientro rapidi, in quanto il sistema funziona sempre alla massima prestazione senza tempi morti, come accade per il controllo in corrente. Questa strategia è stata studiata con i simulatori sviluppati. Il modello *dumbbell*, e il filo flessibile inestensibile offrono risultati molto interessanti, ma quando anche la dinamica longitudinale è inclusa usando l'approccio a massa concentrate si può notare che lo smorzatore da solo non è sufficiente a garantire la stabilità. Infatti la dinamica di skip-rope inizia a lentamente a svilupparsi perturbando notevolmente la dinamica del filo. Tuttavia se il sistema viene integrato con una porzione di filo inerte, da inserire dopo quello conduttivo, è possibile aumentare la coppia di gradiente di gravità, e assicurare maggior stabilità ed un rapido rientro.

**Dispiegamento del filo:** è una questione molto critica, perché da essa dipende il successo della missione. Durante la vita operativa del satellite il filo è mantenuto all'interno di un involucro, avvolto su un rocchetto, e al termine della missione deve essere deploiaato così da iniziare la manovra di deorbiting.

I meccanismi di deployment si dividono in stazionari (passivi) e motorizzati (attivi). Se progettato correttamente, un deployment stazionario è più leggero e più semplice di un deployer motorizzato, che di solito è utilizzato per sistemi che devono recuperare il filo (ad esempio le missioni TSS), o accorciarlo durante la missione. Un deployer passivo è particolarmente adatto per il dispiegamento di fili a sezione circolare e la cui lunghezza è mantenuta costante alla fine dell'operazione. Tali dispositivi sono stati usati, ad esempio, con successo per le missioni SEDS e PMG.

Diversi concetti sono stati studiati al fine di trovare la soluzione migliore nel caso della geometria a nastro. L'analisi ha evidenziato che un sistema passivo a bobina mobile (un disco libero di ruotare attorno al suo asse) è preferibile ad una bobina fissa in quanto il nastro potrebbe torcersi mentre esce lungo l'asse della bobina e produrre un elevato attrito o addirittura causare inceppamento. Inoltre un deployer non-motorizzato è adatto per un nastro largo 1-3 cm, come quelli previsti per questo tipo di applicazioni. Dal punto di vista della

strategia di controllo tale configurazione è moto simile ad uno stazionario perché la velocità di svolgimento del filo non può essere controllato direttamente (attraverso un motorino), ma piuttosto lo sarà cambiando la frizione (prodotta da un meccanismo di freno).

Il primo obiettivo è stato individuare alcuni profili di riferimento da seguire per arrivare alla fine del dispiegamento soddisfando tutti i requisiti. La traiettoria ottimale è calcolata risolvendo un problema al contorno non-lineare, dove sono fissate le condizioni iniziali, e oltre all'accelerazione fornita dal gradiente di gravità, il deployment è aiutato da un piccolo propulsore (a bassa spinta) montato nella massa d'estremità. Per questo motivo un codice di ottimizzazione è stato scritto per ricavare i profili nel caso di fili lunghi 6 km e 10 km, rappresentativi per gli scenari ipotizzati. In ciascuna configurazione, mezza lunghezza è usata per la parte intera del cavo che è necessaria per fornire stabilità al moto d'assetto durante il rientro. Alcune traiettorie interessanti sono state calcolate, e garantiscono il completo dispiegamento fino alla lunghezza obiettivo e piccole ampiezze di librazione.

Infine il freno da montare all'interno del deployer è stato incluso e simulato per controllare il tether durante il deployment. Si tratta di un sistema a due barre sottili che possono toccare la superficie della bobina rotante in modo da rallentarne la velocità angolare. Le due barre sono fissati all'involucro esterno del deployer, quindi non ruotano con la bobina, e hanno un solo grado di libertà, in quanto incernierati ad una delle due estremità.

La geometria del meccanismo è stata realizzata in SIMPACK, un software per la dinamica multibody, mentre in controllo e il confronto della traiettoria seguita avviene in Simulink, che restituisce l'input per azionare il freno, in modo da inseguire il profilo ottimale precedentemente calcolato. Dalle simulazioni si nota che il freno funziona correttamente, e sia le librerie che il dispiegamento, seguono l'andamento desiderato arrivando alla fine dell'operazione con errori piccoli e limitati. Infine ulteriori casi sono stati analizzati per dimostrare le capacità della legge di controllo nel fornire un valido deployment anche in presenza di errori o condizioni operative differenti da quelle previste.





# Chapter 1

## Introduction

From the beginning of space exploration tethers have captured the attention of several researchers because of its numerous applications. Initially thought and proposed by M. Grossi and G. Colombo in the 1970's, a space tethered system is formed by three essential elements: the satellite containing the tether, before the deployment, and all the electrical and mechanical parts necessary for its correct functioning; the wire connecting the satellite with the tip mass, usually several km-s long and characterized by a very small sectional area; the tip mass: released from the spacecraft it provides the gravity gradient tension to deploy the tether and stabilization during the whole operation. These systems are very useful devices that can be utilized in different fields, as for example atmosphere probe, rotating controlled-gravity laboratory, space elevator, transfer momentum, aerocapture for planetary exploration, Jupiter inner magnetosphere observatory, ...

In the last years several missions flew mounting tethered system to test the functionality, deployments techniques, dynamics and gather data. In 1992 the Tethered Satellite System (TSS-1) [5], developed by ASI and mounted on board of Shuttle mission STS-46, was an important mission to study the dynamics of a 20km long tether. But some problems of the deployment mechanism stopped the wire after only 260m. A year after the Plasma Motor Generator (PMG) experiment was launched to test the ability of a hollow cathode assembly (HCA) to provide a low impedance bipolar electrical current between a spacecraft and the ionosphere. Then in 1993-1994 the Small Expandable Deployer System (SEDS-1 and SEDS-2 [13]), two missions of Marshall Space Flight Center, demonstrated with success the capability of deploying a small payload using a 20 km long tether. In 1996 the electrodynamic tether, as system to produce electric current exploiting the external environment, was investigated by the TSS-1R mission mounted on board of the space shuttle Columbia (STS-75). In such an occasion the goals of the experiment were to demonstrate some of the important applications of the tether for the research about space plasma physics, the measurements of the electro-motional field, the current in the tether, the changing resistance in the tether and the charged particle distributions around a highly charged spherical satellite. The 20 km long wire was successfully deployed, but an electric arch caused the brake of the tether and so the failure of mission. Anyway the data gathered in the first hours and transmitted to the Earth was very useful to understand the nature of the charged particles in the ionosphere and how the collection of electrons happens. In the same year the Tether Physics and Survivability (TiPS) Experiment of US Naval Research Laboratory was put in orbit. It was formed by two payload connected by a 4 km long tether, and provided further information about the dynamics of the system and the sensitivity to damage from the space debris. In 1997, the European Space Agency (ESA) launched the Young Engineers' Satellite (YES) into GTO with a 35 km double-strand tether, and planned to deorbit a probe at near-interplanetary speed by swinging deployment of the tether system. For

safety considerations, after having reached the operative orbit, the tether was not deployed. The YES was switched on however to perform a number of secondary technology demonstration experiments. More recently, in 2007, other two missions were launched: Multi-Application Survivable Tether (MAST) for better studying the survivability of the tether in the space, but the deployment of the wire stopped after only 1km, and the YES2, an experiment for students sponsored always by ESA for investigating the reentry of a little capsule employing a 32 km tether. The communications system on the capsule failed, and the capsule was lost, but deployment telemetry indicated that the tether deployed to full length and that the capsule presumably deorbited as planned. In 2010 the Tether Technologies Rocket Experiment (T-REX) on board of sounding rocket S-520-25 was successfully launched reaching its maximum altitude of some 300 km. The aim of the experiment was to conduct basic experiments on the electrodynamic tether in the ionosphere and to control the attitude of a robot using a tether under the micro-gravity environment. The 300m long tape tether deployed as scheduled using the foldaway flat tether concept.

## 1.1 Electrodynamic Tethers and Applications

In the last years the electrodynamic tethers (EDT) concept has been deeply explored for its important technological implications [90][91]. Such a system can be thought as a simple conductive wire, where an electric current flows along it, and can work in passive or active mode. Basically it is a probe in mesothermal flow at highly positive (or negative) bias, with a large or extremely large 2D sheath, which may show effects from the magnetic self-field of its current and have electrons adiabatically trapped in its ram front. Passive tethers exploit electromagnetic laws to collect electrons from the ionosphere, while active ones are fed by an internal power generator and use the ionosphere to close the circuit. Beyond technical applications ranging from propellantless propulsion to power generation in orbit, EDTs allow broad scientific uses such as generating electron beams and artificial auroras, exciting Alfvén waves and whistlers, modifying the radiation belts and exploring interplanetary space and the Jovian magnetosphere.

The fundamental area of application of tethers (investigated through this thesis) is propellantless transportation: if a conductive tether carries a current as a result of interaction with the magnetized ionosphere, it will experience a Lorentz force. The space debris proliferation has focused the attention of science committee on passive tethers as deorbiting system. In fact the Earth's environment is particular favorable to fly such a system: the high electron density surrounding the planet at LEO orbits and the modest (if compared to other planetary magnetic fields, like Jupiter) magnetic field generate a non-negligible inducted potential, which lets the collection of electrons at the anodic end. Since Newton's third law applies to magnetic forces between steady-current systems, a net power loss is seen to occur in the tether-plasma interaction. The Lorentz force, generated by the interaction between the electric current flowing along the wire and the surrounding magnetic field, is a drag in LEO for both prograde and retrograde orbits. Like atmospheric drag, magnetic drag is a dissipative kinetic mechanism arising from the motion of orbiting tether/spacecraft relative to the corotating magnetized plasma, which induces the current in the tether. Deorbiting will be a perfect application for the slow, ambient dependent, average action of the Lorentz force of an ED-tether. Already by means moderate tether lengths a satellite can be reentered from LEO in few months, as a function of orbital parameters of the spacecraft. EDTs represent a very advantageous alternative to traditional chemical thrusters typically utilized, because it happens without ejection of propellant, as opposite rockets or electrical thrusters, and power supply.

In 1972, Nobel Prize winner H. Alfvén observed that the electric field at the highly conducting magnetized plasma around a wire travelling in the solar wind would be negligible in the plasma frame. The nonrelativistic electric-field transformation between reference frames respectively moving with ambient plasma and wire then shows that, at the plasma around and in the frame of the wire, there would be a so called “motional” field, which is given by the wire-to-plasma relative velocity times the ambient magnetic field  $B$ . The electromotive force for a wire of length  $L$  could drive a current in the wire, and makes powering of electrical thrusters for propulsion in interplanetary travel, possible.

A very interesting application of EDT systems concerns Jupiter. In fact, because of both rapid rotation (about ten hours period) and low mean density ( $1.32 \text{ g/cm}^3$ ), the stationary orbit of the planet is one third the relative distance for Earth. In turn, the magnetic field  $B$  at its surface is greater than at Earth’s by one order of magnitude (with the motional field near Jupiter more than one order of magnitude greater). As a result, there is magnetospheric plasma co-rotating beyond the stationary radius  $r_S$ , allowing for Lorentz thrust on tethers in prograde Jovian orbit beyond it. Insertion in orbit and touring the Jovian moons afterwards, which are transport applications of interest, prove possible, and a tens of kilometers long tape (with mass as a sensible fraction of the full spacecraft mass) is required. Radiation dose accumulated at repeated passes through the Jovian radiation belts appears as the limiting factor for such missions. This makes missions that avoid the belts, such as NASA’s Juno mission, particularly interesting. Typical power needs may be generated with tethers of moderate size and little effects on orbital dynamics because of the great gravitational attraction of Jupiter. This would also apply to a mission final stage, with a spacecraft starting in circular, equatorial orbit, safe below the Radiation Belts, at radius  $1.3/1.4R_J$ . A light, few kilometers long, thin tape bare-tether could make the spacecraft spiral in a controlled manner, over several months, while generating power onboard. A number of scientific goals might be attained. From its slowly decaying orbit the spacecraft could carry out spatially resolved observations as required for understanding transport in the atmosphere, and broad studies on its variability over different time scales. The proximity to Jupiter would allow highly accurate determination of magnetic and gravity fields and water content.

A tether carrying a steady current in the orbital frame ( $\omega = \vec{v}_{rel} \cdot \vec{k}$ , where  $\vec{k}$  is the wave vector), radiates waves with refraction index  $n = ck/\omega \gg 1$ , just allowing slow extraordinary (SE), fast magnetosonic (FM) and Alfvén (A) wave emission into the ionospheric cold plasma. It was recently suggested that current modulation in tethers could generate nonlinear, low frequency wave structures attached to the spacecraft. Whistlers could be excited by a planar array of electrodynamic tethers, made of two perpendicular rows of tethers that carry equal time-modulated currents with a  $90^\circ$  phase shift. The array would fly in the orbital equatorial plane, stabilized by the gravity gradient, which is perpendicular to the geomagnetic field when ignoring its tilt, and would serve to study wave interactions in space plasmas.

There is recent interest in artificially modifying the high-energy particle populations trapped in the Earth radiation belts. Their densities are small (typically  $10\text{m}^{-3}$ ) and natural replenishment rates are slow enough. Then, calculations of electron loss rates due to several natural mechanisms (Whistler waves or Coulomb scattering), and due to a few high power VLF ground antennas suggest that man-made wave injections can be a dominant depletion channel. Using ground stations for intentional belt clean-up is inefficient, however, because only a fraction of order of 1% of kilohertz power is coupled to whistler radiation through “plasma ducts” in the ionosphere. On the other hand, in situ emission by an orbiting spacecraft carrying a very long antenna (a tether) might be practical.

## 1.2 Space Debris

Since the 1957 launch of Sputnik I, humanity has been launching satellites into orbit, and dead SCs, upper stages and fragments due to explosion and collision fragments have been left in the space provoking nowadays a huge risk of impact with the operative missions [15][64]. All these objects, created by humans and no longer useful for any purpose, are called space debris and orbit around the Earth at high velocity. They include slag and dust from solid rocket motors, surface degradation products, coolant released, clusters of small needles, and residues of impacts of micrometeoroids or other debris onto spacecrafts. A recent estimation, done in 2008, about the mission flown till now tells approximately 6000 satellites have been placed into orbit since 1957, but only 800 are operative and roughly 45% of these are in LEO and GEO, while the most of the other dead satellite became and generated space debris. Public alarm over the debris problem has recently been aggravated by the rapid increase in the number of countries with direct access to space. Also, there have been several catastrophic events over the last three years, though the event altitude made a difference as regards debris. On 11 January 2007, a Chinese missile destroyed their Feng Yun 1C satellite at 862 km altitude, creating a 40000 piece debris field, with about 2500 trackable objects; on 10 Feb 2009, an American communication satellite, Iridium 33, collided with a Russian military satellite, Kosmos-2251, at 776 km altitude above Siberia, at a relative speed of almost 12km/s, again spreading a large amount of debris [15].

The United States Space Surveillance Network tracks, correlates and catalogues 21000 pieces above 5-10cm in LEO, which arose from in-orbit break-ups, from some 200 explosions due to residual fuel (and from less than 10 collisions). But that's not all, another big problem is that debris hitting debris create smaller pieces. A flux of pieces per unit area and time ranges over a large spectrum of sizes. That flux dominates over the natural meteoroid environment above the sub-millimetre size. Below 1mm, there is slag and dust that arose from more than 1000 solid rocket firings, and release from surface materials of old satellites and rocket bodies, due to impacts and/or surface degradation. Collisions among fragments larger than 10cm could trigger a Kessler cascade. The Kessler process originates in explosion fragments colliding with large objects and result in collision fragments, which may collide themselves with large objects, and produce further fragments. Finally collisions between fragments could result in a catastrophic cascade. Estimations suggest there are may exist 20000 pieces in the size range above 10cm. Also, over half a million pieces larger than 1cm, which could likely disable a satellite. And many millions of pieces above 1mm, their possible damaging effects being destruction of subsystems on board a spacecraft.

Moreover we must take into account that the great part of the estimated space debris are small particles, whose impact with the satellite cause highly destructive damages, similar to sandblasting. In fact the kind of impact generating during the collision is called hypervelocity, referring to a very high velocity, and in particular, to that situations in which sound velocity in the target's material is lower than the velocity of the impactor. This means the strength of material upon impact is very small compared to inertial stresses, so it has not the possibility to deformate to absorb impact energy. Hence the surface of the satellite hit by the object explodes in the region near the collision point generating a cloud of new debris and compromising the functionality of that subsystem or, worst, provoking the failure of the mission.

So the amount of space debris is continuously increasing becoming in the last two decade a serious problem to face and limit for guaranteeing to the new missions the access to the space in the future. That's why important actions must be taken for mitigating this threat, and why the reentry of the satellite must be included in order to limit as much as possible the proliferation of new debris. In this

contest the Inter-Agency Space Debris Coordination Committee (IADC) prepared and suggested a policy with the main guidelines about the procedure to follow carefully during the design of the satellite in order to foresee its reentry at the end of mission or its moving far from any orbit interesting for science or commercial scopes.

### 1.3 BETs Project

In this critical background the Bare Electrodynamic Tethers (BETs) project, called “Propellantless deorbiting of space debris by bare electrodynamic tethers” and financed by the European Commission through the FP7 funds, fits in with [92][93]. The aim of this project is focused on the study and design of an electromagnetic tether to be deployed by spacecrafts at the end of their operative lives to remove mechanical energy from their nominal orbit, and thereby decrease altitude, leading the faster re-entry till low quotes, where the Earth’s atmosphere is plenty to assure its total destruction before impacting on the surface.

An electrodynamic tether, as other components of a satellite, is a complex and heterogeneous system including a very wide range of aspects [82]. In fact the aim of BETs is to propose a system involving the interaction with the environment to generate an electric current along the wire, without any power supply from the satellite. For this reason the tethered system must be viewed from different point (electrical, mechanical, ...), in order that every part works in the right way.

Anodic contact is the hardest part: NASA/ASI TSS-1 (1992) and TSS-1R (1996) tethers carried insulation throughout their length and a big spherical conductor at the anodic end to collect electrons; the likewise insulated NASA PMG tether (1993) used a hollow-cathode device as anode, too. Both schemes prove inefficient. A breakthrough occurred in 1991 with the Bare Tether concept introduced by the Sanmartin [85], which would do away with the need for anodic device: a bare tether would collect electrons in the Orbital-Motion-Limited (OML) regime of cylindrical Langmuir probes [86], over an uninsulated tether segment coming out polarized positive. Collection can be efficient because the cross-section radius will be large compared with neither plasma Debye length nor gyroradius; also, substantial collection is possible because the positive segment may be kilometers long. The OML current to a thin-tape tether is proportional to the electron (particle) density  $N_e$  (which is equal to the ion density), to the collection area of the lateral surface of the tape, and to the electron velocity under the motional electromotive force voltage drop,  $\sqrt{2q_e v_{rel} BL/m_e}$ .

Current exchange is critical to an ED tether scheme. State-of-the-art hollow-cathode devices make for effective (low-impedance) cathodic contact. Further, they consume expellant at the hollow cathode at a negligible rate (an “equivalent” specific impulse, proportional to tether length, is typically orders of magnitude larger than in standard Ion Thrusters); the magnetic force itself requires no propellant. Actually, it might be possible, in the future, to use cathodic devices requiring no expellant at all, like field-emission array cathodes (FEACs). In any case, a tethered system proves the more convenient the longer the mission, because wire and related hardware make system dry-mass dominant.

The scientific/technological objective of the project is to prove that a tether system is an efficient system, capable of deorbiting a satellite in few months as a function of orbital parameters. Deorbiting altitudes from 800 to 1000 km, for a range of orbital inclination and satellite mass, will be considered in the project. A prototype tether would be designed, built and tested in the ground, for deorbiting a representative mass/orbit satellite. Approximate scaling laws would then be determined to simply adapt results to a broad range in those satellite parameters.

The work to do includes studies of plasma-tether interaction under ambient-plasma variations along

orbit, performance dependence on orbital altitude/inclination, and trade-off against alternative systems; numerical simulations of current to a bare tether; and studies of orbit/tether dynamics, and of both tether survival and the tether itself as debris. Other tasks involve the design and manufacturing of the tether as a tape with possible materials-structure both along its length and in its cross section, and a study of materials; the deployment strategy, and design/manufacturing of subsystems: tether-deployment mechanism and end-mass, electric control and driving module, electron-ejecting plasma contactor, and interface elements; and microgravity tests, and hypervelocity-impact and tether-current laboratory tests.

### 1.3.1 BETs Team and Work Packages

BETs Team is composed by seven members, mainly European, expert in several fields of applied sciences.

Participants	Country
UNIVERSIDAD POLITECNICA DE MADRID	Spain
CISAS, UNIVERSITÀ DEGLI STUDI DI PADOVA	Italy
ONERA	France
COLORADO STATE UNIVERSITY	United States
EMXYS	Spain
DLR	Germany
TECNALIA-INAS	Spain

Table 1.1: BETs Team

Each team member has several work packages to complete, whose topics can be divided as follows:

- i. Determining design criteria for sizing the three disparate dimensions of a tape tether, which appear in different effects dependent on ambient conditions that vary as spacecraft and tether lose altitude (plasma density, motional electric field). In fact the thickness of the wire introduces the characteristic length  $L^*$  which determines ohmic effects when compared with actual length  $L$ ; the width, when compared with Debye length (and electron gyroradius), determines whether current collection lies beyond the OML law regime. At last orbital inclination does fundamentally determine angles among field  $B$ , tether and spacecraft velocity, and tether along the vertical, affecting both Lorentz force direction and Lorentz drag power. Deorbiting from near-polar orbits poses a particular challenge in that the magnetic field lies nearly in the orbital plane, thus reducing the efficiency of vertical tethers.
- ii. Determining the relevance of a variety of orbit/tether-system dynamical effects. This requires:
  - (a) defining system characteristics like tether tip mass, tether type (all conductive or combined with a non-conductive portion) in relation to the deployment requirements of a light-mass deployer design;
  - (b) estimating the stability of tether oscillations as function of system parameters (tether length, system mass distribution, orbital altitude, etc.), and developing control laws, suitable for simple implementation, to stabilize tether oscillations, both in and off the orbital plane, at orbital altitudes where passive stability might be not sufficient;

- (c) evaluating the deorbit performance of stable light tether systems attached to different masses.
- iii. Determining a more accurate current to bare-tape law. Up to now the simulations lead at the Massachusetts Institute of Technology and Michigan University confirmed a detailed theory that ignores magnetic field  $B$  and orbital motion. These simplifications are sensible because the electron gyroradius will be large compared with the tether cross section and because the plasma flow past the tether is mesothermal, but there is a standing paradox to the contrary. Under conditions applying, the highly positive tether would ram hypersonic ions making  $N_i$  exceed its unperturbed value over a front region large compared with the Debye length, whereas  $N_e$  would remain below its unperturbed value everywhere, thus breaking quasineutrality. Adiabatic trapping, a basic phenomenon in collisionless plasmas was proposed to explain the paradox; this need be placed on a firm basis through very thorough simulations and chamber tests.
- iv. Determining the amount of charge ejected by the hollow cathode over the entire deorbit history, as affected by satellite mass and initial altitude. The hollow cathode might need operate over a large range of emission current, low at the beginning and high near the end of mission; and it might need also operate at minimum flow rate for a given condition of current, and use flow systems that are capable of providing a varying flow rate. It might be possible to work with expellant built in (“stored”) into the spacecraft structure itself.
- v. Determining requirements on an electronic control module that faces high operation voltage and power under mass and volume limitations. Expected high voltages (of the order of 1kV with delivered currents over 1A), pose severe requirements on magnetic components (input and output filter coil and transformer), power semiconductors, and materials used. The Project would consider integrated magnetics design (planar coils and transformers to improve volume distribution), DC/DC converter topologies, and power control methods under parallel power processing architectures. These innovations will produce a knowhow in high voltage power systems with powers one order of magnitude above those in current use, increasing the impact of the project on other relevant space (and even industrial) applications.
- vi. Determining the survivability of the tether itself to debris and micrometeoroids. The US Naval Research Laboratory (NRL), round-wire TiPS tether survived 12 years in orbit at altitude and inclination in the range here considered; a tape might survive longer due to the disparate character of width and thickness. This will involve estimating and assessing experimentally both damage to a tape caused by impactors with size much smaller than its width that hit it frontwise, and damage due to hits (nearly) edgewise. This would allow computing the overall survivability to hypervelocity impacts by taking into account incoming impactors at all angles. Hypervelocity impact tests will need be carried out. Modeling the effect of tape geometry could be compared to test results.
- vii. Determining tape structure as regards materials, both lengthwise and in its cross section. The tape might need a leading dielectric segment to help deployment; a bare conductive segment collecting current; and an insulated conductive segment next to the satellite to prevent arcing. A triple junction with the conductive segment polarized negative with respect to the plasma may result in arcing, which might be avoided by smoothing the electric field at the junction through use of a semiconductor sleeve. For a tape, heating is largely due to solar irradiation, as

opposed to heating from (accelerated) electron impact and to ohmic heating. Resulting large temperature oscillations would require a high-emissivity conductive coating.

- viii. Determining a passive deployment strategy for a conductive tape; with no retrieval needed, deployment need not be motorized either. Passive deployment of a wide tape along the axis of a stationary spool might result in jamming. The gravity gradient in LEO may make spinning to keep the tether taut unnecessary even at 1000 km altitude. Deployment should thus end in minimum libration of endmass and tether. In the absence of the centrifugal forces that would accompany spinning, the tape will need the leading plastic segment to help deployment till the gravity gradient takes over. The deployer itself might be ejected as part of the end mass.

### 1.3.2 CISAS

The work packages delivered to CISAS include three main topics: dynamics of the tether during deorbiting, deployment techniques and hypervelocity impact tests.

The work about the dynamics of EDT system can be separated in two main parts: tether dynamics and control, and orbital dynamics and performance analysis [113][114]:

- The former concerns the investigation, through analysis and simulation, about the dynamics of the flexible tether subjected to environmental perturbations (i.e. atmospheric drag at low altitudes and electrodynamic forces) to evaluate operational limits and to derive control strategies. The tether of an EDT system is subjected to many forces and torques: gravity gradient forces and torques that keep it taught and aligned with the local vertical and perturbation forces that tend to bend the tether and displace it from the local vertical. Among other perturbation forces, the electrodynamic forces and atmospheric drag (especially at low altitudes) have dominant effects, and as demonstrated by previous studies, the Lorentz forces eventually destabilize the librational and lateral (bending) dynamics of the tether. Consequently, an EDT system without any control may be forced to operate either for a short duration of time or at a low tether current (and hence with a low orbital decay). A first goal of this part is to characterize the dependencies of tether dynamics of a light bare tether system upon the system parameters. Then a second goal will involve the derivation of control strategies that are simple to implement, based on partial knowledge of the state vector, and capable of keeping the tether stable and hence making possible a fast orbital decay.
- The latter wants to better analyze and simulate the orbital dynamics of the system for realistic operational conditions to optimize the deorbiting performance of the EDT for payloads with various masses, orbital altitudes, and inclinations. For this reason an accurate dynamics simulator will be built for this type of analysis. The simulator will model the bending dynamics of the tether, have an Orbital Motion Limited (OML) electron collection model for the bare tether anode, a IGRF magnetic model, a IRI ionospheric density model, a MSIS atmospheric density model, a 4x4 gravity field (more than adequate for this application), and a tether thermal model that includes solar illumination, IR Earth radiation and albedo, ohmic heating of tether, tether IR emissivity and an electric resistance that depends upon the tether temperature. The simulation model will have to run relatively fast (i.e., it must not to be overloaded with unnecessary, high-frequency, elastic modes) because the number of simulations to be run is high. The goal of this package is to characterize the deorbiting performance to optimize some of the key system parameters.

The development of deployment strategies are extremely necessary for aligning the tether close to the local vertical at the end of the maneuver. Our objective is to reach the goal using as simple as possible deployment and control mechanisms, which will be designed by German partner.

Deploying a relatively-wide tape tether is a critical point because it will require the development of a specialized deployer design which in turn establishes the maximum velocity and acceleration that the deployer can sustain. The goal is to define strategies that provide a realistic description of the deployment for a tape tether, aligning it along the local vertical.

Hypervelocity impact tests are very important to assess the on-orbit survivability of tether designs subjected to the micrometeoroid and orbital debris (M/OD) threat. The risk assessment will include two aspects:

- the numerical evaluation of the M/OD impact probability on selected orbits, based upon the most recent environment models;
- the experimental derivation of ballistic limit equations (BLE) for tape tethers: engineering relations describing the combination of M/OD parameters (size, speed and impact angle) which is sufficient to just cut a given tether. Special attention will be paid to the assessment of tape tether vulnerability to shallow angle impacts



# Chapter 2

## Mathematical Models

In literature we can find two main models to describe the dynamics of a tethered system: the former simplifies the satellite like a rigid dumbbell model that cannot deform, the latter is more accurate and considers the wire as flexible. The dumbbell model is very useful to get rapid information about the system, investigate its performance and identify operative orbital scenarios. Instead the flexible wire gives a detailed description of attitude dynamics, studying also the lateral bending caused by the electrodynamic and aerodynamic force distributed along the tether. It helps us to get a complete representation of tether instantaneous shape including its first modal frequencies

### 2.1 Dumbbell Model

In the dumbbell model the tether is a thin rigid rod with mass  $m_t$  and length  $L$ , connecting two tips masses  $m_{sat}$  and  $m_B$ , the satellite and the ballast mass, respectively. The system is considered as undeformable and ignores all the elastic phenomena [1]. The plainness of this model allows to study the dynamical system by means of analytical approaches, and to derive simply equations of motion for an immediate numerical implementation. This method lets to investigate the main instability induced by the geometry of the system, eliminating those related to tether flexibility.

In the following a control technique by damping the libration energy in excess is proposed and investigated. The damper, placed between the satellite and the electrodynamic tether, permits to keep stable the tethered system around the instantaneous equilibrium position that is a function of the position and tether size. To study this kind of control strategy the simple dumbbell model is not sufficient, so other two model have been implemented to deal in a better way and consider in part the flexibility of the wire, but still with dumbbell elements.

#### 2.1.1 References Frames

In order to draw the equations of motion four reference systems have been adopted. The orbital motion will be studied with respect to inertial reference frame, while the attitude motion is easier to analyze with respect to body reference frame. To obtain the information about the local magnetic field, atmospheric and electron density we must refer to a geocentric system because all these greatness follow the diurnal rotation motion of the Earth. In the end, neglecting the contribution due to the torsion, the tether moves around the local vertical and this motion can be described by two libration angles: in-plane  $\theta$  and out-of-plane  $\varphi$ , see 2.1.

1. The Inertial reference frame I,  $O(\hat{i}, \hat{j}, \hat{k})$ :

$O$ : Origin of the Earth's center of mass

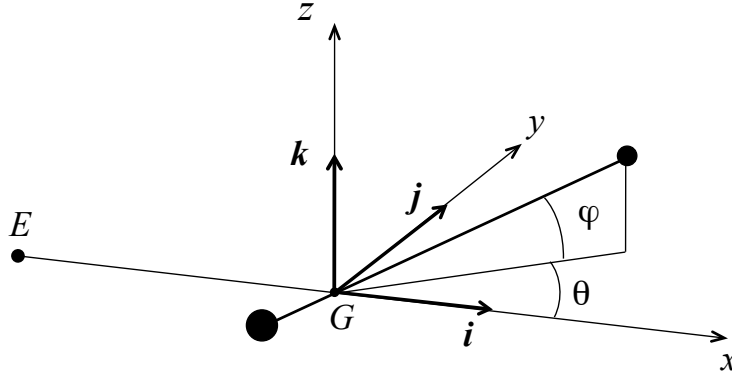


Figure 2.1: Synodic reference frame

$X_I$  - axis (unit vector  $\hat{i}$ ): pointing toward the first Aries point

$Z_I$  - axis (unit vector  $\hat{j}$ ): aligned with the Earth's rotational axis

$Y_I$  - axis (unit vector  $\hat{k}$ ): as a consequence

2. The Geocentric reference frame E, O( $\hat{e}_1, \hat{e}_2, \hat{e}_3$ ):

O: Origin of the Earth's center of mass

$x_E$  - axis (unit vector  $\hat{e}_1$ ): placed in the equatorial plane and pointing toward the Greenwich meridian

$z_E$  - axis (unit vector  $\hat{e}_2$ ): aligned with the Earth's rotational axis

$y_E$  - axis (unit vector  $\hat{e}_3$ ): in the equatorial plane as a consequence

3. The Synodic reference frame S, G( $\hat{s}_1, \hat{s}_2, \hat{s}_3$ ):

G: Tethered satellite's center of mass

$x_S$  - axis (unit vector  $\hat{s}_1$ ): placed in the orbital plane and aligned along the radial direction

$z_S$  - axis (unit vector  $\hat{s}_2$ ): perpendicular to orbital plane and aligned with the angular momentum unit vector

$y_S$  - axis (unit vector  $\hat{s}_3$ ): in the orbital plane as a consequence

4. The Body reference frame B, G( $\hat{b}_1, \hat{b}_2, \hat{b}_3$ ):

G: Tethered satellite's center of mass

$x_B$  - axis (unit vector  $\hat{b}_1$ ): pointing from  $m_{sat}$  toward  $m_B$

$y_B$  - axis (unit vector  $\hat{b}_2$ ): in the orbital plane and perpendicular to

$z_B$  - axis (unit vector  $\hat{b}_3$ ): as a consequence

The relations between each reference frame can be evaluated by means of opportune rotational matrices:

$$[R]_I^E = \begin{bmatrix} \cos \theta_E & -\sin \theta_E & 0 \\ \sin \theta_E & \cos \theta_E & 0 \\ 0 & 0 & 1 \end{bmatrix}$$

Where  $\theta_E$  is the rotation of the Earth around its axis:  $\theta_E = \Omega_E(t-t_0) = 2\pi(t-t_0)/T$ , and  $T$  the length of the sidereal day. For passing from the inertial frame to the synodic one four rotations are necessary in order to place the local reference system exactly in the center of mass of the satellite:

$$[R]_I^S = [R]_\Omega [R]_\theta [R]_\omega [R]_i$$

With  $\Omega$ ,  $i$ ,  $\omega$  and  $\theta$  the respective orbital parameters: argument of ascending node, inclination, argument of perigee and true anomaly.

$$[R]_{\Omega} = \begin{bmatrix} \cos \Omega & -\sin \Omega & 0 \\ \sin \Omega & \cos \Omega & 0 \\ 0 & 0 & 1 \end{bmatrix} \quad [R]_i = \begin{bmatrix} \cos i & 0 & -\sin i \\ 0 & 1 & 0 \\ \sin i & 0 & \cos i \end{bmatrix}$$

$$[R]_{\omega} = \begin{bmatrix} \cos \omega & -\sin \omega & 0 \\ \sin \omega & \cos \omega & 0 \\ 0 & 0 & 1 \end{bmatrix} \quad [R]_{\theta} = \begin{bmatrix} \cos \theta & -\sin \theta & 0 \\ \sin \theta & \cos \theta & 0 \\ 0 & 0 & 1 \end{bmatrix}$$

To determine the rotational matrix that brings to the body reference frame we must evaluate the libration angles and the orientation of three unit vectors  $\hat{\mathbf{u}}_1$ ,  $\hat{\mathbf{u}}_2$  and  $\hat{\mathbf{u}}_3$

$$[R]_S^B = \begin{bmatrix} \cos \theta \cos \phi & -\sin \theta & -\cos \theta \sin \phi \\ \sin \theta \cos \phi & \cos \theta & -\sin \theta \sin \phi \\ \sin \phi & 0 & \cos \phi \end{bmatrix}$$

So to pass from an inertial reference frame to body one becomes extremely easy, and it's sufficient to multiply the rotational matrices just calculated:

$$[R]_I^B = [R]_S^B [R]_I^S$$

An important property of rotational matrices is about its inverse, that is equal to the transpose matrix:

$$[R]_B^I = ([R]_I^B)^{-1} = ([R]_I^B)^T$$

### 2.1.2 Description of the Model

To describe the geometry and the mass distribution of a tethered satellite, in general it's helpful to introduce the  $m$ ,  $\lambda$  and  $\phi$  parameters. Instead of treating with the masses  $m_{sat}$ ,  $m_B$  and  $m_T$  other three variables can be defined from these: the total mass of the system is  $m = m_{sat} + m_B + m_T$ ,  $\lambda = m_T/m$  is the fractional of system mass, and  $\phi$  is the angle of mass, so calculated:

$$\cos^2 \phi = \frac{1}{m} \left[ m_{sat} + \frac{1}{2} m_T \right] \Rightarrow m_{sat} = m \left[ \cos^2 \phi - \frac{1}{2} \lambda \right] \quad (2.1)$$

$$\sin^2 \phi = \frac{1}{m} \left[ m_B + \frac{1}{2} m_T \right] \Rightarrow m_B = m \left[ \sin^2 \phi - \frac{1}{2} \lambda \right] \quad (2.2)$$

So called  $\vec{r}_G$  the position vector of the barycentre of the system from the centre of the Earth, the positions  $\vec{r}_1$  and  $\vec{r}_2$  of the two tip masses are determined by the following equations:

$$\begin{cases} \vec{r}_1 = \vec{r}_G - L \sin^2 \phi \hat{\mathbf{u}} \\ \vec{r}_2 = \vec{r}_G + L \cos^2 \phi \hat{\mathbf{u}} \end{cases}$$

The parameter  $\phi$  provides information about the position of barycenter, in particular the parameter  $h_G$  gives its distance from the mass  $m_B$ :  $h_G = L \cos^2 \phi \hat{\mathbf{u}}$ . The angle of mass cannot assume any values, but must be comprised in the interval  $[\phi_{min}, \phi_{max}]$ :

$$\begin{cases} \phi_{min} = \sin^{-1} \left( \sqrt{\frac{\lambda}{2}} \right) (m_B = 0) \\ \phi_{max} = \cos^{-1} \left( \sqrt{\frac{\lambda}{2}} \right) (m_{sat} = 0) \end{cases}$$

In the self-balanced configuration, where the tips masses are equal  $\phi = \frac{\pi}{4}$  and barycenter is exactly in the middle of the tether.

To know how the mass is distributed in the whole system is essential to study the attitude dynamics. The moment of inertia relative to a line perpendicular to the tether through  $G$  is  $I_s = \frac{1}{12}mL^2(3\sin^2\phi - 2\lambda)$ , and the inertial tensor in the body reference frame becomes:

$$[R]_\theta = \begin{bmatrix} 0 & 0 & 0 \\ 0 & I_s & 0 \\ 0 & 0 & I_s \end{bmatrix}$$

### 2.1.3 Orbital Motion

The orbital path followed by the EDT depends on all the forces acting on the system. In a detailed analysis the contributions are several, because the dynamics is affected by numerous interaction with the surrounding environment. We define three main contribution to the orbital dynamics: the gravitational, electrodynamic and aerodynamic forces, because are the major effects acting on the satellite in our orbital scenario.

#### Gravity Force

A tethered system can be long several kilometers, so its interaction with the Earth's gravitational field must be studied as that of an extended body. To investigate the gravitational effects some assumptions must be made, and in first approximation, the potential model of the gravity can be considered as spherical, and the higher harmonics of the gravitational potential neglected.

The potential of gravitational forces over the tether is given by:

$$V_{gr} = - \int_m \frac{\mu}{r} dm \quad (2.3)$$

where  $\mu = GM$  is the gravitational parameter of the attracting body (with  $G$  the universal gravitational constant and  $M$  the Earth's mass), and  $r$  the position of the infinitesimal mass  $dm$ .  $V_{gr}$  can be divided into three contributions:  $V_{gr} = V_{msat} + V_{mB} + V_T$ , where each term is given by:

$$V_{m_1} = -\frac{\mu}{r_1} m_{sat} \quad (2.4)$$

$$V_{m_B} = -\frac{\mu}{r_2} m_B \quad (2.5)$$

$$V_T = - \int_{m_T} \frac{\mu}{r} dm_T \quad (2.6)$$

The position of mass  $m_{sat}$  can be rewritten as:

$$r_1^2 = r_G^2 + L^2 \sin^4 \phi - 2L \sin^2 \phi \vec{r}_G \cdot \hat{u} = r_G^2 \left[ 1 - 2 \frac{L}{r_G} \sin^2 \phi \left( \frac{\vec{r}_G}{r_G} \cdot \hat{u} \right) + \frac{L^2}{r_G^2} \sin^4 \phi \right] \quad (2.7)$$

Substituting in the Eq. 2.4

$$V_{m_{sat}} = -\frac{\mu}{r_1} m_{sat} = -\frac{\mu}{r_G \sqrt{1 - 2 \frac{L}{r_G} \sin^2 \phi \left( \frac{\vec{r}_G}{r_G} \cdot \hat{u} \right) + \frac{L^2}{r_G^2} \sin^4 \phi}} m_{sat} \quad (2.8)$$

The square root at the denominator can be traced back to a well-known mathematical expression, and hence developed in series of Legendre polynomials:

$$\frac{1}{\sqrt{1 - 2\frac{L}{r_G} \sin^2 \phi \left( \frac{\vec{r}_G}{r_G} \cdot \hat{u} \right) + \frac{L^2}{r_G^2} \sin^4 \phi}} = \frac{1}{\sqrt{1 - 2\eta \cos \alpha + \eta^2}} = \sum_{n=0}^{\infty} \eta^n P_n[\cos \alpha] \quad (2.9)$$

With

$$\begin{cases} \eta &= \frac{L}{r_G} \sin^2 \phi \\ \cos \alpha &= \frac{\vec{r}_G}{r_G} \cdot \hat{u} \end{cases}$$

and  $\alpha$  representing the angle between the orientation of the wire and the local vertical. The first Legendre polynomials are:

$$\begin{cases} P_0[x] &= 1 \\ P_1[x] &= x \\ P_2[x] &= \frac{3x^2 - 1}{2} \\ P_3[x] &= \frac{5x^3 - 3x}{2} \\ P_4[x] &= \frac{35x^4 - 30x^2 + 3}{8} \end{cases}$$

The expression of gravitational potential of mass  $m_{sat}$  becomes:

$$V_{m_{sat}} = -\frac{\mu}{r_G} m_{sat} \sum_{n=0}^{\infty} \left( \frac{L}{r_G} \sin^2 \phi \right)^n P_n[\cos \alpha] \quad (2.10)$$

And in analogous way for mass  $m_B$ :

$$V_{m_B} = -\frac{\mu}{r_G} m_B \sum_{n=0}^{\infty} \left( -\frac{L}{r_G} \cos^2 \phi \right)^n P_n[\cos \alpha] \quad (2.11)$$

For what concerns the tether, the position of the infinitesimal element  $dm$  can be written as a function of a non dimensional variable  $s$  which varies in the interval  $[-\sin 2\phi, \cos 2\phi]$ :

$$\vec{r} = \vec{r}_G + sL\hat{u} \quad (2.12)$$

so

$$r^2 = r_G^2 + (sL)^2 + 2sL\vec{r}_G \cdot \hat{u} = r_G^2 \left[ 1 + 2\frac{L}{r_G} s \left( \frac{\vec{r}_G}{r_G} \cdot \hat{u} \right) + \left( \frac{L}{r_G} s \right)^2 \right] \quad (2.13)$$

Substituting Eq. 2.13 in Eq. 2.6

$$V_T = - \int_{m_T} \frac{\mu}{r} dm_T = \frac{\mu}{r} m_T \int_{-\sin^2 \phi}^{\cos^2 \phi} \frac{ds}{\sqrt{1 + 2\frac{L}{r_G} s \left( \frac{\vec{r}_G}{r_G} \cdot \hat{u} \right) + \left( \frac{L}{r_G} s \right)^2}} \quad (2.14)$$

The argument of the integral can be again developed in terms of Legendre polynomials

$$\begin{aligned} V_T &= -\frac{\mu}{r_G} m_T \int_{-\sin^2 \phi}^{\cos^2 \phi} \sum_{n=0}^{\infty} (-1)^n \left( \frac{L}{r_G} \right)^n s^n P_n[\cos \alpha] ds = \\ &= -\frac{\mu}{r_G} m_T \sum_{n=0}^{\infty} \frac{(-1)^n}{n+1} \left( \frac{L}{r_G} \right)^n [(\cos^2 \phi)^{n+1} - (-\sin^2 \phi)^{n+1}] P_n[\cos \alpha] \end{aligned} \quad (2.15)$$

Therefore the whole gravitational potential (till to  $n = 3$ ) becomes:

$$V_{gr} = -\frac{\mu}{r_G} m \left[ 1 + \left( \frac{L}{r_G} \right)^2 a_2 P_2[\cos \alpha] - \left( \frac{L}{r_G} \right)^3 a_3 P_3[\cos \alpha] \right] \quad (2.16)$$

With  $a_i$  coefficients independent on the size of the tether:

$$\begin{cases} a_1 = 0 \\ a_2 = \frac{1}{12} (3 \sin^2 2\phi - 2\lambda) \\ a_3 = \frac{1}{4} \cos 2\phi (\sin^2 2\phi - \lambda) \end{cases}$$

The resulting gravitational force acting on the satellite is given by the classical formula:

$$\vec{F}_{gr} = - \int_m \frac{\mu}{r^3} \vec{r} dm = \nabla V_{gr} \quad (2.17)$$

And so

$$\vec{F}_{gr} = - \frac{\mu}{r^2} m \left[ \hat{r} + \sum_{n=2}^{\infty} \left( \frac{L}{r} \right)^n a_n (S_n[\cos \alpha] \hat{r} - S_{n-1}[\cos \alpha] \hat{u}) \right] \quad (2.18)$$

Where the  $S_n[\cos \alpha]$  are the derivatives of Legendre polynomials:

$$\begin{cases} S_0[x] = 1 \\ S_1[x] = 3x \\ S_2[x] = \frac{3}{2} (5x^2 - 1) \\ S_3[x] = \frac{5}{2} (7x^3 - 3x) \\ S_4[x] = \frac{15}{8} (21x^4 - 14x^2 + 1) \end{cases}$$

Long tether affects the orbital motion of the whole system with second order terms provoking little perturbations, which magnitude is proportional to the  $(\frac{L}{r})^n$  ratio. Therefore when the satellite stays at high altitudes, mounts short tethers or the tip masses are much more heavy than tether one these perturbations can become very little respect to all the other forces (in particular the Lorentz one), so negligible in first approximation.

## Electrodynamic Force

Along the orbit the tether crosses continuously the magnetic field lines generating according to the Faraday's law a differential of potential  $\Delta V$  between the two ends:

$$\Delta V = L (\vec{v}_{rel} \times \vec{B}) \quad (2.19)$$

where  $\vec{v}_{rel}$  is the satellite relative velocity to the magnetic field. If the electric circuit is closed, a current  $I(s)$  can flow along the wire in direction from the Earth to the space if the tether moves eastward. This current interacts with the geomagnetic field and a drag Lorentz force is induced in the opposite direction of the orbital motion:

$$\vec{F}_{el} = \int_L I(s) \hat{u} \times \vec{B} ds \quad (2.20)$$

## Aerodynamic Force

The atmospheric density decrease in exponential trend versus the quote, therefore its effects become predominately at low altitude, causing a rapid decay of the satellite. The magnitude of aerodynamic force depends strongly on the geometry of the vehicle and in particular on the frontal surface:

$$\vec{F}_a = - \frac{1}{2} \int_A \rho c_D (\vec{v}_{rel} \cdot \hat{n}) \vec{v}_{rel} dA \quad (2.21)$$

Where  $\rho$  is the atmospheric density,  $c_D$  the drag coefficient (typically  $\approx 2$ ) and  $\hat{n}$  the unit vector perpendicular to the element surface. The relative velocity  $\vec{v}_{rel}$  is the same just evaluated for the Lorentz force, because we consider both magnetic field and atmosphere moving together with the Earth's rotation.

### 2.1.4 Attitude Motion

The attitude dynamics of the tether are governed by the angular momentum  $\vec{H}$ , that is the product between the inertial tensor  $\mathbf{I}$  and angular velocity  $\vec{\omega}$ :  $\vec{H} = \mathbf{I}\vec{\omega}$ . Its variation is due to the gravitational, electrodynamic and aerodynamic torques acting on the satellite:

$$\frac{d\vec{H}}{dt} = \vec{M}_{gr} + \vec{M}_{el} + \vec{M}_a \quad (2.22)$$

The angular velocity  $\vec{\omega}$  is given by:

$$\vec{\omega} = \hat{\mathbf{u}} \times \dot{\hat{\mathbf{u}}} + \alpha \hat{\mathbf{u}} \quad (2.23)$$

Where  $\dot{\hat{\mathbf{u}}}$  is the time derivative of tether orientation in the inertial reference frame, and  $\alpha$  the component along the tether. In general  $\alpha$  is very little, so negligible. Supposing the tether cannot lengthen or shorten the time variation of  $\vec{H}$  is:

$$d\vec{H} = \frac{d}{dt}(\mathbf{I}\vec{\omega}) = \mathbf{I}\dot{\hat{\mathbf{u}}} \times \dot{\hat{\mathbf{u}}} = \vec{M}_{gr} + \vec{M}_{el} + \vec{M}_a \quad (2.24)$$

In the body reference frame the attitude dynamics can be expressed as a function of libration angle in two non-linear and coupled differential equations:

$$\ddot{\theta} = \dot{\omega}_{orb} + 2(\dot{\theta} + \omega_{orb})\dot{\varphi} \tan \varphi + \vec{M}_{gr,\theta}^B + \vec{M}_{el,\theta}^B + \vec{M}_{a,\theta}^B \quad (2.25)$$

$$\ddot{\varphi} = -\frac{1}{2} \sin 2\varphi (\dot{\theta} + \omega_{orb})^2 + \vec{M}_{gr,\varphi}^B + \vec{M}_{el,\varphi}^B + \vec{M}_{a,\varphi}^B \quad (2.26)$$

#### Gravitational Torque

The gravity gradient torque is substantially due to how the mass is distributed respect to the center of mass of the satellite. The gravitational forces generate a momentum that tends to stabilize the satellite aligning it around its minimum inertia axes. Its mathematical expression is provide by:

$$\vec{M}_{gr} = - \int_m (\vec{r} - \vec{r}_G) \times \frac{\mu}{r^3} \vec{r} dm \quad (2.27)$$

Neglecting the terms of the order of  $\frac{L}{r}$  it is possible to obtain an approximated expression for  $\vec{M}_{gr}$ :

$$\vec{M}_{gr} \approx \frac{3\mu}{r^3} \hat{s}_1 \times (\mathbf{I} \circ \hat{s}_1) = \frac{3\mu}{r^3} I_s (\hat{\mathbf{u}} \times \hat{\mathbf{s}}) (\hat{\mathbf{u}} \cdot \hat{s}_1) \quad (2.28)$$

With the unit vector  $\hat{s}_1$  along the local vertical pointing to the zenith. Then in the body reference frame  $\vec{M}_{gr}^B$  is only function of  $\theta$  and  $\varphi$ :

$$\vec{M}_{gr}^B = \begin{pmatrix} 0 \\ M_{gr,\varphi}^B \\ M_{gr,\theta}^B \end{pmatrix} = -3I_s \omega_{orb}^2 \begin{pmatrix} 0 \\ \cos^2 \theta \sin \varphi \cos \varphi \\ \sin \theta \cos \theta \cos \varphi \end{pmatrix} \quad (2.29)$$

#### Electrodynamic Torque

The Lorentz torque  $\vec{M}_{el}$  caused by the current  $I(s)$  flowing along the wire is:

$$\vec{M}_{el} = J_1 \hat{\mathbf{u}} \times (\hat{\mathbf{u}} \times \vec{B}) \quad (2.30)$$

Where  $\vec{B}$  is the magnetic field of the Earth at  $\vec{r}_G$ , and  $J_1$  is a coefficients depending on the current profile:

$$J_1 = \int_{-\sin^2 \phi}^{\cos^2 \phi} I(s) (h_G - Ls) ds \quad (2.31)$$

In the body reference frame the unit vector  $\hat{u}$  assumes a particularly easy form:

$$\hat{u} = \begin{pmatrix} 1 \\ 0 \\ 0 \end{pmatrix}$$

So the electrodynamic torque becomes:

$$\vec{M}_{el}^B = \begin{pmatrix} 0 \\ M_{el,\varphi}^B \\ M_{el,\theta}^B \end{pmatrix} = -J_1 \begin{pmatrix} 0 \\ B_y^B \\ B_z^B \end{pmatrix} \quad (2.32)$$

With  $\vec{B}^B = [R]_E^B \vec{B}^E$ . In literature several models of Earth magnetic field exist: the non-tilted dipole, the tilted dipole, the eccentric offset dipole and the more accurate International Geomagnetic Reference Field (IGRF). The IGRF is a mathematical global model developed in series of Legendre, whose spherical harmonic coefficients are upload every five years.

The parameter  $\epsilon$ , that quantifies the intensity of the electrodynamic interaction with respect to the gravity gradient stability action, can be introduced. It is defined as the ratio between the two torques:

$$\epsilon = \frac{M_{el}}{M_{gr}} \quad (2.33)$$

and if we consider the simple dipole model:

$$\epsilon = \frac{J_1}{I_s} \frac{\mu_m}{\mu_E} \quad (2.34)$$

### Aerodynamic Torque

In the inertial reference system the aerodynamic torque is:

$$\vec{M}_a^I = -\frac{1}{2} \int_A (\vec{r} - \vec{r}_G) \times \rho c_D (\vec{v}_{rel} \cdot \hat{n}) \vec{v}_{rel} dA \quad (2.35)$$

And in the body reference frame becomes:

$$\vec{M}_a^B = \begin{pmatrix} 0 \\ M_{a,\varphi}^B \\ M_{a,\theta}^B \end{pmatrix} = [R]_I^B \vec{M}_a^I \quad (2.36)$$

### Linearized Attitude Motion

The linearization of the equations, that is significant in the case of little oscillation, let to obtain some interesting information about the attitude motion and, in particular, about the eigen-frequencies. After having done the opportune simplification the dynamical system can be written as:

$$\ddot{\theta} = -3\omega_{orb}^2 \theta \quad (2.37)$$

$$\ddot{\varphi} = -4\omega_{orb}^2 \varphi \quad (2.38)$$

Now the equations are decoupled and can be easily solved by means of Laplace transform:

$$\begin{aligned}\Theta s^2 &= -3\omega_{orb}^2 \Theta & (s^2 + 3\omega_{orb}^2) \Theta &= 0 \\ \Psi s^2 &= -4\omega_{orb}^2 \Psi & (s^2 + 4\omega_{orb}^2) \Psi &= 0\end{aligned}\quad (2.39)$$

And so, the typical eigen-frequencies are:  $\sqrt{3}f_{orb}$  for the in-plane motion and  $2f_{orb}$  for the out-plane one, respectively.

## 2.2 Flexible Tether

In the past a number of methods for modeling the tether flexibility have been used. They can be divided into continuous [21][69][97] and discrete models [16][19][35][53][72][81]. Continuous approach becomes very complex and cumbersome when also electrodynamic and other forces acts on the satellite, because they are function of several parameters as the temperature, the position, deformation and instantaneous shape of the tether. So this method leads to many numerical difficulties when we want to simulate the dynamics of the tether for high numbers of modes. To solve the motion of the whole system, avoiding mathematical complications, we can follow two main ways: the former technique considers the tether as inextensible and divides it in  $n$  rigid bars, while the latter is more accurate and evaluates also the axial deformation discretizing the wire as a series of lumped masses connected by massless elastic springs and dampers. For both cases the solution becomes more and more precise as the number of elements used increases, but this grows rapidly the computational time required for the solution. So the number of elements will be a tradeoff between a good prediction of the real motion and the minimization of the integration time without loss of fundamental information about critical aspects of the system.

### 2.2.1 Tension Along the Tether

In a tethered system, two masses orbiting at different heights share a common orbital frequency  $\omega_{orb}$ , so they must be subject to a tether tension, which compensate the excess or reduction in the velocity. In fact the upper mass runs at high velocity in order to follow the same orbit, while the lower mass must be slower waiting the rest of system spaces the same orbital angle.

The motion of the tether relative to inertial reference system can be described by a set of partial differential equations:

$$\frac{1}{L} \frac{\partial}{\partial s} \vec{Y} + \vec{f}_{el} + \vec{f}_a = \rho_T \frac{\partial^2}{\partial t^2} \vec{r} \quad (2.40)$$

where  $\vec{Y}$ ,  $\vec{f}_{el}$  and  $\vec{f}_a$  are the tension, Lorentz and aerodynamic forces per unit of length at the element  $dm$ , respectively. These equations must be integrated all along the wire with the opportune initial and boundary conditions at both the ends:

$$\begin{aligned}m_{sat} \ddot{\vec{r}}_1 &= \vec{Y}_1 + \vec{F}_{gr,1} & \text{at } s = s_1 \\ m_B \ddot{\vec{r}}_2 &= -\vec{Y}_2 + \vec{F}_{gr,2} & \text{at } s = s_2\end{aligned}\quad (2.41)$$

In deriving the expression and profile of tensile force along the wire we can assume three main kind of tether: massless tether, massive inextensible tether, massive extensible tether.

### 2.2.2 Massless Tether

If, in first approximation, we assume that all the force acting on the tether are masic and so dependent on the linear density  $\rho_T$  then Eq. 2.40 simplifies in:

$$\frac{1}{L} \frac{\partial}{\partial s} \vec{Y} = 0 \quad (2.42)$$

is that the tension is constant along the cable and assumes value:

$$\vec{Y} = m_{sat} \left( \ddot{\vec{r}}_1 + \frac{\mu}{r_1^3} \vec{r}_1 \right) = -m_{sat} \left( \ddot{\vec{r}}_2 + \frac{\mu}{r_2^3} \vec{r}_2 \right) \quad (2.43)$$

In the particular case the satellite follows a circular orbit:

$$Y = \frac{\mu m_{sat} m_B}{r_1^2 r_2^2} \frac{r_2^3 - r_1^3}{m_{sat} r_1 + m_B r_2} (\hat{\vec{r}}_2 - \hat{\vec{r}}_1) \quad (2.44)$$

In general Lorentz force cannot be modeled as masic force, because function of the electrodynamic interaction with the magnetic field. So Eq. 2.40 is

$$\frac{1}{L} \frac{\partial}{\partial s} \vec{Y} + \vec{f}_{el} = 0 \quad (2.45)$$

Supposing an electric current constant along the tether and integrating this set of partial differential equations with the same boundary conditions. The Lorentz force  $\vec{f}_{el}$  acts always perpendicular to the tether, bending it like a bow, so change the direction of the tension but no its magnitude, that remains constant along all the wire.

### 2.2.3 Massive Inextensible Tether

When also the mass of the tether is considered the tension must vary from an end to the other, because of the gravity forces acting in each infinitesimal element. In the case of inert tether, is that Lorentz force negligible, the tension increases moving away from  $m_{sat}$  reaching its maximum in the baycenter of the system, then decreases till to the value  $Y_2$ .

In electrodynamic applications all the contributions must be take into account, therefore the tension will change both in direction and intensity passing from  $m_{sat}$  and  $m_B$ . As it has just been said the dumbbell model is a particularly simple model and neglects several important effects. In fact, in a real system the tether is not perfectly rigid, and its flexibility affects the stability of the motion. Starting from the dumbbell configuration it's possible to develop more accurate models dividing the tether in several rigid rod connected to each other by means of spherical joints letting two degree of freedom. The torsional motion of the wire is neglected for the sake of simplicity and because no significant for our scope. So for every elements we add into the system we must determine its attitude and position respect to satellite. In such a model the tension is no directly evaluated (as we will see after in the lump masses approach), but anyway each elements affects the other through the joints, in fact the equations of motion are highly coupled.

In the following two cases are shown using two and three bars to discretize the tether. The equations of motion have been evaluated using *Mathematica*, a mathematical manipulator very useful to manage long equations and obtain analytical expressions. This approach is very powerful when the number of elements are fews, because the set of equations is compact and easier to be evaluated than lump masses case. But as the elements increase the equations becomes very difficult to treat, because extremely coupled. That's way the number of rods has been limited to three.

#### Two Bars Model

To evaluate the Lagrange function of the 2-Bars model, the Earth's gravity field is assumed spherical, so for the attitude dynamics we neglect the contribution of superior harmonics. Moreover we consider short tether so the ratio  $l/R_E$  tends to zero and the gravitational potential for unit of mass can be linearized as follows:

$$V_g = -\frac{\mu}{R_E} \left[ 1 - \frac{x \cdot i}{R_E} + \frac{3}{2} \left( \frac{x \cdot i}{R_E} \right) - \frac{1}{2} \frac{x \cdot x}{R_E^2} \right] \quad (2.46)$$

where  $(x, y, z)$  is the position of the point with respect to the synodic reference system orbiting around the Earth with angular velocity  $\omega$ . Instead the inertia acceleration can be derived from a velocity-dependent potential:

$$V_i = \mu m \left( \gamma^0 \cdot x - (\omega \times x)^2 - \frac{\omega \cdot (x \times \dot{x})}{2} \right) \quad (2.47)$$

where  $\gamma^0$  is the acceleration of the origin of the reference system. The kinetic energy for unit mass can be written as:

$$T = \frac{1}{2} \dot{x} \cdot \dot{x} \quad (2.48)$$

The lagrange function is evaluated integrating the sum of these three terms all along the tether:

$$\begin{aligned} L &= \int_0^{l_{tot}} \rho (T - V_g + V_i) dl \\ &= \int_0^{l_1} \rho (T - V_g + V_i) dl + \int_{l_1}^{l_2} \rho (T - V_g + V_i) dl + m_b (T - V_g + V_i) |_{l=l_1+l_2} \end{aligned} \quad (2.49)$$

where  $l_{tot}$ ,  $l_1$  and  $l_2$  are respectively the total length of the wire, and the length of each portion. Called  $l$  the generic point along the first part of the wire  $l_1$ , the position  $x$  and velocity  $\dot{x}$  will be:

$$x = l \begin{Bmatrix} \cos \theta_1 \cos \varphi_1 \\ \sin \theta_1 \cos \varphi_1 \\ \sin \varphi_1 \end{Bmatrix} \quad \dot{x} = l \begin{Bmatrix} -\sin \theta_1 \cos \varphi_1 \dot{\theta}_1 - \cos \theta_1 \sin \varphi_1 \dot{\varphi}_1 \\ \cos \theta_1 \cos \varphi_1 \dot{\theta}_1 - \sin \theta_1 \sin \varphi_1 \dot{\varphi}_1 \\ \cos \varphi_1 \dot{\varphi}_1 \end{Bmatrix}$$

while in the electrodynamic portion  $l_2$ :

$$\begin{aligned} x &= l_1 \begin{Bmatrix} \cos \theta_1 \cos \varphi_1 \\ \sin \theta_1 \cos \varphi_1 \\ \sin \varphi_1 \end{Bmatrix} + l \begin{Bmatrix} \cos \theta_2 \cos \varphi_2 \\ \sin \theta_2 \cos \varphi_2 \\ \sin \varphi_2 \end{Bmatrix} \\ \dot{x} &= l_1 \begin{Bmatrix} -\sin \theta_1 \cos \varphi_1 \dot{\theta}_1 - \cos \theta_1 \sin \varphi_1 \dot{\varphi}_1 \\ \cos \theta_1 \cos \varphi_1 \dot{\theta}_1 - \sin \theta_1 \sin \varphi_1 \dot{\varphi}_1 \\ \cos \varphi_1 \dot{\varphi}_1 \end{Bmatrix} + l \begin{Bmatrix} -\sin \theta_2 \cos \varphi_2 \dot{\theta}_2 - \cos \theta_2 \sin \varphi_2 \dot{\varphi}_2 \\ \cos \theta_2 \cos \varphi_2 \dot{\theta}_2 - \sin \theta_2 \sin \varphi_2 \dot{\varphi}_2 \\ \cos \varphi_2 \dot{\varphi}_2 \end{Bmatrix} \end{aligned}$$

The whole expression of Lagrangian function has been evaluated integrating Eq. 2.49 all along the tethered satellite. We can recognize three main contributions: the first two are very similar to that provided by dumbbell system, and respectively due to  $l_1$  and  $l_2$ , while the third term represents the coupling between the two parts.

$$\begin{aligned} L &= \frac{1}{6} l_1^2 \omega^2 (m_1 + 3(m_2 + m_B)) \left[ \cos^2 \varphi_1 \left( 3 \cos^2 \theta_1 + (1 + \dot{\theta}_1)^2 \right) + \dot{\varphi}_1^2 \right] \\ &+ \frac{1}{6} l_2^2 \omega^2 (m_2 + 3m_B) \left[ \cos^2 \varphi_2 \left( 3 \cos^2 \theta_2 + (1 + \dot{\theta}_2)^2 \right) + \dot{\varphi}_2^2 \right] \\ &+ \frac{1}{2} l_1 l_2 \omega^2 (m_2 + 2m_B) [3 \cos \theta_1 \cos \theta_2 \cos \varphi_1 \cos \varphi_2 \\ &+ \cos(\theta_1 - \theta_2) \cos \varphi_1 \cos \varphi_2 (1 + \dot{\theta}_1)(1 + \dot{\theta}_2) \\ &- \sin(\theta_1 - \theta_2) \sin \varphi_1 \cos \varphi_2 (1 + \dot{\theta}_2) \dot{\varphi}_1 \\ &+ \sin(\theta_1 - \theta_2) \cos \varphi_1 \sin \varphi_2 (1 + \dot{\theta}_1) \dot{\varphi}_2 \\ &+ \cos \varphi_1 \cos \varphi_2 \dot{\varphi}_1 \dot{\varphi}_2 + \cos(\theta_1 - \theta_2) \sin \varphi_1 \sin \varphi_2 \dot{\varphi}_1 \dot{\varphi}_2] \end{aligned} \quad (2.50)$$

The equations of motion can be found out choosing as generalized coordinates the libration angles  $\theta_1, \theta_2, \varphi_1, \varphi_2$ , and as independent variable the time t.

$$\frac{d}{dt} (\partial_{\dot{q}_i} L) - \partial_{q_i} L = (Q_{el} + Q_a)_i \quad (2.51)$$

We obtain a set of four second-order differential equation, which can be reformulated in a simpler matrix form, separating the different contributions:

$a_{ij}$  is the dynamical matrix

$b_i$  is the right terms vector: it contains the factors of the equation  $\frac{d}{dt} (\partial_{\dot{q}_i} L) - \partial_{q_i} L = 0$  that don't multiply the acceleration terms

$c_i$  is the electrodynamic generalized force vector

$d_i$  is the aerodynamic generalized force vector

$$\begin{bmatrix} a_{11} & a_{12} & a_{13} & a_{14} \\ a_{21} & a_{22} & a_{23} & a_{24} \\ a_{31} & a_{32} & a_{33} & a_{34} \\ a_{41} & a_{42} & a_{43} & a_{44} \end{bmatrix} \begin{bmatrix} \ddot{\theta}_1 \\ \ddot{\theta}_2 \\ \ddot{\varphi}_1 \\ \ddot{\varphi}_2 \end{bmatrix} = \begin{bmatrix} b_1 \\ b_2 \\ b_3 \\ b_4 \end{bmatrix} + \begin{bmatrix} c_1 \\ c_2 \\ c_3 \\ c_4 \end{bmatrix} + \begin{bmatrix} d_1 \\ d_2 \\ d_3 \\ d_4 \end{bmatrix} \quad (2.52)$$

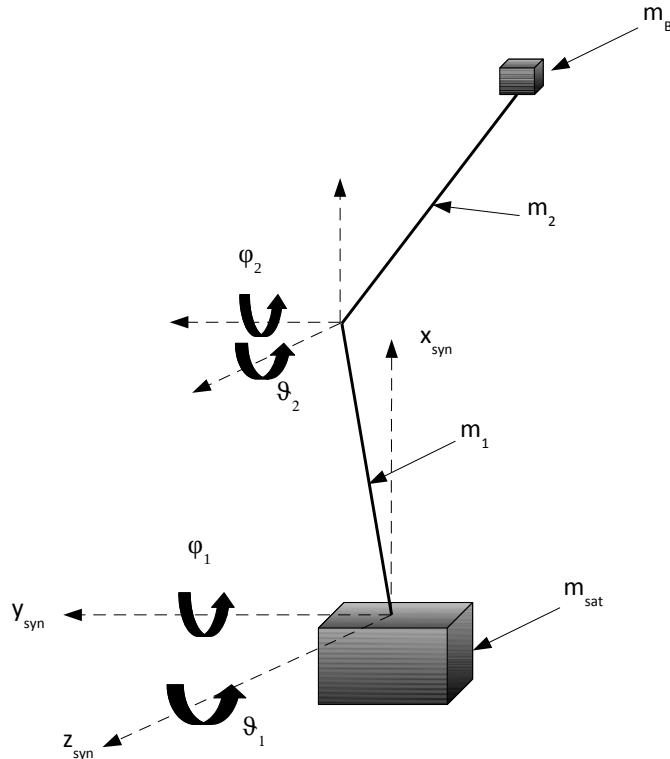


Figure 2.2: Two Bars Model of EDT system

$$\begin{bmatrix} \ddot{\theta}_1 \\ \ddot{\theta}_2 \\ \ddot{\varphi}_1 \\ \ddot{\varphi}_2 \end{bmatrix} = \begin{bmatrix} a_{11} & a_{12} & a_{13} & a_{14} \\ a_{21} & a_{22} & a_{23} & a_{24} \\ a_{31} & a_{32} & a_{33} & a_{34} \\ a_{41} & a_{42} & a_{43} & a_{44} \end{bmatrix}^{-1} \left( \begin{bmatrix} b_1 \\ b_2 \\ b_3 \\ b_4 \end{bmatrix} + \begin{bmatrix} c_1 \\ c_2 \\ c_3 \\ c_4 \end{bmatrix} + \begin{bmatrix} d_1 \\ d_2 \\ d_3 \\ d_4 \end{bmatrix} \right) \quad (2.53)$$

$$\begin{aligned}
 a_{11} &= \frac{1}{3}l_1^2(m_1 + 3(m_2 + m_B))\omega^2 \cos^2 \varphi_1 \\
 a_{12} &= \frac{1}{2}l_1 l_2(m_2 + 2m_B)\omega^2 \cos(\theta_1 - \theta_2) \cos \varphi_1 \cos \varphi_2 \\
 a_{13} &= a_{31} = a_{24} = a_{42} = 0 \\
 a_{14} &= \frac{1}{2}l_1 l_2(m_2 + 2m_B)\omega^2 \sin(\theta_1 - \theta_2) \cos \varphi_1 \cos \varphi_2 \\
 a_{22} &= \frac{1}{3}l_2^2(m_2 + 3m_B)\omega^2 \cos^2 \varphi_2 \\
 a_{23} &= a_{32} = -\frac{1}{2}l_1 l_2(m_2 + 2m_B)\omega^2 \sin(\theta_1 - \theta_2) \sin \varphi_1 \cos \varphi_2 \\
 a_{33} &= \frac{1}{3}l_1^2(m_1 + 3(m_2 + m_B))\omega^2 \\
 a_{34} &= a_{43} = \frac{1}{2}l_1 l_2(m_2 + 2m_B)\omega^2 (\cos \varphi_1 \cos \varphi_2 + \cos(\theta_1 - \theta_2) \sin \varphi_1 \sin \varphi_2) \\
 a_{44} &= \frac{1}{3}l_2^2(m_2 + 3m_B)\omega^2
 \end{aligned}$$

$$\begin{aligned}
 b_1 &= -\frac{1}{6}l_1^2(m_1 + 3(m_2 + m_B))\omega^2 \cos^2 \varphi_1 \left( 3 \sin 2\theta_1 \cos \varphi_1 - 4 \sin \varphi_1(1 + \dot{\theta}_1)\dot{\varphi}_1 \right) \\
 &- \frac{1}{2}l_1 l_2(m_2 + 2m_B)\omega^2 \cos \varphi_1 \left( \cos \varphi_2 (\sin \theta_1 \cos \theta_2(4 + \dot{\theta}_2(2 + \dot{\theta}_2)) - \cos \theta_1 \sin \theta_2(1 + \dot{\theta}_2)^2) \right. \\
 &\left. - \sin(\theta_1 - \theta_2) \cos \varphi_2 \dot{\varphi}_2^2 - 2 \cos(\theta_1 - \theta_2) \sin \varphi_2(1 + \dot{\theta}_2)\dot{\varphi}_2 \right) \\
 b_2 &= -\frac{1}{6}l_2^2(m_2 + 3m_B)\omega^2 \cos^2 \varphi_2 \left( 3 \sin 2\theta_2 \cos \varphi_2 - 4 \sin \varphi_2(1 + \dot{\theta}_2)\dot{\varphi}_2 \right) \\
 &+ \frac{1}{2}l_1 l_2(m_2 + 2m_B)\omega^2 \cos \varphi_2 \left( \cos \varphi_1 (\sin \theta_1 \cos \theta_2 - 4 \cos \theta_1 \sin \theta_2 + \sin(\theta_1 - \theta_2)\dot{\theta}_1(2 + \dot{\theta}_1)) \right. \\
 &\left. + 2 \cos(\theta_1 - \theta_2) \sin \varphi_1(1 + \dot{\theta}_1)\dot{\varphi}_1 + \sin(\theta_1 - \theta_2) \cos \varphi_1^2 \right) \\
 b_3 &= -\frac{1}{12}l_1^2(m_1 + 3(m_2 + m_B))\omega^2 \sin 2\varphi_1 \left( 5 + 3 \cos 2\theta_1 + 2\dot{\theta}_1(2 + \dot{\theta}_1) \right) \\
 &- \frac{1}{2}l_1 l_2(m_2 + 2m_B)\omega^2 \left( \sin \varphi_1 \cos \varphi_2 (\sin \theta_1 \sin \theta_2(1 + \dot{\theta}_2)^2 + \cos \theta_1 \cos \theta_2(4 + \dot{\theta}_2(2 + \dot{\theta}_2))) \right. \\
 &\left. - 2 \sin(\theta_1 - \theta_2) \sin \varphi_1 \sin \varphi_2(1 + \dot{\theta}_2)\dot{\varphi}_2 + (\cos(\theta_1 - \theta_2) \sin \varphi_1 \sin \varphi_2 - \cos \varphi_1 \sin \varphi_2)\dot{\varphi}_2^2 \right) \\
 b_4 &= -\frac{1}{12}l_2^2(m_2 + 3m_B)\omega^2 \sin 2\varphi_2 \left( 5 + 3 \cos 2\theta_3 + 2\dot{\theta}_3(2 + \dot{\theta}_3) \right) \\
 &- \frac{1}{2}l_1 l_2(m_2 + 2m_B)\omega^2 \left( \cos \varphi_1 \sin \varphi_2 (\sin \theta_1 \sin \theta_2(1 + \dot{\theta}_1)^2 + \cos \theta_1 \cos \theta_2(4 + \dot{\theta}_1(2 + \dot{\theta}_1))) \right. \\
 &\left. - 2 \sin(\theta_1 - \theta_2) \sin \varphi_1 \sin \varphi_2(1 + \dot{\theta}_1)\dot{\varphi}_1 + (\cos(\theta_1 - \theta_2) \cos \varphi_1 \sin \varphi_2 - \sin \varphi_1 \cos \varphi_2)\dot{\varphi}_1^2 \right)
 \end{aligned}$$

$$\begin{aligned}
 c_1 &= J_1(B_y \cos^2 \varphi_1 + (B_x \cos \theta_1 + B_z \sin \theta_1) \cos \varphi_1 \sin \varphi_1) \\
 &+ I_2 l_1 l_2 \cos \varphi_1 (B_y \cos(\theta_1 - \theta_2) \cos \varphi_2 + (B_x \cos \theta_1 + B_z \sin \theta_1) \sin \varphi_2) \\
 c_2 &= J_1(B_y \cos^2 \varphi_2 + (B_x \cos \theta_2 + B_z \sin \theta_2) \cos \varphi_2 \sin \varphi_2) \\
 c_3 &= J_1(B_z \cos \theta_1 + B_x \sin \theta_1) + I_2 l_1 l_2 ((B_z \cos \theta_2 + B_x \sin \theta_2) \cos \varphi_1 \cos \varphi_2 \\
 &- B_y \sin(\theta_1 - \theta_2) \sin \varphi_1 \cos \varphi_2 + (B_z \cos \theta_1 - B_x \sin \theta_1) \sin \varphi_1 \sin \varphi_2) \\
 c_4 &= J_2(B_z \cos \theta_2 + B_x \sin \theta_2)
 \end{aligned}$$

$$\begin{aligned}
 d_1 &= \frac{1}{2}l_1 \cos \varphi_1 ((f_{a,z}^1 + 2f_{a,z}^2) \cos \theta_1 - (f_{a,x}^1 + 2f_{a,x}^2) \sin \theta_1) \\
 d_2 &= \frac{1}{2}l_2 \cos \varphi_2 (f_{a,z}^1 \cos \theta_2 - f_{a,x}^2) \sin \theta_2 \\
 d_3 &= \frac{1}{2}l_1 ((f_{a,y}^1 + 2f_{a,y}^2) \cos \varphi_1 + ((f_{a,x}^1 + 2f_{a,x}^2) \cos \theta_1 + (f_{a,z}^1 + 2f_{a,z}^2) \sin \theta_1) \sin \varphi_1) \\
 d_3 &= \frac{1}{2}l_2 (f_{a,y}^2 \cos \varphi_2 + (f_{a,x}^2 \cos \theta_2 + f_{a,z}^2 \sin \theta_2) \sin \varphi_2)
 \end{aligned}$$

Where  $f_a^1$  and  $f_a^2$  are the aerodynamic forces calculated in the synodic reference frame and acting on the rigid rod element and the electrodynamic tether, respectively. By adding at the attack point a damping mechanism, which will be explained better in the Chapter 7, proportional to angle velocities  $\dot{\theta}_1$  and  $\dot{\varphi}_1$ , the structure of equation set changes as follows

$$\begin{bmatrix} \ddot{\theta}_1 \\ \ddot{\theta}_2 \\ \ddot{\varphi}_1 \\ \ddot{\varphi}_2 \end{bmatrix} = \begin{bmatrix} a_{11} & a_{12} & a_{13} & a_{14} \\ a_{21} & a_{22} & a_{23} & a_{24} \\ a_{31} & a_{32} & a_{33} & a_{34} \\ a_{41} & a_{42} & a_{43} & a_{44} \end{bmatrix}^{-1} \left( \begin{bmatrix} b_1 \\ b_2 \\ b_3 \\ b_4 \end{bmatrix} + \begin{bmatrix} c_1 \\ c_2 \\ c_3 \\ c_4 \end{bmatrix} + \begin{bmatrix} d_1 \\ d_2 \\ d_3 \\ d_4 \end{bmatrix} \right) + \begin{bmatrix} k_\theta \dot{\theta}_1 \\ 0 \\ k_\varphi \dot{\varphi}_1 \\ 0 \end{bmatrix} \quad (2.54)$$

Adopting the same procedure used for the dumbbell configuration, also for the two bars model we can obtain some information about the dynamical behavior of the tethered system. The set of equations must be linearized supposing little oscillations around the local vertical:

$$[a_{ij}]_{lin} \begin{bmatrix} \ddot{\theta}_1 & \ddot{\theta}_2 & \ddot{\varphi}_1 & \ddot{\varphi}_2 \end{bmatrix}^T = [b_j]_{lin} \quad (2.55)$$

where the linearized dynamical matrix  $[a_{ij}]_{lin}$  and vector  $[b_j]_{lin}$  are so defined:

$$[a_{ij}]_{lin} = \begin{bmatrix} \frac{1}{3}l_1^2(m_1 + 3(m_2 + m_B)) & \frac{1}{2}l_1l_2(m_2 + 2m_B) & 0 & 0 \\ \frac{1}{2}l_1l_2(m_2 + 2m_B) & \frac{1}{3}l_2^2(m_2 + 3m_B) & 0 & 0 \\ 0 & 0 & \frac{1}{3}l_1^2(m_1 + 3(m_2 + m_B)) & \frac{1}{2}l_1l_2(m_2 + 2m_B) \\ 0 & 0 & \frac{1}{2}l_1l_2(m_2 + 2m_B) & \frac{1}{3}l_2^2(m_2 + 3m_B) \end{bmatrix}$$

$$[b_j]_{lin} = \begin{bmatrix} -l_1^2(m_1 + 3(m_2 + m_B))\omega_{orb}^2\theta_1 - \frac{1}{2}l_1l_2(m_2 + 2m_B)\omega_{orb}^2(4\theta_1 - \theta_2) \\ \frac{1}{2}l_1l_2(m_2 + 2m_B)\omega_{orb}^2(\theta_1 - 4\theta_2) - l_2^2(m_2 + 3m_B)\omega_{orb}^2\theta_2 \\ -\frac{4}{3}l_1^2(m_1 + 3(m_2 + m_B))\omega_{orb}^2\varphi_1 - 2l_1l_2(m_2 + 2m_B)\omega_{orb}^2\varphi_1 \\ -\frac{1}{3}l_2^2(m_2 + 3m_B)\omega_{orb}^24\varphi_2 - \frac{1}{2}l_1l_2(m_2 + 2m_B)\omega_{orb}^24\varphi_2 \end{bmatrix}$$

The equations must be transformed in according to Laplace, and by solving the determinant of the dynamical matrix the four eigen-frequencies can be drawn characterizing the motion of the wire:

$$\begin{aligned} f_1 &= \sqrt{3}f_{orb} \\ f_2 &= 2f_{orb} \\ f_3 &= \sqrt{3}f_{orb}\sqrt{aL_1^2 + bL_2^2 + cL_1L_2}/\sqrt{dL_1L_2} \\ f_4 &= 2f_{orb}\sqrt{eL_1^2 + fL_2^2 + gL_1L_2}/\sqrt{hL_1L_2} \end{aligned} \quad (2.56)$$

where

$$\begin{aligned} a &= 8(m_2 + 2m_B)(m_1 + 3(m_2 + m_B)) \\ b &= 8(m_2 + 2m_B)(m_2 + 3m_B) \\ c &= 4m_1(m_2 + 3m_B) + 3(3m_2 + 4m_B)(3m_2 + 8m_B) \\ d &= 4m_1(m_2 + 3m_B) + 3m_2(m_2 + 4m_B) \\ \\ e &= 6(m_2 + 2m_B)(m_1 + 3(m_2 + m_B)) \\ f &= 6(m_2 + 2m_B)(m_2 + 3m_B) \\ g &= 4m_1(m_2 + 3m_B) + 3(7m_2^2 + 28m_2m_B + 24m_B^2) \\ h &= 4m_1(m_2 + 3m_B) + 3m_2(m_2 + 4m_B) \end{aligned}$$

The first two frequencies represent the libration motion, typical of the dumbbell system, while the last two describe the deflection of the wire along the in-plane and out-of-plane direction, that as we

expected depends on the configuration chosen for the tether, and so the size and mass of each bar. For example, considering a 5km long tether of mass 13.5kg, and a tip mass about 25kg, the eigen-frequencies are:

$$\begin{aligned} f_1 &= \sqrt{3}f_{orb} \\ f_2 &= 2f_{orb} \\ f_3 &= 10.647f_{orb} \\ f_4 &= 10.694f_{orb} \end{aligned}$$

where  $f_{orb} = \omega_{orb}/2\pi = 1.586 \times 10^{-4} \text{ Hz}$  at an altitude about 1000km.

### Three Bars Model

The lagrange function is provided by summing four terms: three for the tether and one for the tip mass:

$$\begin{aligned} L &= \int_0^{l_{tot}} \rho (T - V_g + V_i) dl \\ &= \int_0^{l_1} \rho (T - V_g + V_i) dl + \int_{l_1}^{l_2} \rho (T - V_g + V_i) dl \\ &+ \int_{l_2}^{l_3} \rho (T - V_g + V_i) dl + m_b (T - V_g + V_i) |_{l=l_1+l_2+l_3} \end{aligned} \quad (2.57)$$

Where the position  $x$  and velocity  $\dot{x}$  in the portions  $l_1$   $l_2$  and  $l_3$  are, respectively:

$$\begin{aligned} x &= l \begin{Bmatrix} \cos \theta_1 \cos \varphi_1 \\ \sin \theta_1 \cos \varphi_1 \\ \sin \varphi_1 \end{Bmatrix} & \dot{x} &= l \begin{Bmatrix} -\sin \theta_1 \cos \varphi_1 \dot{\theta}_1 - \cos \theta_1 \sin \varphi_1 \dot{\varphi}_1 \\ \cos \theta_1 \cos \varphi_1 \dot{\theta}_1 - \sin \theta_1 \sin \varphi_1 \dot{\varphi}_1 \\ \cos \varphi_1 \dot{\varphi}_1 \end{Bmatrix}, \\ x &= l_1 \begin{Bmatrix} \cos \theta_1 \cos \varphi_1 \\ \sin \theta_1 \cos \varphi_1 \\ \sin \varphi_1 \end{Bmatrix} + l \begin{Bmatrix} \cos \theta_2 \cos \varphi_2 \\ \sin \theta_2 \cos \varphi_2 \\ \sin \varphi_2 \end{Bmatrix} \\ x &= l_1 \begin{Bmatrix} -\sin \theta_1 \cos \varphi_1 \dot{\theta}_1 - \cos \theta_1 \sin \varphi_1 \dot{\varphi}_1 \\ \cos \theta_1 \cos \varphi_1 \dot{\theta}_1 - \sin \theta_1 \sin \varphi_1 \dot{\varphi}_1 \\ \cos \varphi_1 \dot{\varphi}_1 \end{Bmatrix} + l \begin{Bmatrix} -\sin \theta_2 \cos \varphi_2 \dot{\theta}_2 - \cos \theta_2 \sin \varphi_2 \dot{\varphi}_2 \\ \cos \theta_2 \cos \varphi_2 \dot{\theta}_2 - \sin \theta_2 \sin \varphi_2 \dot{\varphi}_2 \\ \cos \varphi_2 \dot{\varphi}_2 \end{Bmatrix} \end{aligned}$$

and

$$\begin{aligned} x &= l_1 \begin{Bmatrix} \cos \theta_1 \cos \varphi_1 \\ \sin \theta_1 \cos \varphi_1 \\ \sin \varphi_1 \end{Bmatrix} + l_2 \begin{Bmatrix} \cos \theta_2 \cos \varphi_2 \\ \sin \theta_2 \cos \varphi_2 \\ \sin \varphi_2 \end{Bmatrix} + l \begin{Bmatrix} \cos \theta_3 \cos \varphi_3 \\ \sin \theta_3 \cos \varphi_3 \\ \sin \varphi_3 \end{Bmatrix} \\ \dot{x} &= l_1 \begin{Bmatrix} -\sin \theta_1 \cos \varphi_1 \dot{\theta}_1 - \cos \theta_1 \sin \varphi_1 \dot{\varphi}_1 \\ \cos \theta_1 \cos \varphi_1 \dot{\theta}_1 - \sin \theta_1 \sin \varphi_1 \dot{\varphi}_1 \\ \cos \varphi_1 \dot{\varphi}_1 \end{Bmatrix} + l_2 \begin{Bmatrix} -\sin \theta_2 \cos \varphi_2 \dot{\theta}_2 - \cos \theta_2 \sin \varphi_2 \dot{\varphi}_2 \\ \cos \theta_2 \cos \varphi_2 \dot{\theta}_2 - \sin \theta_2 \sin \varphi_2 \dot{\varphi}_2 \\ \cos \varphi_2 \dot{\varphi}_2 \end{Bmatrix} \\ &+ l \begin{Bmatrix} -\sin \theta_3 \cos \varphi_3 \dot{\theta}_3 - \cos \theta_3 \sin \varphi_3 \dot{\varphi}_3 \\ \cos \theta_3 \cos \varphi_3 \dot{\theta}_3 - \sin \theta_3 \sin \varphi_3 \dot{\varphi}_3 \\ \cos \varphi_3 \dot{\varphi}_3 \end{Bmatrix} \end{aligned}$$

So Lagrangian function becomes:

$$\begin{aligned}
 L = & \frac{1}{6}l_1^2\omega^2(m_1 + 3(m_2 + m_3 + m_B)) \left[ \cos^2\varphi_1 \left( 3\cos^2\theta_1 + (1 + \dot{\theta}_1)^2 \right) + \dot{\varphi}_1^2 \right] \\
 & + \frac{1}{6}l_2^2\omega^2(m_2 + 3(m_2 + m_B)) \left[ \cos^2\varphi_2 \left( 3\cos^2\theta_2 + (1 + \dot{\theta}_2)^2 \right) + \dot{\varphi}_2^2 \right] \\
 & + \frac{1}{6}l_3^2\omega^2(m_3 + 3m_B) \left[ \cos^2\varphi_3 \left( 3\cos^2\theta_3 + (1 + \dot{\theta}_3)^2 \right) + \dot{\varphi}_3^2 \right] \\
 & + \frac{1}{2}l_1l_2\omega^2(m_2 + 2(m_3 + m_B)) [3\cos\theta_1\cos\theta_2\cos\varphi_1\cos\varphi_2 \\
 & + \cos(\theta_1 - \theta_2)\cos\varphi_1\cos\varphi_2(1 + \dot{\theta}_1)(1 + \dot{\theta}_2) \\
 & + \sin(\theta_1 - \theta_2)\cos\varphi_1\sin\varphi_2(1 + \dot{\theta}_1)\dot{\varphi}_2 \\
 & - \sin(\theta_1 - \theta_2)\sin\varphi_1\cos\varphi_2(1 + \dot{\theta}_2)\dot{\varphi}_1 \\
 & + \cos\varphi_1\cos\varphi_2\dot{\varphi}_1\dot{\varphi}_2 + \cos(\theta_1 - \theta_2)\sin\varphi_1\sin\varphi_2\dot{\varphi}_1\dot{\varphi}_2] \\
 & + \frac{1}{2}l_1l_3\omega^2(m_3 + 2m_B) [3\cos\theta_1\cos\theta_3\cos\varphi_1\cos\varphi_3 \\
 & + \cos(\theta_1 - \theta_3)\cos\varphi_1\cos\varphi_3(1 + \dot{\theta}_1)(1 + \dot{\theta}_3) \\
 & + \sin(\theta_1 - \theta_3)\cos\varphi_1\sin\varphi_3(1 + \dot{\theta}_1)\dot{\varphi}_3 \\
 & - \sin(\theta_1 - \theta_3)\sin\varphi_1\cos\varphi_3(1 + \dot{\theta}_3)\dot{\varphi}_1 \\
 & + \cos\varphi_1\cos\varphi_3\dot{\varphi}_1\dot{\varphi}_3 + \cos(\theta_1 - \theta_3)\sin\varphi_1\sin\varphi_3\dot{\varphi}_1\dot{\varphi}_3] \\
 & + \frac{1}{2}l_2l_3\omega^2(m_3 + 2m_B) [3\cos\theta_2\cos\theta_3\cos\varphi_2\cos\varphi_3 \\
 & + \cos(\theta_2 - \theta_3)\cos\varphi_2\cos\varphi_3(1 + \dot{\theta}_2)(1 + \dot{\theta}_3) \\
 & + \sin(\theta_2 - \theta_3)\cos\varphi_2\sin\varphi_3(1 + \dot{\theta}_2)\dot{\varphi}_3 \\
 & - \sin(\theta_2 - \theta_3)\sin\varphi_2\cos\varphi_3(1 + \dot{\theta}_3)\dot{\varphi}_2 \\
 & + \cos\varphi_2\cos\varphi_3\dot{\varphi}_2\dot{\varphi}_3 + \cos(\theta_2 - \theta_3)\sin\varphi_2\sin\varphi_3\dot{\varphi}_2\dot{\varphi}_3]
 \end{aligned} \tag{2.58}$$

As before, the equations of motion can be found out choosing as generalized coordinates the libration angles  $\theta_1, \theta_2, \theta_3, \varphi_1, \varphi_2, \varphi_3$ . Then in matrix form:

$$\begin{bmatrix} a_{11} & a_{12} & a_{13} & a_{14} & a_{15} & a_{16} \\ a_{21} & a_{22} & a_{23} & a_{24} & a_{25} & a_{26} \\ a_{31} & a_{32} & a_{33} & a_{34} & a_{35} & a_{36} \\ a_{41} & a_{42} & a_{43} & a_{44} & a_{45} & a_{46} \\ a_{51} & a_{52} & a_{53} & a_{54} & a_{55} & a_{56} \\ a_{61} & a_{62} & a_{63} & a_{64} & a_{65} & a_{66} \end{bmatrix} \begin{bmatrix} \ddot{\theta}_1 \\ \ddot{\theta}_2 \\ \ddot{\theta}_3 \\ \ddot{\varphi}_1 \\ \ddot{\varphi}_2 \\ \ddot{\varphi}_3 \end{bmatrix} = \begin{bmatrix} b_1 \\ b_2 \\ b_3 \\ b_4 \\ b_5 \\ b_6 \end{bmatrix} + \begin{bmatrix} c_1 \\ c_2 \\ c_3 \\ c_4 \\ c_5 \\ c_6 \end{bmatrix} + \begin{bmatrix} d_1 \\ d_2 \\ d_3 \\ d_4 \\ d_5 \\ d_6 \end{bmatrix} \tag{2.59}$$

$$\begin{aligned}
 a_{11} &= \frac{1}{3}L_1^2(m_1 + 3(m_2 + m_3 + m_B))\omega^2\cos^2\varphi_1 \\
 a_{12} &= a_{21} = \frac{1}{2}L_1L_2(m_2 + 2(m_3 + m_B))\omega^2\cos(\theta_1 - \theta_2)\cos\varphi_1\cos\varphi_2 \\
 a_{13} &= a_{31} = \frac{1}{2}L_1L_3(m_3 + 2m_B)\omega^2\cos(\theta_1 - \theta_3)\cos\varphi_1\cos\varphi_3 \\
 a_{14} &= a_{25} = a_{36} = a_{41} = a_{52} = a_{63} = 0 \\
 a_{15} &= a_{51} = \frac{1}{2}L_1L_2(m_2 + 2(m_3 + m_B))\omega^2\cos\varphi_1\sin(\theta_1 - \theta_2)\sin\varphi_2 \\
 a_{16} &= a_{61} = \frac{1}{2}L_1L_3(m_3 + 2m_B)\omega^2\cos\varphi_1\sin(\theta_1 - \theta_3)\sin\varphi_3 \\
 a_{22} &= \frac{1}{3}L_2^2(m_2 + 3(m_3 + m_B))\omega^2\cos^2\varphi_2 \\
 a_{23} &= a_{32} = \frac{1}{2}L_2L_3(m_3 + 2m_B)\omega^2\cos(\theta_2 - \theta_3)\cos\varphi_2\cos\varphi_3 \\
 a_{24} &= a_{42} = -\frac{1}{2}L_1L_2(m_2 + 2(m_3 + m_B))\omega^2\cos\varphi_2\sin(\theta_1 - \theta_2)\sin\varphi_1 \\
 a_{26} &= a_{62} = \frac{1}{2}L_2L_3(m_3 + 2m_B)\omega^2\cos\varphi_2\sin(\theta_2 - \theta_3)\sin\varphi_3 \\
 a_{33} &= \frac{1}{3}L_3^2(m_3 + 3m_B)\omega^2\cos^2\varphi_3 \\
 a_{34} &= a_{43} = -\frac{1}{2}L_1L_3(m_3 + 2m_B)\omega^2\cos\varphi_3\sin(\theta_1 - \theta_3)\sin\varphi_1 \\
 a_{35} &= a_{53} = -\frac{1}{2}L_2L_3(m_3 + 2m_B)\omega^2\cos\varphi_3\sin(\theta_2 - \theta_3)\sin\varphi_2
 \end{aligned}$$

$$\begin{aligned}
 a_{44} &= \frac{1}{3}L_1^2(m_1 + 3(m_2 + m_3 + m_B))\omega^2 \\
 a_{45} &= a_{54} = \frac{1}{2}L_1L_2(m_2 + 2(m_3 + m_B))\omega^2(\cos\varphi_1\cos\varphi_2 + \cos(\theta_1 - \theta_2)\sin\varphi_1\sin\varphi_2) \\
 a_{46} &= a_{64} = \frac{1}{2}L_1L_3(m_3 + 2m_B)\omega^2(\cos\varphi_1\cos\varphi_3 + \cos(\theta_1 - \theta_3)\sin\varphi_1\sin\varphi_3) \\
 a_{55} &= \frac{1}{3}L_2^2(m_2 + 3(m_3 + m_B))\omega^2 \\
 a_{56} &= a_{65} = \frac{1}{2}L_2L_3(m_3 + 2m_B)\omega^2(\cos\varphi_2\cos\varphi_3 + \cos(\theta_2 - \theta_3)\sin\varphi_2\sin\varphi_3) \\
 a_{66} &= \frac{1}{3}L_3^2(m_3 + 3m_B)\omega^2
 \end{aligned}$$

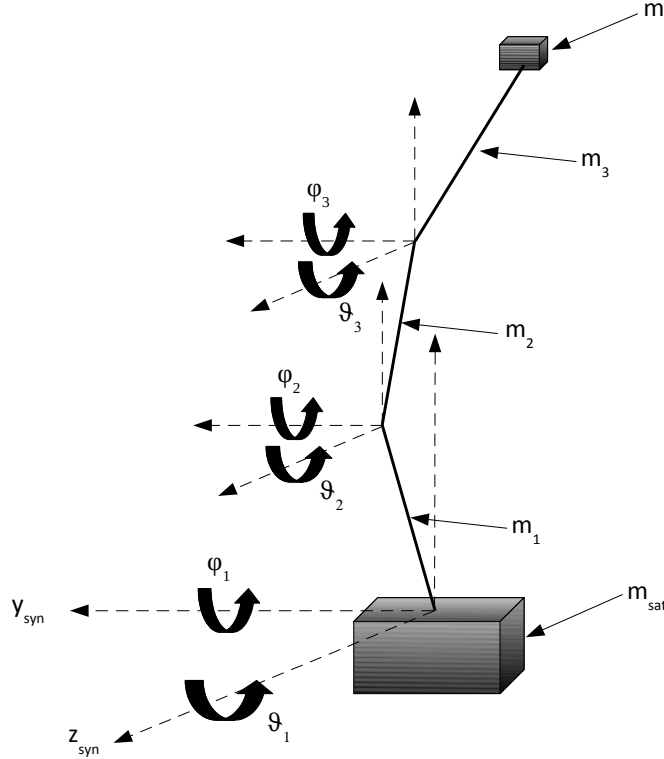


Figure 2.3: Three Bars Model of EDT system

$$\begin{aligned}
 b_1 &= -\frac{1}{6}L_1^2(m_1 + 3(m_2 + m_3 + m_B))\omega^2 \cos\varphi_1(3\cos\varphi_1\sin 2\theta_1 - 4\sin\varphi_1(1 + \dot{\theta}_1)\dot{\varphi}_1) \\
 &\quad - \frac{1}{2}L_1L_2(m_2 + 2(m_3 + m_B))\omega^2 \cos\varphi_1(\cos\varphi_2(4\cos\theta_2\sin\theta_1 - \cos\theta_1\sin\theta_2 \\
 &\quad + \sin(\theta_1 - \theta_2)\dot{\theta}_2(2 + \dot{\theta}_2)) - 2\cos(\theta_1 - \theta_2)\sin\varphi_2(1 + \dot{\theta}_2)\dot{\varphi}_2 + \cos\varphi_2\sin(\theta_1 - \theta_2)\dot{\varphi}_2^2) \\
 &\quad - \frac{1}{2}L_1L_3(m_3 + 2m_B)\omega^2 \cos\varphi_1(\cos\varphi_3(4\cos\theta_3\sin\theta_1 - \cos\theta_1\sin\theta_3 \\
 &\quad + \sin(\theta_1 - \theta_3)\dot{\theta}_3(2 + \dot{\theta}_3)) - 2\cos(\theta_1 - \theta_3)\sin\varphi_3(1 + \dot{\theta}_3)\dot{\varphi}_3 + \cos\varphi_3\sin(\theta_1 - \theta_3)\dot{\varphi}_3^2) \\
 b_2 &= \frac{1}{2}L_1L_2(m_2 + 2(m_3 + m_B))\omega^2 \cos\varphi_2(\cos\varphi_1(\cos\theta_2\sin\theta_1 - 4\cos\theta_1\sin\theta_2 \\
 &\quad + \sin(\theta_1 - \theta_2)\dot{\theta}_1(2 + \dot{\theta}_1)) + 2\cos(\theta_1 - \theta_2)\sin\varphi_1(1 + \dot{\theta}_1)\dot{\varphi}_1 + \cos\varphi_1\sin(\theta_1 - \theta_2)\dot{\varphi}_1^2) \\
 &\quad - \frac{1}{6}L_2^2(m_2 + 3(m_3 + m_B))\omega^2 \cos\varphi_2(3\cos\varphi_2\sin 2\theta_2 - 4\sin\varphi_2(1 + \dot{\theta}_2)\dot{\varphi}_2) \\
 &\quad - \frac{1}{2}L_2L_3(m_3 + 2m_B)\omega^2 \cos\varphi_2(\cos\varphi_3(4\cos\theta_3\sin\theta_2 - \cos\theta_2\sin\theta_3 \\
 &\quad + \sin(\theta_2 - \theta_3)\dot{\theta}_3(2 + \dot{\theta}_3)) - 2\cos(\theta_2 - \theta_3)\sin\varphi_3(1 + \dot{\theta}_3)\dot{\varphi}_3 + \cos\varphi_3\sin(\theta_2 - \theta_3)\dot{\varphi}_3^2) \\
 b_3 &= \frac{1}{2}L_1L_3(m_3 + 2m_B)\omega^2 \cos\varphi_3(\cos\varphi_1(\cos\theta_3\sin\theta_1 - 4\cos\theta_1\sin\theta_3 \\
 &\quad + \sin(\theta_1 - \theta_3)\dot{\theta}_1(2 + \dot{\theta}_1)) + 2\cos(\theta_1 - \theta_3)\sin\varphi_1(1 + \dot{\theta}_1)\dot{\varphi}_1 + \cos\varphi_1\sin(\theta_1 - \theta_3)\dot{\varphi}_1^2) \\
 &\quad + \frac{1}{2}L_2L_3(m_3 + 2m_B)\omega^2 \cos\varphi_3(\cos\varphi_2(\cos\theta_3\sin\theta_2 - 4\cos\theta_2\sin\theta_3 \\
 &\quad + \sin(\theta_2 - \theta_3)\dot{\theta}_2(2 + \dot{\theta}_2)) + 2\cos(\theta_2 - \theta_3)\sin\varphi_2(1 + \dot{\theta}_2)\dot{\varphi}_2 + \cos\varphi_2\sin(\theta_2 - \theta_3)\dot{\varphi}_2^2) \\
 &\quad - \frac{1}{6}L_3^2(m_3 + 3m_B)\omega^2 \cos\varphi_3(3\cos\varphi_3\sin 2\theta_3 - 4\sin\varphi_3(1 + \dot{\theta}_3)\dot{\varphi}_3)
 \end{aligned}$$

$$\begin{aligned}
 b_4 &= -\frac{1}{6}L_1^2(m_1 + 3(m_2 + m_3 + m_B))\omega^2 \sin 2\varphi_1(3 \cos \theta_1^2 + (1 + \dot{\theta}_1)^2) \\
 &- \frac{1}{2}L_1L_2(m_2 + 2(m_3 + m_B))\omega^2(\cos \varphi_2 \sin \varphi_1(4 \cos \theta_1 \cos \theta_2 + \sin \theta_1 \sin \theta_2 \\
 &+ \cos(\theta_1 - \theta_2)\dot{\theta}_2(2 + \dot{\theta}_2)) + 2 \sin(\theta_1 - \theta_2) \sin \varphi_1 \sin \varphi_2(1 + \dot{\theta}_2)\dot{\varphi}_2 + (\cos(\theta_1 - \theta_2) \cos \varphi_2 \sin \varphi_1 \\
 &- \cos \varphi_1 \sin \varphi_2)\dot{\varphi}_2^2) - \frac{1}{2}L_1L_3(m_3 + 2m_B)\omega^2(\cos \varphi_3 \sin \varphi_1(4 \cos \theta_1 \cos \theta_3 + \sin \theta_1 \sin \theta_3 \\
 &+ \cos(\theta_1 - \theta_3)\dot{\theta}_3(2 + \dot{\theta}_3)) + 2 \sin(\theta_1 - \theta_3) \sin \varphi_1 \sin \varphi_3(1 + \dot{\theta}_3)\dot{\varphi}_3 \\
 &+ (\cos(\theta_1 - \theta_3) \cos \varphi_3 \sin \varphi_1 - \cos \varphi_1 \sin \varphi_3)\dot{\varphi}_3^2) \\
 \\ 
 b_5 &= -\frac{1}{6}L_2^2(m_2 + 3(m_3 + m_B))\omega^2 \sin 2\varphi_2(3 \cos \theta_2^2 + (1 + \dot{\theta}_2)^2) \\
 &- \frac{1}{2}L_1L_2(m_2 + 2(m_3 + m_B))\omega^2(\cos \varphi_1 \sin \varphi_2(4 \cos \theta_1 \cos \theta_2 + \sin \theta_1 \sin \theta_2 \\
 &+ \cos(\theta_1 - \theta_2)\dot{\theta}_1(2 + \dot{\theta}_1)) - 2 \sin(\theta_1 - \theta_2) \sin \varphi_1 \sin \varphi_2(1 + \dot{\theta}_1)\dot{\varphi}_1 + (\cos(\theta_1 - \theta_2) \cos \varphi_1 \sin \varphi_2 \\
 &- \cos \varphi_2 \sin \varphi_1)\dot{\varphi}_1^2) - \frac{1}{2}L_2L_3(m_3 + 2m_B)\omega^2(\cos \varphi_3 \sin \varphi_2(4 \cos \theta_2 \cos \theta_3 + \sin \theta_2 \sin \theta_3 \\
 &+ \cos(\theta_2 - \theta_3)\dot{\theta}_3(2 + \dot{\theta}_3)) + 2 \sin(\theta_2 - \theta_3) \sin \varphi_2 \sin \varphi_3(1 + \dot{\theta}_3)\dot{\varphi}_3 \\
 &+ (\cos(\theta_2 - \theta_3) \cos \varphi_3 \sin \varphi_2 - \cos \varphi_2 \sin \varphi_3)\dot{\varphi}_3^2) \\
 \\ 
 b_6 &= -\frac{1}{6}L_3^2(m_3 + 3m_B)\omega^2 \sin 2\varphi_3(3 \cos \theta_3^2 + (1 + \dot{\theta}_3)^2) \\
 &- \frac{1}{2}L_1L_3(m_3 + 2m_B)\omega^2(\cos \varphi_1 \sin \varphi_3(4 \cos \theta_1 \cos \theta_3 + \sin \theta_1 \sin \theta_3 \\
 &+ \cos(\theta_1 - \theta_3)\dot{\theta}_1(2 + \dot{\theta}_1)) - 2 \sin(\theta_1 - \theta_3) \sin \varphi_1 \sin \varphi_3(1 + \dot{\theta}_1)\dot{\varphi}_1 + (\cos(\theta_1 - \theta_3) \cos \varphi_1 \sin \varphi_3 \\
 &- \cos \varphi_3 \sin \varphi_1)\dot{\varphi}_1^2) - \frac{1}{2}L_2L_3(m_3 + 2m_B)\omega^2(\cos \varphi_2 \sin \varphi_3(4 \cos \theta_2 \cos \theta_3 + \sin \theta_2 \sin \theta_3 \\
 &+ \cos(\theta_2 - \theta_3)\dot{\theta}_2(2 + \dot{\theta}_2)) - 2 \sin(\theta_2 - \theta_3) \sin \varphi_2 \sin \varphi_3(1 + \dot{\theta}_2)\dot{\varphi}_2 \\
 &+ (\cos(\theta_2 - \theta_3) \cos \varphi_3 \sin \varphi_2 - \cos \varphi_3 \sin \varphi_2)\dot{\varphi}_2^2) \\
 \\ 
 c_1 &= J_1(B_y \cos \varphi_1^2 + \cos \varphi_1(B_x \cos \theta_1 + B_z \sin \theta_1) \sin \varphi_1) + I_2L_1L_2 \cos \varphi_1(B_y \cos(\theta_1 - \theta_2) \cos \varphi_2 \\
 &+ (B_x \cos \theta_1 + B_z \sin \theta_1) \sin \varphi_2) + I_3L_1L_3 \cos \varphi_1(B_y \cos(\theta_1 - \theta_3) \cos \varphi_3 \\
 &+ (B_x \cos \theta_1 + B_z \sin \theta_1) \sin \varphi_3) + I_3L_2L_3 \cos \varphi_1(\cos \varphi_2 \cos \varphi_3 \sin(\theta_1 - \theta_2)(B_z \cos \theta_3 \\
 &- B_x \sin \theta_3) \sin \varphi_1 + B_y \cos \varphi_3(\cos(\theta_2 - \theta_3) \cos \varphi_1 \cos \varphi_2 + \cos(\theta_1 - \theta_3) \sin \varphi_1 \sin \varphi_2) \\
 &+ (\cos \varphi_1 \cos \varphi_2(B_x \cos \theta_2 + B_z \sin \theta_2) + (B_x \cos \theta_1 + B_z \sin \theta_1) \sin \varphi_1 \sin \varphi_2) \sin \varphi_3) \\
 c_2 &= J_2(B_y \cos \varphi_2^2 + \cos \varphi_2(B_x \cos \theta_2 + B_z \sin \theta_2) \sin \varphi_2) \\
 &+ I_3L_2L_3 \cos \varphi_2(B_y \cos(\theta_2 - \theta_3) \cos \varphi_3 + (B_x \cos \theta_2 + B_z \sin \theta_2) \sin \varphi_3) \\
 c_3 &= J_3(B_y \cos \varphi_3^2 + \cos \varphi_3(B_x \cos \theta_3 + B_z \sin \theta_3) \sin \varphi_3) \\
 c_4 &= J_1(B_z \cos \theta_1 - B_x \sin \theta_1) + I_2L_1L_2(\cos \varphi_1 \cos \varphi_2(B_z \cos \theta_2 - B_x \sin \theta_2) \\
 &- B_y \cos \varphi_2 \sin[\theta_1 - \theta_2] \sin \varphi_1 + (B_z \cos \theta_1 - B_x \sin \theta_1) \sin \varphi_1 \sin \varphi_2) \\
 &+ I_3L_1L_3(\cos \varphi_1 \cos \varphi_3(B_z \cos \theta_3 - B_x \sin \theta_3) - B_y \cos \varphi_3 \sin(\theta_1 - \theta_3) \sin \varphi_1 \\
 &+ (B_z \cos \theta_1 - B_x \sin \theta_1) \sin \varphi_1 \sin \varphi_3) + I_3L_2L_3(\cos(\theta_1 - \theta_2) \cos \varphi_2 \cos \varphi_3(B_z \cos \theta_3 \\
 &- B_x \sin \theta_3) - B_y \cos \varphi_3 \sin(\theta_1 - \theta_3) \sin \varphi_2 + (B_z \cos \theta_1 - B_x \sin \theta_1) \sin \varphi_2 \sin \varphi_3) \\
 c_5 &= J_2(B_z \cos \theta_2 - B_x \sin \theta_2) + I_3L_2L_3(\cos \varphi_2 \cos \varphi_3(B_z \cos \theta_3 - B_x \sin \theta_3) \\
 &- B_y \cos \varphi_3 \sin(\theta_2 - \theta_3) \sin \varphi_2 + (B_z \cos \theta_2 - B_x \sin \theta_2) \sin \varphi_2 \sin \varphi_3) \\
 c_6 &= J_3(B_z \cos \theta_3 - B_x \sin \theta_3) \\
 \\ 
 d_1 &= \frac{1}{2}L_1 \cos \varphi_1((F_{a,z}^1 + 2(F_{a,z}^2 + F_{a,z}^3)) \cos \theta_1 - (F_{a,x}^1 + 2(F_{a,x}^2 + F_{a,x}^3)) \sin \theta_1) \\
 d_2 &= \frac{1}{2}L_2 \cos \varphi_2((F_{a,z}^2 + 2F_{a,z}^3) \cos \theta_2 - (F_{a,x}^2 + 2F_{a,x}^3) \sin \theta_2) \\
 d_3 &= \frac{1}{2}L_3 \cos \varphi_3(F_{a,z}^3 \cos \theta_3 - F_{a,x}^3 \sin \theta_3) \\
 d_4 &= -\frac{1}{2}L_1((F_{a,y}^1 + 2(F_{a,y}^2 + F_{a,y}^3)) \cos \varphi_1 + ((F_{a,x}^1 + 2(F_{a,x}^2 + F_{a,x}^3)) \cos \theta_1 \\
 &+ (F_{a,z}^1 + 2(F_{a,z}^2 + F_{a,z}^3)) \sin \theta_1) \sin \varphi_1) \\
 d_5 &= -\frac{1}{2}L_2((F_{a,y}^2 + 2F_{a,y}^3) \cos \varphi_2 + ((F_{a,x}^2 + 2F_{a,x}^3) \cos \theta_2 + (F_{a,z}^2 + 2F_{a,z}^3) \sin \theta_2) \sin \varphi_2) \\
 d_6 &= -\frac{1}{2}L_3(F_{a,y}^3 \cos \varphi_3 + (F_{a,x}^3 \cos \theta_3 + F_{a,z}^3 \sin \theta_3) \sin \varphi_3)
 \end{aligned}$$

In this case the eigen-frequencies cannot be evaluated analytically, but only numerically, after having linearized the equations. In fact *Mathematica* can calculate analytically the roots of a polynomials only up to degree eight, while in the case of the three bars model the characteristic polynomial has degree twelve. So the software is not able to provide an analytical expression of the frequencies, but giving in input the size of each tether element and tip mass, it's possible to obtain directly their value. Using the same example considered for the two bars model the six eigenfrequencies are:

$$\begin{aligned} f_1 &= \sqrt{3}f_{orb} \\ f_2 &= 2f_{orb} \\ f_3 &= 9.9906f_{orb} \\ f_4 &= 10.1262f_{orb} \\ f_5 &= 21.9178f_{orb} \\ f_6 &= 22.0093f_{orb} \end{aligned}$$

#### 2.2.4 Massive Extensible Tether

The most interesting case is that of extensible, and so deformable, tether. From mechanics of vibration we know that a tensile force causes a local deformation proportional to its magnitude:

$$\xi = \frac{ds - ds_0}{ds_0} = \frac{Y}{E_Y A} \Rightarrow Y = E_Y A \xi \quad (2.60)$$

Where  $E_Y$  and  $A$  are the elastic Young module of the material and the transversal area withstanding the normal stress. Substituting in Eq. 2.40:

$$\frac{\partial}{\partial s} \left( \frac{E_Y A \xi}{L} \hat{\mathbf{u}} \right) + \vec{f}_{el} + \vec{f}_a = \rho_T \frac{\partial^2}{\partial t^2} \vec{r} \quad (2.61)$$

With  $\hat{\mathbf{t}}$  the unit vector tangent to the wire:

$$\hat{\mathbf{t}} = \frac{1}{L} \frac{\partial \vec{r}}{\partial s}, \quad (2.62)$$

Gravity and electrodynamic forces can excite longitudinal and transverse vibration whose frequencies are:

$$\begin{cases} f_{long} = \frac{1}{2\pi} \sqrt{\frac{E_Y A}{m_T L}} \\ f_{trasv} = \frac{1}{2\pi} \sqrt{\frac{T}{m_T L}} \end{cases} \quad (2.63)$$

Longitudinal frequency is very high for space tethers, and so it may lead to stiff problem in numerical integration

#### 2.2.5 Lump Masses Model

An investigation of the full dynamics is carried out by means a finite element method: the physical system is approximated by a discretized model, and the dynamics of such a model are numerically integrated to determine and represent the dynamics of the continuous physical system.

The main assumptions we made in our discretized model are:

1. Each lumped element is assigned a mass proportional to the length of tether it replaces
2. Each lumped elements acts as the center of application of external forces such as gravity, electrodynamic interaction, atmospheric drag,...

3. Each lumped element pair is coupled by an internal force representing the stress-strain relation by characteristic of the tether and directed along the unit vector joining the pair.
4. Each lumped element is assigned an external area proportional to the length of tether it replaces and with outward normal perpendicular to the unit vector joining it with the next element.
5. Each lumped element acts as the accumulation point for the heating and cooling fluxes for the segment of tether it replaces.

Let  $\mathbf{v}_k$  the state vector of the  $k$  lumped mass. It includes the position and velocity with respect to the inertial reference frame and its temperature:

$$[\mathbf{v}_k] = \begin{pmatrix} \vec{r}_k \\ \vec{v}_k \\ T_k \end{pmatrix} \quad (2.64)$$

Respect to the dumbbell model we have added a further variable. The temperature is very important for the dynamical motion because affects the electrical and mechanical properties of the tether, and so the electrodynamic and tether visco-elastic forces.

If we discretize the tether in  $N$  elements, we will have  $N + 2$  state vectors, where the first indicates the lower mass  $m_1$  and the last the upper one  $m_2$ . The equations specifying the orbital, attitude and thermal dynamics are:

$$[\dot{\mathbf{v}}_k] = \begin{bmatrix} \vec{v}_k \\ \frac{1}{m_k} (\vec{F}_{gr} + \vec{F}_{el} + \vec{F}_a + \vec{Y}) \\ \frac{1}{m_k c_k} (Q_{sol} + Q_{al} + Q_e + Q_a + Q_{ohm} - Q_{rad}) \end{bmatrix} \quad (2.65)$$

Where  $\vec{F}_{gr}$ ,  $\vec{F}_{el}$ ,  $\vec{F}_a$  and  $\vec{Y}$  are the gravitational, electrodynamic, aerodynamic and tether visco-elastic forces, respectively, acting on the  $k$  element, while  $Q_{sol}$ ,  $Q_{al}$ ,  $Q_e$ ,  $Q_a$ ,  $Q_{ohm}$  and  $Q_{rad}$  the thermal fluxes due the sun, albedo, Earth, atmospheric drag, ohmic losses and the radiation cooling, and  $c_k$  the thermal heat capacity. The solution requires  $7(N + 2)$  initial conditions in additions to all the physical parameters of the tethered system.

### Tether Internal Force

In a visco-elastic model the tether internal force can be separate in two main contribution: the elastic and damping term:

$$\vec{Y}_k = \vec{F}_{elas,k} + \vec{F}_{damp,k} \quad (2.66)$$

Where

$$\vec{F}_{elas,k}(\vec{r}_k, \vec{r}_{k+1}) = \frac{E_{Y_k} A_k}{l_k^0} |\vec{r}_{k+1} - \vec{r}_k| - l_k^0 [1 + \alpha_{T,k} (T_k - T_k^0)] \hat{u}_k \quad (2.67)$$

$$\vec{F}_{damp,k}(\dot{\vec{r}}_k, \dot{\vec{r}}_{k+1}) = b_k |\dot{\vec{r}}_{k+1} - \dot{\vec{r}}_k| \hat{u}_k \quad (2.68)$$

And is the unit vector between the masses  $m_k$  and  $m_{k+1}$ :

$$\hat{u}_k = \frac{\vec{r}_{k+1} - \vec{r}_k}{|\vec{r}_{k+1} - \vec{r}_k|}$$

With  $\alpha_{T,k}$ ,  $l_k^0$  and  $b_k$  the thermal expansion coefficient, the unstretched length of tether element  $k$  and material damping constant, respectively.

### Solar thermal flux

The flux due to the absorption of solar radiation is the main factor for the heating of the tether. The variation of temperature depends on the area exposed to sun rays and mechanical properties of the wire, in particular its absorptivity  $\alpha_s$ :

$$Q_{rad,k} = \alpha_s J_s [w (\hat{\mathbf{u}}_s \cdot \hat{\mathbf{u}}_2) + h (\hat{\mathbf{u}}_s \cdot \hat{\mathbf{u}}_3)] \Delta s_k \quad (2.69)$$

Where  $J_s$  is the solar flux,  $\hat{\mathbf{u}}_s$  is the solar unit vector and  $\hat{\mathbf{u}}_2, \hat{\mathbf{u}}_3$  the unit vectors of the  $k$  element as defined before,  $w$ ,  $h$ , and  $\Delta s_k$  respectively the width, thickness and length of that element of wire. Solar radiation heats the tether only when the satellite stays out the shadow cone. In the orbital region where it is behind the Earth, the solar flux is zero. This eclipse condition is explained in Fig. 2.4.

The arrow defines the orientation of sun vector, while the cylinder represents the shadow region

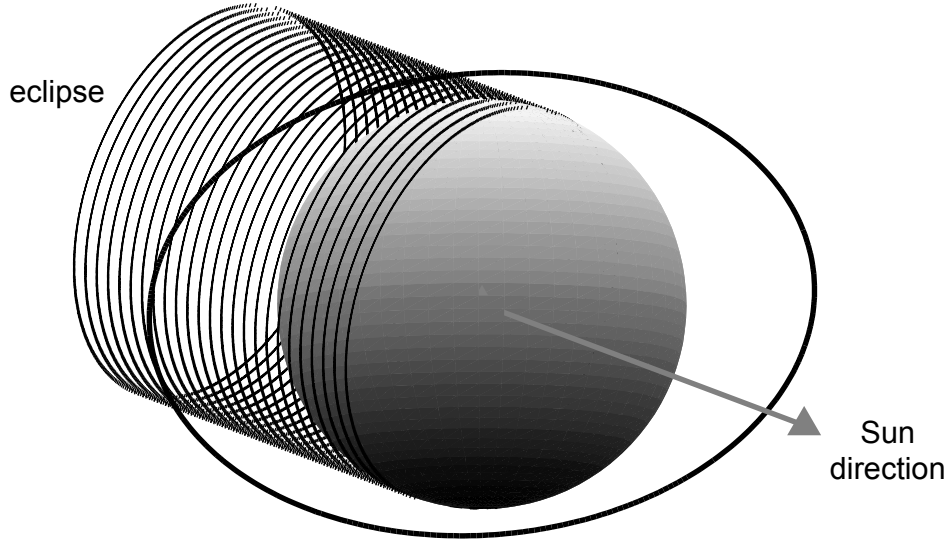


Figure 2.4: Shadow region of the orbit

behind the Earth. When the satellite reaches this zone the tether temperature falls down drastically, because it loses the main thermal contribution.

### Earth Thermal Flux

The infrared flux received from the Earth can be evaluated by

$$Q_{e,k} = 2\varepsilon J_e f (w + h) \Delta s_k \quad (2.70)$$

Where  $\varepsilon$  is the infrared absorptivity,  $J_e$  is the energy flux irradiated by the Earth,  $\sigma_B$  the Stefan-Boltzman constant,  $T_e$  the temperature of the Earth,  $f$  is the view factor and  $\delta$  the angle subtended by the Earth to the  $k$  element:

$$\begin{aligned} J_e &= \sigma_B T_e^4 \\ f &= \frac{\delta - \sin \delta \cos \delta}{\pi} \\ \delta &= \sin^{-1} \left( \frac{R_E}{r} \right) \end{aligned}$$

## Albedo Thermal Flux

The albedo flux represents the solar radiation reflected by the Earth towards the satellite. Called  $a$  the albedo coefficient:

$$Q_{e,k} = 2a\alpha_s J_s f(w + h) \Delta s_k \quad (2.71)$$

## Aerodynamic Thermal Flux

The aerodynamic drag warms up the wire because of the impact of molecules on it. This mechanism can be described as:

$$Q_{drag,k} = \frac{1}{2} \rho_{atm} v_{rel,k}^2 [w(\vec{v}_{rel,k} \cdot \hat{\mathbf{u}}_2) + h(\vec{v}_{rel,k} \cdot \hat{\mathbf{u}}_3)] \Delta s_k \quad (2.72)$$

where  $\vec{v}_{rel,k}$  is the relative velocity between the  $k$  element and the atmosphere.

## Ohmic and Electron Impact Losses

The collection of the electron present in the Earth's ionosphere brings two important heating processes. The first is the heat due the impact of electrons on the tether surface.

$$Q_{EI,k} = \int \left( \frac{dI(s)}{ds} \right) \Delta V(s) ds_k \quad (2.73)$$

The second is generated by the flowing of a current  $I$  through an electric resistance  $R$ , as consequence of the Ohm's law.

$$Q_{ohm,k} = \int I^2(s) R(s) ds_k \quad (2.74)$$

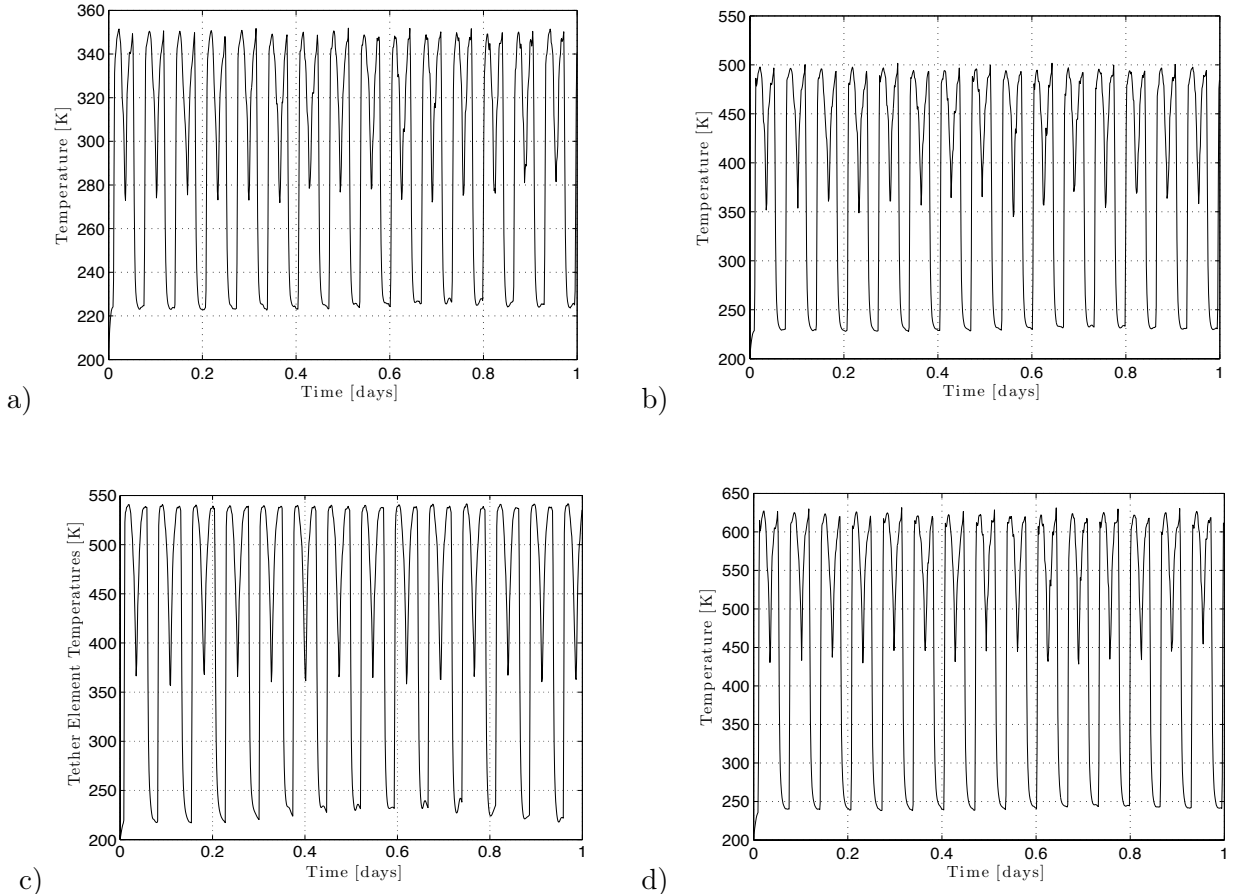
Where  $I(s)$ ,  $\frac{dI(s)}{ds}$ ,  $V(s)$  and  $R(s)$  are respectively the current along the  $k$  element, its derivate with respect to  $s$  coordinate, the potential difference and the electric resistance.

## Radiative Cooling

The radiative cooling is the only mechanism by which the tether can lose thermal energy and maintain an acceptable temperature and a high electric conductivity. The mathematical formula of this process is:

$$Q_{rad,k} = 2\varepsilon(w + h)\Delta s_k \sigma_B T_k^4 \quad (2.75)$$

The temperature of tether, as just explained by the equations of the thermal balance (see Eq. 2.65), depends mainly on solar and Earth's flux, and so on the absorption coefficients  $\alpha_s$  and  $\varepsilon$ , that define the optical properties of the surface. As a function of these coefficients the maximum temperature of the tether changes, while the minimum one (when the satellite is behind the Earth) depends only on the view factor between the satellite and the planet. When the ratio  $\alpha_s/\varepsilon$  becomes high the wire absorbs a great amount of solar radiation, but it cannot dissipate enough heat by radiative cooling. Figure 2.5 shows the temperature variation during the orbit for different values of  $\alpha_s/\varepsilon$  (1 - 4.6 - 7 - 12). It's easy to note how the maximum (when the tether is completely illuminated by the sun) tends rapidly to increase as  $\alpha_s/\varepsilon$  enlarges. High temperatures can be critical, because the electric resistance of the tether increases lowering the current collected from the environment, and the mechanical properties of the wire becomes weaker letting longer longitudinal deformation.


 Figure 2.5: Temperature profile: a)  $\alpha_s/\varepsilon=1$ , b)  $\alpha_s/\varepsilon=4.6$ , c)  $\alpha_s/\varepsilon=7$ , d)  $\alpha_s/\varepsilon=12$ 

### 2.2.6 Normal Modes

In order to evaluate analytically the transversal normal modes of vibration we consider a simplified bi-dimensional model, with two equal masses at the end of the wire and much more heavy than tether. These assumptions let us to approximate the tension as constant along the wire. Moreover the only force acting on the system are the tether internal force due to elastic deformations. So respect to a synodic reference frame the positions of  $m_{sat}$  and  $m_B$  remain invariant, so we can treat our system like a flexible elastic string fixed at the extremities and discretize it into  $N$  particles, each of mass  $dm$ . The particles are labeled from 0 to  $N + 1$ , where 0 and  $N + 1$  indentify  $m_{sat}$  and  $m_B$ . Each lumped mass is subject to two tensional force, whose direction depends on the respective position of the previous and following masses (see Fig. 2.6). If the transversal displacements  $y$  are little we can write that the force acting on the mass  $dm_k$  as

$$F_k = -\frac{Y}{L} (y_k - y_{k-1}) + \frac{Y}{L} (y_{k+1} - y_k) \quad (2.76)$$

And the differential equation of motion of the  $p$ th particle becomes

$$\frac{d^2 y_k}{dt^2} + 2\omega_0^2 y_k - \omega_0^2 (y_{k+1} - y_k) \quad (2.77)$$

where

$$\omega_0^2 = \frac{T}{mL} \quad (2.78)$$

So we get a set of  $N + 2$  differential equations in the variables  $y_{0,\dots,N+1}$ . To solve it and seek the normal modes we can look for sinusoidal solutions such that each particle oscillates with the same

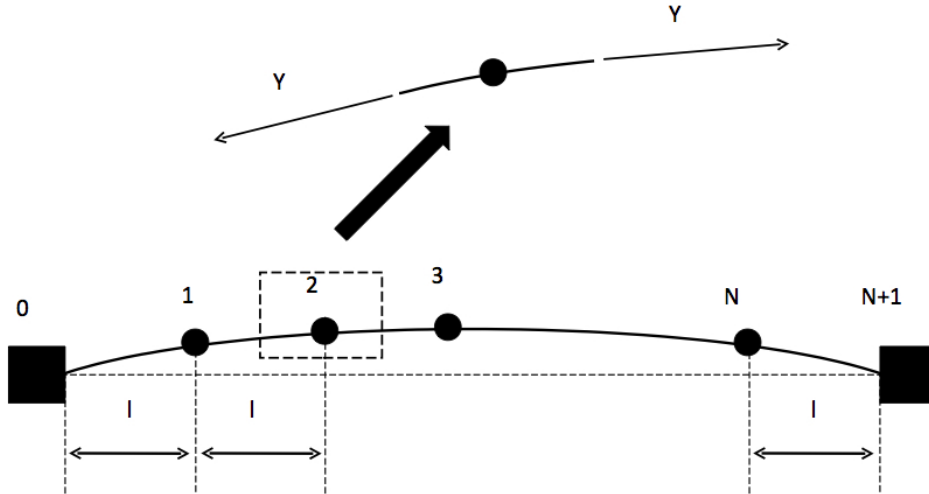


Figure 2.6: Lump masses discretization of the tether

frequency. For example we can set the solution

$$y_k = A_k \cos \omega t \quad (2.79)$$

where  $A_k$ ,  $\omega$  and  $t$  are the amplitude, frequency of vibration of the  $k$ -th particle and time, respectively. The objective is to find the values of  $A_k$  and  $\omega$  for which the solution searched satisfy the set of differential equations:

$$\begin{aligned} (2\omega_0^2 - \omega^2) A_0 - \omega_0^2 A_1 &= 0 \\ (2\omega_0^2 - \omega^2) A_1 - \omega_0^2 (A_2 + A_0) &= 0 \\ &\vdots \\ (2\omega_0^2 - \omega^2) A_k - \omega_0^2 (A_{k+1} + A_{k-1}) &= 0 \\ &\vdots \\ (2\omega_0^2 - \omega^2) A_N - \omega_0^2 (A_{N+1} + A_{N-1}) &= 0 \\ (2\omega_0^2 - \omega^2) A_{N+1} - \omega_0^2 A_N &= 0 \end{aligned} \quad (2.80)$$

The  $k$ -th equation can be reformulated as

$$\frac{A_{k+1} + A_{k-1}}{A_k} = \frac{2\omega_0^2 - \omega^2}{\omega_0^2} \quad (2.81)$$

For any particular value of  $\omega$ , the right side is constant, and therefore the ratio on the left must be a constant, too, and independent of the mass  $k$ -th. Now the question is what value must be assigned to the coefficient  $A_k$  in such a way the relation is always satisfied, and at the same time the amplitude of motion of masses  $m_{sat}$  and  $m_B$  is zero:  $A_0 = A_{N+1} = 0$ .

Supposing that the amplitude of particle  $p$  is expressible in the form

$$A_k = C \sin k\vartheta \quad (2.82)$$

Where  $\vartheta$  is some angle, then Eq. 2.81 becomes:

$$A_{k+1} + A_{k-1} = C [\sin(k+1)\vartheta + \sin(k-1)\vartheta] = 2C \sin k\vartheta \cos \vartheta = 2A_k \cos \vartheta \quad (2.83)$$

$$\frac{A_{k+1} + A_{k-1}}{A_k} = 2 \cos \vartheta \quad (2.84)$$

This means the right-hand side of Eq. 2.84 is a constant, independent of  $k$ , and this condition can be used to satisfy all the  $N$  equations of system 2.80. So, what remains to do is to find the value of the angle  $\vartheta$ , imposing the boundary conditions:  $A_k = 0$  for  $k = 0$  and  $k = N + 1$ . This can be easily satisfied imposing that  $(N + 1)\vartheta$  is set equal to any integral multiple of  $\pi$ :

$$(N + 1)\vartheta = n\pi \quad (n = 1, 2, 3, \dots)$$

$$\vartheta = \frac{n\pi}{N + 1}$$

Substituting in Eq. 2.82:

$$A_k = C \sin\left(\frac{kn\pi}{N + 1}\right) \quad (2.85)$$

We are interesting about the normal modes of vibration of the system:

$$\frac{A_{k+1} + A_{k-1}}{A_k} = \frac{2\omega_0^2 - \omega^2}{\omega_0^2} = 2 \cos \frac{n\pi}{N + 1} \quad (2.86)$$

Therefore

$$\omega^2 = 2\omega_0^2 \left[1 - \cos\left(\frac{n\pi}{N + 1}\right)\right] = 4\omega_0^2 \sin^2\left(\frac{n\pi}{2(N + 1)}\right) \quad (2.87)$$

And the eigenfrequencies are:

$$f = \frac{\omega}{2\pi} = \frac{\omega_0}{\pi} \sin\left(\frac{n\pi}{2(N + 1)}\right) \quad (2.88)$$

Different values of the integer  $n$  define different normal mode frequencies:  $\omega_n = 2\omega_0 \sin(n\lambda)$ , where  $\lambda = \frac{1}{2} \frac{\pi}{N+1}$ . So the motion of a given particle depends both on its number along the wire ( $k$ ) and on the mode number ( $n$ ), and the amplitude of the motion can be written as:

$$A_{k,n} = C_n \sin\left(\frac{kn\pi}{N + 1}\right) \quad (2.89)$$

Where  $C_n$  defines the amplitude with which the particular mode  $n$  is excited, and the displacement of mass  $k$ -th is:

$$y_{k_n}(t) = A_{k,n} \cos \omega_n t \quad (2.90)$$

The first vibration mode is given by  $n = 1$  (see Fig. 2.7)

$$y_{k_1}(t) = C_1 \sin\left(\frac{k\pi}{N + 1}\right) \cos \omega_1 t \quad (k = 1, 2, \dots, N)$$

At a given instant of time, the factor  $C_1 \cos \omega_1 t$  is the same for all the particles, only the  $\sin\left(\frac{k\pi}{N+1}\right)$  factor distinguishes the displacements of each lumped mass. As the time  $t$  increases each particle oscillates in the transversal direction with frequency  $\omega_1$ .

The second mode of vibration, for  $n = 2$ , is:

$$y_{k_2}(t) = C_2 \sin\left(\frac{2k\pi}{N + 1}\right) \cos \omega_2 t \quad (k = 1, 2, \dots, N)$$

If the number of particles is odd then there will be one at the center of the tether that will remain at rest, as it can be seen in Fig. 2.9. In the end in Fig. 2.10 the shape of the first five modes are reported. The full vibration will be defined by a linear combination of each single mode, is that a superimposition of  $N$  different sine functions.

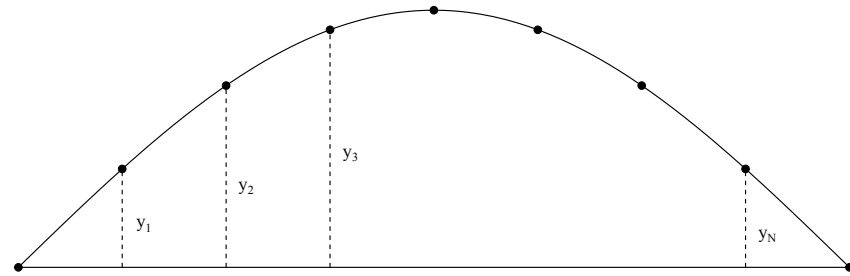


Figure 2.7: First mode of vibration

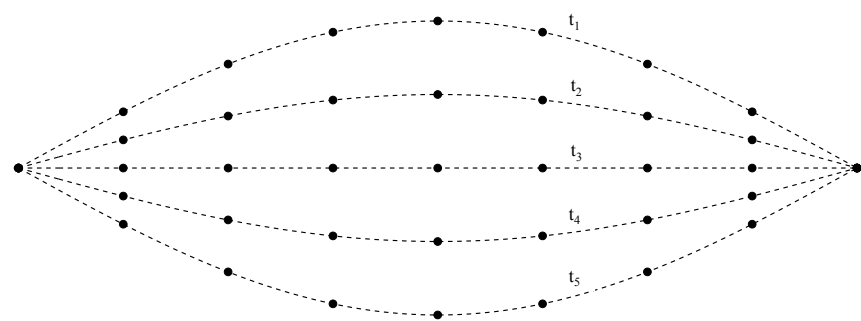


Figure 2.8: First mode oscillation

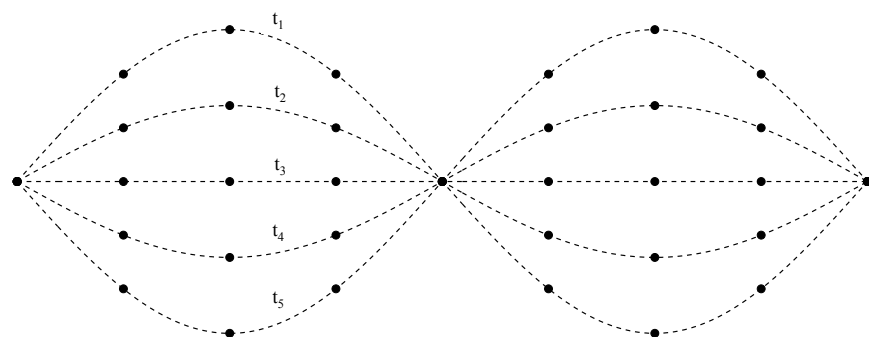


Figure 2.9: Second mode of vibration

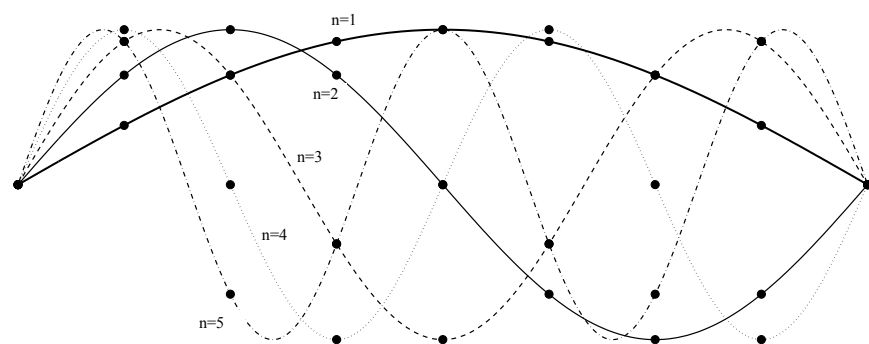


Figure 2.10: First five modes of vibration

# Chapter 3

## Earth's Environment

The performances of an electrodynamic tether depend on several parameters, as the orbital altitude, inclination, intensity of magnetic field and electron density. In order to investigate the dynamics of our satellite we need reference environmental models that approximate the real nature of Earth's atmosphere, magnetic field and gravity attraction. In literature exist several models, some more accurate and other simpler and faster to implement, and in general the choice of which code to use must rely on the tradeoff between accuracy and computational time. In our work we want to simulate the behavior of a tethered satellite in detail, so we will adopt the most accurate models present nowadays in literature, as IRI, IGRF, MSIS and a  $4 \times 4$  gravity field respectively for the ionosphere, magnetic field, atmosphere and gravitational potential.

### 3.1 Ionosphere

The ionosphere can be defined as the region of the Earth's atmosphere where the concentration of free electrons is so large that it affects radio waves. The ionosphere was discovered when it was observed that radio waves can propagate over large distances, and therefore the existence of an electrical conductive layer in the upper atmosphere, which could reflect the waves, was investigated. The electrically conductive region stretches from about 50 km to 500 km above the ground, and the concentration of electrons  $N_e$  varies from  $10^7$  particles per  $m^3$  at 50 km to a maximum of  $10^{12}$  particles per  $m^3$  at 250-300 km. The ionosphere is formed when energetic electromagnetic and particle radiation from the sun and space ionize air molecules, creating plasma in the upper atmosphere. This plasma is weakly ionized and the ratio between electron density and density of neutral air never becomes just larger than  $10^{-7}$ , even at the altitude when  $N_e$  reaches its maximum. The regular ionospheric layers are formed by extreme ultraviolet (EUV) and X-ray radiation from the sun, and have a characteristic variation with the time of day and latitude. In polar regions (latitude higher than  $65^\circ$ ), energetic electrons and protons precipitate along the magnetic field lines and give rise to particle impact ionization. Generally ionosphere is divided in three fundamental regions:

1. D-region (50-90km)
2. E-region (95-150km)
3. F-region (150-500km)

The main processes involved in their formation are photoionization by sun, losses due to recombination and transport phenomena. The electron concentration in these layers varies with the exposure

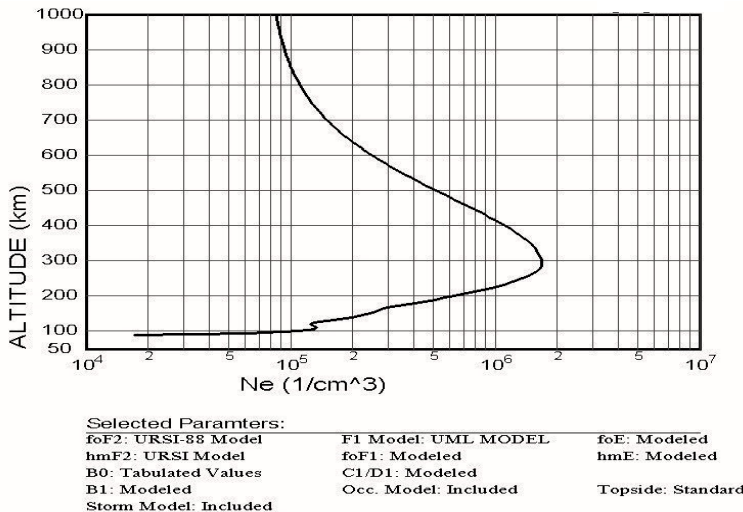


Figure 3.1: International Reference Ionosphere model: electron density versus altitude

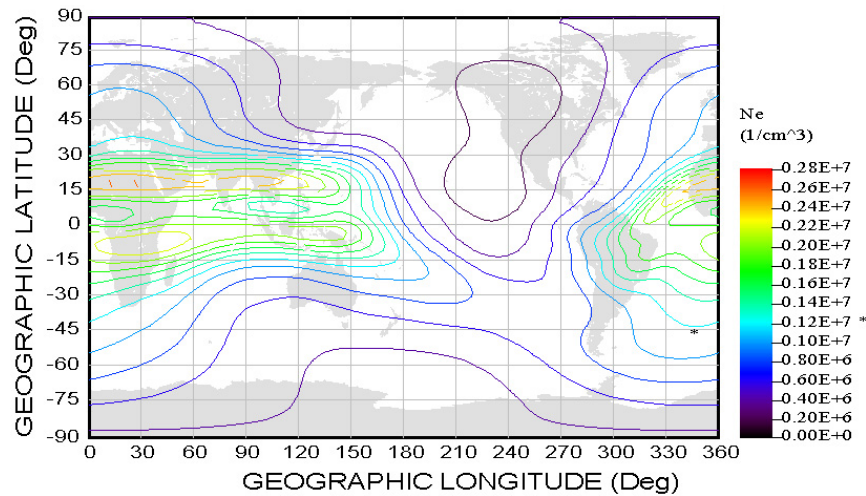


Figure 3.2: International Reference Ionosphere model: electron density as a function of latitude and longitude

to different types of radiation, different types of recombination and various transport processes, and none of the layers behave exactly like the ideal Chapman layer with respect to variations in altitude, time of day, and latitude. In addition, none of the layers disappear totally when the sun is below the horizon, because of scattered radiation, and transport mechanisms, which can transport plasma from a sunlight region to a dark region of the atmosphere. At night the F layer is the only layer of significant ionization present, while the ionization in the E and D region is extremely low. During the day, the D and E region become much more heavily ionized, as does the F region, which develops an additional, weaker region of ionization known as the F1 layer. The F2 layer persists by day and night and is the region mainly responsible for the refraction of radio waves. Several models have been implemented to simulate the dynamics of ionosphere, and in the last decades the International Reference Ionosphere (IRI) has become the reference one. IRI is the standard model recommended for international use by the scientific unions Committee on Space Research (COSPAR) and International Union of Radio Science (URSI). IRI, like many other international standard models (e.g., CIRA, MSIS, IGRF), is an empirical model, which provides monthly averages of the electron density, the ion composition ( $O^+$ ,  $H^+$ ,  $He^+$ ,  $NO^+$ ,  $O_2^+$ ,  $N_2^+$ , cluster ions), the electron and ion

temperatures. In this work such a model is used in to estimate the collection of electrons, and so the electric current flowing along an electrodynamic tether.

## 3.2 Magnetic Field

The geomagnetic field can be expressed as the gradient of a scalar potential  $V_B$ , usually defined as an orthogonal expansion in spherical harmonics. Respect to geocentric reference frame the expansion of  $V_B$  in spherical harmonics can be written as:

$$V_B(r, \lambda, \phi) = R_E \sum_{n=1}^{\infty} \sum_{m=1}^{\infty} \left( \frac{R_E}{r} \right)^{n+1} (g_n^m \cos m\lambda + h_n^m \sin m\lambda) P_n^m(\cos \phi) \quad (3.1)$$

where  $R_E$  is the Earth's equatorial radius,  $\lambda$  is the position longitude,  $\phi$  the co-latitude, and  $P_n^m(\cos \phi)$  are the quasi Schmidt-normalized associated Legendre functions of degree  $n$  and order  $m$ . This expansion is an infinite series, but in practice it is usually limited to  $n = 10$  or  $n = 12$ . Hence the magnetic field can be evaluated by deriving Eq. 3.1 along the three directions:

$$\vec{B} = \nabla V_B(r, \lambda, \phi) \quad (3.2)$$

In literature we can find three main models that describe and approximate the nature of Earth's magnetic field:

1. Dipolar magnetic field
2. Eccentric magnetic field
3. International Geomagnetic Reference Field IGRF

### 3.2.1 Dipolar Magnetic Field

The main contribution in the spherical harmonic expansion comes from the first terms with  $n = 1$ . It is the field produced by a dipole with centre coinciding with that of the Earth and dipole axis inclined with respect to the polar one. The expression of  $\vec{B}$  becomes:

$$\vec{B} = \mu_m \left( \frac{R_E}{r} \right)^3 ((3\hat{u}_m \cdot \hat{r}) \hat{r} - \hat{u}_m) \quad (3.3)$$

In geocentric coordinates the direction of magnetic dipole  $\hat{u}_m$  is:

$$\hat{u}_m = \begin{pmatrix} \sin \beta_m \cos \alpha_m \\ \sin \beta_m \sin \alpha_m \\ \cos \beta_m \end{pmatrix} \quad (3.4)$$

With  $\beta_m$  the magnetic dipole co-latitude, and  $\alpha_m$  the dipole magnitude:

$$\alpha_m = \alpha_{m,0} + \Omega_E t \quad (3.5)$$

In the above formulas  $R_E$  is the Earth radius,  $B_{eq}$  is the dipole magnetic field intensity at the distance  $R_E$  on the dipole equator, while  $\Omega$  the Earth angular velocity. A fit of the latter two parameters can be derived directly from the first Schmidt-normalized coefficients of the IGRF-11 Earth magnetic field model:

$$B_{eq} = \sqrt{g_{10}^2 + g_{11}^2 + h_{11}^2} \simeq 29.9 \mu\text{T}$$

$$\beta = \sin^{-1} \left( \frac{\sqrt{g_{11}^2 + h_{11}^2}}{B_{eq}} \right) \simeq 9.7^\circ$$

It is interesting to remark that the magnetic field has been experiencing a slight decrease in intensity together with a considerable decrease in tilt angle during the last half century.  $B_{eq}$  has decreased from 30.9 nT in 1965 to 30.2 nT in 1995 and is expected go down to 29.9 nT in 2015. Most importantly, the tilt angle  $\beta$  is estimated as 11.5 deg in 1965, 10.7 deg in 1995 and 9.7 deg in 2015.

### 3.2.2 Eccentric Dipolar Magnetic Field

This model approximates the geomagnetic field with a dipole which is not necessarily located at the centre of the Earth. The criterion to use, in order to determine the dipole offset, must fit the observed data minimizing the gap with the real magnetic field. The eccentric dipole so obtained has the same moment as the centred dipole and the same orientation of its axis, but in terms of the geographic Cartesian coordinate system it is displaced with respect to the Earth's centre at a position  $\vec{\delta}$ :

$$\vec{B} = \mu_m \left( \frac{R_E}{r_d} \right)^3 ((3\hat{u}_m \cdot \hat{r}_d) \hat{r}_d - \hat{u}_m) \quad (3.6)$$

where  $\vec{r}_d = |\vec{r} - \vec{\delta}|$  and  $\hat{r}_d = \frac{\vec{r} - \vec{\delta}}{r_d}$ .

The use of an eccentric dipole magnetic field model represents a resonable compromise between accuracy and mathematical complexity. While the magnetic moment direction  $\hat{u}_m$  is the as same as the centered dipole one, the offset vector  $\vec{\delta}$  in geocentric coordinates can be computed as follows:

$$\vec{\delta} = (\xi, \eta, \zeta)^T = (\xi_0 \cos \Omega t + \eta_0 \sin \Omega t, \eta_0 \cos \Omega t - \xi_0 \sin \Omega t, \zeta_0)^T,$$

where

$$\begin{bmatrix} \xi_0 \\ \eta_0 \end{bmatrix} = \begin{bmatrix} \cos \phi & \sin \phi \\ -\sin \phi & \cos \phi \end{bmatrix} \begin{bmatrix} \tilde{\xi}_0 \\ \tilde{\eta}_0 \end{bmatrix}$$

$$\tilde{\xi}_0 = \frac{L_1 - g_{11}P}{3B_{eq}^2} r_E$$

$$\tilde{\eta}_0 = \frac{L_2 - h_{11}P}{3B_{eq}^2} r_E$$

$$\tilde{\zeta}_0 = \frac{L_0 - g_{10}P}{3B_{eq}^2} r_E$$

$$L_0 = 2g_{10}g_{20} + \sqrt{3}(g_{11}g_{21} + h_{11}h_{21})$$

$$L_1 = -g_{11}g_{20} + \sqrt{3}(g_{10}g_{21} + g_{11}g_{22} + h_{11}h_{22})$$

$$L_2 = -h_{11}g_{20} + \sqrt{3}(g_{10}h_{21} - h_{11}g_{22} + g_{11}h_{22})$$

$$P = L_0g_{10} + L_1g_{11} + L_2h_{11}$$

$$\phi = \tan^{-1} \frac{h_{11}}{g_{11}}.$$

In the above equation  $\tilde{\xi}_0, \tilde{\eta}_0, \tilde{\zeta}_0$  and  $\phi$  are, respectively, the position of the dipole center in geographic coordinates and the east longitude of the dipole moment vector. Using the coefficients of Table 3.1 they result  $\tilde{\xi}_0 = -396.8$  km,  $\tilde{\eta}_0 = 341.4$  km,  $\tilde{\zeta}_0 = 269.3$  km and  $\phi = -72.6^\circ$  providing:

$$\begin{cases} \xi_0 = -444.3 \text{ km} \\ \eta_0 = -276.8 \text{ km} \\ \zeta_0 = 269.4 \text{ km} \end{cases}$$

So the position vector  $\vec{r}_d$  can be written as:

$$\vec{r}_d = r (\cos \omega t + \epsilon_\xi \cos \Omega t + \epsilon_\eta \sin \Omega t, \cos i \sin \omega t + \epsilon_\eta \cos \Omega t - \epsilon_\xi \sin \Omega t, \sin i \sin \omega t + \epsilon_\zeta)^T$$

with:

$$(\epsilon_\xi, \epsilon_\eta, \epsilon_\zeta) = (\xi_0, \eta_0, \zeta_0) / r.$$

### 3.2.3 International Geomagnetic Reference Field

IGRF evaluates the magnetic field components along the three directions directly from Eq. 3.2. The  $g_n^m$  and  $h_n^m$  coefficients till to degree and order 13 are calculated every five years, from Earth based and satellite measurements of the geomagnetic field, by the International Association of Geomagnetism and Aeronomy (AIGA).

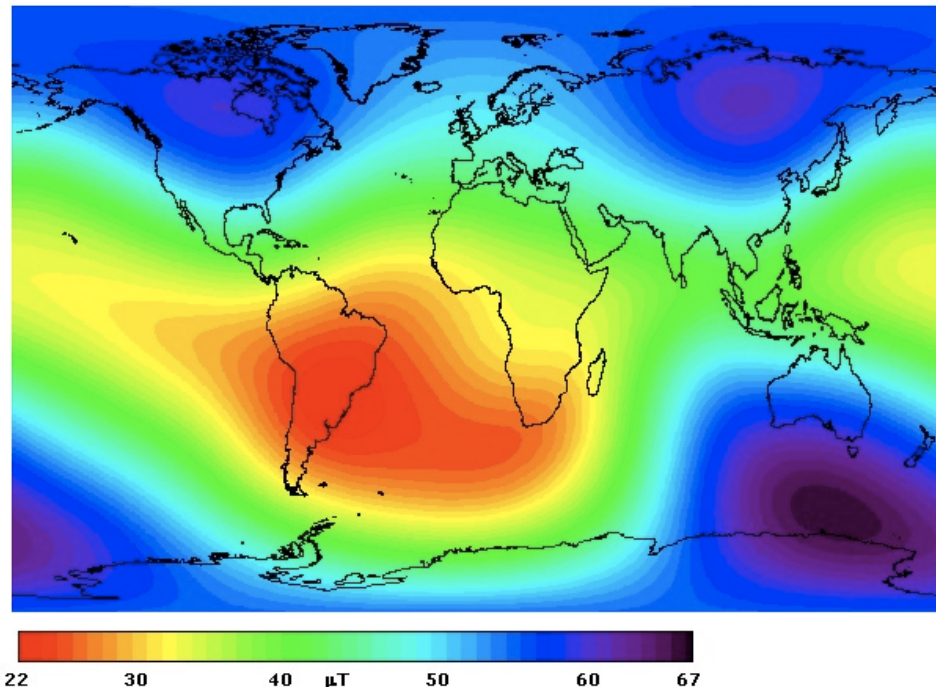


Figure 3.3: IGRF magnetic field

## 3.3 Atmosphere

The atmosphere of Earth is a layer of gases, whose average temperature at the surface is 14-15°C, surrounding the planet and retained by its gravity. Near the grounds the atmosphere contains, by volume, roughly 78.09% nitrogen, 20.95% oxygen, 0.93% argon, 0.039% carbon dioxide, and small amounts of other gases. Air also contains a variable amount of water vapor, on average around 1%. Up to a height of approximate 100 km the gases are mixed by turbulence and their relative proportion remain constant. At greater heights, where there is no turbulence, each one is distributed as though it alone were present. It is said to be in diffusive equilibrium. The level at which turbulence

n	m	$g_n^m$	$g_n^m$
1	0	-29496.5	0
1	1	-1585.9	4945.1
2	0	-2396.6	0
2	1	3026.0	-2707.7
2	2	1668.6	-575.4
3	0	1339.7	0
3	1	-2326.3	-160.5
3	2	1231.7	251.7
3	3	634.2	-536.8
:	:	:	:
13	11	0.4	-0.2
13	12	-0.3	-0.5
13	13	-0.3	-0.8

Table 3.1: IGRF  $g_n^m$  and  $h_n^m$  coefficients

ceases may be called the turbopause: it is a sharply defined and lies at about 100 km. At greater heights, the lack of turbulence enables a condition of diffusive separation to be established, in which the vertical distribution of each neutral gas depends on its molecular weight. The distribution of chemically active gases, however, may be influenced to some extent by photochemical reactions as well as by diffusion. This is especially true for the ionization which attains a diffusely controlled distribution only at heights well above the F2 peak, at 400 km or so. Earth's atmosphere has a mass of about  $5 \times 10^{18}$  kg, three quarters of which is within about 11 km of the surface, and it becomes thinner and thinner with increasing altitude, with no definite boundary between the atmosphere and outer space. Earth's atmosphere can be divided into five main layers, which are mainly determined by whether temperature increases or decreases with altitude. From highest to lowest, these layers are: troposphere, stratosphere, mesosphere, thermosphere and exosphere. Then there is the magnetosphere that is formed principally by charged particles, whose dynamics are governed by Earth's magnetic field. Moreover within these five principal layers there are several layers determined by other properties: ozone layer, ionosphere, planetary boundary layer.

The atmospheric drag is a crucial aspect for space missions, because changes slowly its motion lowering the orbit. This interaction depends mainly on atmospheric density, which is a function of altitude, and in first approximation it falls down with exponential law as the quote increases.

In this work the Mass Spectrometer Incoherent Scatter NRLMSISE-00 model has been adopted to evaluate the atmospheric density and neutral temperature and densities from ground to thermospheric heights. Below 72.5 km the model is primarily based on the MAP Handbook tabulation of zonal average temperature and pressure by Barnett and Corney, data from the National Meteorological Center, Pitot tube, falling sphere, and grenade sounder rocket measurements, while above 72.5 km the data are taken from space shuttle flights.

### 3.4 Gravitational Field

The gravitational attraction of a large body, as the Earth is given by the integral

$$U = G \int_V \frac{\rho(s)}{|\vec{r} - \vec{s}|} d^3 s \quad (3.7)$$

Where  $G$  is universal attraction constant,  $\rho$  and  $V$  the density and volume of the body,  $\vec{s}$  the

position of an element  $dm$  of the body, and  $\vec{r}$  the coordinate of the point at which the potential  $U$  is evaluated.

Our planet is not a perfectly spherical body, and the mass is not homogeneously distributed. In fact there are mountains, plain zones, deserts, oceans, and also behind the surface the density change moving toward to its core. So, in order to take into account all these effects, the Earth's gravitational field can be expressed by means of expansion in spherical harmonics.

$$U(r, \lambda, \phi) = \frac{GM}{r} \left[ 1 - \sum_{n=2}^{\infty} \left( \frac{R_E}{r} \right)^n J_n P_n^0(\cos \phi) + \sum_{n=2}^{\infty} \sum_{m=1}^{\infty} \left( \frac{R_E}{r} \right)^n (C_n^m \cos m\lambda + S_n^m \sin m\lambda) P_n^m(\cos \phi) \right] \quad (3.8)$$

Where  $r, \lambda, \phi$  have the same meaning of that explained for the magnetic model. The first term is that of a perfectly spherical body, while the others  $J_n, C_n^m$  and  $S_n^m$  represent the superior order harmonics. The coefficients  $J_n$  identify the zonal harmonics, which are symmetric respect to the equator, while  $C_n^m$  and  $S_n^m$  the tesseral ( $n \neq m$ ) and sectorial ( $n = m$ ) harmonics. After the uniform term,  $J_2$  is the greatest contribution and it means the flattening of the poles.

The gravity acceleration at  $\vec{r}$  will be the gradient  $U$  respect to  $r, \lambda, \phi$

$$\vec{g} = \nabla U(r, \lambda, \phi) \quad (3.9)$$

$n$	$m$	$C_n^m$	$S_n^m$
1	1	0	0
2	1	-0.2411x10-9	0.1543x10-8
2	2	0.1574x10-5	-0.9038x10-6
3	1	0.2191x10-5	0.2687x10-6
3	2	0.3089x10-6	-0.2115x10-6
3	3	0.1006x10-6	0.1972x10-6
4	1	-0.5088x10-6	-0.4491x10-6
4	2	0.7834x10-7	0.1482x10-6
4	3	0.5918x10-7	-0.1201x10-7
4	4	-0.3983x10-8	0.6525x10-8

Table 3.2: Gravity field tesseral and sectorial coefficients

$n$	$J_n$
1	0
2	0.1083x10-2
3	-0.2532x10-5
4	-0.1620x10-5

Table 3.3: Gravity field zonal coefficients

And with respect to a geocentric reference frame:

$$\begin{aligned}
 g_x &= \left\{ \frac{1}{r} \frac{\partial U}{\partial r} - \frac{r_z}{r^2 \sqrt{r_x^2 + r_y^2}} \frac{\partial U}{\partial \phi} \right\} r_x - \left\{ \frac{1}{r_x^2 + r_y^2} \frac{\partial U}{\partial \lambda} \right\} r_y \\
 g_y &= \left\{ \frac{1}{r} \frac{\partial U}{\partial r} - \frac{r_z}{r^2 \sqrt{r_x^2 + r_y^2}} \frac{\partial U}{\partial \phi} \right\} r_y + \left\{ \frac{1}{r_x^2 + r_y^2} \frac{\partial U}{\partial \lambda} \right\} r_x \\
 g_z &= \frac{1}{r} \frac{\partial U}{\partial r} r_z + \frac{\sqrt{r_x^2 + r_y^2}}{r^2} \frac{\partial U}{\partial \phi}
 \end{aligned} \tag{3.10}$$

All the harmonics affect the orbital motion generating important perturbation:  $J_2$  provokes the regression of nodes line and the rotation of apside line,  $J_3$  changes the orbital inclination,  $J_{22}$  is the terms taking into account the ellipticity of equatorial plane and is particularly important for geosynchronous satellite because generates little oscillations around stable points.

## Chapter 4

# Electrodynamic Bare Tethers

Electrodynamic tethers (ED) are useful systems to extract electrical power at expense of the plasmasphere of a planet. High electron density and strong magnetic field let that a current flows along the wire feeding inboard instrumentation. The interaction between magnetic field and electric current generates a distributed Lorentz force along the wire.

An electrodynamic tether system is made up of a thin conductive wire connected to the satellite. The other thread termination is generally occupied by a tip mass, which facilities the deployment of the cable and helps in stabilizing the system through gravity gradient force.

The tether model we consider is a bare EDT of length  $L$ , width  $w$  and thickness  $h$ , made up with conductive material of density  $\rho$  and conductivity  $\sigma$ , which are function of temperature profile. In this study we are working with short wires, hence it is reasonable to assume that the quantities  $N_e$  and  $B$  are constant along the tether, because their variation are too little to be meaningful for the electrodynamic interaction.

The main hypothesis made in this thesis, and in general for every work about bare electrodynamic tethers, lies in the assumption that current collection process takes place in the orbital motion limited (OML) regime, which is the optimal case for cylindrical probes. In fact given the disparity between tether longitudinal and transversal dimensions, every point of the tether would collect electrons as if it belongs to an uniformly polarized cylinder. This assumption has three main consequences:

1. since the ratio of the intensity variation within the anodic and cathodic regions is proportional to the square root of the relation between the electronic and ionic mass  $\mu = \sqrt{m_e/m_i}$  (this value is usually small, and depends on the presence of ions of different species: the most abundant ion in the ionosphere is the atomic oxygen  $O_2$ , for which  $\mu = 1/172$ ), the decrease in the intensity along the cathodic region will be considerably smaller than the increase in the anodic area per unit length;
2. the resulting current profile has been obtained considering high potential differences as compared with the plasma temperature. Therefore, the study is confined to plasmas without collisions, no magnetized and following a Maxwellian distribution function.
3. for a cylindrical tether with radius  $R_t$ , the OML law is valid for  $r_t$  lower than the upper limit  $r_t^{max}$ , which, for one plasma temperature and fulfilling the assumption of the high potential bias, is  $r_t^{max} \approx \lambda_D$ , where  $\lambda_D$  is the length of Debye. Slightly above of the OML regime, the decrease in the collected current in comparison with the OML is small, around 5% for  $r_t = 2r_t^{max}$ . An important property of the collection on the OML regime is that, in general, it is applicable to convex sections; for the case of a thin tape of width  $w$  and thickness  $h$ , with

the thickness much lower than the width ( $h \ll w$ ) the OML law is valid for:  $t < 4r_t^{max}$ . On other hand, in a magnetized plasma, the OML law is valid, at least, for  $\lambda_D \ll l_e$ , where  $l_e$  is the thermal electron gyroradius, that is, the radius of rotation of an electron in a plane normal to the magnetic field. It has been confirmed experimentally that the OML law is satisfied (with a 10% margin) in motional plasmas whereas the relative velocity was lower than the thermal velocity of the electrons:

$$\frac{T_\infty}{m_i} \ll \frac{v_{orb}^2}{2} \ll \frac{T_\infty}{m_e}$$

where  $v_{orb}$  is the tether orbital velocity. The ionic distribution and, as a consequence, the structure of the electric potential will be highly anisotropic, but the OML law depends only on the electric distribution, that remains basically Maxwellian.

Being the whole tether the anode, an EDT system, from an electric point of view, is formed mainly by other three elements: the cathodic contactors, necessary to close the circuit within the ionosphere; an interposed load, that can be used to feed useful electric charges; and all the electronics necessary to control that the system works correctly. In the case of active EDT (this mode is not studied in this case, because we are only interested to passive system) the electric circuit needs a potential source to provide a continuous flux of electrons along the tether.

The cathodic contactors considered in this work are the hollow contactors, because these devices are able to emit high currents at low power. In the most efficient operational mode the potential drop between plasma and contactor is quasi constant as the current varies, and it is within the range 15-30V. Moreover, the expelled mass used for its operation is negligible.

The electrical resistance will usually model in an easy way those devices intended to take advantage of the electric intensity flowing through the cable. The resistance is in series in the circuit and the symbol  $Z_{load}$  will be used for it.

An EDT system can work in two main operational regimes: passive tethers, in which the charged particles flow in opposite direction to the induced electric field, and active tethers, in which they are driven along the same direction of the induced electric field. In a prograde Earth orbit, each of these regimes can be obtained and corresponds to the two basic goals that it is possible to pursue with the use of an electrodynamic cable: power generation and thrust. In order to obtain the latter, it is necessary to have a power generator that allows to reverse the current direction, see Fig. 4.1.

## 4.1 Electric Current Profile

A no isolated or partially isolated tether represents an efficient generator of current. This consideration is worth because the area of collection can be increased using longer tether, satisfying at the same time the condition about the *Debye length*. The potential difference in correspondence of the anode (the whole tether) is generated simply moving the cable through the magnetic field. The relative motion causes an electric field (called motional electric field), and induces a potential difference  $\Delta V$  along the cable, expressed by the following equation:

$$\Delta V = \int_L \vec{v}_{rel} \times \vec{B} \cdot d\vec{l} \quad (4.1)$$

where  $\vec{v}_{rel}$  is the relative velocity of the tether respect the magnetic field lines. Plasma has been assumed fixed to the magnetic field and corotating with the planet:

$$\vec{v}_{rel} = \vec{v}_{orbital} - \vec{v}_{plasma} \quad (4.2)$$

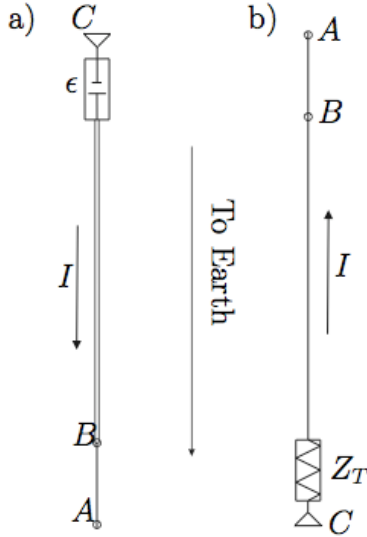


Figure 4.1: Operation Modes: a) active (thruster), b) passive (generator and orbital drag)

$$\vec{v}_{planet} = \vec{v}_{plasma} = \vec{\omega}_{planet} \times \vec{r}_{S/C} \quad (4.3)$$

where  $\vec{r}_{S/C}$  is the state vector of satellite,  $\vec{B}$  the magnetic field vector of the planet and  $d\vec{l}$  the differential element of cable length:

$$\vec{L} = \int_L d\vec{l} = L\hat{u} \quad (4.4)$$

#### 4.1.1 Electric Circuit Equations

The motional electric field  $\vec{E}$ , measured in Volts per meter [ $V/m$ ] is given by:

$$\vec{E} = (\vec{v}_{S/C} - \vec{v}_{plasma}) \times \vec{B} \quad (4.5)$$

The effective motional electric field must be obtained by projecting the vector  $\vec{E}$  along the tether unit vector  $\hat{u}$ :

$$E_t = \vec{E} \cdot \hat{u} = E_\pi \cos \gamma \quad (4.6)$$

with  $\gamma$  the angle between the motional electric field and the tether versor, and  $E_\pi$  the module of  $\vec{E}$ . The maximum differential of potential at tether ends happens when it is aligned with the vector  $\vec{E}$ , whose mathematical expression can be formulated as:

$$\vec{E} \approx \begin{bmatrix} v_{rel,x}^I \\ v_{rel,y}^I \\ v_{rel,z}^I \end{bmatrix} \times \begin{bmatrix} B_x^I \\ B_y^I \\ B_z^I \end{bmatrix} = \begin{bmatrix} v_{rel,y}^I B_z^I - v_{rel,z}^I B_y^I \\ v_{rel,z}^I B_x^I - v_{rel,x}^I B_z^I \\ v_{rel,x}^I B_y^I - v_{rel,y}^I B_x^I \end{bmatrix}$$

If the tether works in passive mode the electrodynamic interaction generates a drag force that lowers the satellite's orbit bringing it slowly to deorbit.

The motional electric field due to the relative motion of the EDT with respect to the magnetic lines drives the collection of electrons from the ionosphere on the anodic region of cable. To let an electric current flows along the tether driven by the potential difference between anode and cathode, a plasma contactor is inserted at the cathodic end of the tether to expel the electrons (see Fig. 4.2).

When electrical circuit is closed electrons are collected in the upper region of the wire along the

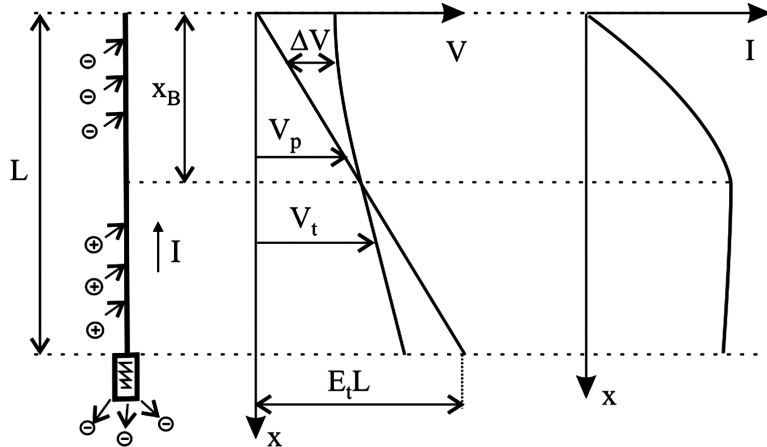


Figure 4.2: Electric current profile

positively biased segment. The electric current profile is highly non-linear and reaches the maximum at  $x_B$  where the potential bias  $\Delta V$  goes to zero. Then in the general case in which the potential drop of the plasma contactor  $V_c$  and/or the impedance  $Z_{load}$  of the applied load is not zero the lower portion of the tether will result negatively biased with respect to the plasma and will collect ions, therefore the electric current decreases. The current collection is here assumed to take place in the orbital motion limited (OML) regime, and the equations governing it along the wire are:

$$\frac{d\Phi}{dx} = \frac{I}{\sigma wh} - E_t \quad (4.7)$$

$$\frac{dI_a}{dx} = \frac{p}{\pi} q_e N_e \sqrt{2 \frac{q_e}{m_e} \Delta V} \quad (4.8)$$

$$\frac{dI_c}{dx} = -\frac{p}{\pi} q_e N_e \sqrt{-2 \frac{q_e}{m_i} \Delta V} \quad (4.9)$$

Where  $I$  is the electric current ( $I_a$  and  $I_c$  respectively the current flowing in the anodic and cathodic segments),  $p$  the perimeter of the wire ( $p = 2(w + h)$ ),  $q_e$  the electron charge,  $m_e$  the electron mass,  $m_i$  the mass of the most abundant ion species.

The electrons, collected by the anodic end from the surrounding environment, flow through the tether till to the cathode, where they are expelled into the ionosphere. This continuous replenishment of electrons is driven by the motional electric field projected along the wire and the local electron density, and happens at expense of Earth's environment. In order to obtain the electric profile along the tether we must solve a set of two differential equations with boundary condition, and it will have to satisfy the circuit equation:

$$E_t L = \Delta V_A + \Delta V_{TETHER} + \Delta V_{LOAD} + \Delta V_C \quad (4.10)$$

Where  $E_t L$  represents the differential of potential induced by Faraday's law, while the potential drops  $\Delta V_A$ ,  $\Delta V_{TETHER}$ ,  $\Delta V_{LOAD}$  and  $\Delta V_C$  happens at anode, along the tether, load and cathode, respectively. The drop along the tether depends on its electric resistance, and so on the geometry of transverse area, the length, material and its temperature.

Equation 4.10 must respect three boundary conditions:

$$\begin{cases} I = 0, \quad \Delta V = \Delta V_A & x = 0 \\ \Delta V_A = \Delta V_C + I_{x=L} Z_{LOAD} & x = L \end{cases}$$

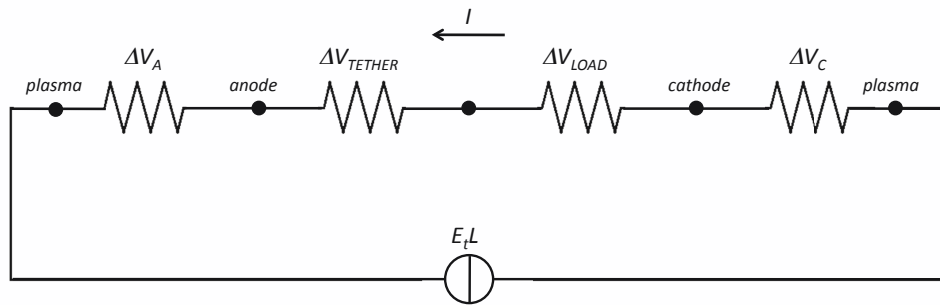


Figure 4.3: Tether electric circuit

These conditions plus Eq. 4.10 define the whole tethered electric circuit. Equations 4.7 – 4.9 must be solved iteratively in order to find the right anodic condition to arrive at the cathode fulfilling 4.10. As example (see Fig. 4.4), we consider a tether whose characteristic are reported in Table 4.1. The anodic part of the tether, long about 1800m, collects electrons until the potential along the wire is zero, then it begin to attract ions, being negative biased, provoking a slight decrease of the current in the cathodic region.

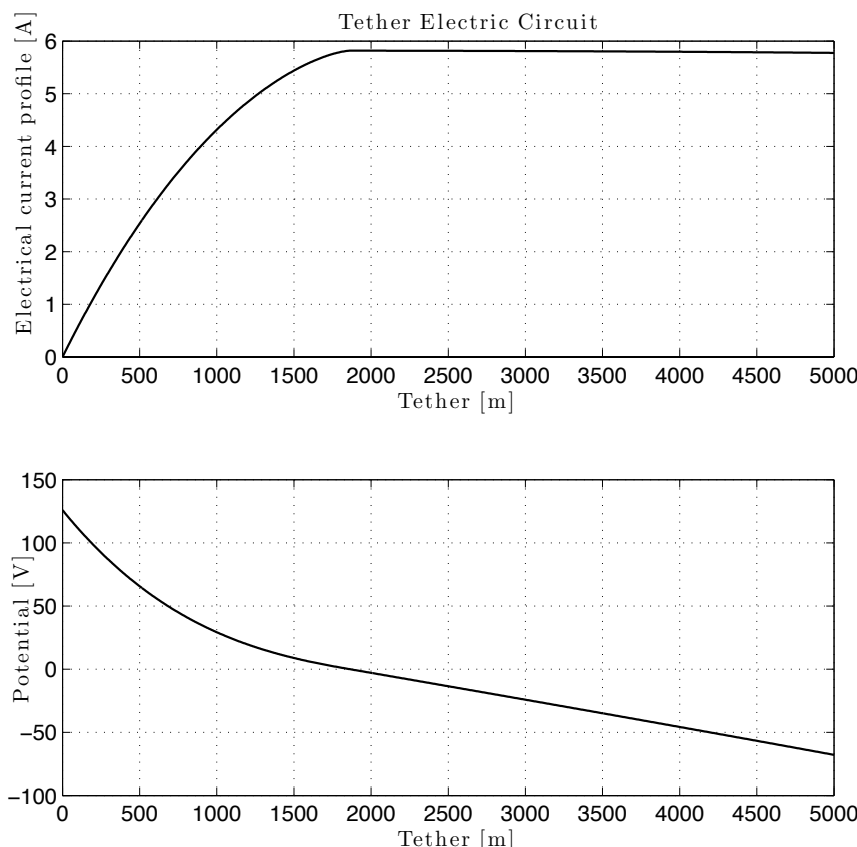


Figure 4.4: Electric current profile obtained by numerical model

$L$	5km
$w$	2cm
$h$	0.1mm
$\sigma$	$4.514 \times 10^7$
$R_{TETHER}$	$110.7\Omega$
$E_t$	$0.15V/m$
$N_e$	$8.27 \times 10^{11} m^{-3}$
$\Delta V_C$	$10V$
$Z_{LOAD}$	$10\Omega$

Table 4.1: Tether parameters

#### 4.1.2 Nondimensional Electric Circuit Equations

Called  $k = wh/(w + h)$  the characteristic transversal length, then the characteristic length  $L^*$ , a typical parameters of bare tethers, is given by:

$$L^* = \frac{(m_e E_t)^{1/3}}{q_e 2^{7/3}} \left( 3\pi \frac{\sigma k}{N_e} \right) \quad (4.11)$$

and the following nondimensional variables can be defined:

$$\xi = \frac{k}{L^*} \in [0, l_t]$$

$$l_t = \frac{L}{L^*}$$

$$i = \frac{I}{I_{sc}}$$

$$\phi = \frac{\Phi}{E_t L^*}$$

where  $I_{sc} = \sigma E_t w h$  is the short-circuit current. So, the nondimensional equations take the form:

$$\frac{d\phi}{d\xi} = i - 1 \quad (4.12)$$

$$\frac{di_a}{d\xi} = \frac{3}{4} \sqrt{\phi} \quad \text{if } \xi \leq \xi_B \quad (4.13)$$

$$\frac{di_c}{d\xi} = -\frac{3}{4} \mu \sqrt{|\phi|} \quad \text{if } \xi > \xi_B \quad (4.14)$$

with  $\xi_B = x_B/L$ , the point where the potential  $\phi = 0$ .

The potential drop in the cathodic region ( $\xi > \xi_B$ ) can be written as:

$$\frac{\Delta V_{BC}}{E_t L^*} = \int_{\xi_B}^{l_t} i(\xi) d\xi = \int_{\xi_B}^{l_t} \left( \frac{d\phi}{d\xi} \right) d\xi = l_t - \xi_B + \phi_C$$

and the third condition for the closure of tether electric circuit takes the following nondimensional form:

$$(\Omega i_C + \tilde{V}_{CC}) l_t + \phi_C = 0 \quad (4.15)$$

where  $\phi_C$  is the potential bias at the cathodic end,  $\tilde{V}_{CC} = V_{CC}/(E_t L)$  is the nondimensional form of  $V_{CC}$  and  $\Omega = Z_{load} = R_T$  is the nondimensional form of the interposed load and  $R_T = L/(\sigma wh)$

is the electrical resistance of the tether.

The calculation of the tether current profile requires the boundary value problem, initial and boundary conditions, and tether circuit equation to be solved. The problem must be tackled numerically to obtain the following parameters: 1) the profiles of the current  $i$  and potential  $\phi$ , 2) the maximum current  $i_B$ , 3) the current at the cathodic end  $i_C$ , and 4) the length of the tether anodic segment,  $\xi_B$ .

The integration of the problem is straightforward and can be performed using different algorithms.

#### 4.1.3 Resolution Algorithms

A Boundary Value Problem (BVP) is a system of ordinary differential equations with solution and derivative values specified at more than one point. Most commonly, the solution and derivatives are specified at just two points (the boundaries) defining a two-points boundary value problem. In practice, most BVPs arise as a combination of equations defining various orders of derivatives. In an explicit BVP system, the boundary conditions and the right hand sides of the ordinary differential equations can involve the derivatives of each solution variable up to one order less than the highest derivative of that variable appearing on the left hand side of the ODE defining the variable.

The words two-points refer to the fact that the boundary condition is evaluated at the solution at the two interval endpoints, usually the initial and end positions.

An easier way to solve the problem lays in determining the current profile all along the tether varying the initial conditions about the anodic potential drop  $\phi_A$  until to satisfy the condition at the cathode (Eq. 4.15). Even if particularly slow, bisection algorithm can be used to change the initial value of  $\phi_A$  and arrive at the solution. The main drawback of this strategy is that it requires to solve at every interaction the set of differential equations, and so a lot of computational time. In literature there are other better techniques to solve problem: the semi-analytical [52][83] and the asymptotic [9] methods. Even if they reach the solution in two different ways, they start from the same idea: instead of calculating the whole profile at every iteration, they, before, solve a no-linear equation to find the position of  $\xi_B$  and then the differential set of equations, only once. These methods are very efficient, and let to save a lot of computational time limiting the number of numerical operations required.

#### Semi-Analytical Method

An easier technique to solve the problem is to find a variable which describes the length arc of the solution in the state space and related to the non dimensional length of the electrodynamic tether. In order to do so, the state variables will be expressed in terms of an arc length, represented by the letter  $\nu$ . The nondimensional variables of variables, just introduced, are used to reduce the problem to quadratures, and Eqs. 4.12 – 4.14 are manipulated and rewritten as it follows:

$$\phi = (i_B - i)^{2/3} (2 - i_B - i)^{2/3} \quad \text{if } \phi > 0 \quad (4.16)$$

$$\phi = -\frac{1}{\mu^{2/3}} (i_B - i)^{2/3} (2 - i_B - i)^{2/3} \quad \text{if } \phi < 0 \quad (4.17)$$

The approach on the cathodic and anodic segments are slightly different. In the anodic end, where  $\phi > 0$ , the current profile is described by Eq. 4.12 and 4.13, with the following boundary conditions:

$$\xi = 0 \Rightarrow i = 0, \quad \phi = \phi_A$$

$$\xi = \xi_B \Rightarrow i = i_B, \quad \phi = 0$$

The value of  $\phi_A$  is an unknown, and must be calculated finding the position of point  $B$ , and so  $\xi_B$  and  $i_B$ . Starting from the expression 4.20, and introducing it in the first of the circuit differential equations, it is possible to obtain parametric expressions for both  $\xi$  and  $i$ :

$$\begin{aligned}\phi(i) &= (i_B - i)^{2/3} (2 - i_B - i)^{2/3} \quad \text{if } \phi > 0 \\ i(\nu) &= 1 - (1 - i_B) \cosh(\nu) \\ \xi(\nu) &= \frac{4}{3} (i - i_B)^{1/3} [f(\nu_0) - f(\nu)]\end{aligned}\tag{4.18}$$

where  $\nu \in [0, \nu_0]$ ,  $\nu_0 = \cosh^{-1} \left( \frac{1}{1-i_B} \right)$  and  $f(x) = \int_0^x \sinh^{1/3} \zeta d\zeta$ . This description is valid for  $i_B \neq 1$ . When  $i_B = 1$  the previous relations take the following aspect:

$$\begin{aligned}\phi(i) &= (1 - i)^{4/3} \\ \xi(\nu) &= 4 \left[ 1 - (1 - i)^{1/3} \right]\end{aligned}\tag{4.19}$$

with  $i \in [0, 1]$ .

In the cathodic region ( $\phi < 0$ ) the current profile due to Eq. 4.12 and 4.14, with boundary conditions:

$$\xi = \xi_B \Rightarrow i = i_B, \quad \phi = 0$$

$$\xi = l_t \Rightarrow i = i_C, \quad \phi = \phi_C$$

And rearranging the equation as before, we obtain:

$$\begin{aligned}\phi(i) &= -\frac{1}{\mu^{2/3}} (i_B - i)^{2/3} (2 - i_B - i)^{(2/3)} \\ i(\nu) &= 1 - (1 - i_B) \cosh(\nu) \\ \xi(\nu) &= \frac{4}{3} (i - i_B)^{1/3} \left[ f(\nu_0) + \frac{f(\nu)}{\mu^{2/3}} \right]\end{aligned}\tag{4.20}$$

where  $\nu \in [0, \nu_T]$ , being  $\nu_T$  the value of the arc length correspondent to  $\xi(\nu_T) = l_t$ , and, therefore, an unknown of the problem.

So, the two unknowns in the parametric representation of the solution are  $i_B$  and  $\nu_T$ , and the solution should satisfy:

$$\xi(\nu_T) = l_t \Omega l_t i_C + \tilde{V}_{CC} l_t + \phi_C = 0\tag{4.21}$$

In this way, the formulation of the problem is close and, in general, it will be well posed.

Supposed a tentative non dimensional intensity  $i_B \in [0, 1]$ , in first place, the boundary condition in terms of the intensity is solved and checked, after that, if the solution corresponds to the given non dimensional length. In order to do that, an intensity  $i_C$  is used as unknown, instead of  $\nu_T$ . In fact, for a more compact formulation of this computational strategy, a change of variable is used:  $i_C = i_B - \epsilon$ . A sistem of two equations with two unknowns  $(\epsilon, i_B)$  is obtained where there is a number of parameters:  $\mu$ ,  $l$ ,  $\Omega$  and  $\tilde{V}_{CC}$  are obtained.

$$\begin{aligned}\mu^{2/3} (\Omega l_t i_B + \tilde{V}_{CC} l_t) &= \mu^{2/3} \Omega l_t \epsilon + \epsilon^{2/3} (2(1 - i_B) + \epsilon)^{2/3} \\ \mu^{2/3} l_t &= \frac{4}{3} (1 - i_B)^{1/3} [\mu^{2/3} f(\nu_0) + f(\nu_T)]\end{aligned}$$

with  $\nu_T = \cosh^{-1} \left( \frac{\epsilon}{1-i_B} \right)$ . That is, the boundary condition on the state space is enforced firstly, considering there is a degree of freedom ( $i_B$ ) which comes from the parametrization of the solution, and checking after that if the corresponding arc length provides  $\xi = l_t$ . This formulation presents two advantages respect to the former scheme. Firstly, taking into account that the fall of intensity

along the cathodic segment is small for common tether lengths and electric loads, the approximation  $i_C = i_B - \epsilon$  (with  $\epsilon \ll 1$ ) is adequate; and it can be used as guess in the iterative process:

$$\epsilon_0 \approx \frac{\mu \left[ \Omega l_t i_B + \tilde{V}_{CC+l_t} \right]^{3/2}}{2(1-i_B)}$$

Then, the equation in  $\epsilon$  (with  $i_B$  as parameter) is simpler than the correspondent integral equation for  $v_T$ . In this case, more efficient methods for searching roots can be used, as the Newton-Raphson method.

Once noted the position  $\xi_B$  the whole electric profile ( $\phi, i$ ) can be calculated along the wire integrating Eqs. 4.12 - 4.14

### Asymptotic Method

This algorithm provide an high-accuracy solution for the current and potential profile by using perturbation theory. Just like semi-analytical approach, the asymptotic method utilizes the non-dimensional formulation, because it allows to treat the problem with a perturbation technique in which a parameter  $\epsilon$ , defined as the ratio between tether ohmic and contact impedance, quantifies the influence of ohmic effects on the final solution:

$$\frac{d\phi}{d\xi} = ei - 1 \quad (4.22)$$

$$\frac{di_a}{d\xi} = \frac{3}{2}\alpha_0\sqrt{\phi} \quad \text{if } \xi \leq \xi_B \quad (4.23)$$

$$\frac{di_a}{d\xi} = -\frac{3}{2}\alpha_0\mu\sqrt{-\phi} \quad \text{if } \xi > \xi_B \quad (4.24)$$

where

$$\epsilon = \frac{I_{ch}}{\sigma wh E_t} \quad (4.25)$$

$$I_{ch} = \frac{4}{3} \frac{(w+h)}{\pi} N_e \sqrt{2 \frac{E_t}{m_e} q_e^3 L^3} \quad (4.26)$$

$$\alpha_0 = \frac{4}{3} \frac{(w+h)}{\pi} \frac{q_e N_e}{I_{ch}} \sqrt{2 \frac{E_t}{m_e} L^3} \quad (4.27)$$

The parameter  $\epsilon$  is very important and depends on the tether geometry and conductivity  $\sigma$ , the local plasma density  $N_e$  and on the projected motional electric field.

The algorithm foresees to expand the Eqs. 4.22 - 4.24 as a function of  $\epsilon$  in order to transform the differential problem to an algebraic one. The procedure is rather complex and the expressions cumbersome, so that's why here the obtained equations aren't reported, but I refer to Bombardelli's work "Asymptotic Solution for the Current Profile of Passive Bare Electrodynamic Tethers"[9] for a full description of the model. The author gives an exhaustive overview of electrical behavior of a ED tether. In particular he analyzes in detail the possible regimes (small and large ohmic effects) and the effects of the electric load: for each case he provides the best equations describing the electric current collection satisfying the circuit condition at the cathode.

In this work I chose to use the asymptotic method for the routine of the orbital simulator, dedicated to the determination the electric current profile, because the best trade-off between accuracy and computational time required for the solution.

## Method Comparison

A comparison test has been led in *Matlab* environment to show the validity of the two models. Supposing the bisection algorithm the most accurate, since it integrates every time directly the OML equations without any other assumption, the semi-analytical and asymptotic model are compared with it to estimate their precision.

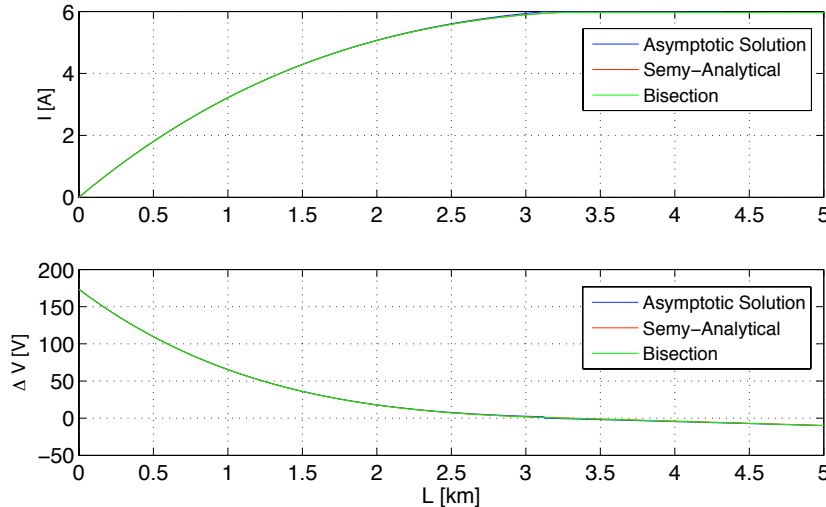


Figure 4.5: Model Comparison

Figure 4.5 reported the electric current and potential profiles for the following conditions:

```

Tether length      = 5000.000000 [m]
Tether width       = 1.000000e-02 [m]
Tether thickness    = 1.000000e-04 [m]
Tether temperature   = 270.000000 [K]
Tether resistance    = 120.843975 [ohm]
Tether conductivity = 4.137567e+07 [1/(ohm*m)]
Drop at cathode     = 10.000000 [1/(ohm*m)]
Electrical load      = 0.000001 [ohm]
Electromotive field = 0.150000 [V/m]
Electron Density     = 5.000000e+11 [1/m^3]
  
```

```

Ratio between tether ohmic and contact impedance: epsilon = 4.493458
Short-circuit current nondimensional abscissa: xi_hat      = 0.925379
Nondimensional drop at cathode: v_HC                      = 0.013333
  
```

The bisection model is very slow and requires several seconds to obtain the solution, while the asymptotic one is the fastest taking only 0.038900 to solve the circuit.

**Asymptotic Solution**

Large ohmic effects:  $\xi_B = 0.624619$   
Dimensional  $\xi_B$  position 3123.093320 [m]  
Averaged current along the tether = 4.705540

Time required for Asymptotic Solution Method: 0.038900 [s]  
Potential at Anode = 173.508523  
Ohmic loss along the tether = 568.636169  
Potential at tether end = -10.000006  
Potential drop at the load = 0.000006  
Potential drop at the load plus potential drop at the cathode = 10.000006

---

**Semy-Analytical Method**

Time required for Semy-Analytical Method: 0.152095 [s]  
Potential at Anode = 173.344776  
Ohmic loss along the tether = 563.273004  
Potential at tether end = -9.756715  
Potential drop at the load = 0.000006  
Potential drop at the load plus potential drop at the cathode = 10.000006

---

**Shooting Method**

Time required for Shooting Bisection Method: 7.428683 [s]  
Number of iteration for the convergence: 20

Potential at Anode = 173.339903  
Ohmic loss along the tether = 1133.481756  
Potential at tether end = -9.918674  
Potential drop at the load = 0.000006  
Potential drop at the load plus potential drop at the cathode = 10.000006

---

The profiles, evaluated by each algorithm, are very close and the errors little. The major uncertainty lays in the calculation of zero-potential point, but the it is very limited and less than 5%.

---

**--- Errors Evaluation at Anode**

Errors Asymptotic Solution Method  
Potential relative error = 0.096967 %

Errors Semy-Analytical Method  
Potential relative error = 0.002502 %

---

--- Errors Evaluation at Zero-bias abscissa

Errors Asymptotic Solution Method  
 Current relative error = 0.392590 %  
 Zero-bias position relative error = 4.899716 %

Errors Semy-Analytical Method  
 Current relative error = 0.051388 %  
 Zero-bias position relative error = 0.487211 %

---

--- Errors Evaluation at Cathode

Errors Asymptotic Solution Method  
 Current relative error = 0.036883 %  
 Potential relative error = 0.819985 %

Errors Semy-Analytical Method  
 Current relative error = 0.052734 %  
 Potential relative error = 1.632878 %

---

## 4.2 Energetic Considerations

For a bare tether working in the generator regime, there are two significant parameters related to the power developed by the electrodynamic forces acting on the system:

1. the power dissipated in the whole system  $W_d$
2. the power obtained in the interposed load  $Z_{load}$ ,  $W_g$ .

The first term gives the loss of mechanical energy associated with the deorbiting process, and the second one is the energy that can be used onboard the orbiter to perform some task.

The power dissipated by the electrodynamic force along a tether element  $dl$  is

$$dW_d = \vec{v} \cdot (\hat{u} \times \vec{B}) I(l) dl$$

and assuming that the velocity of each element of the wire is equal to the orbital velocity of the satellite, the overall dissipated power will be

$$W_d = \vec{v} \cdot (\hat{u} \times \vec{B}) \int_0^L I(l) dl = -E_t \int_0^L I(l) dl$$

And in terms of the nondimensional variables, such an expression becomes:

$$W_d = -E_t L I_{sc} \frac{1}{l_t} \int_0^{l_t} i(\xi) d\xi = -E_t L I_{sc} \frac{U(l_t, \Omega)}{l_t}$$

and  $U(l_t, \Omega)$  can be calculated as follows:

$$U(l_t, \Omega) = \int_0^{l_t} i(\xi) d\xi = l_t - \phi_A + \phi_C$$

So in nondimensional terms it results:

$$\frac{W_d}{E_t L I_{sc}} = - \left( 1 - \frac{\phi_A - \phi_C}{l_t} \right) = -\eta_t$$

where  $\eta_t$  is the tether efficiency as deorbiter:

$$\eta_t = 1 - \frac{\phi_A - \phi_C}{l_t} \quad (4.28)$$

The power obtained in the interposed load is given by

$$Wg = I_C^2 Z_{load} = E_t L I_{sc} i_C^2 \Omega$$

which, taking into account the tether-circuit equation, can be written as:

$$\frac{Wg}{E_t L I_{sc}} = i_C \left( \frac{|\phi_C|}{l_t} - \tilde{V}_{CC} \right) \approx \frac{i_C |\phi_C|}{l_t} \quad (4.29)$$

For the deorbiting, the interposed load must be as small as possible in order to minimize the power generated. The limit in which  $Z_{load} = 0$  represent as the ideal case for this kind of applications. Assuming both  $\mu$  and  $V_{CC}$  very small, and  $Z_{load} = 0$ , the tether-circuit equation provides  $\phi_C$ , and this condition holds under only two conditions: either  $i_B = 1$  or  $l_t = \xi_B$ . This gives rise to two regimes for fulfilling  $\phi_C = 0$ :

1. In the short tether regime ( $l_t < 4$  and  $t_t = \xi_B$ ), the segment BC (see Fig. 4.1b) disappears; that is, the entire tether is inside the anodic segment AB. Therefore, in this regime the relation  $l_t = \xi_B$  is always satisfied.

The power dissipated by the system in this regime is:

$$\frac{W_d}{E_t L I_{sc}} = - \left( 1 - \frac{[i_B (2 - i_B)]^{2/3}}{\xi_B} \right)$$

and hence is also function of  $i_B$ .

The upper extreme of this segment appears for  $l_t = \xi_B = 4$  and  $i_B = 1$ , where the transition to the long tether regime takes place.

2. In the long tether regime ( $i_B = 1$  and  $\xi_B = 4$ , and the solution for the cathodic segment  $\xi > \xi_B$  is trivial:  $\phi(\xi) = 0$  and  $i(\xi) = 1$ ). The power dissipated by the system in this regime is:

$$\frac{W_d}{E_t L I_{sc}} = - \left( 1 - \frac{1}{l_t} \right)$$

and is only a function of  $l_t$ .



# Chapter 5

## EDT Dynamics

The dynamics of electrodynamic tethers have been studied for both rigid and flexible wire. By using dumbbell model a spectral analysis has been carried out to investigate the main frequencies affecting the motion of the satellite. By means of lump masses model the main features of lateral vibrational modes has been analyzed for both inert and ED tethers.

### 5.1 Spectral Analysis of a Rigid Dumbbell Tethered System

The spectral response of electrodynamic force has been analyzed, studying the main frequencies that modulate its magnitude and direction along the orbital path. Fourier transform has been applied to in-plane and out of-plane components of the Lorentz force. All three kinds of magnetic field have been used in way to observe how much the spectrum changes passing from a simple model, as centered dipole, to a much more accurate as IGRF. The results have been parameterized as a function of orbital inclination, and several plots have been reported about the most meaningful frequencies in order to understand as they change passing from prograde to retrograde orbits.

#### 5.1.1 Spectral analysis with different magnetic fields

Truncated at degree  $n = 1$ , the series 3.1 provides the field of a dipole centred at the geographic Earth's centre having an axis inclined with respect to the geographic axis, because it includes only the terms  $g_1^0$ ,  $g_1^1$  and  $h_1^1$ . Instead, as already explained the eccentric dipole model represents an approximation of the series stopped at  $n = 2$  and, and uses the coefficients  $g_1^0$ ,  $g_1^1$ ,  $g_2^0$ ,  $g_2^1$ ,  $g_2^2$ , and  $h_1^1$ ,  $h_2^1$ ,  $h_2^2$  to evaluated the center of the dipole, that has the same momentum and orientation of the centred one.

The spectral analysis has been led for a satellite following a circular orbit with tether always aligned along the local vertical. At every point the current flowing along the tether is the short circuit current, the maximum possible for the configuration chosen. These assumptions are necessary in order to find the frequencies characterizing the Lorentz force, in fact at each inclination the data must be collected for several days at regular temporal steps to get well-distinguishable frequencies by means of Fourier transform.

## Dipole magnetic model

In the synodic reference frame used,  $F_{el,y}$  represents the component in plane along the fly direction, while  $F_{el,z}$  describes the contribution perpendicular to orbital plane. The dipole model simplifies the magnetic field expression, but losing important information about it. Its expression in the inertial frame is:

$$\vec{B}_{Dip}^I = \mu_m \left( \frac{R_E}{r} \right)^3 \begin{pmatrix} 3\hat{\mathbf{u}}_m \cdot \hat{\mathbf{r}}) \hat{r}_x - \sin(\beta_m) \cos(\alpha_m) \\ (3\hat{\mathbf{u}}_m \cdot \hat{\mathbf{r}}) \hat{r}_y - \sin(\beta_m) \sin(\alpha_m) \\ (3\hat{\mathbf{u}}_m \cdot \hat{\mathbf{r}}) \hat{r}_z - \cos(\beta_m) \end{pmatrix} \quad (5.1)$$

The dipole model is defined only by frequencies  $f_E$ ,  $f_{orb}$  and  $2f_{orb}$ , the same components that we can find in the Lorentz force by means Fourier transform. In particular  $f_E$  and  $2f_{orb}$  modulate  $F_{el,y}$ , while  $f_{orb}$  modulates  $F_{el,z}$ . The force is also characterized by another very important frequency,  $f_{rel}$ , due to relative motion between satellite and ionospheric plasma:

$$f_{rel} = f_{orb} \left( 1 + \frac{|\vec{v}_{rel}|}{|\vec{v}|} \right) \quad (5.2)$$

So in the  $F_{el,y}$  and  $F_{el,z}$  spectrums (see Fig. 5.1) we can find respectively the terms  $(f_E + f_{rel}$ ,  $2f_{orb} \pm f_{rel}$ ) and  $(f_{orb} \pm f_{rel})$ .

## Eccentric dipole magnetic model

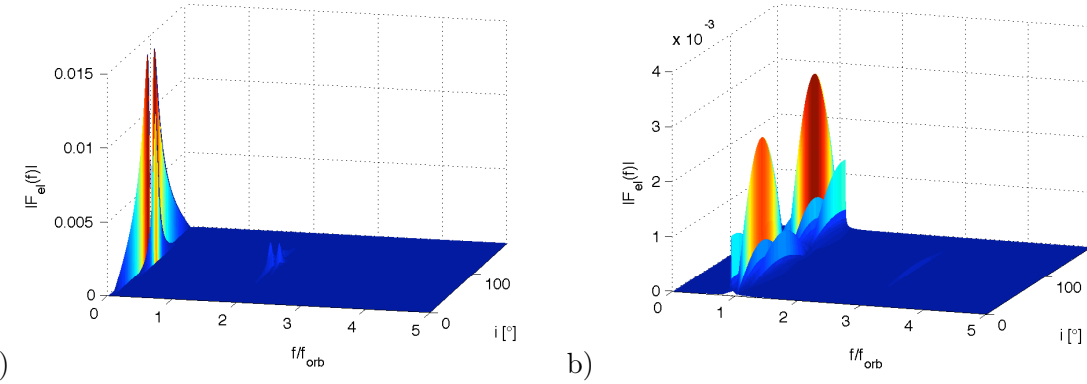
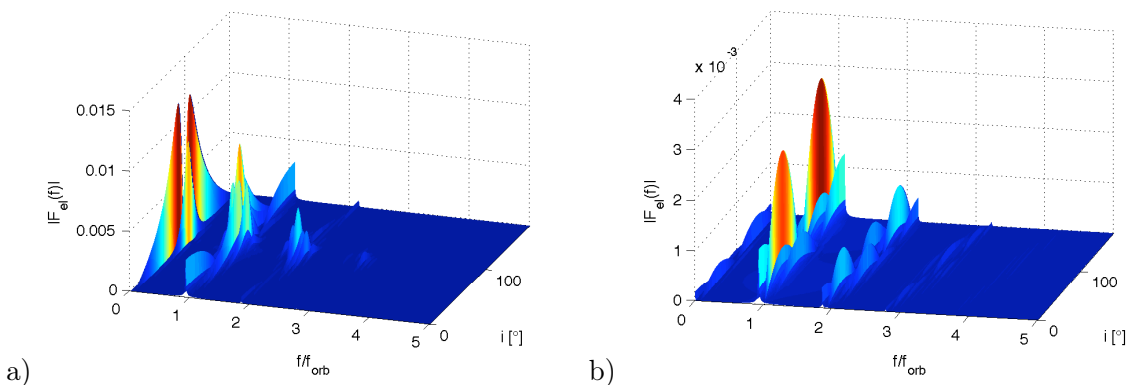
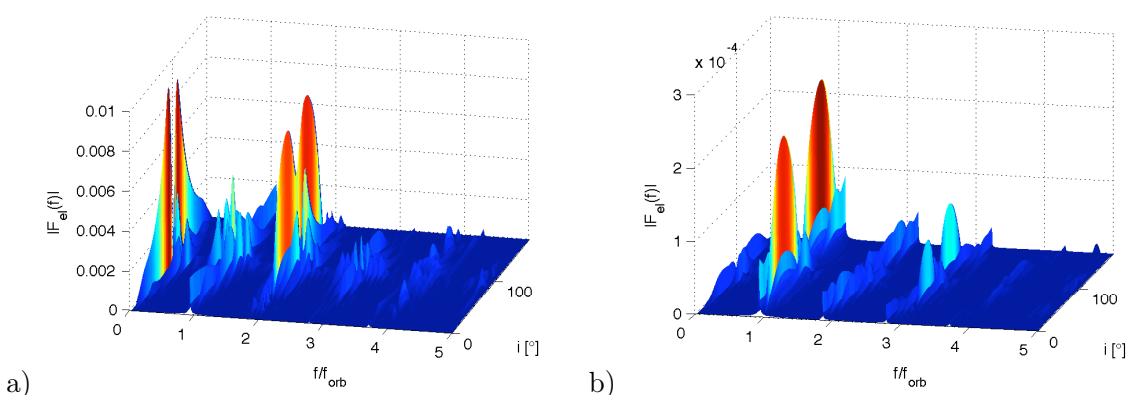
The analysis, led by the eccentric dipole model explained in 3.2.2, is more accurate than simple centered one. In fact introducing the offset it lets to recover the main frequency components:  $f_E$ ,  $f_E + f_{rel}$ ,  $f_{orb} \pm if_{rel}$ ,  $2f_{orb} \pm if_{rel}$  and  $3f_{orb} \pm if_{rel}$ , with  $i = 0, 1, 2$ . Instead, terms higher than  $3f_{orb}$  are too small to be detected (see Fig. 5.2).

## IGRF magnetic model

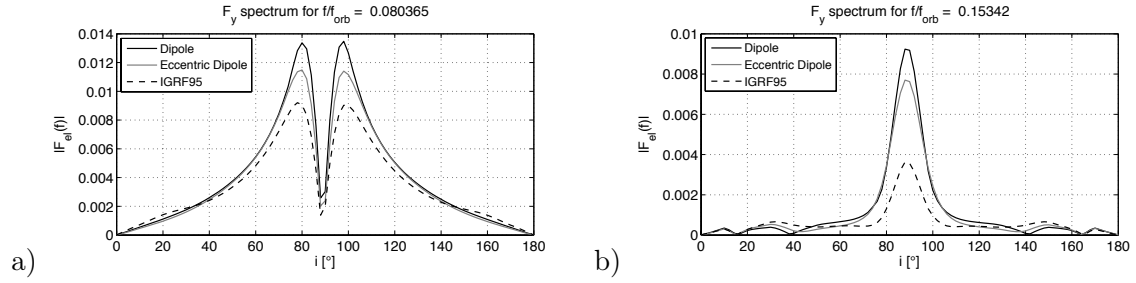
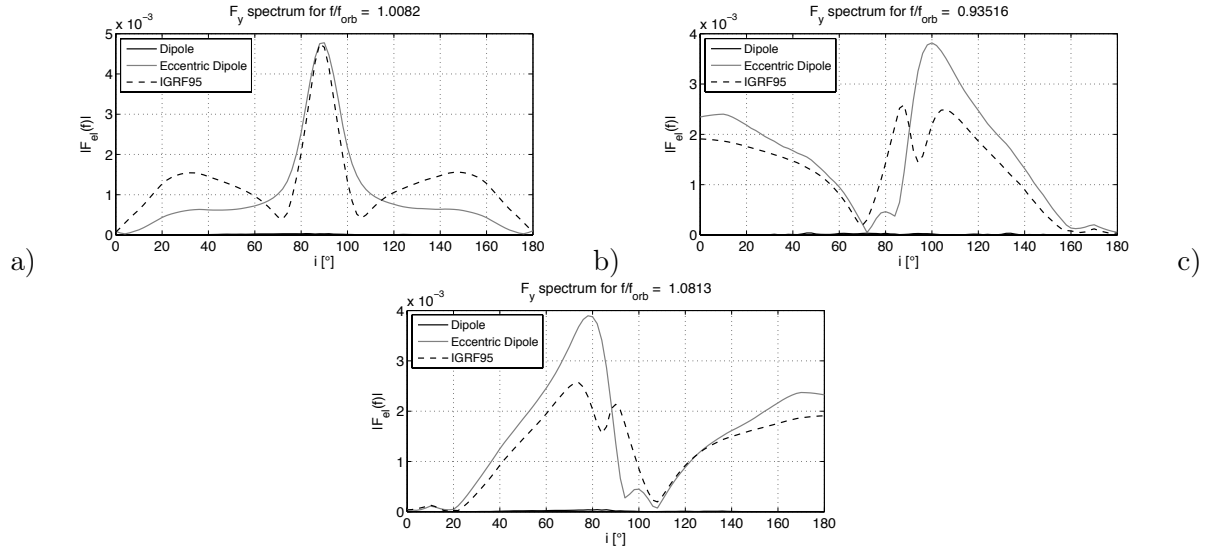
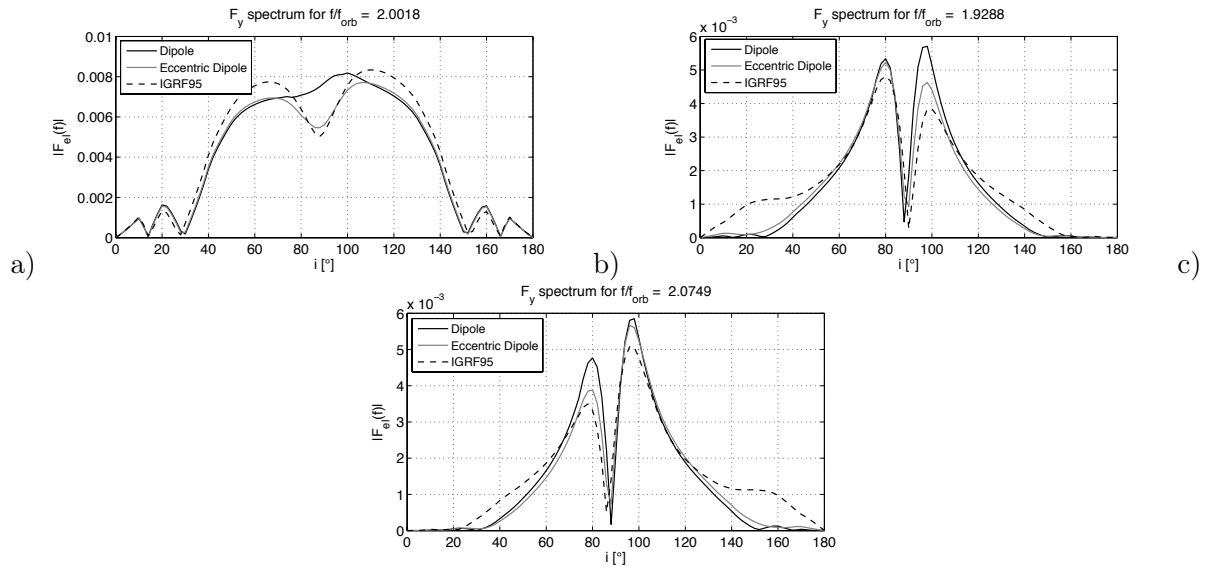
The International Geomagnetic Reference Field takes into account all the mean features of Earth's magnetic field, which anomalies cause the appearance of new frequencies affecting the electrodynamic force. In fact the more accurate IGRF model permits to individuate frequencies till to  $4f_{orb}$ , while the higher ones are too low and decrease till to disappear in the 3D spectral response graph (see Fig. 5.3). Instead the trend of lower terms is very close to those determined by eccentric dipole model, even if the peaks are slightly smaller, because part of energy has been distributed to the other excited components.

## Frequencies affecting the in-plane component of Lorentz force

It's interesting to note the effects of the inclination on the most meaningful frequency. The component due to the rotation motion of the Earth  $F_{el,y}(f_E)$  (see Fig. 5.4a) is zero at equatorial and polar orbit, but it has the maximum at high inclination. Moreover its contribution is symmetrical for prograde and retrograde orbits. The component at the same frequency plus the relative one  $F_{el,y}(f_E + f_{rel})$  (see Fig. 5.4b) is null at zero inclination orbit, and maximum polar orbit. Also the terms at orbital frequency and its multiples  $F_{el,y}(f_{orb})$  and  $F_{el,y}(2f_{orb})$  (see Fig. 5.5) have their

Figure 5.1: Spectral analysis for dipole magnetic model: a)  $F_{el,y}$  component, b)  $F_{el,z}$  componentFigure 5.2: Spectral analysis for dipole magnetic model: a)  $F_{el,y}$  component, b)  $F_{el,z}$  componentFigure 5.3: Spectral analysis for IGRF magnetic model: a)  $F_{el,y}$  component, b)  $F_{el,z}$  component

maximum for high inclination orbit. Instead  $F_{el,y}(f_{\text{orb}} + f_{\text{rel}})$  and  $F_{el,y}(f_{\text{orb}} - f_{\text{rel}})$  have quasi symmetrical trends with respect to  $90^\circ$  inclination:  $F_{el,y}(f_{\text{orb}} - f_{\text{rel}})$  is very intense at low inclination prograde and at polar orbits, and decrease to zero for retrograde ones, while  $F_{el,y}(f_{\text{orb}} - f_{\text{rel}})$  at opposite is considerable at low inclination retrograde and at polar orbits, but negligible for equatorial prograde paths.

Figure 5.4: Spectral term at: a)  $F_{el,y}(f_E)$ , b)  $F_{el,y}(f_E + f_{rel})$ Figure 5.5: Spectral term at: a)  $F_{el,y}(f_{\text{orb}})$ , b)  $F_{el,y}(f_{\text{orb}} - f_{\text{rel}})$ , c)  $F_{el,y}(f_{\text{orb}} + f_{\text{rel}})$ Figure 5.6: Spectral term at: a)  $F_{el,y}(2f_{\text{orb}})$ , b)  $F_{el,y}(2f_{\text{orb}} - f_{\text{rel}})$ , c)  $F_{el,y}(2f_{\text{orb}} + f_{\text{rel}})$ 

## 5.2 Shape Modes of a Flexible Tethered System

In this section early results of numerical simulations are presented. The behavior of an electrodynamic tether has been analyzed with a new orbital simulator, developed in Fortran. The code

implements the governing equations of a flexible tethered system to simulate the dynamical evolutions of orbital and attitude motion perturbed by aerodynamic and electrodynamic forces. A lump-mass approach has been followed with the tether discretized in several lumps, whose inertial properties are concentrated at equally distanced points, while the visco-elastic forces act along the massless links between the lumps. The trajectory described by each mass is projected into the orbital reference frame to highlight the radial, in-plane and out-of-plane components. Moreover the thermal dependency has been included in the full simulation because both the distances between the lump masses and the tensions acting along them are function of the temperatures of each node. A block diagram illustrates the architecture of the code (see Fig. 5.7). The time and position variables are passed to the environmental routines to calculate the electron density of the ionosphere, magnetic field, atmospheric density and exposition to solar and terrestrial radiation. This information is used to estimate the Lorentz and aerodynamic forces, and the thermal fluxes. The electric current flowing along the tether is a function of its temperature and the induced potential, which according to the Faraday's law depends on the relative velocity of the satellite with respect to the magnetic field. The ohmic losses and electron impacts are also included as contributions to the thermal dynamics of the wire. The relative positions and the velocities of the lump masses give the local deformation of the tether and the magnitude of the elastic force, which is also a function of the temperature through the linear expansion coefficient. Finally, numerical integration routines (DOPRI) are used to integrate the differential equations of the motion and provide the state vector for every lump mass.

### 5.2.1 Eigen-Frequencies

The normal modes of vibration of the tether can be excited in two main ways. The first one consists of loading the whole wire by means of an uniform distributed force. Then the mechanical load is released after few seconds to study the free motion of the particles subjected to internal tensional forces. The most important problem of this approach is due to the difficulty about exciting all the  $N$  modes. In fact because of the symmetry it tends to stimulate the odd ones, while those even are practically absent. The second strategy concerns an appropriate choice of the initial lateral velocity conditions of the lump masses. By providing an in-plane component of the velocity (or in alternative an initial lateral displacement) it is possible to obtain a more rich and complete frequency spectrum. In particular, in our case, only the first two lump masses are initially set with a in-plane velocity different from zero, while all the others are at rest along the local vertical, as shown in Fig. 5.8.

The frequency spectrum analysis has been led as it follows. First, a simplified model of taut tether with blocked end masses (the same one used to derive the expressions of the eigen-frequencies in Section 2.2.6) has been considered in order to test and verify it comparing the calculated eigen-frequencies with those drawn from the theory. The equations of motion have been integrated for several cases, by diving the rod in equal segments starting from one till ten lump masses.

Successively the same discretized model has been utilized for a tethered system flying along an equatorial circular orbit has been considered. Two important features distinguish the two models: the first is about the end masses, which are free to move into the space, the second one concerns the velocity of the points. In fact in this configuration each mass has an inertial velocity different to zero, because the centrifugal acceleration must balance the gravity attraction towards the Earth. But, with respect to the synodic reference frame (orbiting with the satellite) each point results steady if the tether maintains its equilibrium position along the local vertical, because the synodic velocity has all the components null. Exciting the first masses with a lateral component, the vibrational dynamics

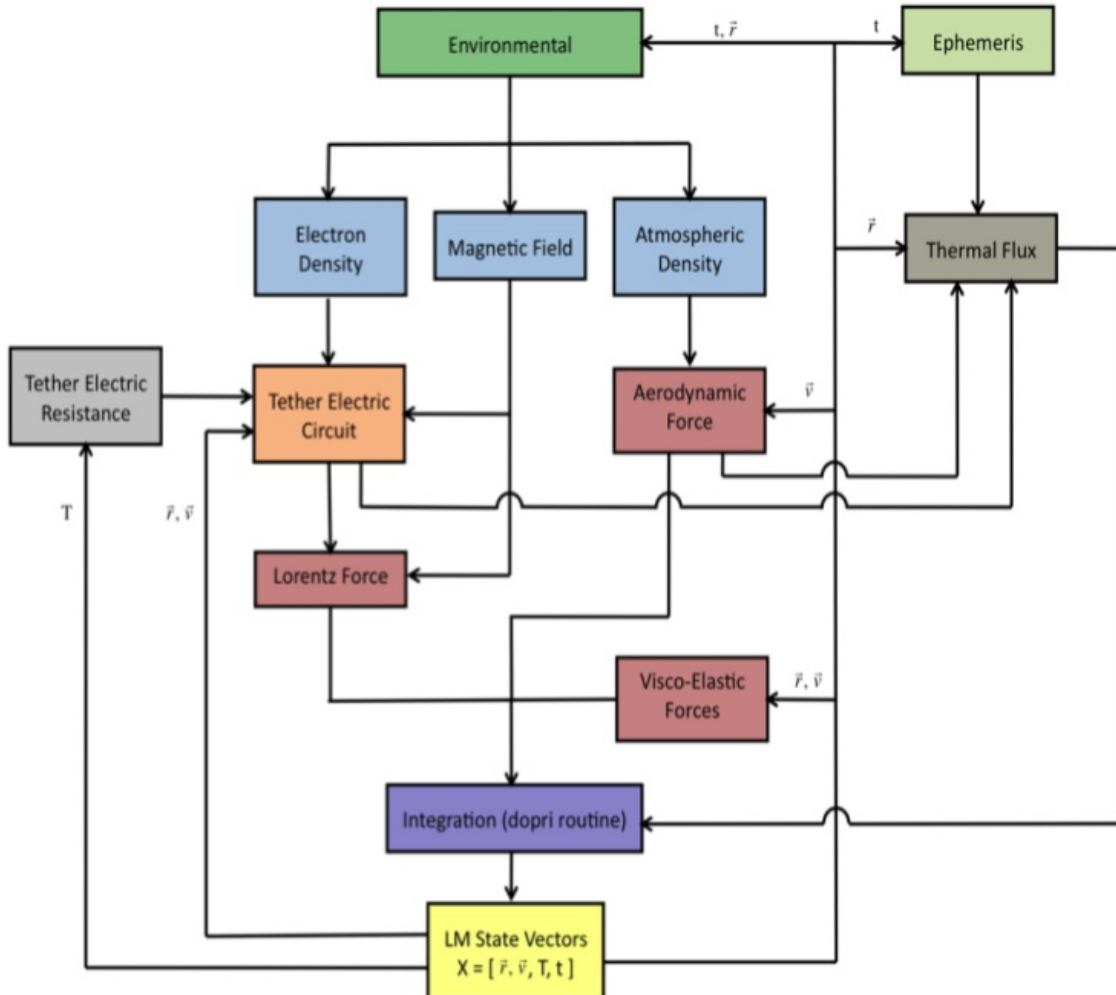


Figure 5.7: Block diagram of simulation code

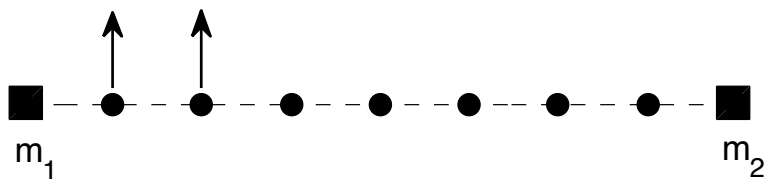


Figure 5.8: Initial in-plane conditions

will be transmitted to all the other nodes, which begins to oscillate around the equilibrium point following a lateral trajectory that is the linear combination of all the  $N$  modes. By calculating the Fourier transform of this motion for each discretization from one to ten modes all the eigen-frequencies have been determined, and so compared with those expected by the theory.

### 5.2.2 Taut wire

To test the model an aluminum tether long 5km has been adopted with a sectional area about  $10^{-6}\text{m}^2$  ( $10^{-2}\text{m} \times 10^{-4}\text{m}$ ). As consequence of its geometry the total mass of the wire becomes 13.5kg. The tension, acting in longitudinal direction, has been chosen equal to 0.5N. This is a reasonable

force for applications with space tethers, and it corresponds to that would pull the rod when the reduced mass is approximately 25kg (a value very close to cases which will be investigated in this project). In Table 5.1 the eigen-frequencies (mHz) determined for each case have been reported. The first mode defines the larger bowing of the tether, while the other frequencies are associated at lower energies. This fact can be easily seen plotting the motion of one of the lump masses and its respective spectrum (see Figs. 5.9-5.10). In Fig. 5.11 the comparison between the eigen-frequencies obtained by the Fourier analysis and those expected from the Eq. 2.88 are shown for the case of 10 nodes. The spectral lines in black refer to numerical results, while the grey ones to theoretical frequencies. As it can be noted the lines are very close each other demonstrating good agreement between the two numerical and analytical models. Moreover we can note that the last frequencies tends to the cut-off frequency, is that the maximum term the model can evaluate by means of this discretization. The cut-off frequency is reached following a sine law, as explained by Eq. 2.88, with the argument of the sinusoid ranging between 0 and  $\pi/2$ . Therefore approaching to the higher frequencies the distance between them is more and more little, till to arrive asymptotically to the cut-off limit value permitted for the number of nodes chosen.

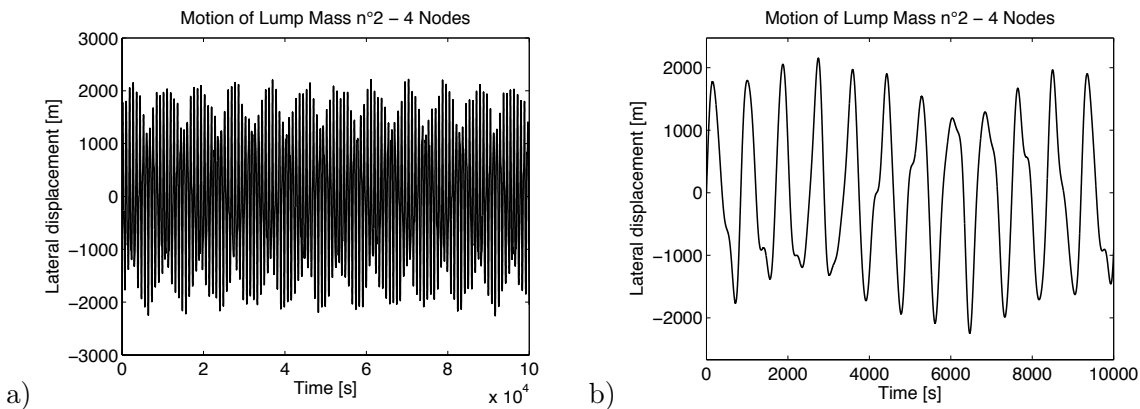


Figure 5.9: Lateral deflection of the lump masses n

Table 6 these values, for the 10 lump masses configuration, are further compared with the frequencies of a continuum element, which corresponds to the particular case of infinite number of nodes:

$$f_n = \frac{n}{2L} \sqrt{\frac{Y}{\rho_L}} \quad (5.3)$$

where  $\rho_L$  is the linear density of the wire and  $n$  the mode we consider. For the same case, in Fig. 5.12, the eigen-frequencies of lump model are plotted as a function of the number of nodes.

At low frequencies 10 nodes are enough to describe the lateral deflection of the wire, because lump and continuum models oscillate approximately at the same pulsation. Instead at higher values the difference augments, since that the lump model tends to the cut-off frequency, while continuum model increases linearly.

### 5.2.3 Inert Tethered Satellite

In the following, the main vibration modes of an inert tether orbiting around the Earth have been determined. For the sake of simplicity, only for these simulations we neglect the thermal dynamics, because we want exclusively to study the mechanical response of the system to an impulse

Modes \ Nodes	1	2	3	4	5	6	7	8	9	10
1	0.88									
2	1.08	1.86								
3	1.16	2.14	2.80							
4	1.22	2.30	3.16	3.70						
5	1.24	2.40	3.38	4.12	4.60					
6	1.26	2.46	3.52	4.40	5.08	5.50				
7	1.28	2.50	3.62	4.60	5.42	6.01	6.38			
8	1.30	2.54	3.70	4.74	5.66	6.38	6.92	7.26		
9	1.31	2.56	3.75	4.85	5.84	6.66	7.34	7.84	8.14	
10	1.32	2.58	3.80	4.94	5.98	6.88	7.66	8.28	8.74	9.02

Table 5.1: Taut wire eigen-frequencies [mHz]

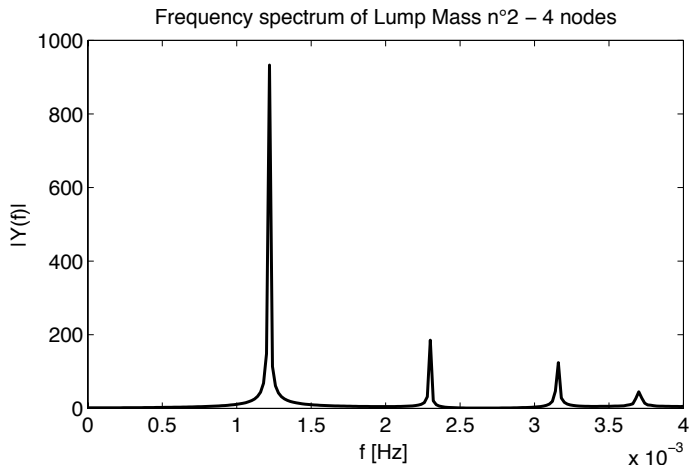


Figure 5.10: Spectrum of lump mass n° 2 for a taut wire discretized in four nodes

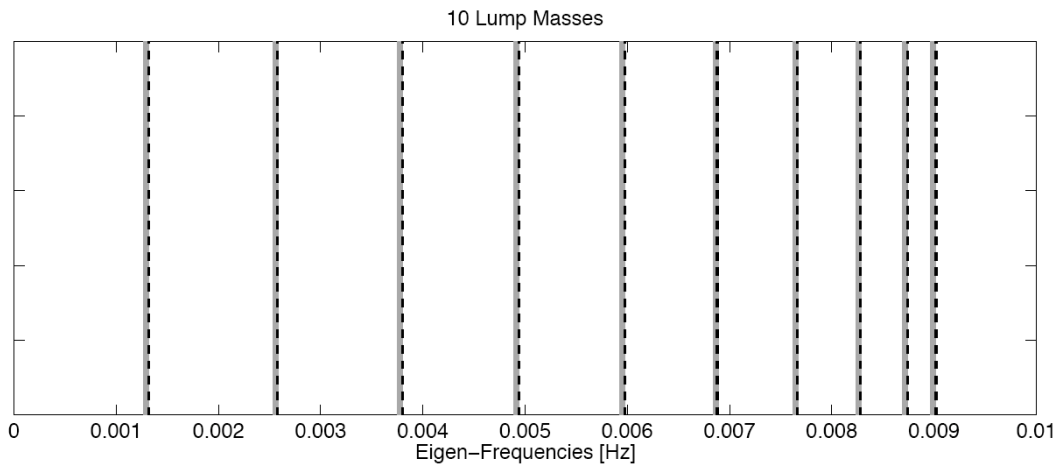


Figure 5.11: Comparison between spectral lines obtained numerically and those expected from theory for a taut wire discretized in 10 nodes

Modes	$f_{taut-wire}$	$f_{expected}$	$f_{continuum}$
1	1.32	1.29	1.36
2	2.58	2.56	2.72
3	3.80	3.77	4.08
4	4.94	4.91	5.44
5	5.98	5.95	6.80
6	6.88	6.87	8.16
7	7.66	7.64	9.53
8	8.28	8.26	10.89
9	8.74	8.72	12.25
10	9.02	8.99	13.61

Table 5.2: Comparison between the eigen-frequencies numerically obtained, theoretically expected and those of a continuum taut wire

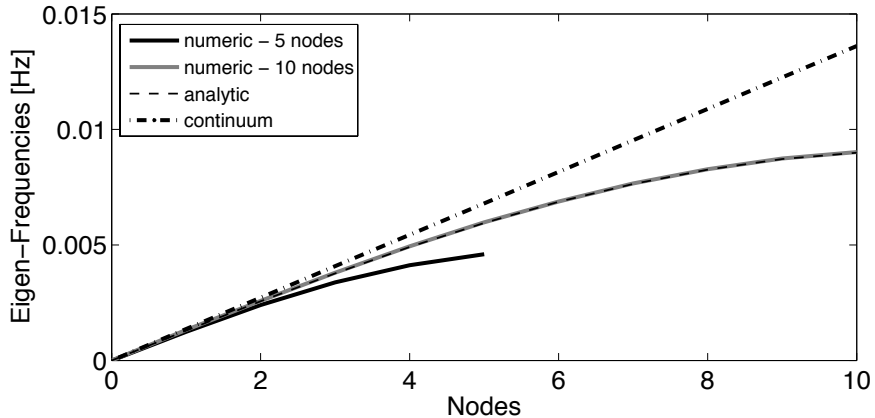


Figure 5.12: Comparison of the eigen-frequencies for a taut wire

and observe which lateral modes are excited and how. Figure 5.3 reports all the eigen-frequencies calculated analyzing the spectral response of the in-plane component of the motion (see Figs. 5.13-5.17) for the central lump mass. The initial condition has been chosen in order to excite only this term and maintain the out-of-plane oscillation null (see Fig. 5.14). This hypothesis is necessary to test our model avoiding coupling between the two librations. The simulation refers to a tethered satellite formed by a tether 5km long and mass 13.5kg, two end masses about 50kg, so the reduced mass of the system is approximately 25kg. The tension along the wire, shown in Fig. 5.16, is variable in the time because it derives from the elastic longitudinal deformation of the tether. It has a transitory, where the free components is extinguished by the viscous term, then it goes to a stationary condition, forced by the gravity gradient term, and oscillates around a mean value about 0.55N. This average tension has been used in Eq. 2.88 for comparing the dynamics of the tether orbiting around the Earth with that of a taut wire. Fig. 5.17 illustrates the spectrum of the in-plane deflection and highlight how most of all the first two frequencies are very important for the motion, while the others have very low energy. A very meaningful spectral line is that indicated with the label In-Plane Libration, because it defines the frequency of oscillation of the system as rigid body. It can be analytically calculated from the equation of motion in the case of little oscillation and is

proportional to the orbital frequency forb:  $f_{in-plane} = \sqrt{3} f_{orb} = 3.3 \times 10^{-4} \text{Hz}$ .

Modes Nodes \	In-plane	1	2	3	4	5	6	7	8	9	10
1	0.331	0.95									
2	0.331	1.13	1.83								
3	0.331	1.24	2.23	2.72							
4	0.331	1.29	2.36	3.18	3.71						
5	0.331	1.34	2.49	3.48	4.26	4.80					
6	0.331	1.37	2.56	3.62	4.57	5.25	5.74				
7	0.331	1.38	2.61	3.74	4.76	5.60	6.23	6.66			
8	0.331	1.40	2.65	3.74	4.89	5.87	6.61	7.20	7.60		
9	0.331	1.41	2.68	3.81	5.05	5.98	6.85	7.59	8.15	8.49	
10	0.331	1.41	2.72	3.84	5.10	6.14	7.10	7.93	8.60	9.08	9.43

Table 5.3: Eigen-frequencies [mHz] of a tethered satellite, orbiting around the Earth

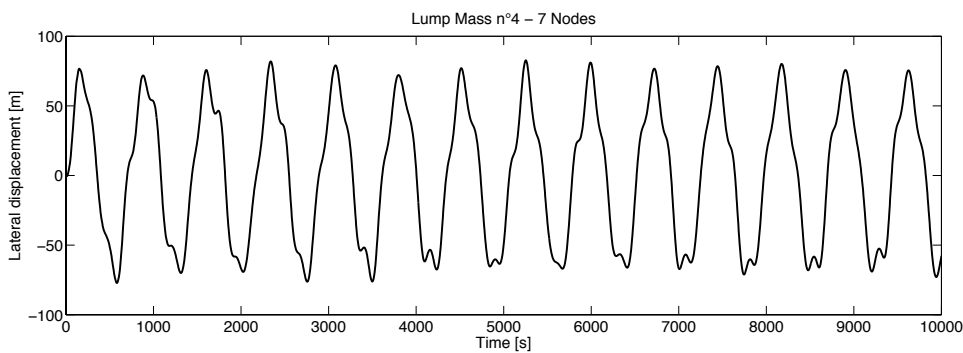


Figure 5.13: Zoom of the in-plane deflection of the lump masses n°4 for a tethered satellite, orbiting around the Earth, discretized in 7 nodes

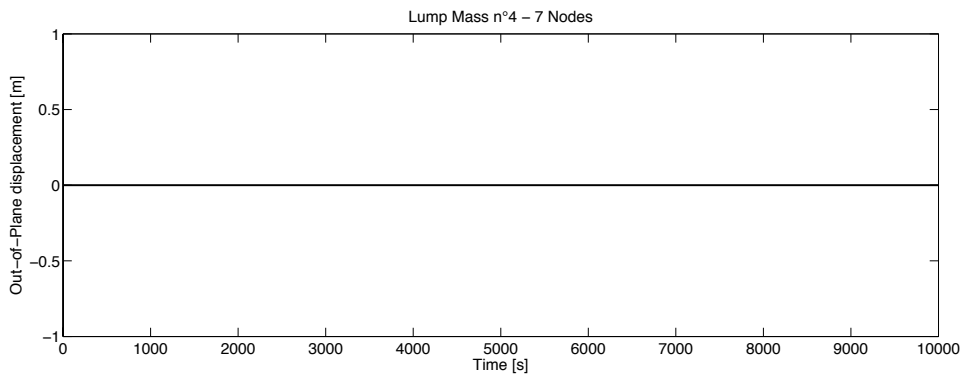


Figure 5.14: Zoom of the out-of-plane component of the lump masses n°4 for a tethered satellite, orbiting around the Earth, discretized in 7 nodes

The effects of longitudinal dynamics are more evident on the plot of radial displacement 5.15.

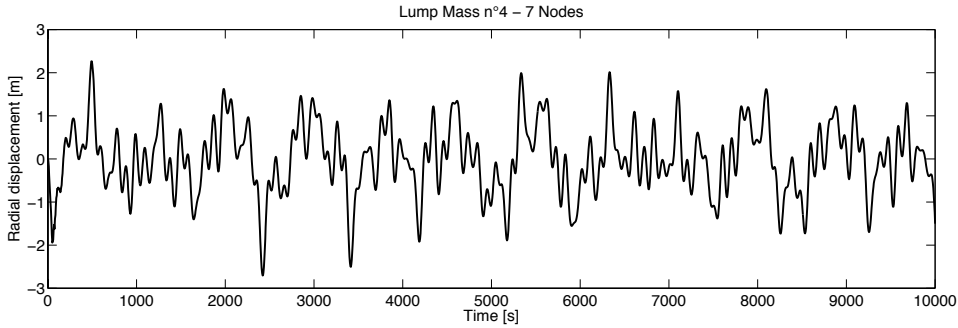


Figure 5.15: Zoom of the radial component

In fact respect to the lateral deflection the radial component is characterized by higher frequencies associated to the elastic behavior of the rod, explained by Eq. 2.63.

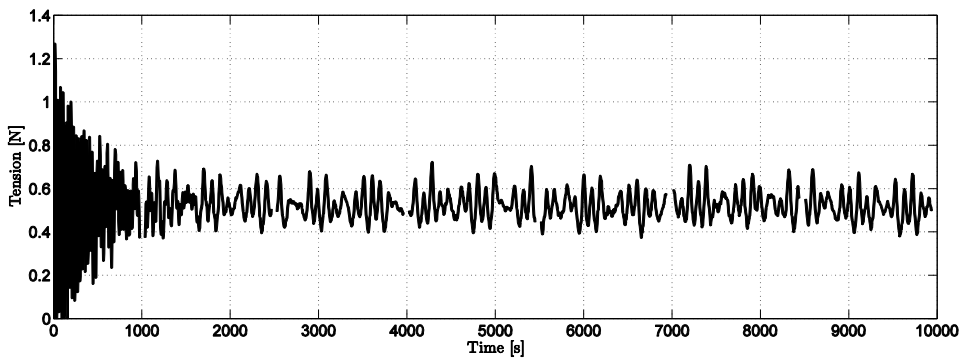


Figure 5.16: Zoom of the mean tension [N] along the tether

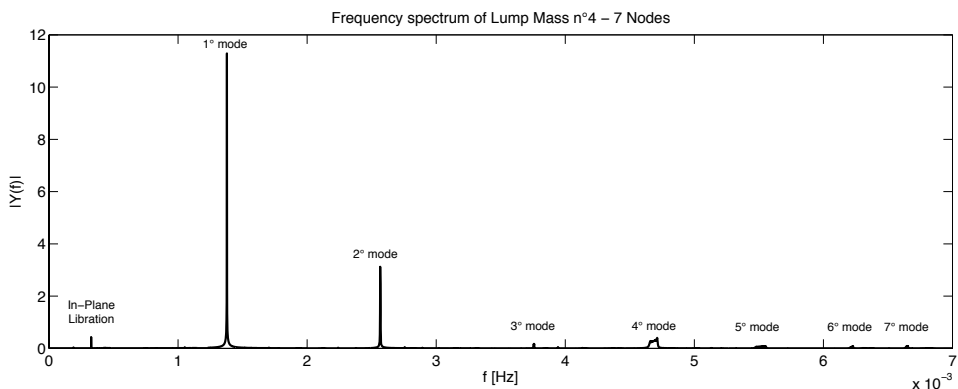


Figure 5.17: Spectrum of lump mass n°4 for a tethered satellite, orbiting around the Earth, discretized in 7 nodes

At last, in Figs. 5.18-5.19 the comparison between numerical model and analytic expression of the eigen-frequencies is depicted, showing again that this model is very suitable to simulate the dynamics of a tethered satellite.

The last two columns of Table 5.4 contain the relative errors committed in the evaluation of eigen-frequencies with 5 and 10 nodes, respectively. The errors tend to be more and more little as

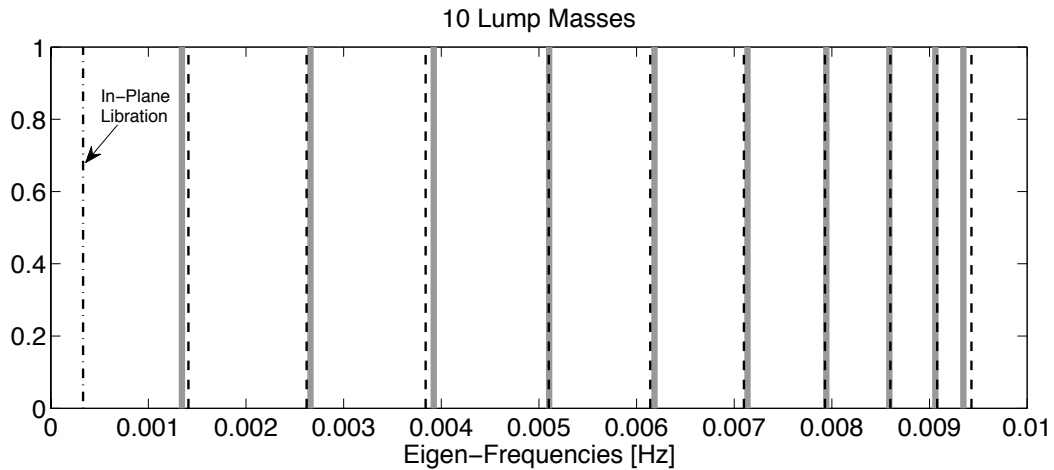


Figure 5.18: Comparison between spectral lines obtained numerically and those expected from theory for a tethered satellite, orbiting around the Earth, discretized in 10 nodes.

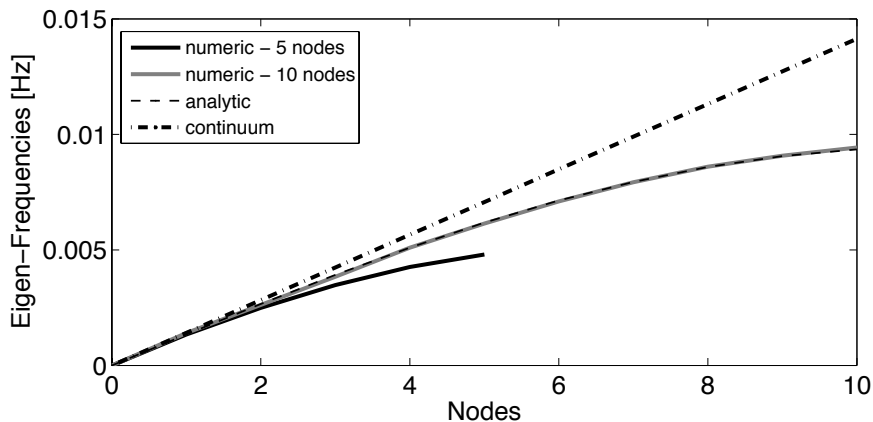


Figure 5.19: Comparison of the eigen-frequencies for a tethered satellite, orbiting in LEO

Modes	$f_{tether}$	$f_{expected}$	$f_{continuum}$	$\epsilon_{5nodes}[\%]$	$\epsilon_{10nodes}[\%]$
1	1.40	1.34	1.41	4.96	0.71
2	2.62	2.66	2.83	12.01	7.42
3	3.84	3.92	4.24	17.92	9.43
4	5.10	5.10	5.66	24.73	9.89
5	6.14	6.18	7.07	32.11	13.15
6	7.10	7.14	8.49		16.37
7	7.93	7.94	9.90		19.90
8	8.60	8.59	11.31		23.96
9	9.08	9.06	12.73		28.67
10	9.43	9.35	14.14		33.31

Table 5.4: Comparison between the eigen-frequencies numerically obtained, theoretically expected and those of a continuum tethered satellite, orbiting around the Earth

the number of nodes augments, until to reach the same values of continuum case. But, since most part of the energy is in the first frequencies a model with 5 lump masses could be plenty to describe the in-plane motion.

### Test of Fortran ODE Routine

In the previous simulations the set of differential equations has been integrated by means of Fortran routine dopri5.f, a code developed by Hairer and Wanner (<http://www.unige.ch/hairer/>). It is an explicit Runge-Kutta method due to Dormand and Prince, which uses six function evaluations to calculate fourth- and fifth-order accurate solutions. To verify the accuracy of the ODE routine a simple test has been carried out integrating the orbital motion of a satellite around the Earth at an altitude about 600km. Neglecting any perturbing force and considering the gravity as the only force acting on the body, it will describe a closed keplerian orbit. The error of the integrator after 500 days (a simulation time much higher than that expected for electrodynamic deorbiting) is approximately 12m, a more than acceptable value for our aim.

#### 5.2.4 Simulations

The following section presents a set of simulations run to study the response of the satellite for different cases of inert tethers and electrodynamic tethers. For each situation we have considered a configuration as close as possible to the real one: the tethered system is formed by a wire 5km long, satellite and tip mass respectively about 1000kg and 25kg. For this choice of parameters size the reduced mass and tension along the tether are near to that obtained in the previous analysis, so this makes the results about the eigen-frequencies easily comparable.

#### Inert tethers

In these first simulations we have considered a tethered system forced only by uniform term of Earth's gravity force. The satellite starts in a circular equatorial orbit at an altitude of about 250km with zero initial libration, so aligned along the local vertical. Hence we perturb the equilibrium condition of the first lump masses  $lm_1$  providing a lateral in-plane displacement about 50m, and observe the evolution of the motion. The first lump masses begins to oscillate around the equilibrium position because come back by the tension along the wire, and transfers part of its energy to all the other masses exciting the libration of the rigid body and the frequencies of flexible tether. Since the only damping mechanism present in the system is the internal friction of the wire, the energy losses are very low and the lateral oscillations maintain their maximum amplitude practically unaltered during the time.

Several simulations have been run to further investigate the dynamics of the satellite as the number of nodes increases, and draw the attention to other important parameters as the longitudinal motion, internal forces, in-plane libration and maximum lateral deflection. In order to emphasize the importance in the choice of the number of nodes to describe the tether for our successive studies, the pictures here reported are so organized: the in-plane graphs shows six cases that correspond to a subdivision in 1, 2, 3, 5 and 10 lump masses (see Figs. 5.20 - 5.25), respectively, while the other interesting variables have been selected in correspondence of the central lump mass for the 5 nodes case. We know by adding nodes into the model we improve the description of the whole dynamics till to higher frequencies, which however are much less excited than first three modes and librational one. Moreover, observing Fig. 5.19, we can see that the relative errors in the evaluation of first three

frequencies with respect to continuum case are less than 20%. So we can conclude that a model with at least 5 nodes is less accurate than a 10 nodes model, but it is plenty for our aim, because given the elevate number of long simulation to do we must find a smart tradeoff between accuracy and computational time. Figure 5.26 provides the in-plane oscillation of tether with respect to the local vertical. The initial perturbing velocity doesn't cause large librations, which remain smaller than 0.06deg. At last, 5.27 describes the radial components of the lighter end mass and the lengthening of the central tether element due to gravity gradient tension. After an initial transitory governed by Hook's law and internal friction term, the tether element length, tension and damping force (see Figs. 5.29-5.30) reach an equilibrium configuration. Instead the radial component is still subjected to in-plane component, in fact we can note the same frequency terms in the graph.

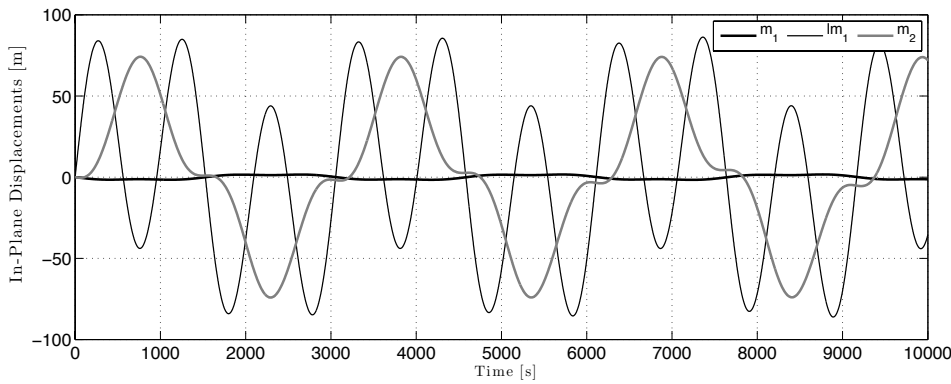


Figure 5.20: In-Plane motion - 1 node

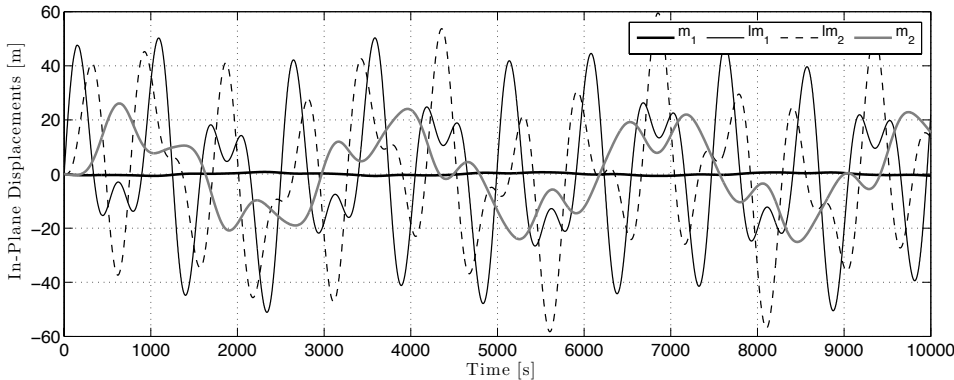


Figure 5.21: In-Plane motion - 2 nodes

### Electrodynamic tethers

Electrodynamic tethers have received a lot of interests in the last two decades as alternative de-orbiting means for propellantless maneuvers. The dynamics of an EDT system has been firstly investigated studying the main features of in-plane and out-of-plane motion when force by Lorentz force, then some uncontrolled cases are presented to stress the importance of adequate control laws in order to avoid instabilities. As explained in the chapter 4 the electrons collected from the environment generate an electric current, whose profile is not uniform along the wire, but it has a minimum at the anodic end, a maximum at the  $x_B$  position, and then diminishes slowly till the cathode. This

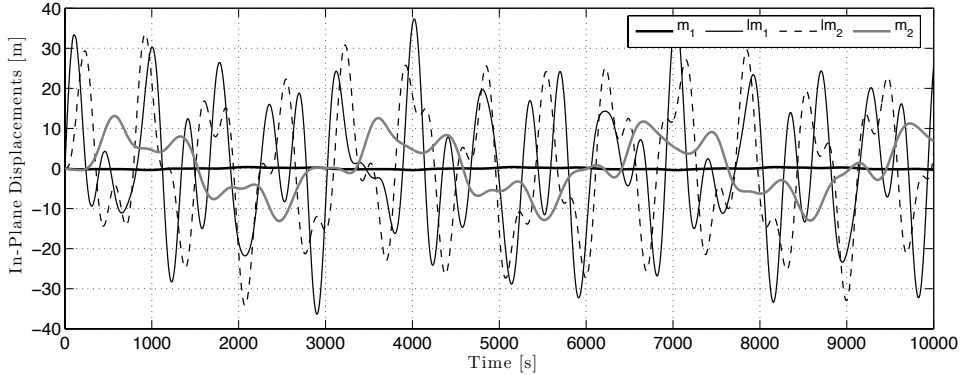


Figure 5.22: In-Plane motion - 3 nodes

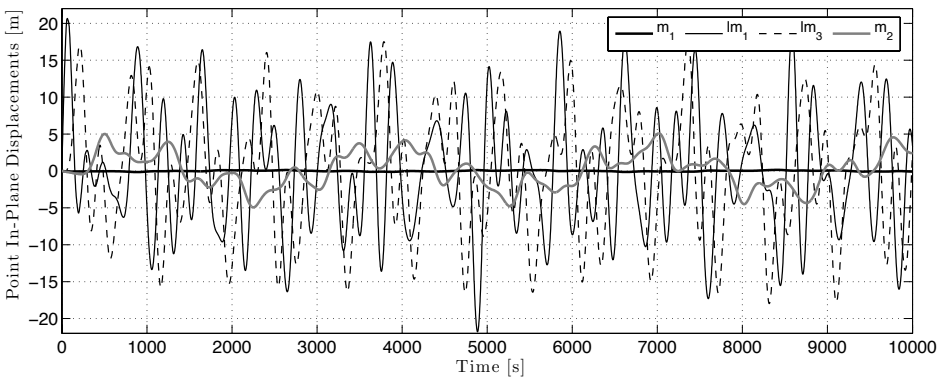


Figure 5.23: In-Plane motion - 5 nodes

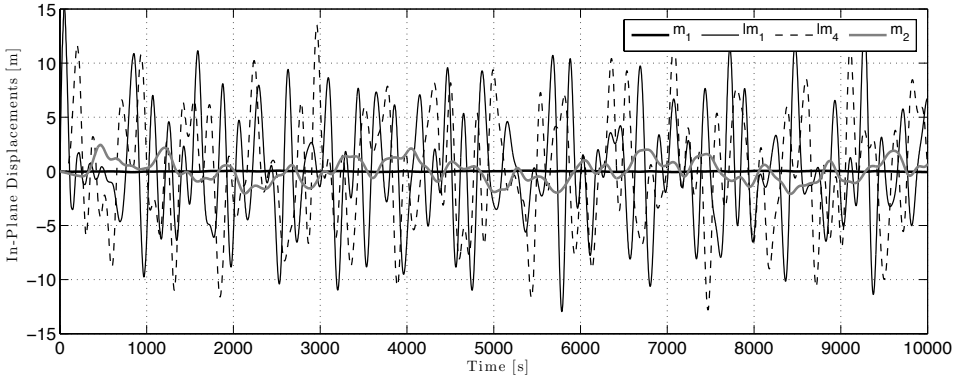


Figure 5.24: In-Plane motion - 7 nodes

is an important aspect to take in consideration for the spectral content of the lateral dynamics, and especially for stability considerations as the center of pressure of electrodynamic load far from the center of mass of the system. Moreover Lorentz force always acts perpendicularly to magnetic field and local tether direction braking the orbital motion and at the same time exciting the out-of-plane libration, which in turns couples into the in plane one. In Figs. 5.31-5.35 the trend of in-plane, out-of-plane and radial motion is shown for the following initial conditions: circular equatorial orbit at 1000km of altitude, and masses  $m_1$  ( $m_{sat}$ ) and  $m_2$  ( $m_B$ ) about 10000 kg and 25kg, respectively. The choice of masses is justified by the fact that at this altitude the electrodynamic interaction begins

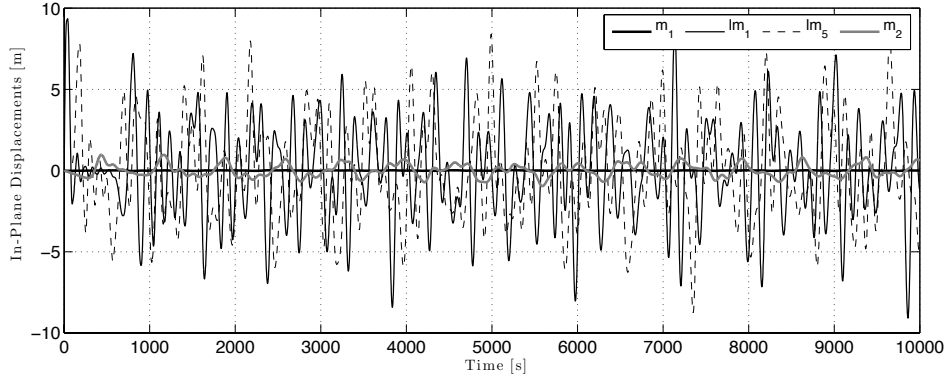


Figure 5.25: In-Plane motion - 10 nodes

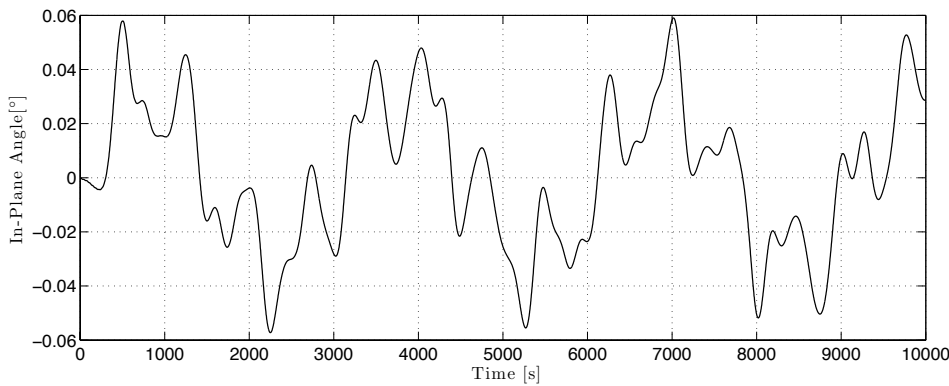


Figure 5.26: In-Plane libration angle

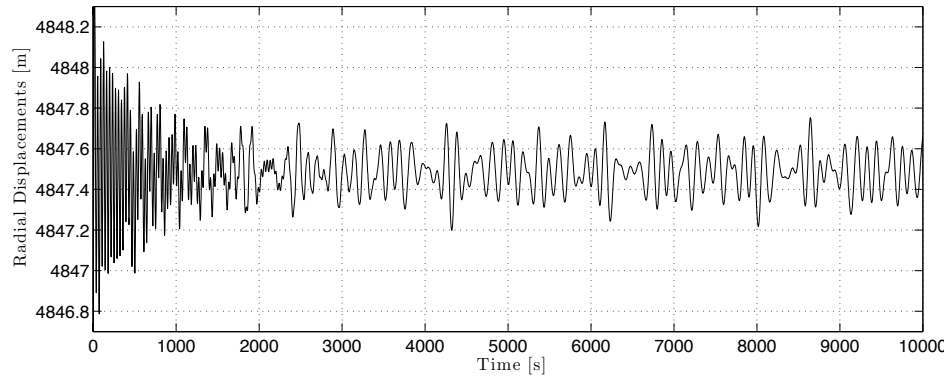


Figure 5.27: Radial displacement

to be significant, but to study the dynamics of the wire we prefer an unperturbed orbit, which can be obtained by increasing the inertia of the system. The environment introduces two new important frequencies (see Fig. 5.35) due the rotation of the Earth around its spin axis ( $f_{Earth}=1.2\times10^{-5}Hz$ ) and the relative motion  $f_{rel}$  between the spacecraft and Earth's plasma, which affects the motional electric field and consequently the electric current:

$$f_{rel} = f_{orb} \left( 1 + \frac{v_{rel}}{v_{S/C}} \right) \quad (5.4)$$

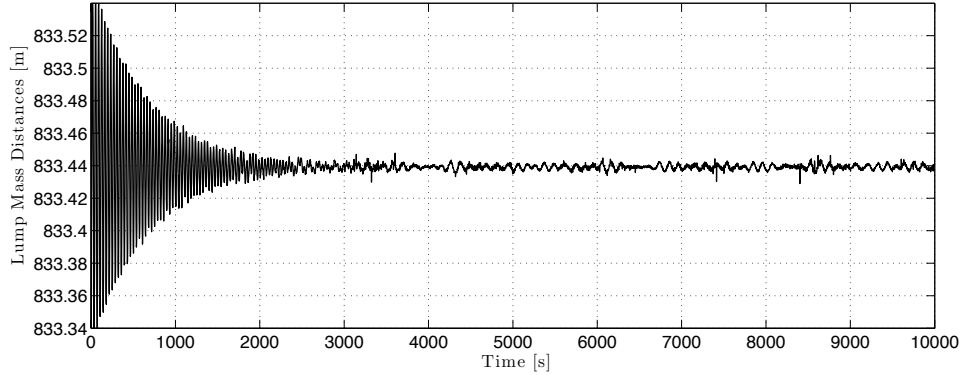


Figure 5.28: Distance between the lump masses evaluated at the middle of the tether - 5 nodes

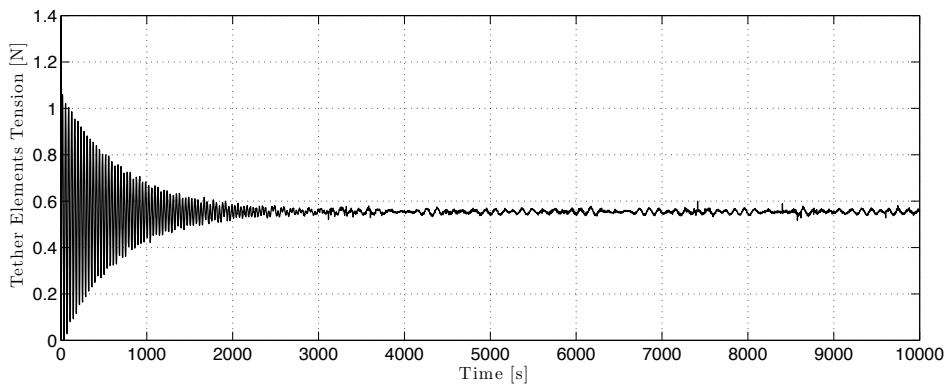


Figure 5.29: Tension evaluated at the middle of the tether - 5 nodes

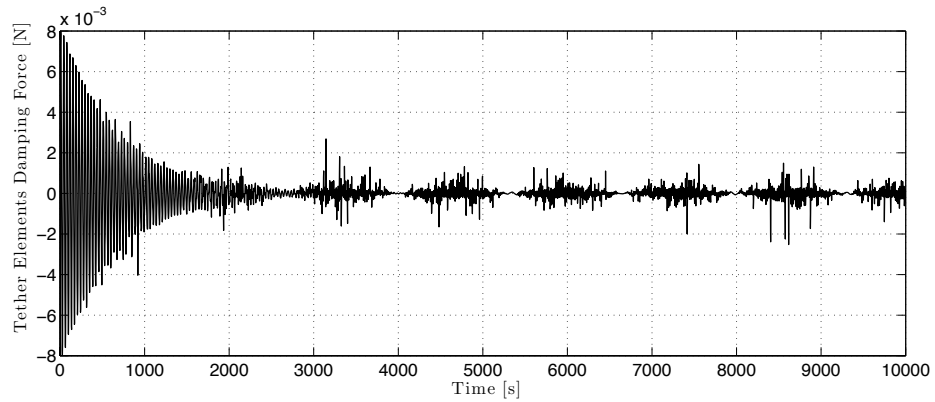


Figure 5.30: Damping force evaluated at the middle of the tether - 5 nodes

In summary we can notice the out-of-plane libration with frequency  $2f_{orb}$  that is excited by the in-plane component of the magnetic field through coupling. The most important bending mode of the tether is the first ( $f_1 \approx 1.16\text{Hz}$  for a mean tension about  $0.44\text{N}$ ), while the other are less present, even if the coupling between in-plane and out-of-plane libration becomes important. In this simulation we have also taken into account the thermal response of the tether because the temperature is a determinant factor for the electric current as the electric resistance of the wire extremely variable because of the solar flux. The temperature reaches a maximum when the radius vector is perpendicular to solar direction, being the tether area exposed to the radiation maximum,

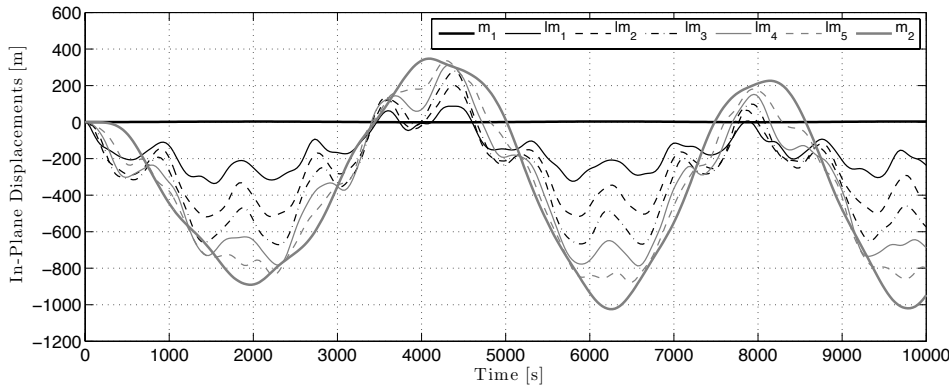


Figure 5.31: In-Plane motion forced by electrodynamic drag - 5 nodes

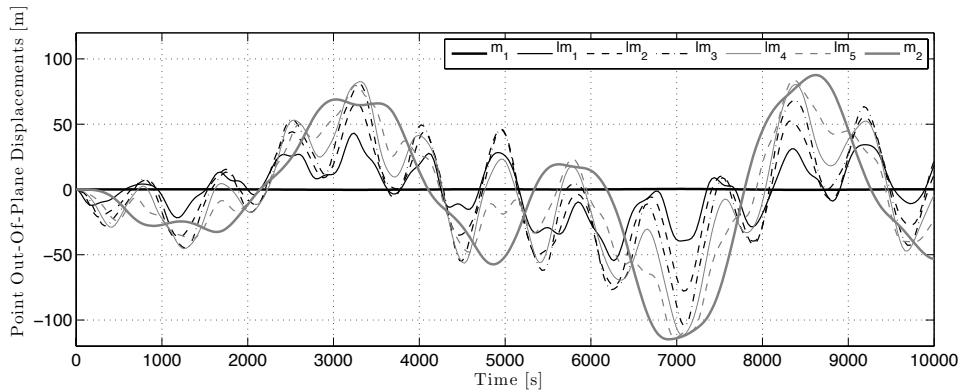


Figure 5.32: Out-Of-Plane motion forced by electrodynamic drag - 5 nodes

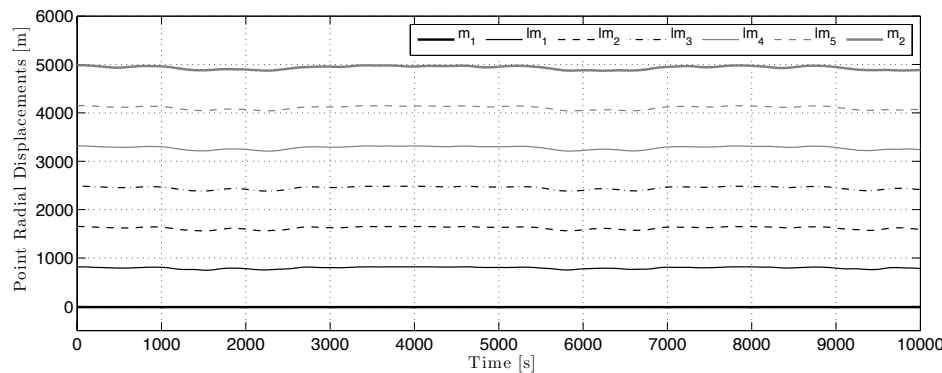


Figure 5.33: Radial motion forced by electrodynamic drag - 5 nodes

then it reaches the minimum on the night side of Earth where it is heated by the infrared radiation. The temperature has important effects on tension force (see Fig. 5.39), because the transitions from light to shadow and vice versa cause drastic changes in the elastic response, which takes several seconds to damp out the free oscillation.

The environment variables drive the collection of electron toward the anodic end. In Fig. 5.41, the electron density, magnetic field, motional electric field and atmosphere density are plotted along the orbit showing the diurnal variation between light and dark side of the Earth. Figures 5.40-5.42 show the average electric current along the wire vs. time and the Lorentz force that can be generated for

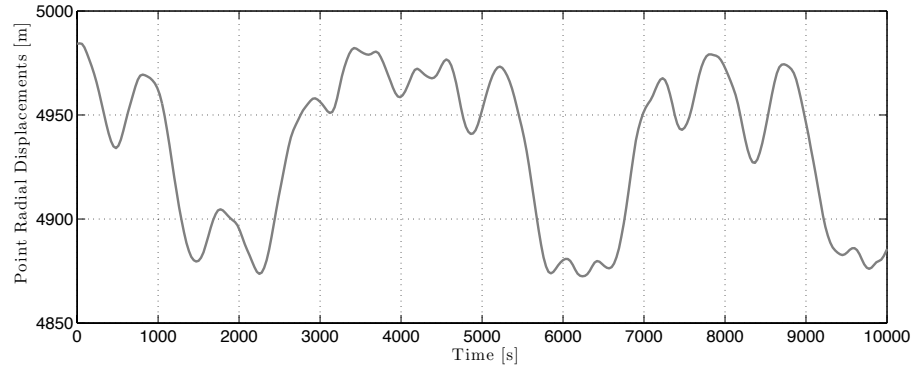


Figure 5.34: Radial motion of mass  $m_2$  forced by electrodynamic drag - 5 nodes

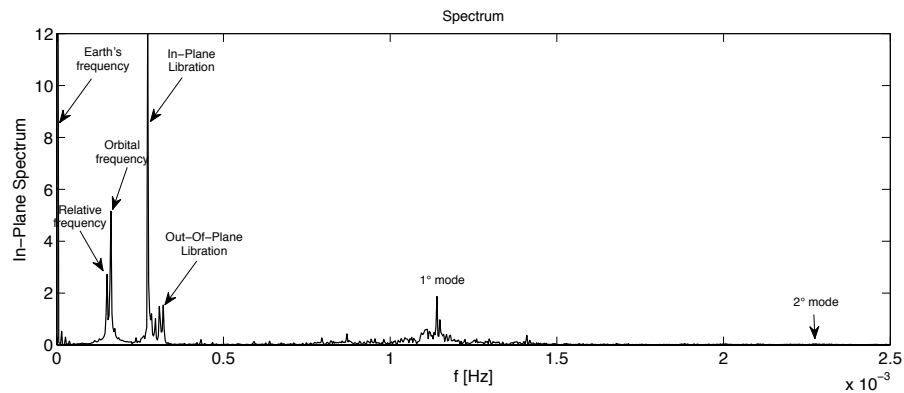


Figure 5.35: Spectrum of in-plane motion forced by electrodynamic drag - 5 nodes

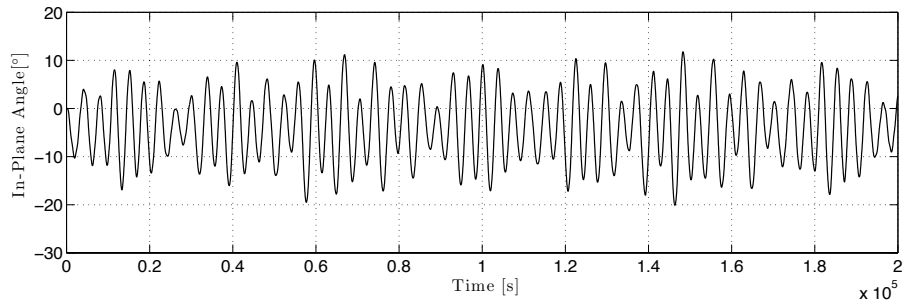


Figure 5.36: In-Plane angle of the tether forced by electrodynamic drag - 5 nodes

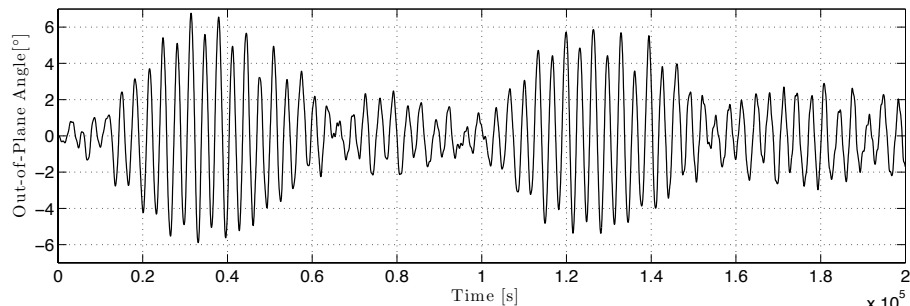


Figure 5.37: Out-Plane angle of the tether forced by electrodynamic drag - 5 nodes

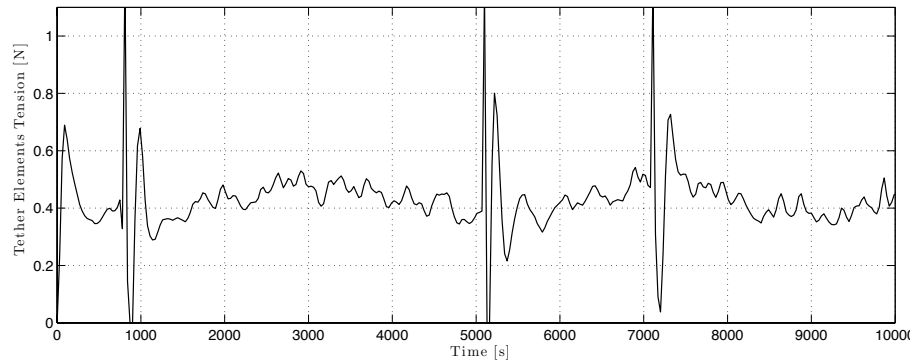


Figure 5.38: Tension along the tether evaluated at the middle of the wire - 5 nodes

deorbiting. Also the aerodynamic force is plotted in order to show the great difference in magnitude between them at this altitude and to remark that electrodynamic tether is a very suitable system for these maneuvers. At last Figs. 5.43-5.44 show the temperature of the wire and electric resistance, whose variations cause substantial changes in the ohmic losses, and so on the performances.

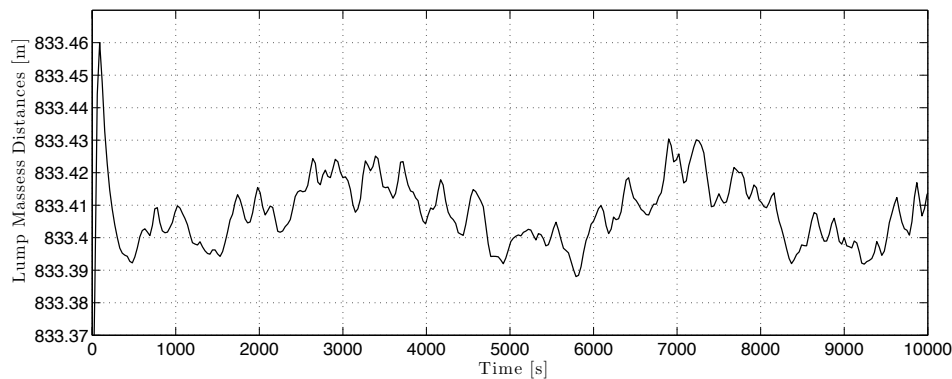


Figure 5.39: Length of lump mass segment evaluated at the middle of the tether - 5 nodes

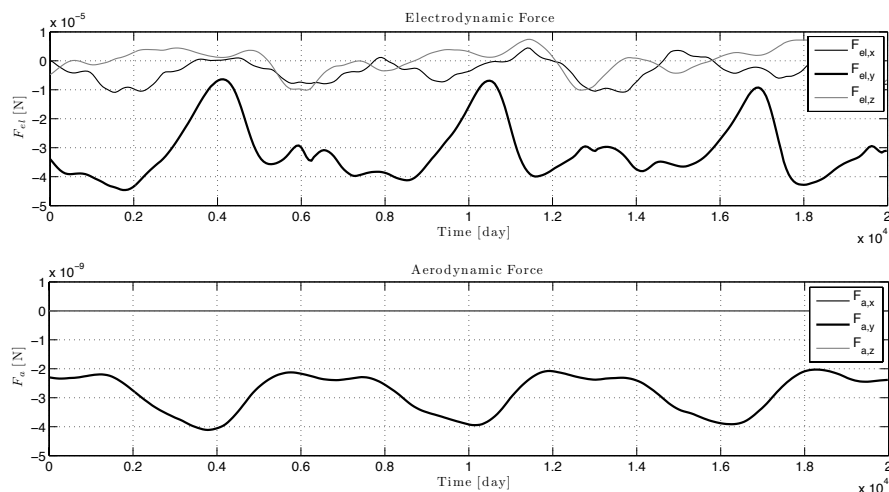


Figure 5.40: Electrodynamics and aerodynamic total forces acting on the center of mass of the system

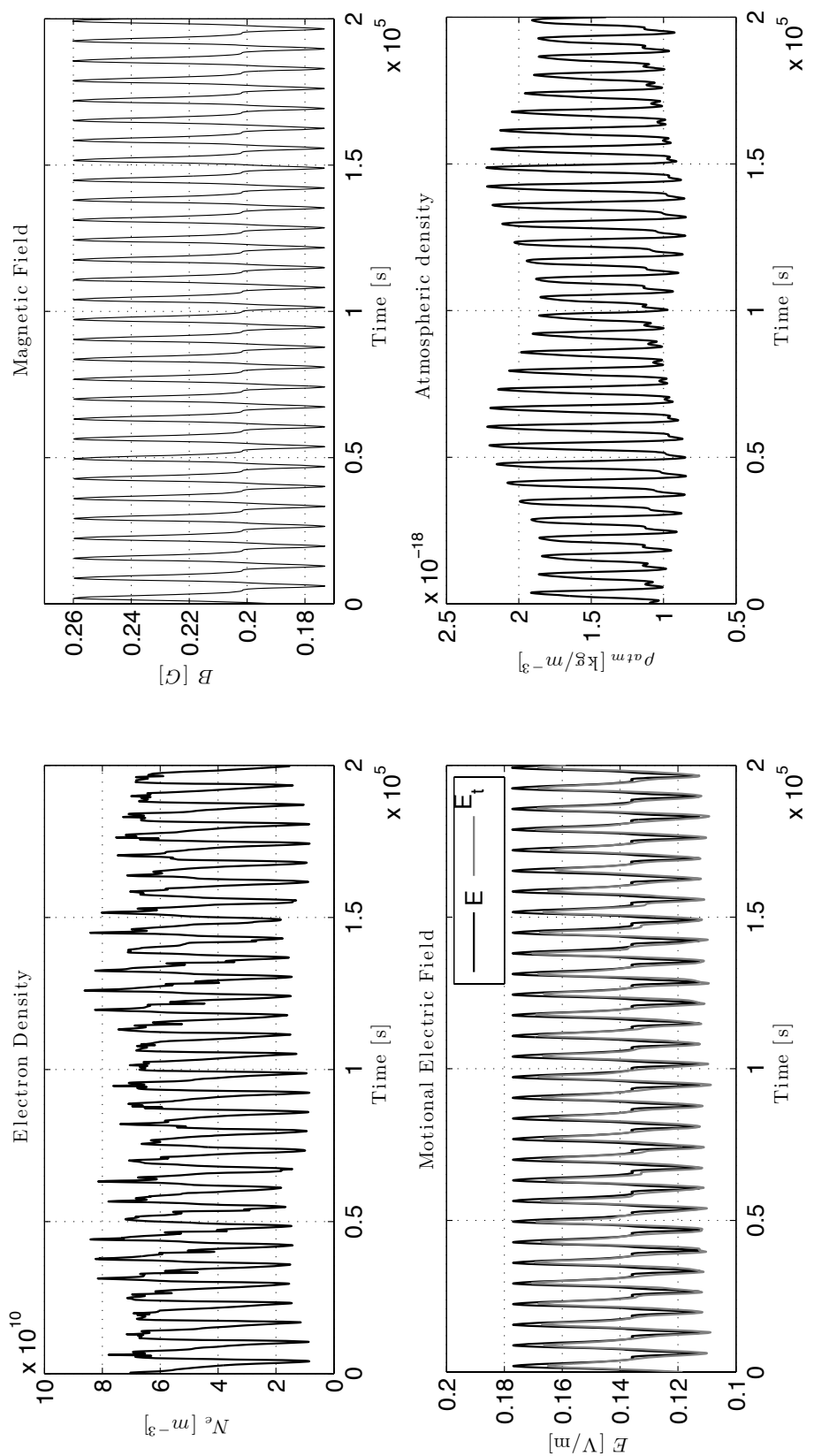


Figure 5.41: Environmental parameters

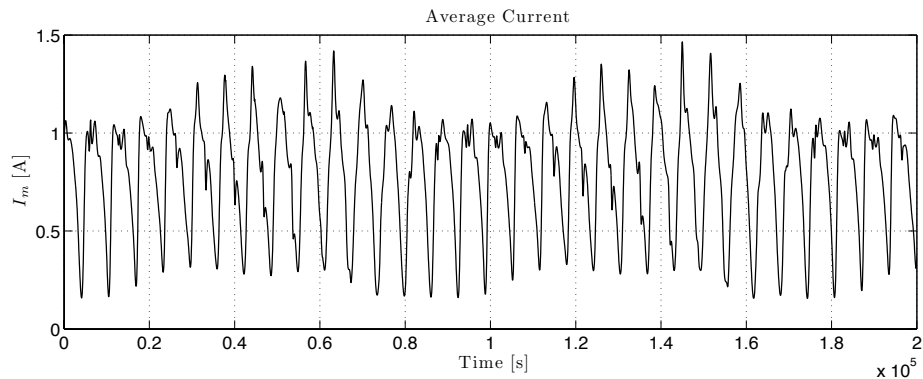


Figure 5.42: Average electric current along the tether

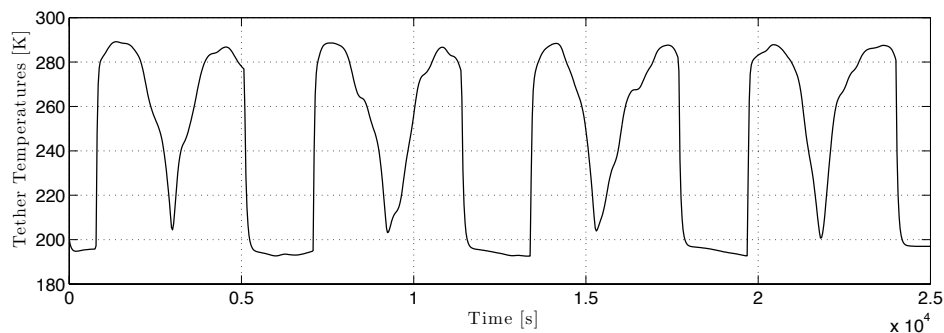


Figure 5.43: Temperature of the tether evaluated at the middle of the wire

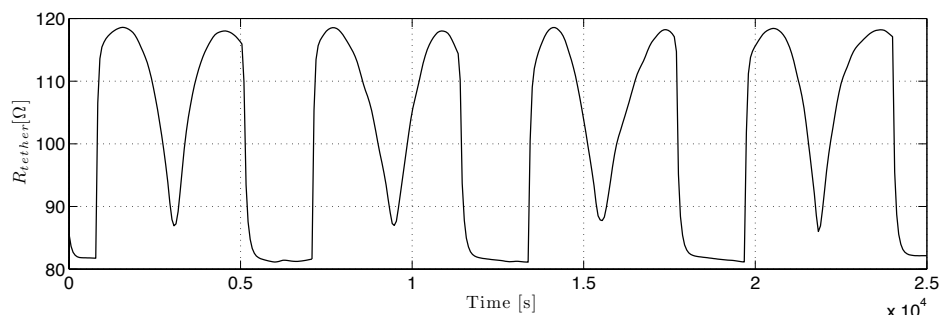


Figure 5.44: Electric resistance of the tether

# Chapter 6

## Deorbiting Performance

This chapter is dedicated to the description of a simple algorithm used to draw analytical equations for evaluating the reentry time of an EDT satellite. The model obtained is based on three main assumptions: gravity-gradient stabilized tether (always aligned along the local vertical), circular inclined low earth orbits, average electric current equal to short circuit one.

This model can be very useful for first preliminary analysis, because they provide quick information for understanding the dependency of the EDT performance on the orbit inclination. Moreover it has been built starting directly from the general expression of the magnetic field. Here the harmonic expansion has been stopped at the third order, but can be extended till higher orders for increasing the accuracy.

Under the assumptions made and considering an inertial reference system the orbital position  $\vec{r}$  of the satellite, its velocity  $\vec{v}$  and the orbital momentum vector  $\vec{h}$  can be written as:

$$\begin{aligned}\vec{r} &= r\hat{u}_r = r \begin{bmatrix} \cos \omega t \\ \cos i \sin \omega t \\ \sin i \sin \omega t \end{bmatrix} & \vec{v} &= \omega r \hat{u}_v = \omega r \begin{bmatrix} -\sin \omega t \\ \cos i \cos \omega t \\ \sin i \cos \omega t \end{bmatrix} \\ \vec{h} &= \omega r^2 \hat{u}_h = \omega r^2 \begin{bmatrix} 0 \\ -\sin i \\ \cos i \end{bmatrix}\end{aligned}$$

where  $r$  is the orbit radius and  $\omega = \sqrt{\mu/r^3}$  is the orbit angular velocity,  $\mu$  being the Earth gravitational constant. Instead the right ascension of the ascending node of the orbit has been set to zero with no loss of generality (see Fig. 6.1).

The magnetic field vector  $\vec{B}$  at a generic position is described, with respect to a geocentric reference frame  $(x_E, y_E, z_E)$ , by Eq. 3.2. Therefore, in order to express it with respect to an inertial coordinate system  $(X_I, Y_I, Z_I)$ , it must be multiplied by a rotation matrix, which takes into account the Earth's diurnal rotation around its spin axis:

$$\vec{B}^I = [R]_E^I \vec{B}^E$$

Since the tether is aligned with the orbit local vertical at all times the corresponding motional electric field projected along the tether yields:

$$E_t = [(\vec{v} - \vec{v}_{pl}) \times \vec{B}]^T \cdot \hat{u}_r = B_\perp v + \Omega_E r (B_r \cos \gamma - B_z) \quad (6.1)$$

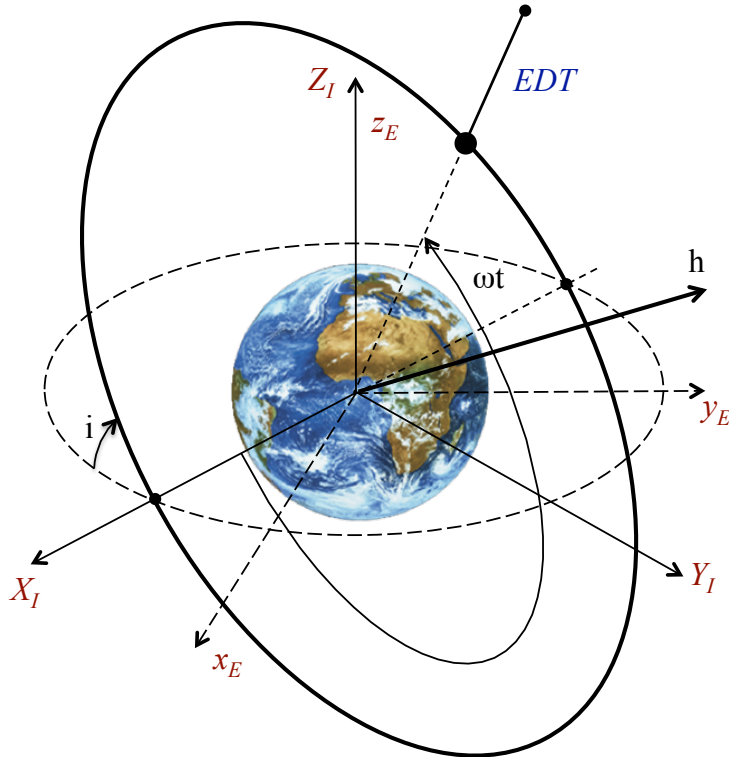


Figure 6.1: Circular reference orbit

With  $\vec{v}_{pl} = [0, 0, \Omega_E]^T \times \vec{r}$  the velocity of the corotating plasmasphere and,  $B_\perp$ ,  $B_r$ ,  $B_z$  are, respectively, the local magnetic field components orthogonal to the orbital plane, along the orbit radius and along the  $z$  axis, finally  $\gamma$  is the angle between the spacecraft radial position and the  $z$  axis, i.e. the spacecraft colatitude. Since  $\Omega_E r \ll v$  in LEO the previous equation can be simplified:

$$E_t = B_\perp v \left[ 1 + \frac{\Omega r (B_r \cos \gamma - B_z)}{B_\perp v} \right] \approx B_\perp v \quad (6.2)$$

The tangential component of the Lorentz force acting on the tether can be computed as:

$$F = I_{av} B L \left[ (\hat{u}_r \wedge \hat{u}_B)^T \hat{u}_v \right] = -I_{av} B_\perp L \quad (6.3)$$

For an ideally designed tether we then have:

$$F \approx -\sigma A v B_\perp^2 L \quad (6.4)$$

Because deorbiting a large space satellite would normally require several weeks if not months it's convenient to replace the instantaneous force with its average value  $\bar{F}$  computed over one Earth rotation period, namely:

$$\bar{F} = \frac{\int_0^{2\pi\Omega_E} F dt}{2\pi\Omega_E}$$

After inserting the previous expression in the Gauss planetary equation for the time evolution of the orbit semimajor axis  $a$  and neglecting all additional perturbation forces we finally obtain:

$$\frac{da}{dt} = \frac{2a^2 v}{\mu} \frac{\bar{F}}{m_{tot}} \quad (6.5)$$

where  $m_{tot}$  is the total EDT satellite mass. Under the hypothesis that the orbit evolves while remaining almost circular ( $\mu/a = v^2$ ), in Eq. (6.5) the semimajor axis can be replaced by the

orbital radius:

$$\frac{dr}{dt} = -\frac{2r\sigma ALB_{\perp}}{m_{SC}} \quad (6.6)$$

So the reentry time required can be evaluated as:

$$\Delta t = - \int_{r_0}^{r_f} \frac{m_{SC}}{2r\sigma ALB_{\perp}} dr \quad (6.7)$$

## 6.1 Perpendicular Component of the Magnetic Field

By means of some cumbersome mathematical passages, the perpendicular component  $B_{\perp}$  of magnetic field can be evaluated directly from the International Geomagnetic Reference Field (IGRF) model. Such a model provides the expression of the magnetic field potential, which can be expressed as a series expansion:

$$V = R_E \sum_{n=1}^{\infty} \sum_{m=0}^n \left( \frac{R_E}{r} \right)^n [g_n^m \cos(\lambda) + h_n^m \sin(\lambda)] P_n^m \cos(\theta) \quad (6.8)$$

where  $g_n^m$  and  $h_n^m$  are the Schmidt-normalized coefficients,  $\lambda$  the longitude and  $\theta$  the co-latitude respect the spherical geocentric reference frame, and  $P_n^m$  are polynomial function of  $\theta$ . In order to get  $B_{\perp}$  along the orbit, we must do some reference system changes and to express the magnetic field in the inertial one.

The first substitution to do is a change of geocentric coordinates from spherical  $(r, \lambda, \theta)$  to cartesian  $(x, y, z)$ :

$$\begin{aligned} r &= \sqrt{x_E^2 + y_E^2 + z_E^2} \\ \lambda &= \cos^{-1} \left( x_E / \sqrt{x_E^2 + y_E^2} \right) \\ \theta &= \cos^{-1} \left( z_E / \sqrt{x_E^2 + y_E^2 + z_E^2} \right) \end{aligned}$$

Hence the magnetic field can be evaluated as gradient of potential function:  $\nabla_{(x,y,z)} V$ , which gives the classic expressions of the tilted dipole limiting the expansion to the first  $(1 \times 1)$  grade and order:

$$\vec{B}_{1 \times 1}^E = \frac{R_E^3}{r^5} \begin{pmatrix} 3x_E(h_{11}y_E + g_{10}z_E) + g_{11}(2x_E^2 - y_E^2 - z_E^2) \\ 3y_E(g_{11}x_E + g_{10}z_E) - h_{11}(x_E^2 - 2y_E^2 + z_E^2) \\ 3z_E(g_{11}x_E + h_{11}y_E) - g_{10}(x_E^2 + y_E^2 - 2z_E^2) \end{pmatrix}$$

$$\vec{B}_{2 \times 2}^E = \vec{B}_{1 \times 1}^E + \vec{B}_{2 \times 2}^E$$

Where

$$\begin{aligned} \vec{B}_{x_{2 \times 2}}^E &= \frac{R_E^4}{r^7} (g_{20}x_E(4z_E^2 - x_E^2 - y_E^2) + 2(2h_{22}y_E(4x_E^2 - y_E^2 - z_E^2) \\ &\quad + g_{22}x_E(3x_E^2 - 7y_E^2 - 2z_E^2) + z_E(5h_{21}x_Ey_E + g_{21}(4x_E^2 - y_E^2 - z_E^2)))) \\ \vec{B}_{y_{2 \times 2}}^E &= \frac{R_E^4}{r^7} (g_{20}y_E(4z_E^2 - x_E^2 - y_E^2) + 4h_{22}x_E(4y_E^2 - x_E^2 - z_E^2) \\ &\quad + 2(g_{22}y_E(7x_E^2 + 2z_E^2 - 3y_E^2) + z_E(5g_{21}x_Ey_E + h_{21}(4y_E^2 - x_E^2 - z_E^2)))) \\ \vec{B}_{z_{2 \times 2}}^E &= \frac{R_E^4}{r^7} (g_{20}(2z_E^2 - 3(x_E^2 + y_E^2))z_E + 2(g_{21}x_E + h_{21}y_E)(4z_E^2 - x_E^2 - y_E^2) \\ &\quad + 10(2h_{22}x_Ey_E + g_{22}(x_E^2 - y_E^2))) \end{aligned}$$

Then, the geocentric  $(x_E, y_E, z_E)$  coordinates must be transformed in inertial one  $(X_I, Y_I, Z_I)$ :

$$\begin{pmatrix} x_E \\ y_E \\ z_E \end{pmatrix} = \begin{bmatrix} \cos \Omega_E t & \sin \Omega_E t & 0 \\ -\sin \Omega_E t & \cos \Omega_E t & 0 \\ 0 & 0 & 0 \end{bmatrix} \begin{pmatrix} X_I \\ Y_I \\ Z_I \end{pmatrix}$$

At least the inertial system  $(X_I, Y_I, Z_I)$  can be expressed as function of orbital parameters  $(\omega, i)$ , and in the particular case of circular orbit with ascending nodes oriented towards Vernal Point  $\gamma$ :

$$(X_I, Y_I, Z_I)^T = r (\cos \omega t, \sin \omega t \cos i, \sin \omega t \sin i)^T \quad (6.9)$$

So the magnetic field can be written as:

$$\vec{B}_{1 \times 1} = \frac{1}{2} \left( \frac{R_E}{r} \right)^3 (B_{x_{1 \times 1}}, B_{y_{1 \times 1}}, B_{z_{1 \times 1}})^T$$

where

$$\begin{aligned} B_{x_{1 \times 1}} &= 3 \cos i \sin 2\omega t (h_{11} \cos \Omega_E t + g_{11} \sin \Omega_E t) + (1 + 3 \cos 2\omega t) (g_{11} \cos \Omega_E t - h_{11} \sin \Omega_E t) \\ &\quad + g_{10} \sin i \sin 2\omega t \\ B_{y_{1 \times 1}} &= (3 \cos^2 i - 2) (h_{11} \cos \Omega_E t + g_{11} \sin \Omega_E t) - 3 \cos^2 i \cos 2\omega t (h_{11} \cos \Omega_E t + g_{11} \sin \Omega_E t) \\ &\quad + 3 \cos i \sin 2\omega t (g_{11} \cos \Omega_E t - h_{11} \sin \Omega_E t) + 3g_{10} \sin 2i \sin^2 \omega t \\ B_{z_{1 \times 1}} &= g_{10} (1 - 3 \cos^2 \omega t) - 3g_{10} \cos 2i \sin^2 \omega t + 3 \sin 2i \sin^2 \omega t (h_{11} \cos \Omega_E t + g_{11} \sin \Omega_E t) \\ &\quad + 3 \sin i \sin 2\omega t (g_{11} \cos \Omega_E t - h_{11} \sin \Omega_E t) \end{aligned}$$

As it has been said before, for electrodynamic tethered application the relevant component is that perpendicular at the orbit, and it can be easily evaluated as:

$$B_{\perp} = \vec{B} \cdot \hat{u}_h = B_{\perp_{1 \times 1}} + B_{\perp_{2 \times 2}} + B_{\perp_{3 \times 3}} \dots B_{\perp_{n \times n}} \quad (6.10)$$

Called  $B_{\perp_{i \times i}}$  the contribution given by the terms of  $i$ -order of the series expansion. In particular the first three contributions are

$$\begin{aligned} B_{\perp_{1 \times 1}} &= \left( \frac{R_E}{r} \right)^3 [g_{10}G_{10} + g_{11}G_{11} + h_{11}H_{11}] \\ B_{\perp_{2 \times 2}} &= 3 \left( \frac{R_E}{r} \right)^4 [g_{20}G_{20} + g_{21}G_{21} + g_{22}G_{22} + h_{21}H_{21} + h_{22}H_{22}] \\ B_{\perp_{3 \times 3}} &= \frac{3}{16} \left( \frac{R_E}{r} \right)^5 [g_{30}G_{30} + g_{31}G_{31} + g_{32}G_{32} + g_{33}G_{33} + h_{31}H_{31} + h_{32}H_{32} + h_{33}H_{33}] \end{aligned} \quad (6.11)$$

With  $G$  and  $H$  functions of the orbital parameters:

$$\begin{aligned} G_{10} &= -\cos i \\ G_{11} &= \sin i \cos \Omega_E t \\ G_{20} &= -\cos i \sin i \sin \omega t \\ G_{21} &= -(\cos i \cos \omega t \cos \Omega_E t + \cos 2i \sin \omega t \sin \Omega_E t) \\ G_{22} &= 2 \cos \omega t \sin i \sin 2\Omega_E t - \cos 2\Omega_E t \sin 2i \sin \omega t \\ G_{30} &= 5 \cos 3i + \cos i (3 + 20 \cos 2\omega t \sin^2 i) \\ G_{31} &= -[20 \cos \Omega_E t \sin 2i \sin 2\omega t + ((3 + 5 \cos 2\omega t) \sin i + 30 \sin 3i \sin^2 \omega t) \sin \Omega_E t] \\ G_{32} &= 10 [\cos 2\Omega_E t (6 \cos 3i \sin^2 \omega t - \cos i (3 + 5 \cos 2\omega t)) - 8 \cos 2i \sin 2\omega t \sin 2\Omega_E t] \\ G_{33} &= 30 [(3 + 5 \cos 2\omega t) \sin i - 2 \sin 3i \sin^2 \omega t] \sin 3\Omega_E t - 4 \cos 3\Omega_E t \sin 2i \sin 2\omega t \end{aligned}$$

$$\begin{aligned}
 H_{11} &= \sin i \sin \Omega_E t \\
 H_{21} &= \cos i \cos \omega t \sin \Omega_E t - \cos 2i \cos \Omega_E t \sin \omega t \\
 H_{22} &= -2 \sin i (\cos \omega t \cos 2\Omega_E t + \cos i \sin \omega t \sin 2\Omega_E t) \\
 H_{31} &= [20 \sin 2i \sin 2\omega t \sin \Omega_E t - \cos \Omega_E t ((3 + 5 \cos 2\omega t) \sin i + 30 \sin 3i \sin^2 \omega t)] \\
 H_{32} &= 10 [(\cos i (3 + 5 \cos 2\omega t) - 6 \cos 3i \sin^2 \omega t) \sin 2\Omega_E t - 8 \cos 2i \cos 2\Omega_E t \sin 2\omega t] \\
 H_{33} &= 30 [\cos 3\Omega_E t (4 \sin^3 i + \cos 2\omega t (5 \sin i + \sin 3i)) + 4 \sin 2i \sin 2\omega t \sin 3\Omega_E t]
 \end{aligned}$$

## 6.2 Reentry Time

To estimate the deorbiting time of the satellite it's necessary to evaluate the average value of the square of  $B_\perp$  (see Eq. 6.4). Since a direct integration is not possible the strategy to follow is this: a first integration respect the orbital motion, then another for the Earth's rotation. The integral is a function of orbital inclination and altitude, and can be separated in two main factors: the former represented by the cosine function of inclination, the latter by the  $k$  coefficients. Increasing the order of the series development the number of terms, and so the accuracy, augment. Figure 6.3 shows the relative error obtained with models till third order, and compared with a much more accurate model of order ten. The error is maximum at high inclination where  $B_\perp$  is minimum and so more critical to determine.

$$\begin{aligned}
 \frac{\Omega_E}{2\pi} \int_0^{\frac{2\pi}{\Omega_E}} \left[ \frac{\omega}{2\pi} \int_0^{\frac{2\pi}{\omega}} (B_{\perp_{1\times 1}})^2 dt \right] dt &= k_{1,0} + k_{1,2} \cos 2i \\
 \frac{\Omega_E}{2\pi} \int_0^{\frac{2\pi}{\Omega_E}} \left[ \frac{\omega}{2\pi} \int_0^{\frac{2\pi}{\omega}} (B_{\perp_{1\times 1}} + B_{\perp_{2\times 2}})^2 dt \right] dt &= k_{2,0} + k_{2,2} \cos 2i + k_{2,4} \cos 4i \quad (6.12) \\
 \frac{\Omega_E}{2\pi} \int_0^{\frac{2\pi}{\Omega_E}} \left[ \frac{\omega}{2\pi} \int_0^{\frac{2\pi}{\omega}} (B_{\perp_{1\times 1}} + B_{\perp_{2\times 2}} + B_{\perp_{3\times 3}})^2 dt \right] dt &= k_{3,0} + k_{3,2} \cos 2i + k_{3,4} \cos 4i + k_{3,6} \cos 6i
 \end{aligned}$$

Each coefficient  $k_{n,c}$  are identified by two number  $n$  and  $c$ : the first represent the order, while the second is the multiplier of inclination in the cosine function,  $\cos ci$ , and it is always even. These coefficients can be written as recursive terms, where the lower order terms are part of the higher one, as represented in the following expressions:

$$\begin{aligned}
 k_{1,0} &= \frac{1}{4} \left( \frac{R_E}{r} \right)^6 [2g_{10}^2 + g_{11}^2 + h_{11}^2] \\
 k_{1,2} &= \frac{1}{4} \left( \frac{R_E}{r} \right)^6 [2g_{10}^2 - g_{11}^2 - h_{11}^2]
 \end{aligned}$$

$$\begin{aligned}
 k_{2,0} &= k_{1,0} + \frac{9}{16} \left( \frac{R_E}{r} \right)^8 [g_{20}^2 + 4g_{21}^2 + 10g_{22}^2 + 4h_{21}^2 + 10h_{22}^2] \\
 k_{2,2} &= k_{1,2} + \frac{9}{8} \left( \frac{R_E}{r} \right)^8 [g_{21}^2 - 4g_{22}^2 + h_{21}^2 - 4h_{22}^2] \\
 k_{2,4} &= -\frac{9}{16} \left( \frac{R_E}{r} \right)^8 [g_{20}^2 - 2(g_{21}^2 - g_{22}^2 + h_{21}^2 - h_{22}^2)]
 \end{aligned}$$

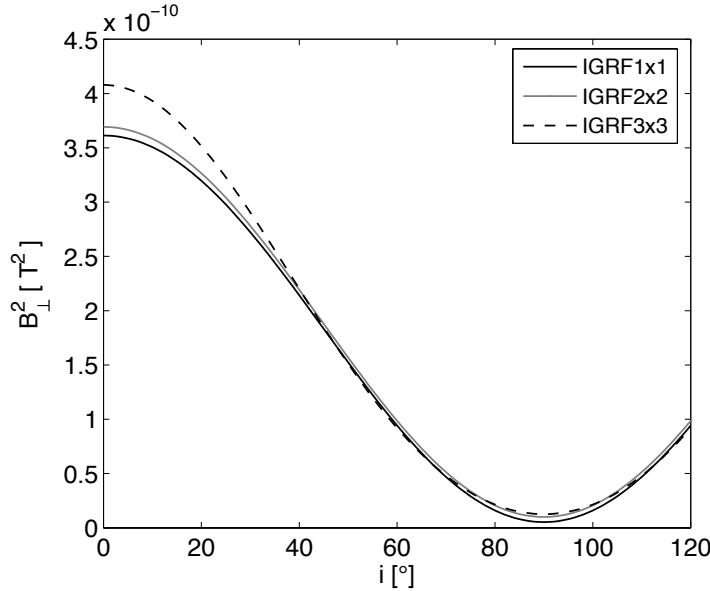


Figure 6.2: Average square orthogonal component of Earth's magnetic field to orbit evaluated for different accuracy of series expansion

$$\begin{aligned}
 k_{3,0} &= k_{2,0} - \frac{9}{32} \left( \frac{R_E}{r} \right)^8 [2g_{10}g_{30} + g_{11}g_{31} + h_{11}h_{31}] \\
 &\quad + \frac{9}{1024} \left( \frac{R_E}{r} \right)^{10} [118g_{30}^2 + 559g_{31}^2 + 6700g_{32}^2 + 27900g_{33}^2 + 559h_{31}^2 + 6700h_{32}^2 + 27900h_{33}^2] \\
 k_{3,2} &= k_{2,2} - \frac{3}{8} \left( \frac{R_E}{r} \right)^8 [4g_{10}g_{30} + 3g_{11}g_{31} + 3h_{11}h_{31}] \\
 &\quad + \frac{9}{2048} \left( \frac{R_E}{r} \right)^{10} [106g_{30}^2 - 13g_{31}^2 + 3700g_{32}^2 - 40500g_{33}^2 - 13h_{31}^2 + 3700h_{32}^2 - 40500h_{33}^2] \\
 k_{3,4} &= k_{2,4} - \frac{15}{32} \left( \frac{R_E}{r} \right)^8 [2g_{10}g_{30} - 3(g_{11}g_{31} + h_{11}h_{31})] \\
 &\quad + \frac{45}{1024} \left( \frac{R_E}{r} \right)^{10} [2g_{30}^2 - 43g_{31}^2 + 580g_{32}^2 - 1260g_{33}^2 - 43h_{31}^2 + 580h_{32}^2 - 1260h_{33}^2] \\
 k_{3,6} &= \frac{675}{2048} \left( \frac{R_E}{r} \right)^{10} [2g_{30}^2 - 9(g_{31}^2 - 4g_{32}^2 + 4g_{33}^2 + h_{31}^2 - 4h_{32}^2 + 4h_{33}^2)]
 \end{aligned}$$

So, the average electrodynamic force acting on the tether can be written as:

$$\bar{F} \approx -\sigma AvL (k_{30} + k_{32} \cos 2i + k_{34} \cos 4i + k_{36} \cos 6i) \quad (6.13)$$

Under the hypothesis made in the beginning the orbital decay is:

$$\frac{dr}{dt} = -\frac{2r\sigma AL}{m_{SC}} [k_{30} + k_{32} \cos 2i + k_{34} \cos 4i + k_{36} \cos 6i] \quad (6.14)$$

And so the reentry time:

$$\Delta t_{3 \times 3} = - \int_{r_0}^{r_f} \frac{m_{SC}}{2r\sigma AL} \frac{1}{[k_{30} + k_{32} \cos 2i + k_{34} \cos 4i + k_{36} \cos 6i]} dr \quad (6.15)$$

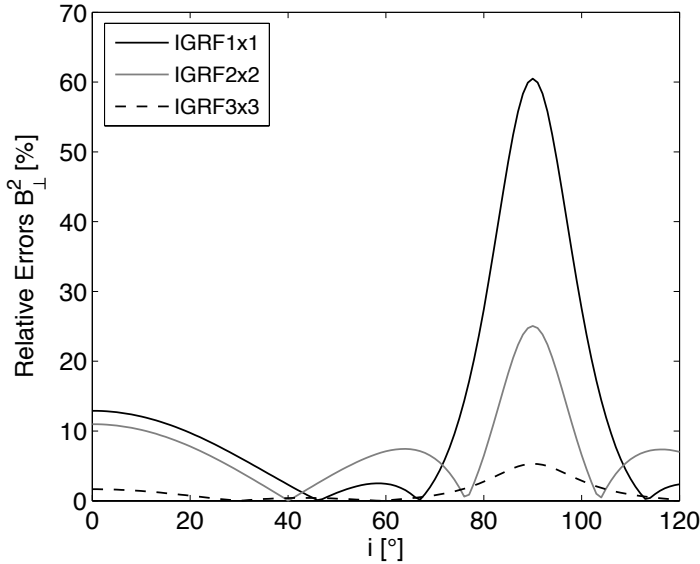


Figure 6.3: Relative error of average square orthogonal component evaluated for different accuracy of series expansion

At last the integral provides:

$$\Delta t_{3 \times 3} = \Delta t_1 + \Delta t_2 + \Delta t_3 \quad (6.16)$$

$$\begin{aligned} \Delta t_1 &= \frac{6(A_2^2 - A_1 A_3) R_E^4 r^2 - 3A_1 A_2 R_E^2 r^4 + 2A_1^2 r^6}{12A_1^3 R_E^6} \\ \Delta t_2 &= \frac{(A_2^4 - 4A_1 A_2^2 A_3 + 2A_1^2 A_3^2) \tan^{-1} \left[ \frac{A_2 R_E^2 + 2A_1 r^2}{R_E^2 \sqrt{4A_1 A_3 - A_2^2}} \right]}{2A_1^4 \sqrt{4A_1 A_3 - A_2^2}} \\ \Delta t_3 &= \frac{A^2 (2A_1 A_2 - A_2^2) \ln [A_3 R_E^4 + A_2 R_E^2 r^2 + A_1 r^4]}{4A_1^4} \end{aligned}$$

where

$$\begin{aligned} A_1 &= \frac{1}{4} [2g_{10}^2 + g_{11}^2 + h_{11}^2 + (2g_{10}^2 - g_{11}^2 - h_{11}^2) \cos 2i] \\ A_2 &= \frac{9}{32} [2g_{20}^2 + 8g_{21}^2 + 20g_{22}^2 - 2g_{10}g_{30} - g_{11}g_{31} + 8h_{21}^2 + 20h_{22}^2 + h_{11}h_{31}] \\ &+ \frac{3}{16} [3g_{21}^2 - 12g_{22}^2 - 4g_{10}g_{30} - 3g_{11}g_{31} + 3h_{21}^2 - 12h_{22}^2 - 3h_{11}h_{31}] \cos 2i \\ &- \frac{3}{32} [6g_{20}^2 - 12g_{21}^2 + 12g_{22}^2 + 10g_{10}g_{30} - 15g_{11}g_{31} - 12h_{21}^2 + 12h_{22}^2 - 15h_{11}h_{31}] \cos 4i \\ A_3 &= \frac{9}{1024} [118g_{30}^2 + 559g_{31}^2 + 6700g_{32}^2 + 27900g_{33}^2 + 559h_{31}^2 + 6700h_{32}^2 + 27900h_{33}^2] \\ &+ \frac{9}{2048} [106g_{30}^2 - 13g_{31}^2 + 3700g_{32}^2 - 40500g_{33}^2 - 13h_{31}^2 + 3700h_{32}^2 - 40500h_{33}^2] \cos 2i \\ &+ \frac{45}{1024} [2g_{30}^2 - 43g_{31}^2 + 580g_{32}^2 - 1260g_{33}^2 - 43h_{31}^2 + 580h_{32}^2 - 1260h_{33}^2] \cos 4i \\ &+ \frac{675}{2048} [2g_{30}^2 - 9g_{31}^2 + 36g_{32}^2 - 36g_{33}^2 - 9h_{31}^2 + 36h_{32}^2 - 36h_{33}^2] \cos 6i \end{aligned}$$

Figure 6.5 shows the time required to deorbit a tethered satellite of mass 1000kg, mounting a wire 5km long and with cross section 1cm×30μm, from an altitude about 1000km to 100km. The graph, spacing the orbital inclination, compares the results obtained by means of analytical reentry time

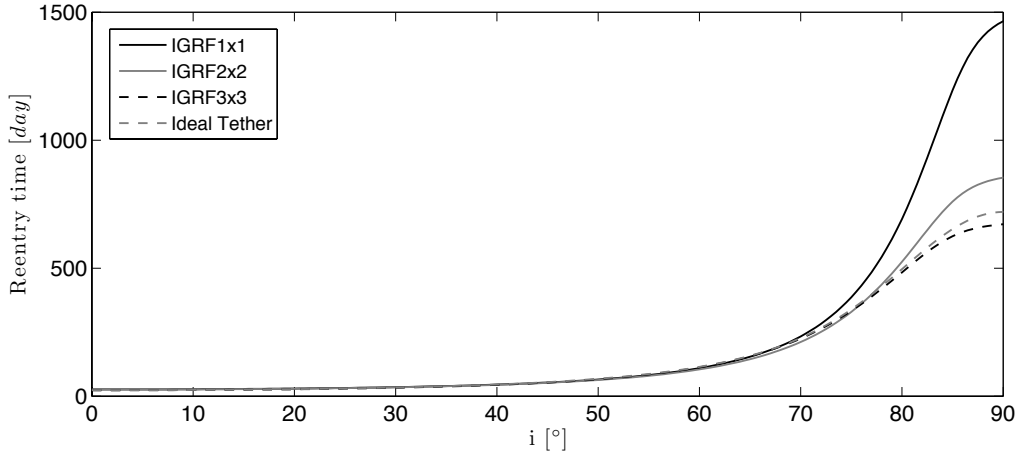


Figure 6.4: Reentry time determined for different accuracy of series expansion

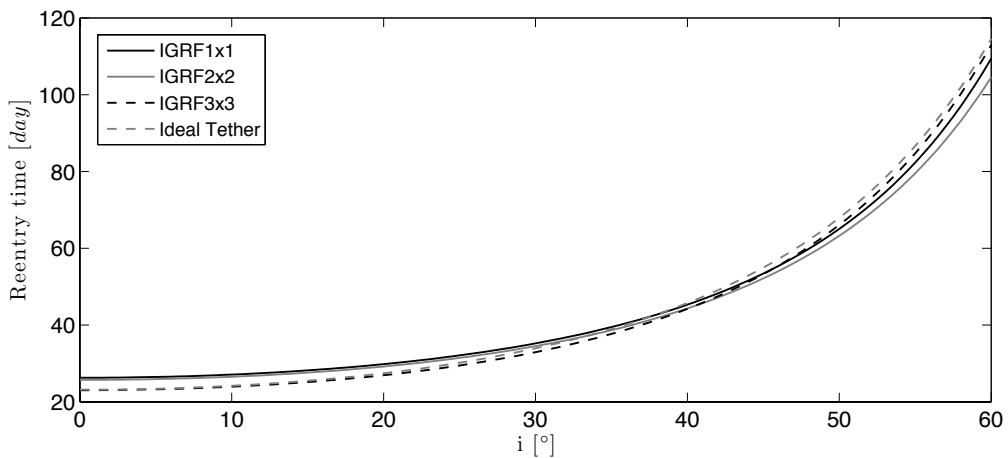


Figure 6.5: Reentry time: zoom at low and middle inclinations

expressions at different accuracy of series expansion with the ideal case. Such a model describes the tether as always aligned along the local vertical and assumes the electric current flowing along the wire is the maximum possible ( $I_{av} = \sigma E_t A$ ). The integration of equations of motion has been carried out supposing that the only external force acting on the tethered system is the electrodynamic one, while the gravity gradient perturbations and aerodynamic drag have been neglected. In a real case the other two components of the magnetic field ( $B_r$  and  $B_z$ ) are not completely negligible, in fact they give a little contribution and cause a variation of the orbital parameters. The major effects of the assumptions made can be seen at the middle inclinations, but anyway the simplified model follows well enough the trend of real case. So the analysis obtained with magnetic model more accurate than IGRF 1×1 gives more reliable results, but they don't take into account the variations of orbital inclination due to the out-of-plane component of electrodynamic force, and this causes a lengthening of reentry time.

# Chapter 7

## Control Techniques

The dynamics of an EDT are extremely unstable because of Lorentz force that pumps continuously energy on the system enlarging both the in-plane and out-of-plane librations. An uncontrolled system can not maintain itself close to the local vertical without an appropriate control strategy, otherwise the libration quickly becomes a rotation.

Control techniques are extremely necessary to provide the optimal conditions for a fast and complete orbital decay. In this chapter new strategies based on an energetic approach have been developed in order to ensure the stability of the tether during the deorbiting.

### 7.1 Uncontrolled EDT Dynamics

An EDT is subjected to a continuously changing electrodynamic torque, whose equilibrium position cannot be described by a static solution. This torque pumps energy into the system enlarging the tether oscillation till to transform it into a rotation. The aim of this section is to identify the critical parameters that govern the EDT dynamics along the orbit studying the decay performance for each configuration, and how long the system can work before going to instability.

The key parameters considered in this work for a parametric analysis of deorbiting maneuvers can be grouped in four main categories: tether size, satellite mass distribution, orbital and environment parameters. In the first group we consider the length, the thickness and the width of the tether; the second one comprises the satellite mass distribution; the third set the orbital inclination and altitude; while the last one consists of the Solar activity index, and so the electron density in the ionosphere. The tether has been tested among all of the above.

It is possible to observe, in Fig. 7.1, how important the tether length is for the evolution of the orbit: the longer the tether, the faster the orbital decay; in fact, the longer the tether the higher the current flowing in the tether and the higher is the destabilising electrodynamic force. In fact the current results in being proportional to the tether length [9][85]. Tether width has a very similar effects, because it augments the collection area and so the electric current. As well thickness increases the current profile because it enlarges the sectional area enhancing tether conductivity.

The mass ratio  $m_B/m_{sat}$ , between the satellite and ballast mass (see Fig. 7.2), is very significant because it changes the position of barycenter of the whole system and so the value of term  $J_1$  (Eq. 2.31). Low mass ratios mean extremely strong electrodynamic torque and so little stability.

The altitude evolution depends strictly on the starting altitude: if the altitude is too high ( $\geq 1400\text{km}$ ) the system lifetime is very long (tens of years). This is, of course, due to the fact that the

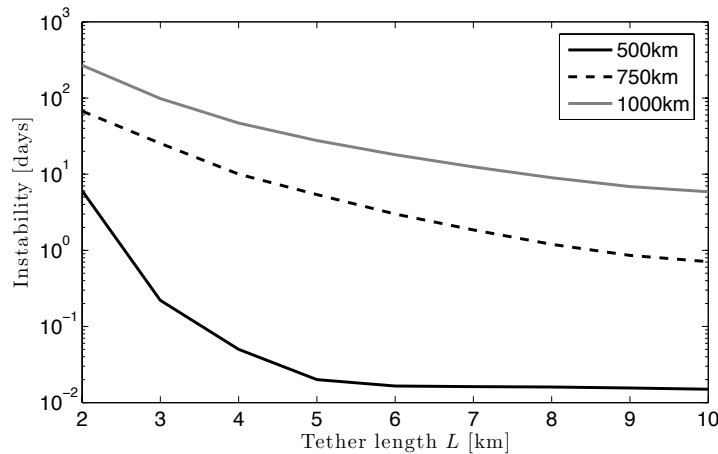


Figure 7.1: Instability vs tether length

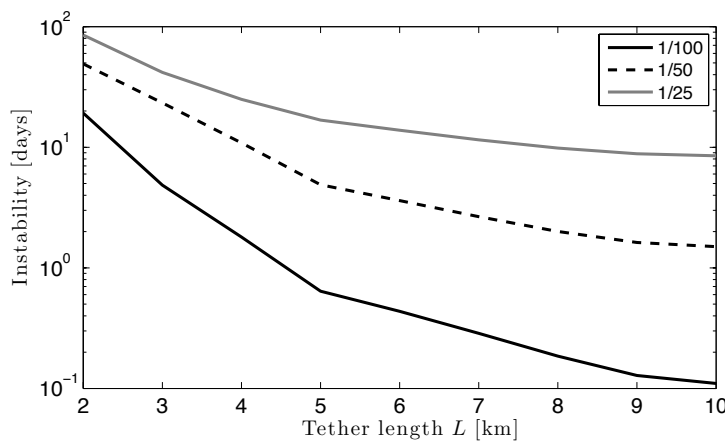


Figure 7.2: Instability vs mass ratio

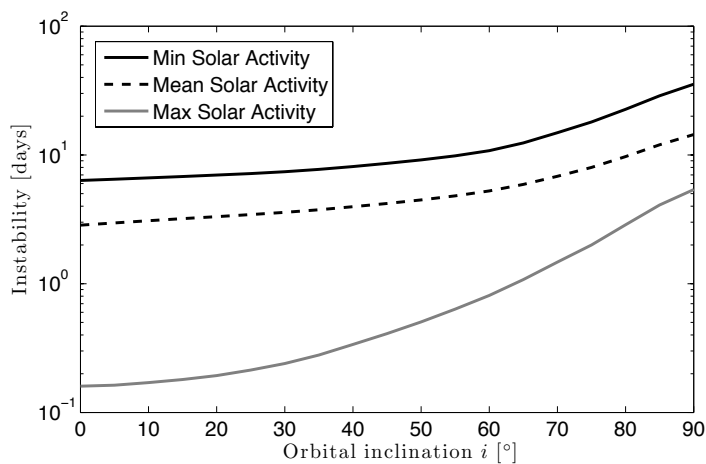


Figure 7.3: Instability vs orbital inclination

produced current is greater at low altitudes, as shown in Fig. 7.1, where the electromagnetic field is higher.

On the other hand, one of the most significant parameters is the initial orbital inclination because it

is strongly related to the Earth electromagnetic field and consequently on tether current and direction of Lorentz force (see Fig. 7.3). The inclination values selected for the simulations are coherent with the orbital debris distribution as measured in the past years [15][64]. Starting orbit inclinations are: 0, 30, 60 and 85°. As expected the higher the inclination the lower is the current because of the geometry of the Earth magnetic field. But the inclination has an important destabilizing effect as explained by Peláez and Lorenzini in [70]. The authors led a nonlinear analysis to study the motion of the EDT system along a periodic orbit, and observed that the destabilization is mainly due to the electrodynamic factor  $\epsilon$  (see Eq. 2.34) and the inclination  $i$ . In fact the eigen-values of the dynamical system can be written as follow:

$$\begin{aligned}\lambda_{1,2} &= 1 + \frac{\pi}{9} \cot i\epsilon^3 \pm j \frac{\pi}{6} \cot^2 i\epsilon^2 + O(\epsilon^4) \\ \lambda_{3,4} &= e^{\pm 2\alpha j} \left\{ 1 \pm \frac{\pi\sqrt{3}}{18} (1 + 4 \cot^2 i) j\epsilon^2 - \frac{\pi}{9} \cot i\epsilon^3 + O(\epsilon^4) \right\}\end{aligned}\quad (7.1)$$

where  $\alpha$  and  $j$  are respectively  $\pi\sqrt{3}$  and the imaginary number. The moduli of these eigen-values are given by:

$$\begin{aligned}|\lambda_{1,2}| &= 1 + \frac{\pi}{9} \cot i\epsilon^3 + O(\epsilon^4) \\ |\lambda_{3,4}| &= 1 - \frac{\pi}{9} \cot i\epsilon^3 + O(\epsilon^4)\end{aligned}\quad (7.2)$$

So there are always two eigenvalues with moduli grater than one that cause instability.

Another important source of instability is given by the eccentricity: circular orbits are much more stable than elliptical ones, since the eccentricity excites the libration of the tether. In fact along the orbit the angular velocity changes a lot perturbing the in-plane and out-of-plane angles. For values beyond 0.3 the system is completely unstable [76][107].

The solar activity is the most significant environmental variables, since the 11-years solar cycle changes the electron density in the ionosphere. Figure 7.3 shows the effect of solar activity at three different data:

- 01 January 1996: Min Solar activity
- 01 January 1998: Mean Solar activity
- 01 January 2000: Max Solar activity

When the solar activity is maximum the tether can collect a major number of electrons [7], therefore higher the solar flux, higher the current is and consequently the destabilising electrodynamic force.

## 7.2 Summary About Techniques Proposed in the Past

In the past different techniques have been studied for the dumbbell. They mainly concern on the self-balanced condition, the control of the current or, under very specific assumptions, on the possibility to insert the librational dynamics of the tethered system along a periodic profile. The first technique wants to delete the electrodynamic torque by means of a precise choose of each part forming the tethered system. Instead periodic orbit strategy tries to insert the in-plane and out-of-plane coupled motion into a closed loop in the phase space. In this way the total energy accumulated after a whole oscillation is zero. At last the current control technique opens and closes the circuit as a function of the libration dynamics. When the energy associated with the oscillation of the wire overcomes a fixed threshold the algorithm control turns on the electric current only when the Lorentz force is opposite to the libration. While the third concept is more realistic and easier to obtain, the other

two are much more restricted, in particular periodic orbit exist only in ideal cases with periodic repeating environmental conditions.

### 7.2.1 Self-Balanced EDT

The basic idea of the *Self-Balanced* concept [74][83] is to cancel the Lorentz torque, since it is the main cause of instability of the electrodynamic tether. As long as the electrodynamic forces are distributed along the cable, there exist a point in which this moment vanishes. If the point is located inside the cable and the center of mass of the system is coincident with that point, the electrodynamic torque does not affect the attitude dynamics. So the idea of the concept is to change some parameters of system in order to bring to zero the arm of the perturbing torque.

In this way, the control problem becomes a design problem of the system, making coincident the center of mass and the application point of the electrodynamic forces. The electrodynamic tether would be, thus, free from the instability when the design of the tether and end masses is suitable. In particular the condition which must be fulfilled to be balanced is gathered in terms of the electric and masic variables.

Adopting the dumbbell system, described in 2.1, the *Self-Balanced* condition can be drawn as follows. Remembering the definition of the electrodynamic factor  $J_1$ , it can be rewritten:

$$\frac{J_1}{\sigma E_t A L^{*2}} = \int_0^L (l_t \cos^2 \phi - \xi) id\xi \quad (7.3)$$

where  $L^*$ ,  $l_t$ ,  $i$  and  $\xi$  are the non-dimensional variables before introduced (see 4.1.2), and the parameter  $\epsilon$  can be separated in:

$$\epsilon = \epsilon_0 \cdot \hat{f} \quad (7.4)$$

where

$$\epsilon_0 = \frac{E_m}{L} \frac{12\Lambda_t}{(3 \sin^2 2\phi - 2\lambda)} \frac{\mu_m \sigma}{\mu_E \rho} \quad (7.5)$$

$$\hat{f} = \int_0^L \left( \cos^2 \phi - \frac{\xi}{l_t} \right) id\frac{\xi}{l_t} \quad (7.6)$$

The factor  $\epsilon_0$  depends on the tether material, the mass distribution and the ratio  $E_t/L$ . Instead the dependency on the ionospheric plasma density takes place in the integral of factor  $\hat{f}$ , that is also a function of the mass distribution through the parameter  $\phi$ .

The idea of the concept is to choose a good distribution of mass in order to obtain zero from the integral 7.6 and cancel the electrodynamic torque. The results obtain with this approach (see [74]) are interesting, but limited by the high values of the tip mass, that must be close to that of the satellite in order to move the center of mass as close as possible to the center of pressure of the distributed Lorentz forces.

In the BETs project we are looking for configuration where the tip mass must be several times littler than that of the satellite (see the ratio in Fig. 7.2), because it must be deployed at the end of life, and most likely will not contain payload. So the *Self-Balanced* is far to be applied in this project.

### 7.2.2 Periodic Orbits

Periodic orbits have the peculiar characteristic that are closed trajectories in the phase plane of the libration motion [37][73]. So the total work done by the electrodynamic forces along a closed loop is zero, because the tether comes back in the same conditions at the beginning of the oscillation.

## Algorithm

The mathematical algorithm, used to evaluate the periodic orbit, is based on the Poincaré's continuation method of continuous orbits of conservative dynamical system [49]. Defined

$$\dot{x} = F(x, \sigma) \quad (7.7)$$

as an autonomous system of  $n$  differential equations depending on the parameter  $\sigma$ , then any solution

$$x = x(t, \xi, \sigma) \quad (7.8)$$

is a functions of the parameter  $\sigma$  and the initial conditions  $\xi = x(0, \xi, \sigma)$ . Supposing that, for a given value  $\sigma = \sigma_0$  of the parameter and initial conditions  $\xi = \xi_0$ , a periodic solution of the system  $x$  will be:

$$x(t, \xi_0, \sigma_0) = x(t + T_0, \xi_0, \sigma_0) \quad (7.9)$$

With  $T_0$  the period of the close motion. The Poincaré's method deals with the problem of evaluate the analytic continuation of the Eq. 7.9 for values of the parameter close to the starting value  $\sigma_0$ :  $\sigma = \sigma_0 + \Delta\sigma$ , with initial conditions  $\xi = \xi_0 + \Delta\xi$  and period  $=_0 + \Delta$ . The new solutions shall verify the periodicity condition:

$$x(T, \xi, \sigma) - \xi = 0 \quad (7.10)$$

Where the existence of the implicit function  $\xi$  is directly related to the nonvanishing of the Jacobian determinant of the left-hand side of 7.10, that can be rewritten as follows:

$$x(T_0 + \Delta T, \xi_0 + \Delta\xi, \sigma_0 + \Delta\sigma) - (\xi_0 + \Delta\xi) = 0 \quad (7.11)$$

and expanding it around  $(T_0, \xi_0, \sigma_0)$  to the first order:

$$(\nabla_\xi x - I) \cdot \Delta\xi + F(x, \sigma_0) \Delta T + \frac{\partial x}{\partial \sigma} \Delta\sigma = \xi_0 - x \quad (7.12)$$

Where  $I$  is the identity matrix. Equation 7.12 provides the scheme for implementing the Poincaré method. In fact for a periodic solution the right term of Eq. 7.12 is zero:

$$(\nabla_\xi x - I) \cdot \frac{\Delta\xi}{\Delta\sigma} + F(x, \sigma_0) \frac{\Delta T}{\Delta\sigma} = -\frac{\partial x}{\partial \sigma} \quad (7.13)$$

and this conditions is exploited to evaluate the new initial conditions  $\xi_1 = \xi_0 + \Delta\xi$  and period  $T_1 = T_0 + \Delta T$  corresponding to the value  $\sigma_1 = \sigma_0 + \Delta\sigma$  of the parameter. Equation 7.13 represent a prediction, and, usually it yields a new solution that is not exactly periodic, that is,  $x(T_1, \xi_1, \sigma_1) - \xi_1 \neq 0$ .

In such a case new corrections  $\Delta\xi_1$  and  $\Delta T_1$  should be computed in order to satisfy the periodicity condition. An iterative correction can be derived from:

$$(\nabla_\xi x - I) \cdot \Delta\xi + F(x, \sigma_1) \Delta T_i = \xi_0 - x \quad (7.14)$$

evaluated at  $(T_i, \xi_i, \sigma_1)$ . However, now the right-hand no longer vanishes.

The partial derivatives of  $x$  with respect to the initial conditions  $\xi$  are computed from the homogeneous variational system:

$$\nabla_\xi \dot{x} = (\nabla_x F) \cdot (\nabla_\xi x) \quad (7.15)$$

starting from the initial conditions

$$(\nabla_\xi x)_{t=0} = I \quad (7.16)$$

that follows from  $x(0, \xi, \sigma) = \xi$ . Analogously, the partial derivative  $\partial x / \partial \sigma$  is a particular solution of the variational equations

$$\frac{d}{dt} \left( \frac{\partial x}{\partial \sigma} \right) = (\nabla_x F) \cdot \frac{\partial x}{\partial \sigma} + \frac{\partial F}{\partial \sigma} \quad (7.17)$$

starting from the initial conditions:

$$\left( \frac{\partial x}{\partial \sigma} \right)_{t=0} = 0 \quad (7.18)$$

Equations 7.12 and 7.14 provide a predictor-corrector scheme for calculating the analytic continuation. The normal procedure is to fix one of the initial conditions and vary the period.

## Numerical Computation

Here some examples of periodic orbit are shown to describe their dynamics in the libration angles phase plane. In particular we want to see how they change as a function of the orbital inclination, that is a very important parameter for the stability of a tethered system, and the electrodynamic interaction.

Figures 7.4-7.5 reports the evaluations of the periodic orbits for two different case ( $\epsilon$  constant and variable), choosing as period the orbital period of the satellite ( $T = T_{orb} = \frac{2\pi}{\omega_{orb}}$ ), in order to close the motion after a whole orbit. As just said, it is a long process, which require several iterations. For the sake of simplicity, in the pictures are reported just three iterations (initial, intermediate and final orbits) to explain how the solution found by the algorithm evolves.

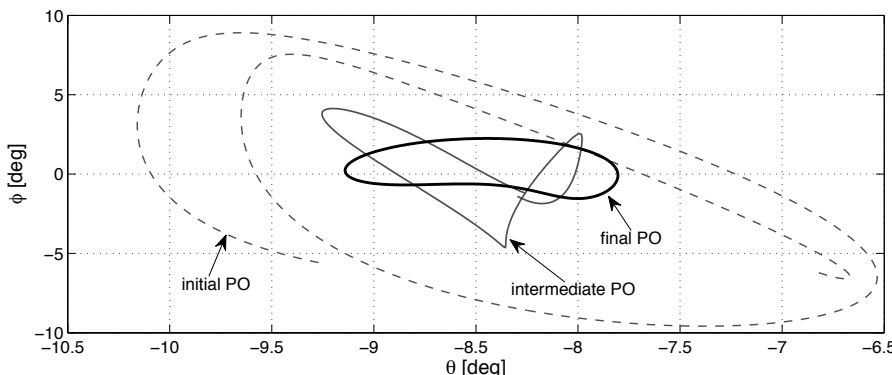
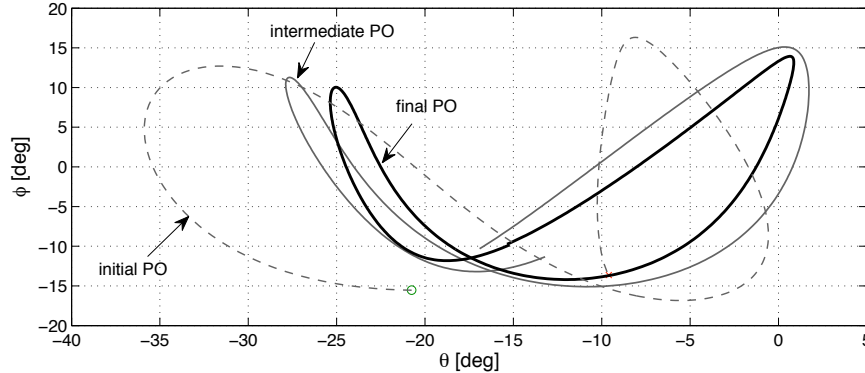


Figure 7.4: Periodic orbit -  $\epsilon$  constant

Figure 7.6 shows the variation of the periodic orbit as a function of the orbital inclination. It is interesting to note how the solution tends to enlarge as the inclination increases. We must take into account that in Fig. 7.6-7.7 the electrodynamic interaction has been considered constant along the orbit, but during deorbiting it changes, since depends on several parameters: first of all the day/night variation, then the libration itself of the wire, and difference of altitude during the reentry. In fact along the orbit the satellite experiences regions (in front of the sun) at high electron density, and then others (in the shadow cone) where the electron population becomes less dense. For taking into account this aspect, in first analysis we can describe the ionosphere by means of a sinusoidal function (see Fig. 7.5).

Figures 7.8 represent the variation of periodic profile as a function of orbital inclination, considering an sinusoidal function for the electric current. Again the motion becomes wider at high inclinations. Several authors [37][73] studied this kind of problem, but considering the electrodynamic interaction

Figure 7.5: Periodic orbit -  $\epsilon$  variable

constant, so limiting the validity of the results. Most recently Williams [111] looked for a solution in the case of varying  $\epsilon$ , and chose a time-delayed predictive control law to chase the reference profile. In his examples the control works in the right way, even if it requires a lot of time to reach the periodic orbit and an active element is necessary to adapt the electric current to the correct next value.

The most important drawbacks that limit this kind of control is given by the fact that an unique periodic orbit doesn't exist, since it is different after each orbit, because the environment conditions change (see 7.9). In fact we can consider, in first approximation, that the orbit is fixed in the inertial frame, while the Earth rotates around its axes, so after an orbit the tethered system will see a different magnetic field, ionosphere, and so a new electrodynamic torque. The control should evaluate the reference profile at each orbit and tries to chase it. But it must happens without actuators and the system doesn't have control authority in the direction, but only on the electric current intensity along the wire. An active control solution by thruster, as proposed in [37], will overcome this problem, but it is too complex and onerous for the mass budget.

Moreover, looking at Eq. 7.2 we must consider that when the inclination increases or the system works at high current (long tethers or low altitude) the instability grows up quickly, making the control not enough.

Therefore, even if very interesting from a mathematical point of view, this strategy is too difficult to implement in a real case, because it depends on a lot of variables that can be only predicted by mathematical model (like the electron density on the ionosphere, or the current along the wire), that could be a little different along the mission. Moreover little errors, without a strong directional control (as thruster), bring slowly to instability.

### 7.2.3 Electric Current Control

One of the most promising strategies is the possibility to act on the current flowing in the EDT. This can be performed in several ways. The philosophy adopted here consists on controlling the current in the simplest way as possible: open and close the circuit, as proposed by Corsi [17] and Takeichi [101].

The current is switched off when the effective Lorenz force is in the direction of the libration and stays on in the opposite case thus producing a net negative work on tether libration (see Fig. 7.10). When  $V_{stab}$  overcomes a threshold value  $V_{th}$  the code must look at the direction of the oscillation respect to Lorentz force. In fact when both are in the same direction the electrodynamic torque

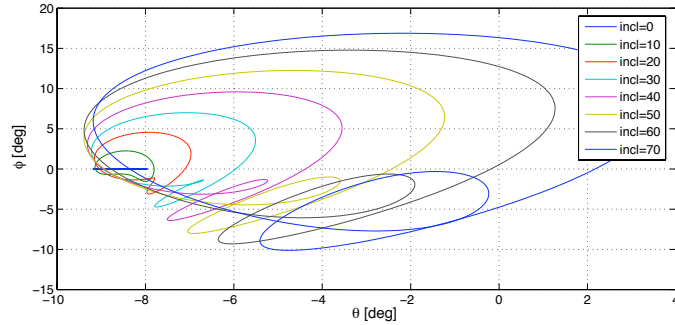


Figure 7.6: Periodic orbit as a function of the orbital inclination ( $\epsilon = \text{constant}$ )

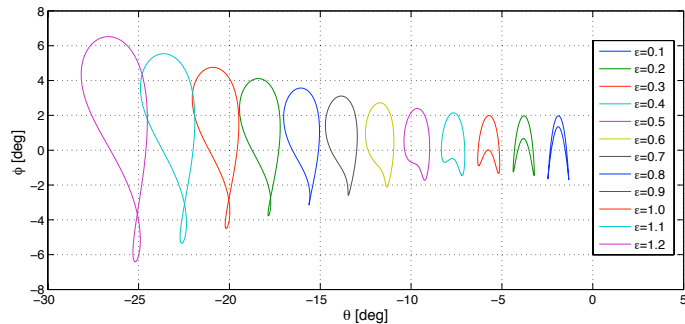


Figure 7.7: Periodic orbit as a function of the  $\epsilon$  parameter

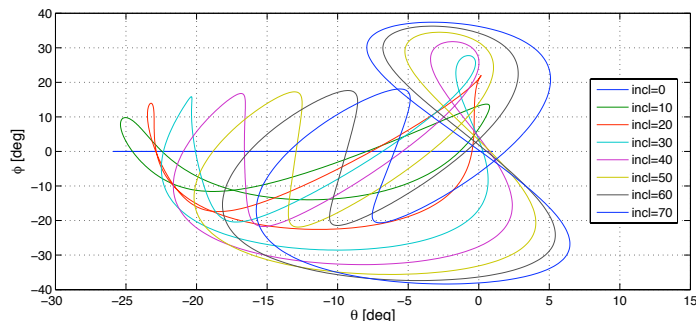


Figure 7.8: Periodic orbit as a function of the orbital inclination ( $\epsilon = \epsilon_0 \sin(\omega_{orb}t)$ )

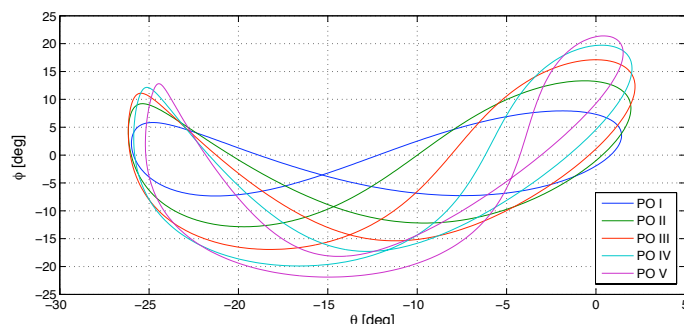


Figure 7.9: Periodic orbit profile changes after each orbit

causes a positive work that amplifies the oscillation, while in the other case the work becomes negative and decreases the rotational kinetic energy. Hence the control routine has to observe the attitude dynamics switching on or off the electric current, by closing and opening the circuit, as a function of the threshold value and oscillation direction.

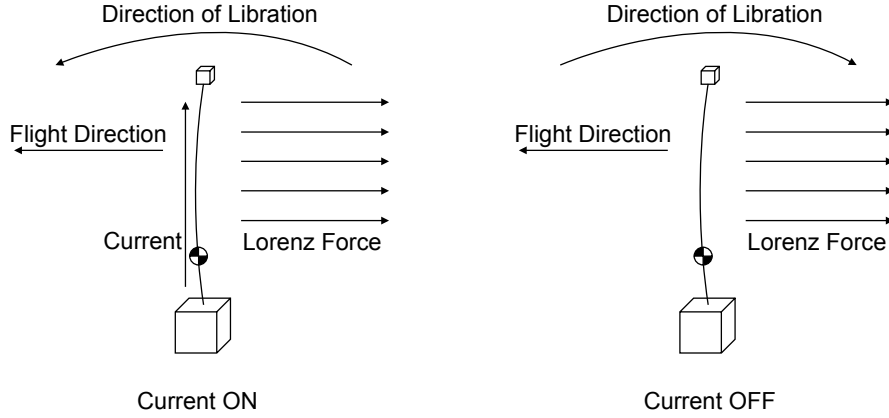


Figure 7.10: Electric current control strategy

The simplest strategy considered is to act on the current via a threshold value of the libration angles (in-plane  $\theta$  or out-of-plane  $\varphi$ ). If the value is lower than a threshold level then the full current is available.

The stability function is derived from the system Hamiltonian and is expressed as:

$$V_{stab} = 4 + \frac{\dot{\varphi} + \cos^2 \varphi (\dot{\theta}^2 - \omega_{orb}^2 (1 + 3 \cos^2 \theta))}{\omega_{orb}^2} \quad (7.19)$$

where  $\theta$ ,  $\varphi$ ,  $\dot{\theta}$  and  $\dot{\varphi}$  are respectively the in-plane and out of plane attitude angles and their derivatives. When  $V_{stab} \geq V_{th}$  (a predefined threshold value) the current control function is activated. An important point to deal with is the choice of the threshold value to use: a low threshold assures small oscillations and so optimal performance, but on the other hand long switched-off period are forecast. A look at the stability function was taken briefly, in order to comprehend its physical meaning. Figure 7.11 report the boundaries of  $V_{stab}$  for some fixed value of  $V_{th}$ . For example if a threshold value  $V_{th} = 1$  is chosen the the in-plane oscillations will remain under about  $35^\circ$  and out-of-plane oscillation under about  $30^\circ$  are allowed. Above these values, stability control is activated.

To open the circuit in order to stop the flowing of the current inside the EDT seems a rather effective strategy of de-orbiting the system and is quite simple to be implemented.

For example, supposing a starting altitude about 1000 km and the following system characteristics are:

- Satellite mass: 1000 kg
- Tether length: 5 km
- Tether width: 1 cm
- Tether thickness: 30  $\mu\text{m}$

the reentry time is:

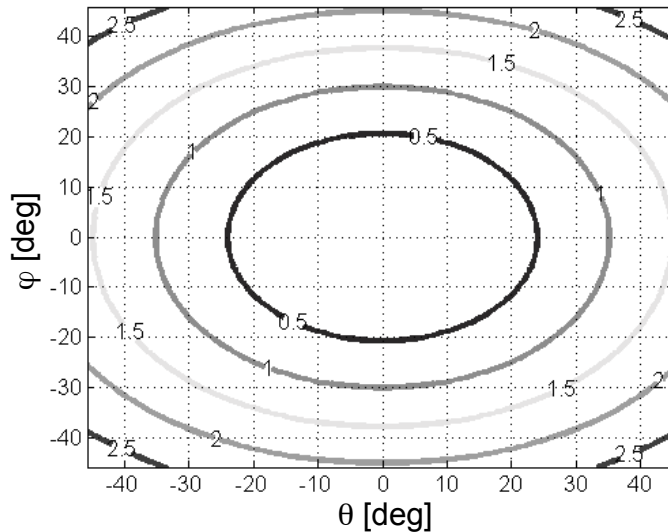


Figure 7.11: Plot of the stability function for different threshold values

incl [°]	$T_{deorbiting}$ [days]	Duty Cycle [%]
0	55.1	88.2
30	82.7	86.5
60	219.5	57.7

Table 7.1: Deorbiting by means of on-off control strategy

Where the *Duty Cycle* represents the operative perceptual of time, is that, when the circuit is closed.

In the next figures the equatorial case is shown. The satellite starts from a circular equatorial orbit at an altitude about 1000km and the threshold value of control function is set equal to 1 (see Fig. 7.12). The deorbiting is simulated during a maximum of solar activity.

The electrodynamic force, whose average value is shown in Fig. 7.13, carries out the deorbiting till low altitudes where the atmosphere becomes quite dense to complete the reentry. In fact at this height aerodynamic load becomes very strong and the torque due to it brings the satellite into instability, since it cannot be controlled as well as electrodynamic one. But this has little importance, because our aim has been reached and the satellite from its initial operative orbit has been brought down at heights where aerodynamic drag can quickly complete the maneuver.

Figure 7.14 describes the libration dynamics of the wire. The oscillation is mainly around the local vertical because the control forces the electric circuit to stay open for long time.

At least in Fig. 7.15 there is a zoom of tether temperature and average electric current. The temperature changes a lot because of solar radiation. When illuminated by sun the tether reaches the maximum temperature, otherwise it goes to equilibrium with Earth's radiation, that is the second most important thermal flux. The electric current is affected by thermal behavior, because tether electric resistance is function of temperature. As it can be seen in Fig. 7.12 the control algorithm forced the circuit to be open for a long time.

The most critical point of this strategy is that for tether longer than 2km the difference of potential between the extremities of the wire is such to provoke an electric arch at the switch, that would

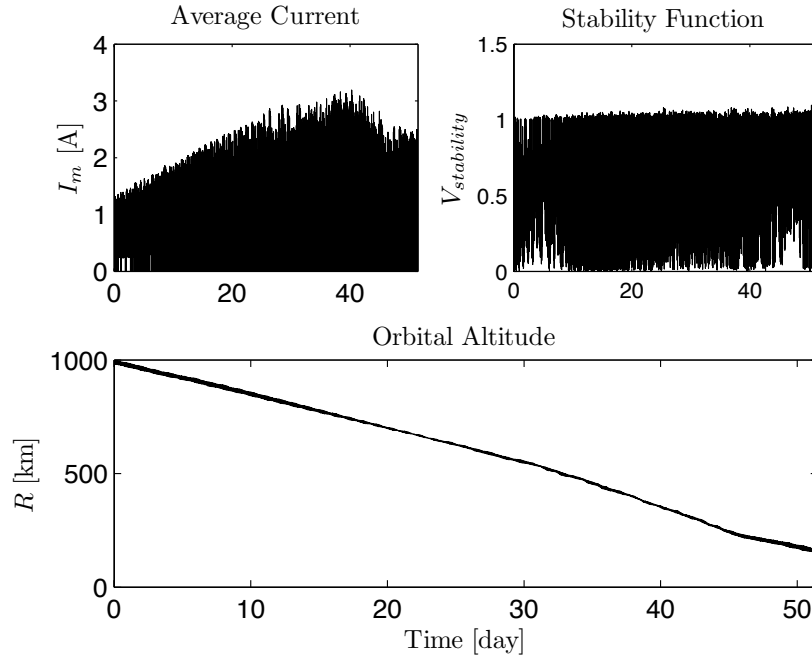


Figure 7.12: Electric current profile, stability function  $V_{stab}$  and orbital semimajor axis

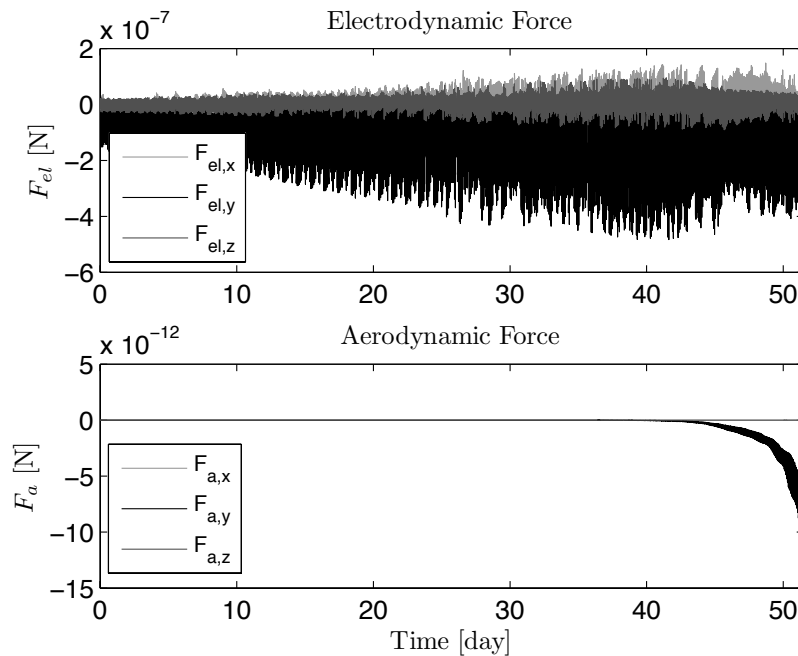


Figure 7.13: Electrodynmaic and aerodynamic forces

damage seriously the tether causing the failure of the mission.

A solution could be an adding load to mount in series to the EDT allowing a lower current to flow in the tether, when the circuit should be opened. A lower current implies a lower Lorenz Force that decreases instability. The drawback of an adding load is given by the heat, generated by ohmic losses, that must be dissipated in the space. So radiator must be included in the system to let the cooling of the component. This translates itself in adding mass that makes the tethered system less competitive respect to other traditional solutions.

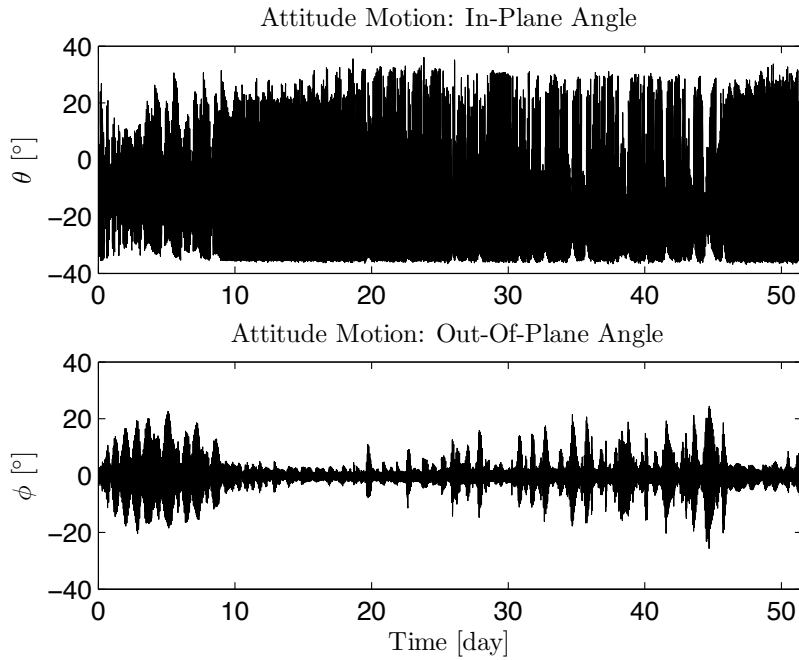


Figure 7.14: In-plane and out-of-plane libration angles

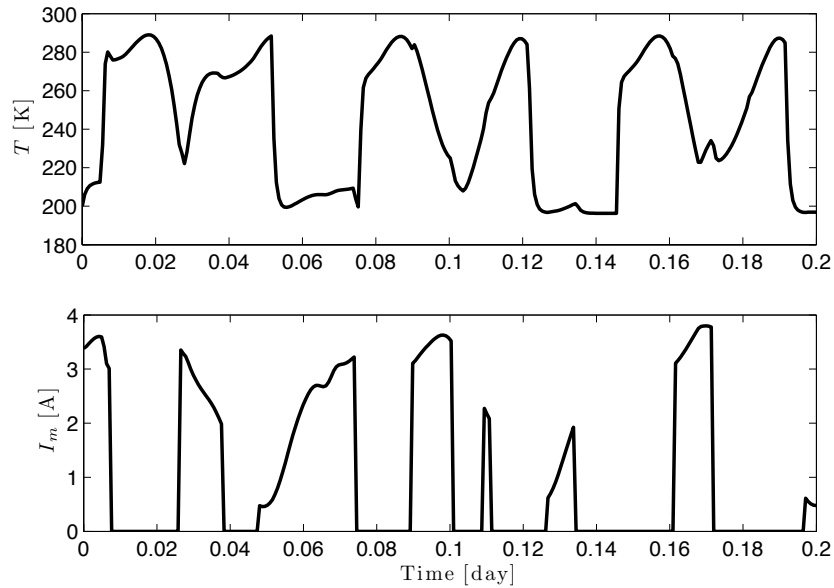


Figure 7.15: Zoom of the temperature and average electric current

### 7.3 Control Techniques Proposed for The BETs Project

In this section a new and different approach for controlling the tethered satellite is presented. Instead of monitoring the oscillations and regulating the electric load, we assume to insert in the satellite a damping mechanism to dissipate the energy pumped in the system by electrodynamic and also aerodynamic forces. The damper is thought to be placed between the satellite and the electrodynamic tether (see 7.16), and permits to keep stable the tethered system around the instantaneous equilibrium position that is a function of the position and tether size.

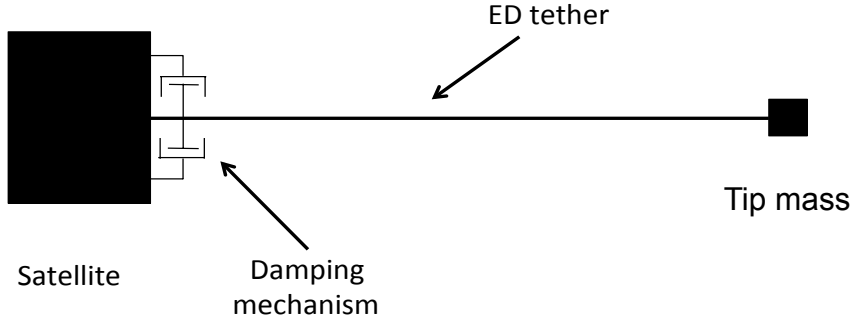


Figure 7.16: Dumbbell model with damping mechanism

To investigate the capability of such a system to control the libration during the deorbiting, several tether models have been considered, with increasing accuracy, which take into account different aspects of dynamical behavior of the tethered system.

### 7.3.1 Results With Dumbbell Model

We started our analysis considering the simple dumbbell model. In this architecture a frictional internal torque is introduced, which slowly dissipates the mechanical energy of attitude motion. The variation of the angular momentum of the system is due not only to the gravitational  $M_{gr}$ , electrodynamic  $M_{el}$  and aerodynamic  $M_a$  torques acting on the satellite, but also to the damping torque  $M_d$ , that is proportional to the librational angular velocities through the coefficients  $k_\theta$  and  $k_\varphi$ :

$$\frac{\vec{H}}{dt} = \vec{M}_{gr} + \vec{M}_{el} + \vec{M}_a + \vec{M}_d \quad (7.20)$$

In the body reference frame the attitude dynamics can be expressed as a function of libration angles in two non-linear and coupled differential equations:

$$\ddot{\theta} = \dot{\omega}_{orb} + 2(\dot{\theta} + \omega_{orb})\dot{\varphi} \tan \varphi + \vec{M}_{gr,\theta}^B + \vec{M}_{el,\theta}^B + \vec{M}_{a,\theta}^B - k_\theta \dot{\theta} \quad (7.21)$$

$$\ddot{\varphi} = -\frac{1}{2} \sin 2\varphi (\dot{\theta} + \omega_{orb})^2 + \vec{M}_{gr,\varphi}^B + \vec{M}_{el,\varphi}^B + \vec{M}_{a,\varphi}^B - k_\varphi \dot{\varphi} \quad (7.22)$$

The next figures depict an example of application of this technique: starting from an equatorial orbit at 500km of altitude (the region where the electron population is densest) the satellite deorbits completely, and the damping mechanism controls the oscillation providing a rapid decay without exhibiting any instability, as shown by Fig. 7.18.

Figures 7.18-7.19 describe the libration dynamics of the tether. The system goes rapidly at equilibrium with the external torques. The phase space diagram shows that after having reached the equilibrium the motion follows an eight-shape trajectory, which depends on the electrodynamic torques due to environmental conditions.

Figure 7.20 shows the Lagrangian function and the trend of electrodynamic and damping works for unit of inertia. The damping action follows quite well the electrodynamic one providing for the dissipation of the energy in excess. The difference between the two is due to coupling between in-plane and out-of-plane motion and their transfer of energy.

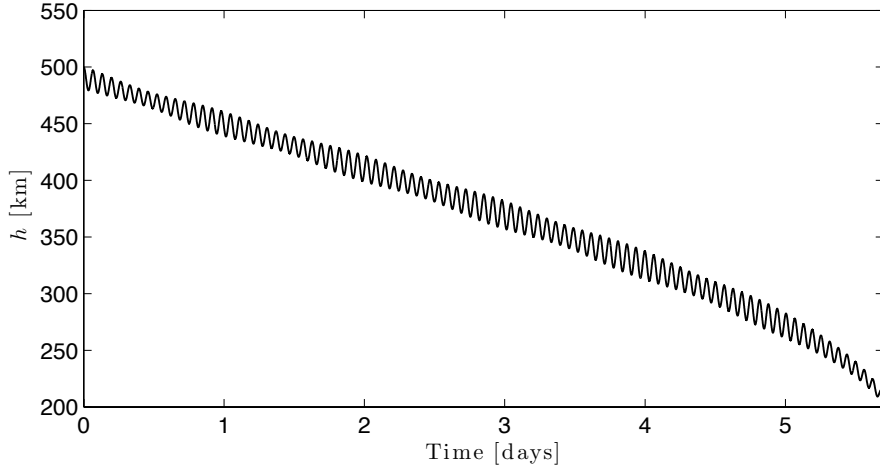


Figure 7.17: Deorbiting by means of damping mechanism

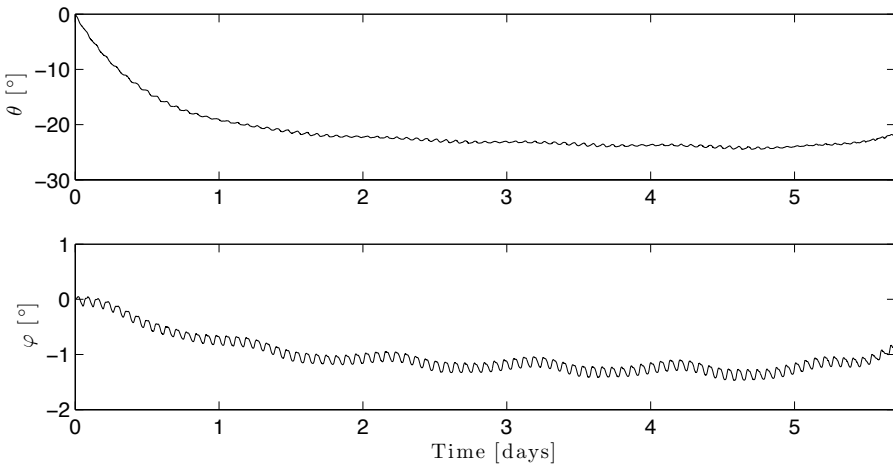


Figure 7.18: Libration dynamics of the tumbbell model with damping mechanism

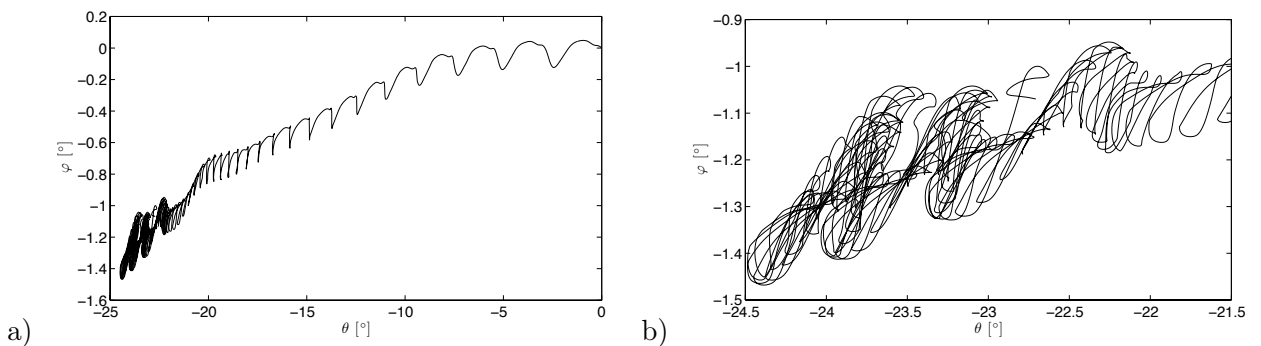


Figure 7.19: Libration dynamics in the phase space  $\theta$ - $\varphi$ : a) whole motion, b) zoom

### 7.3.2 Results With Inextensible Flexible Wire Model

The results provided by the dumbbell model are quite obvious, because they are intrinsic in the equations of motion. In a real system the tether is not perfectly rigid, and its flexibility also affects the capability to damp the oscillation. To take into account this aspect the flexible model has been

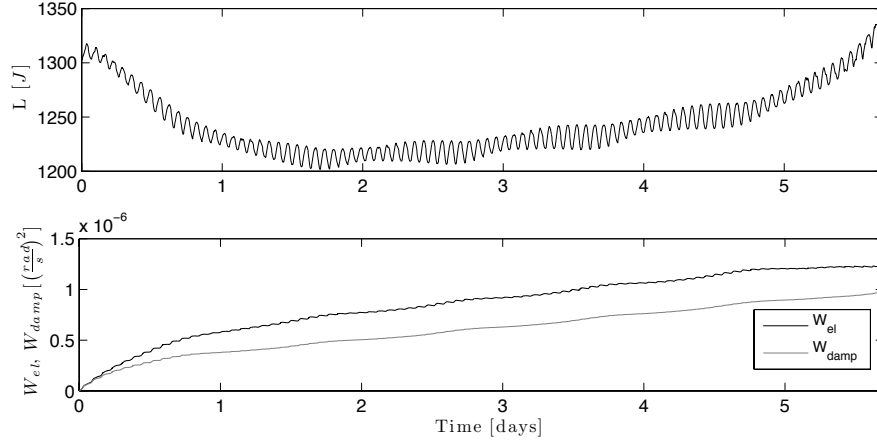


Figure 7.20: Lagrangian Function of the tumbbell model with damping mechanism

adopted: firstly studying it as inextensible (two and three bars models), and then as extensible.

### Two Bars Model

In the Two Bars Model (see section 2.2.3), the tethered system is composed by two elements (see Fig. 2.2). The damping mechanism is supposed to act in the first bar, that directly connected to the satellite, as explained by Eq. 2.54.

In Figs. 7.21-7.24 the results of a simulation are reported to better understand what happens when we include the first flexible mode.

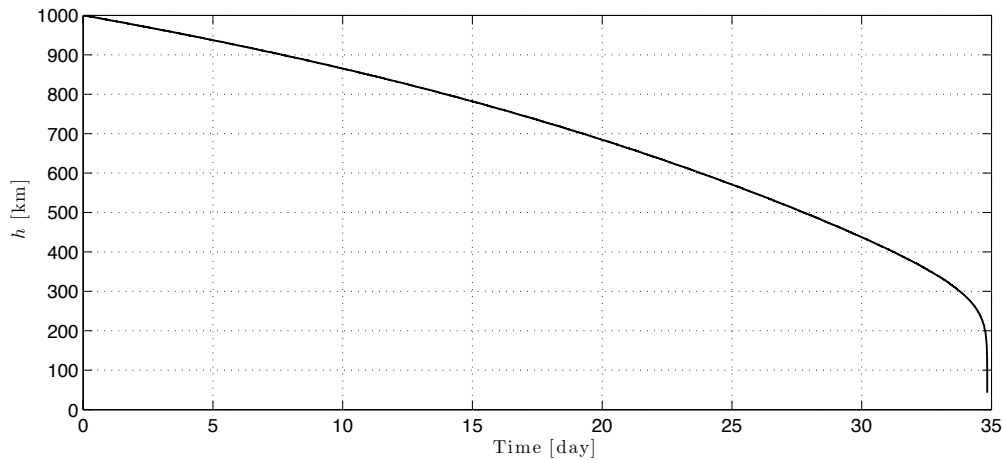


Figure 7.21: Two Bars model: orbital altitude

The satellite reenters without problems maintaining the oscillation very small even if the electric current along the wire is high (more than 2A in the densest region).

This configuration has a strong limit, represented by the fact that the damper acts on a long element, which is described always as rigid. But in a real case, the flexibility of the wire is very important. So for this reason a new version of the Two Bars Model, where the two elements have different length, has been implemented. In particular the first bar is much shorter (at maximum 50m) respect to the second one (see Fig. 7.25), and is treated as a rigid rod, whose aim is to lead the wire (like a fishing

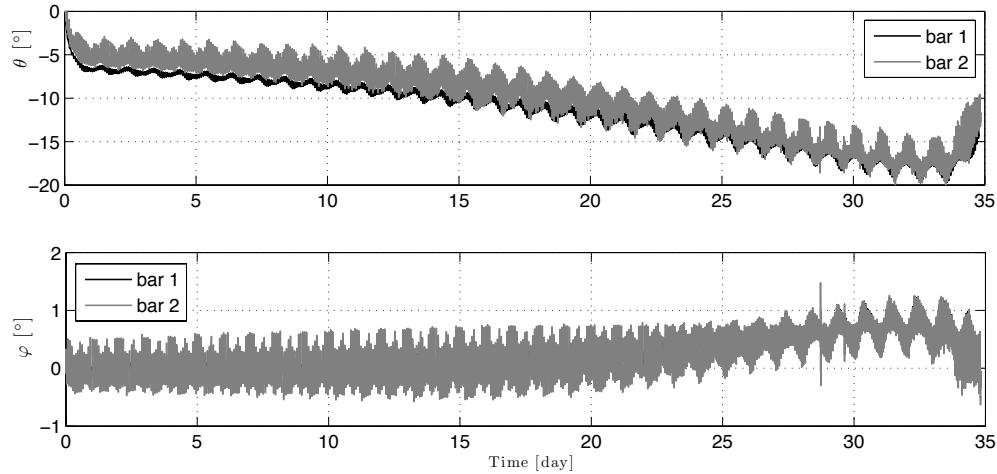


Figure 7.22: Two Bars model: libration angles

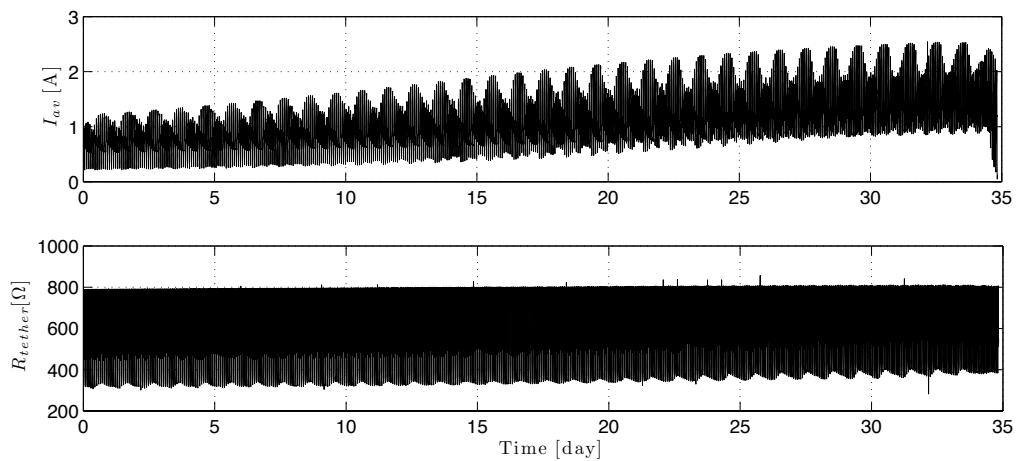


Figure 7.23: Two Bars model: average electric current and electric resistance of the tether

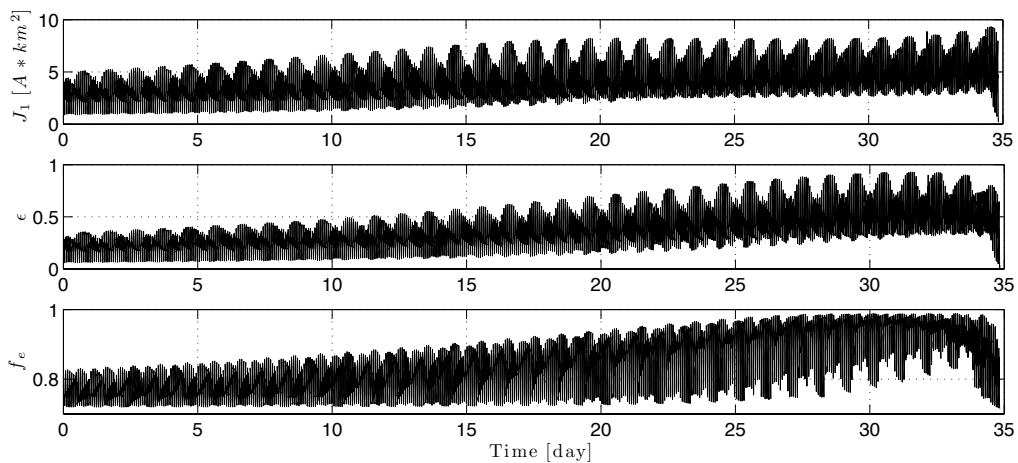


Figure 7.24: Two Bars model: electrodynamic parameters

pole), while the other part represents the real electrodynamic tether that collects the electrons from the ionosphere, and lets the reentry. In this way it's possible to describe more in detail the damping process, taking better into account the flexibility of the wire.

In the *fishing rode* configuration the wire is connected to the satellite by the rigid rod, which has two degrees of freedom respect to the satellite and, thanks to some hinges, it can rotate along two axes. We neglect the third rotation, that could happen respect the longitudinal axis, because no so important for our aim. Hence the friction in the hinges dissipates a little of energy at every oscillations, letting to subtract it from the attitude dynamics of the spacecraft.

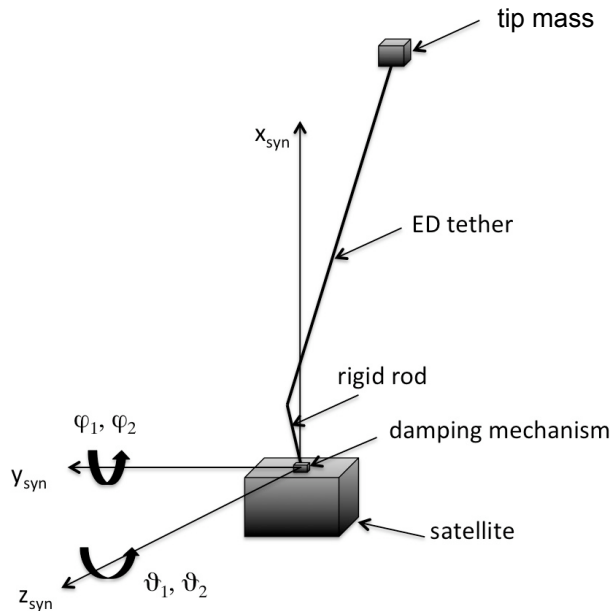


Figure 7.25: Two Bars model with damping mechanism

The main drawback of this model, is just computational: when the first bar is substituted by a very short rod, the eigen-frequencies  $f_{3,4}$  become very high, so the simulator requires much more time to provide the solution. For example considering a rod and an electrodynamic tether, respectively, 5m and 5km long, and a tip mass about 25kg, the eigen-frequencies of the linearized system are:

$$\begin{aligned} f_1 &= \sqrt{3}f_{orb} \\ f_2 &= 2f_{orb} \\ f_3 &= 221.78f_{orb} \\ f_4 &= 221.79f_{orb} \end{aligned}$$

values that can be well observed also in the Fourier analysis of the attitude motion.

#### *Choice of gain k*

The choice of  $k$  coefficients is a crucial aspect, since it depends on several parameters, like the size of each element of the tether, the inertia of the system, the electrodynamic interaction with the environment, etc.

The selection of the right coefficient must be made when the electrodynamic force is most critical, is that, in the region where the electron density is highest: if the damping mechanism is able to

dissipate the libration energy in excess in that situation, then it will control the libration during the whole deorbiting till low altitudes, where the aerodynamic drag will complete the reentry.

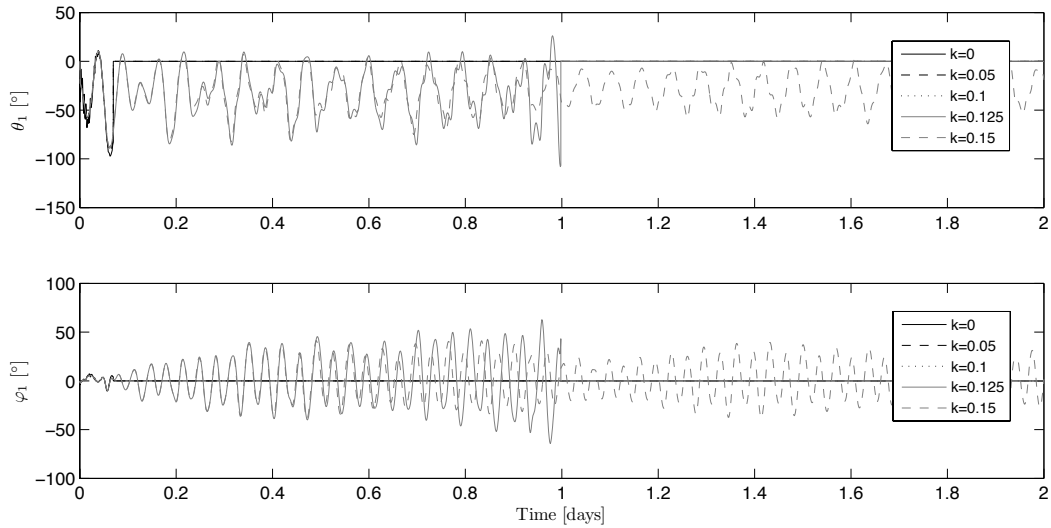


Figure 7.26: Instability of the rod libration as function of the damping coefficient  $k$

To show the importance of damping coefficients the trend of attitude motion is depicted as function of time for different values of  $k_\theta$  and  $k_\varphi$ . For simplicity we have considered the same coefficient  $k$  for the in-plane and out-of-plane motion, moreover the system considered is formed by a rod 5m long an electrodynamic tether 5km long (1cm wide and  $30\mu\text{m}$  thick), a 1000kg satellite and 25kg tip mass.

Figures 7.26-7.27 report the dynamics of attitude motion spacing the coefficient  $k$  from 0 to 1.5. If the value of  $k$  is too low the motion goes rapidly to instability overcoming the oscillation of  $90^\circ$ . Higher values ( $k=0.125$ ) let maintaining the oscillation stable for a day, but then the energy pumped by electrodynamic force becomes such to bring the rigid rod element into rotation. At last, a stable motion is guaranteed with a damping coefficient  $k=0.15$ .

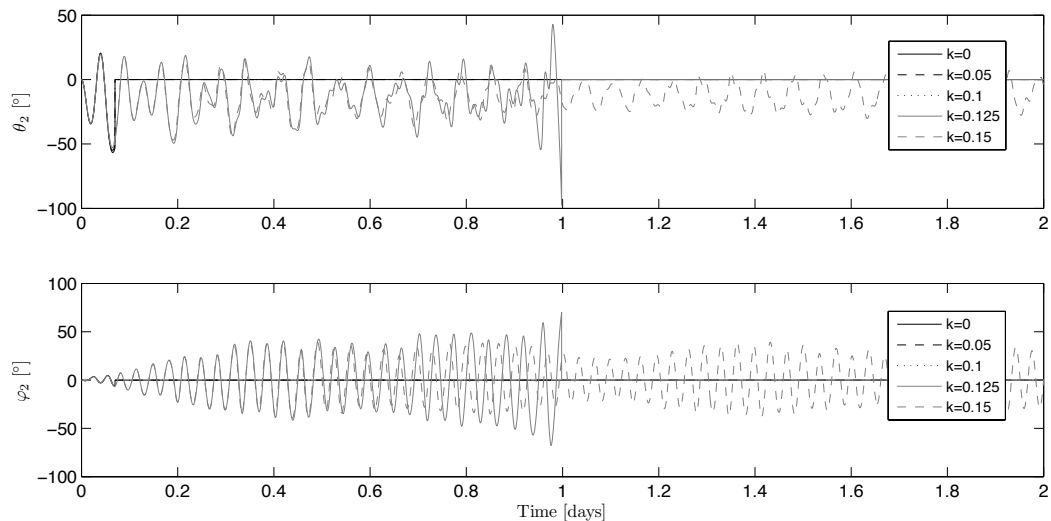


Figure 7.27: Instability of ED tether libration as function of the damping coefficient  $k$

It is interesting to see how the eigen-frequencies  $s$  of the system change when we introduce the damping term. Figure 7.28 show the variation of the real part for both the libration motion and the high frequency components, shown in the previous section, that in the case of damped system can be written as:

$$\begin{aligned} s_{1,2} &= R_{e1} + j f_{1,2} \\ s_{3,4} &= R_{e2} + j f_{3,4} \end{aligned} \quad (7.23)$$

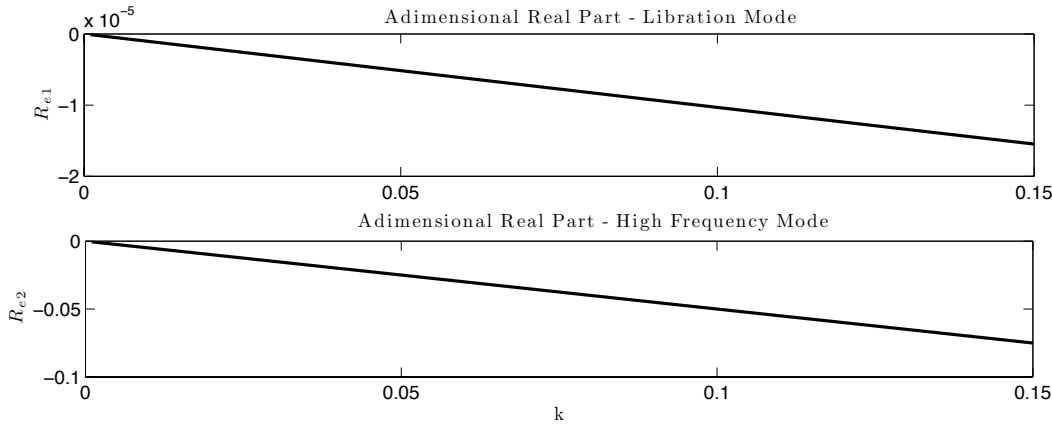


Figure 7.28: Real parts of the eigen-frequencies

The more interesting contribution is provided by the high frequency component. In fact the real part starts from zero augmenting till negative high values, which assure the full control of the system. The damping mechanism puts down immediately the high frequencies, which slow down the integration routine, and then, by subtracting continuously energy, provides the control of libration, too. It is important to specify that the real parts of each couple of eigen-frequencies is negative, because for obtaining their analytical expression the perturbing forces are neglected and only little displacements are considered. What Fig. 7.28 wants to show is that the damping term introduces a positive and stable contribution effect (negative real part), that dissipates energy from the attitude motion letting a safer deorbiting.

### Results

Some numerical results (see Fig. 7.29) about deorbiting performance, from an initial altitude about 1000km, obtained with this model are here reported. For this campaign of simulations we considered the same parameters of the wire and the mass of satellite chosen before (for the evaluation of  $k$ ), but with three different tether length (3-5-10km), spacing the orbital inclination from  $0^\circ$  to  $60^\circ$ , and interpolating the data to obtain information till high inclinations. In the simulation the same damping coefficient has been chosen for both the in-plane and out-of-plane libration ( $k_\theta = k_\varphi = 0.15$ ).

At low inclinations all the configurations work very well and guarantee fast reentry for both short and long system: for a 3km long wire the deorbiting time is approximately two months and half (see Fig. 7.30). While, as expectable, at high inclination the decay time becomes very long for short tether, but it continues to remain reasonably small for long wires. For example at  $60^\circ$  inclined orbits, with a 3km long tether the deorbiting takes approximately a year to complete the maneuvers, but with a 10km long tether it decreases at only 51 days. The configurations chosen are

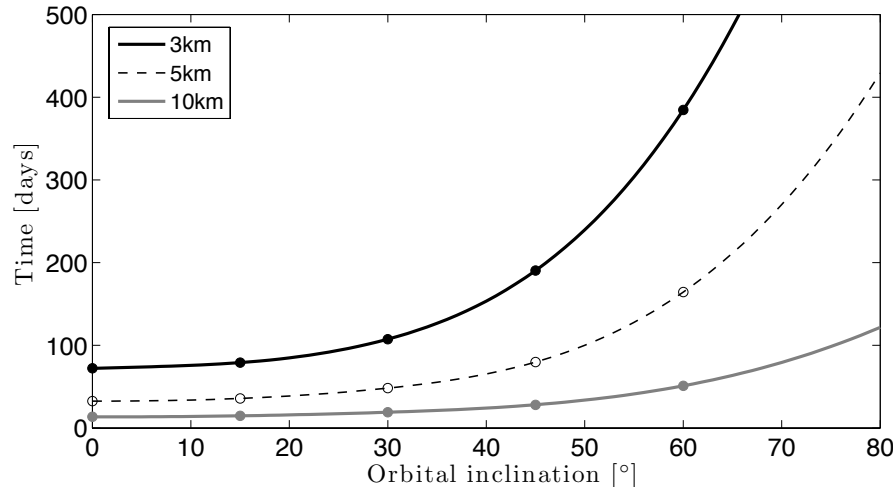


Figure 7.29: Two Bars model controlled by means of damper: reentry time

very light, in fact the mass of the wire for the three lengths are 2.43, 4.05 and 8.1kg, respectively. For low inclination orbits short tethers are adapt to guarantee reasonable reentry saving the mass, while long tethers become preferable at high inclinations, where the more unfavorable environment conditions make EDT system critical.

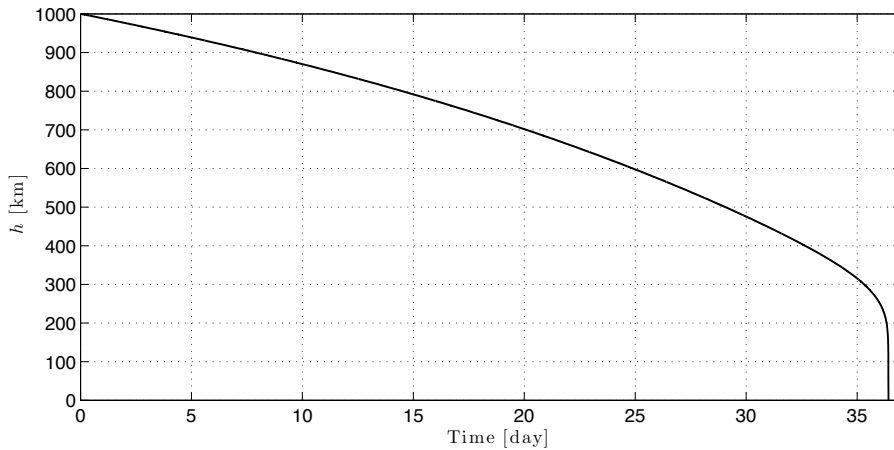


Figure 7.30: Two Bars model controlled by means of damper: orbital altitude

In Figs. 7.31-7.32 the reentry profile, for the case 5km long tether and equatorial orbit, is illustrated. The control is very efficient and maintains the maximum oscillation inside an acceptable range both for in-plane and out-of-plane motion. The angle velocities are affected by rapid acceleration in correspondence of pass of the satellite from sunlight to shadow region, and vice-versa, which provokes a strong change of tether temperature and its resistivity, and so also of the electric current (see Fig. 7.33).

Figure 7.34 shows the Lagrangian function of the system and the work (for unit of inertia) done by electrodynamic work and damping mechanism. The damping term is able to dissipate the most of energy pumped by the electrodynamic force, while a part is transferred to that we called the right term of the equation of motion.

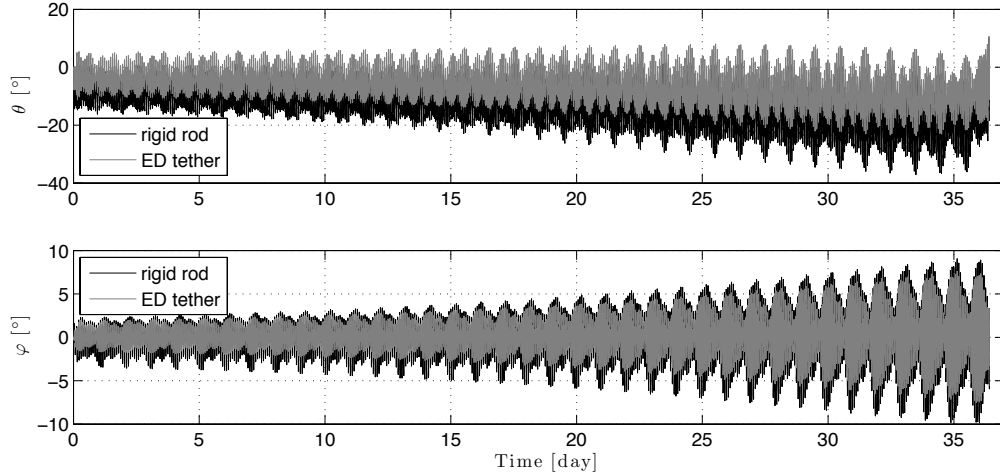


Figure 7.31: Two Bars model controlled by means of damper: libration angles

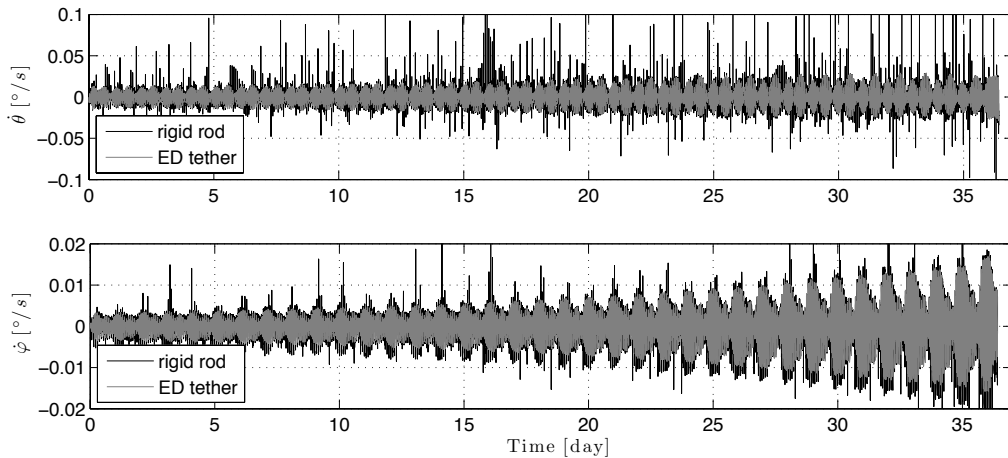


Figure 7.32: Two Bars model controlled by means of damper: libration angular velocities

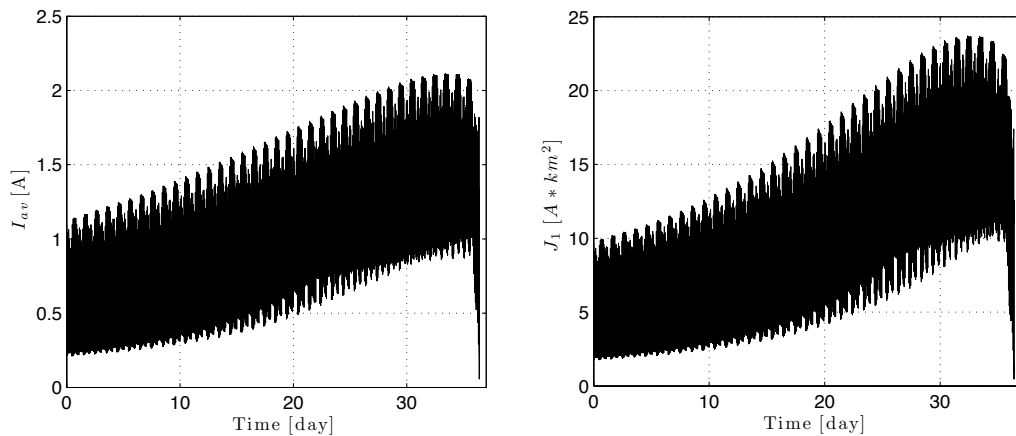


Figure 7.33: Two Bars model controlled by means of damper: mean electric current profile  $I_{av}$  and electrodynamic torque factor  $J_1$

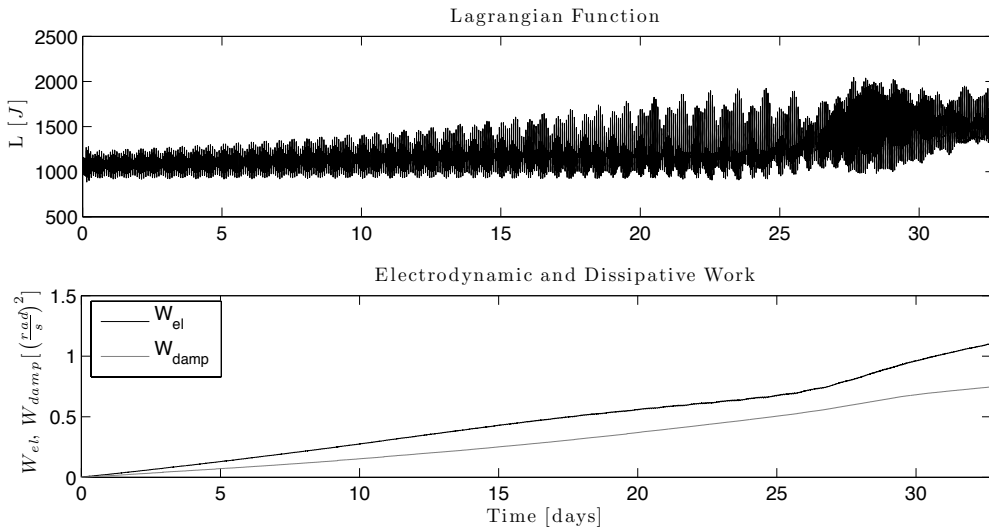


Figure 7.34: Electrodynamic and dissipative work (Inertia momentum =  $5.335 \times 10^8$  [kg\*m<sup>2</sup>]).

A further comparison has been done between different geometries of sectional area. In Table 7.2 we have reported the results obtained deorbiting by a 5km long tether for three different cases, for a satellite initially in an equatorial circular orbit at an altitude of 1000km.

Case	I	II	III
width [cm]	1	2	1
thickness [mm]	0.03	0.03	0.06
rigid rod [m]	5	50	50
k	0.15	0.3	0.3
reentry time [days]	36.4	17.9	19.6

Table 7.2: Comparison between different configuration of the tether

By augmenting the transversal dimension of the wire the reentry becomes faster, because the electrodynamic interaction is stronger. But the system requires higher damping coefficients, and longer rigid rod to maintain the attitude dynamics stable; otherwise the Lorentz force would transform the libration into a rotation and compromise the operation.

The last comparison (see Table 7.3) concerns different ratio of satellite and tip mass ( $m_{sat}/m_B$ ). In particular we want to maintain this system as light as possible, and so have lighter tip mass. For this comparison we have choose three values of ballast mass (10-15-20kg), evaluated the damping coefficient required to satisfy the control and so the reentry time.

The results highlight how this strategy is useful for system with elevate mass ratio, but to guarantee the control the damping coefficients required become very high, and this can be a critic aspect to take into account during the design.

### Three Bars Model

By using the Three Bars Model it's possible to take into account also the second flexible modes. As already explained the configuration is very similar to the last one just studied: the first bar is very short and is subjected to the damper, while the electrodynamic tether is divided in two portions

Case	I	II	III
tip mass [kg]	10	15	20
k	4	1	0.15
reentry time [days], incl = 0°	36.4	32.9	32.6
reentry time [days], incl = 15°	40.4	36.7	35.7
reentry time [days], incl = 30°	55.5	50.6	48.2

Table 7.3: Reentry Time for different configuration of the tether

(see Fig. 7.35) and let the collection of the electrons and the interaction with the environment.

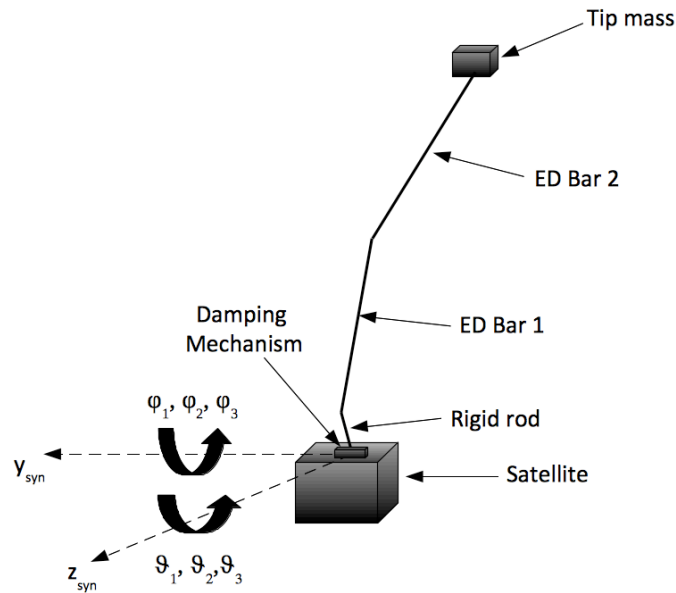


Figure 7.35: Three Bars model with damper

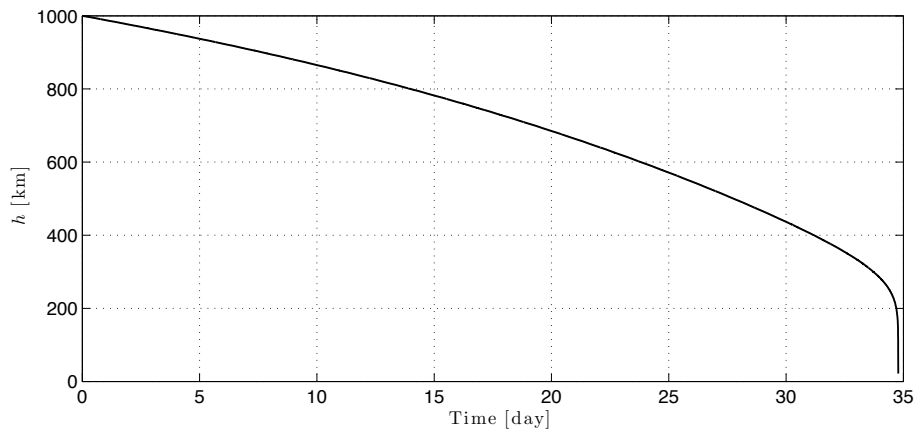


Figure 7.36: ThreeBarsModel controlled by means of damper: orbital altitude

In order to compare the results, the configuration of the tethered system and the damping mechanism are the same chosen before for the previous Two Bars model. The only difference is that the electrodynamic portion is divided in two parts. The time required for the deorbiting doesn't

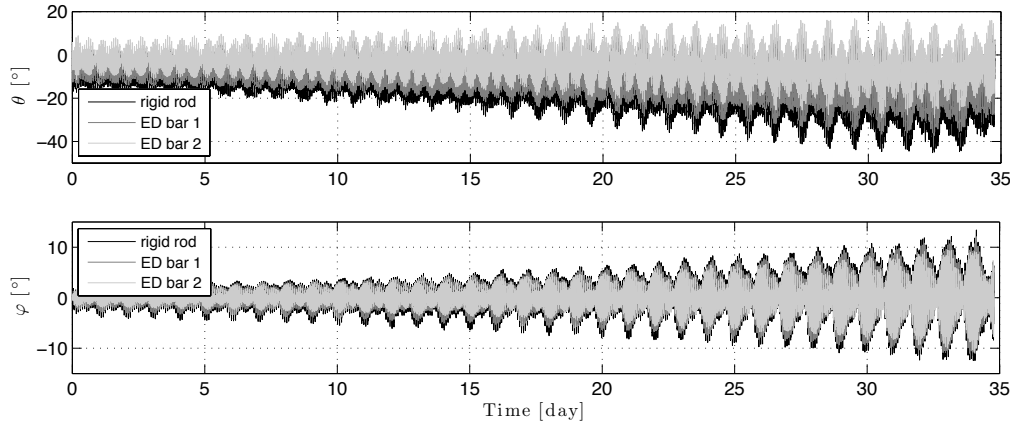


Figure 7.37: ThreeBarsModel controlled by means of damper: libration angles

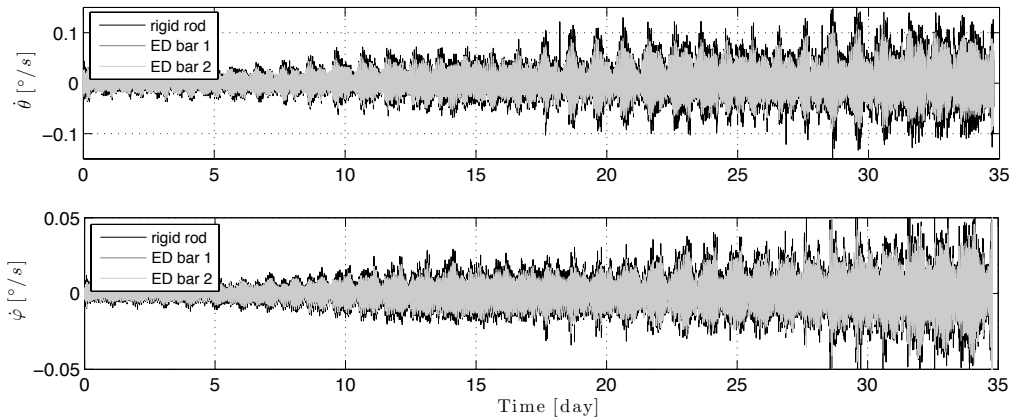


Figure 7.38: ThreeBarsModel controlled by means of damper: libration angular velocities

change so much (see Fig. 7.36), but both the in-plane and out-of-plane libration are a little wider, in particular the first bar is more perturbed since the electrodynamic forces are stronger closer to the satellite (see the electric current profile in Chapter 4).

### 7.3.3 Results With Extensible Flexible Wire Model

The damping mechanism seems to work very well also when we include the second flexible mode, but now we want to investigate the system as a flexible and extensible wire. That's why the lump masses approach is adopted, since it lets to include the longitudinal deformation due to the external forces, and the tension that propagates along the tether. This last parameters is very important during the design, because the section of the wire is very small and the tension (in terms of MPa) becomes high, therefore we have to pay attention that it doesn't overcome the yield point. Moreover we want to study if and how the longitudinal dynamics affects the lateral deflection.

From simulations it's possible to see that in a real case the damper by itself is not sufficient to guarantee a whole and optimum control of the tether oscillations, and the tether tends to describe more and more wide oscillation and go into instability. That's why a new solution has been studied, and a inert element is mounted after the conductive portion in order to increase the stable gravity

gradient torque. This hybrid configuration permits to reach the goal and reentry the satellite till low atmosphere, where the aerodynamic drag is plenty to complete the maneuver. Figure 7.39 shows a simplified description of the system, where we can recognize all the main elements just cited.

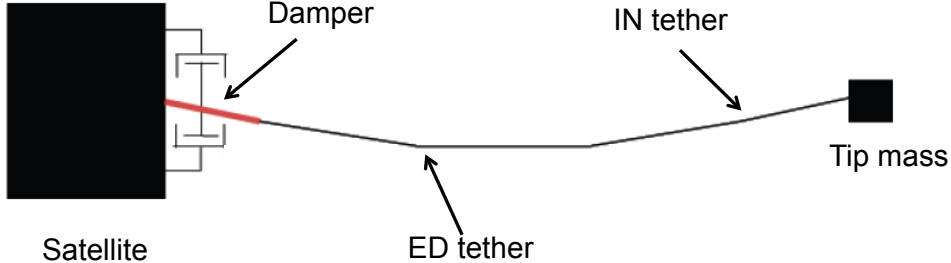


Figure 7.39: Hybrid tethered system: damping mechanism plus inert portion

To better explain what just said, we consider a satellite mounting a 5km electrodynamic tether with width and thickness 1cm and  $30\mu\text{m}$ , respectively. In the first case we add only an inert portion without damper, while in the next one we suppose to insert the damper without the no-conductive part.

In the first example, and as general rule, we consider an inert portion no longer than 5km. In fact, important constraints are the mass and the total tether surface exposed to risk of orbital debris impacts. Figures. 7.40-7.43 describes the dynamics of each lump masses in the synodic reference frame  $G_{xyz}$  ( $G$  barycenter of the tethered system,  $x$  aligned along the radial direction,  $z$  perpendicular to orbital plane and aligned with the angular momentum unit vector,  $y$  in the orbital plane to close the tern) for an equatorial orbit starting from 1000km. The satellite requires approximately 10 days more to decay than the analogous hybrid system (see Fig. 7.49-7.52). This difference is due to the skip-rope motion that affects the lateral dynamics and is rapidly excited by the electrodynamic forces. Even if the system decays completely till low altitude, the skip-rope motion is particularly severe, as we can see from the graphs. In particular the lump masses in the middle of the whole tether are subjected to very high displacements both in-plane and out-of-plane wider than those of the masses at the extremities of the wire. This means the tether is very bowed and rotates around the unbowed configuration with a motion similar to that of a child's skip rope [14], as it can be seen in Fig. 7.43 showing the maximum deflection of the wire. Chapel and Grosserode [14] give a detailed description of skip-rope motion for an unperturbed system. The tethered system evolves around an elliptical motion, whose ellipse precedes respect to the longitudinal axis. But when damping is present in that direction the elliptical motion tends to circularize.

Figures 7.44-7.47 simulate the behavior of the tethered system mounting only the damping mechanism. The dissipated energy isn't enough to assure a stable dynamics, and after approximately 16 days the system goes completely into instability and the libration becomes a rotation. As shown by Fig. 7.48 in a real system we cannot use any damping coefficient, because beyond a certain value the system become too rigid and it isn't anymore able to subtract energy from the attitude dynamics. Every configuration (tether sizes, rigid rod element, mass distribution) presents a typical curve, so the optimum coefficient must be evaluated case by case. In this simulation we can see how the motion is much more regular, because it is not still affected by skip-rope dynamics, but anyway the

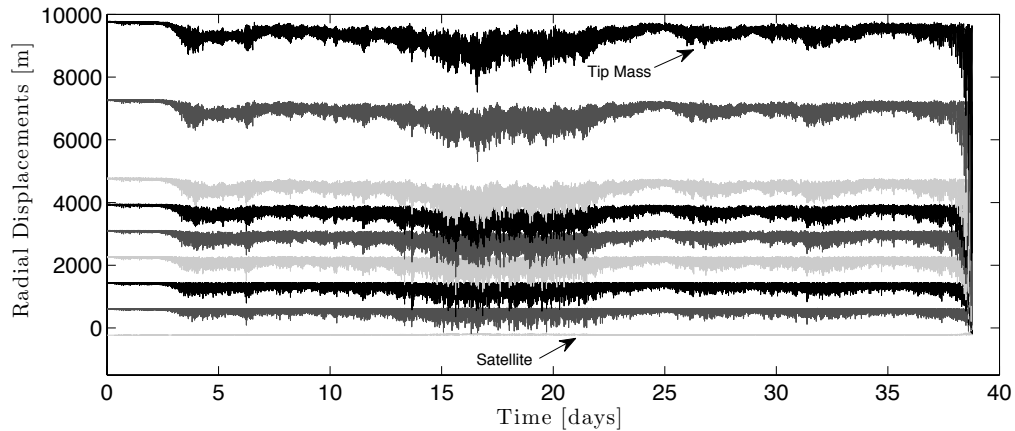


Figure 7.40: Radial displacements - only inert tether

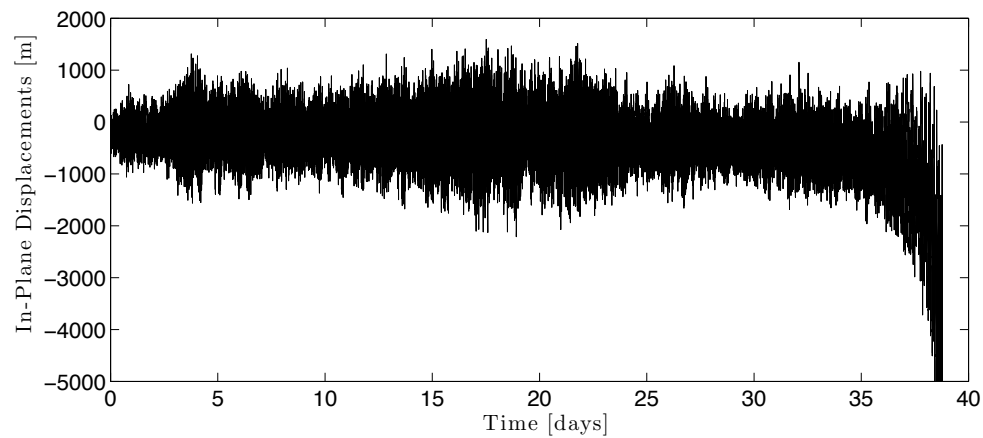


Figure 7.41: In-plane displacements - only inert tether

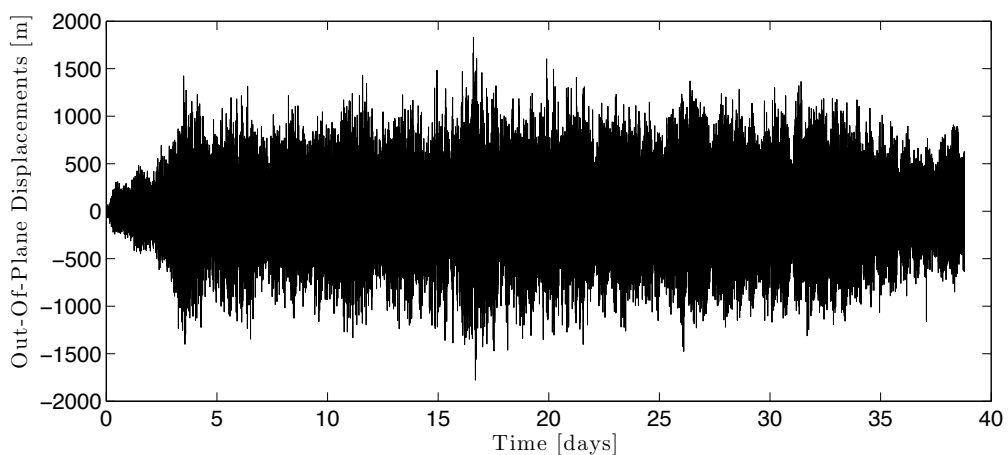


Figure 7.42: Out-of-plane displacements - only inert tether

damper doesn't fulfill the aim and the system becomes instable.

At last, the next figures shown the dynamics of the hybrid system mounting both the inert

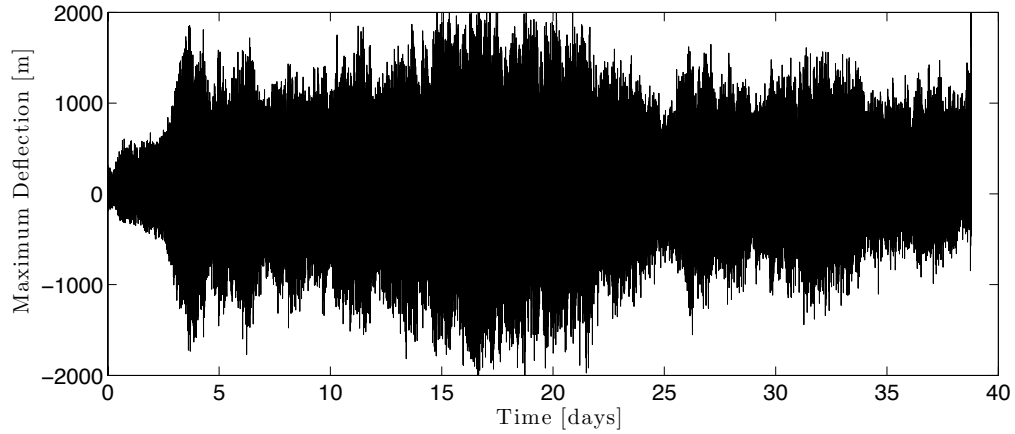


Figure 7.43: Maximum lateral deflection - only inert tether

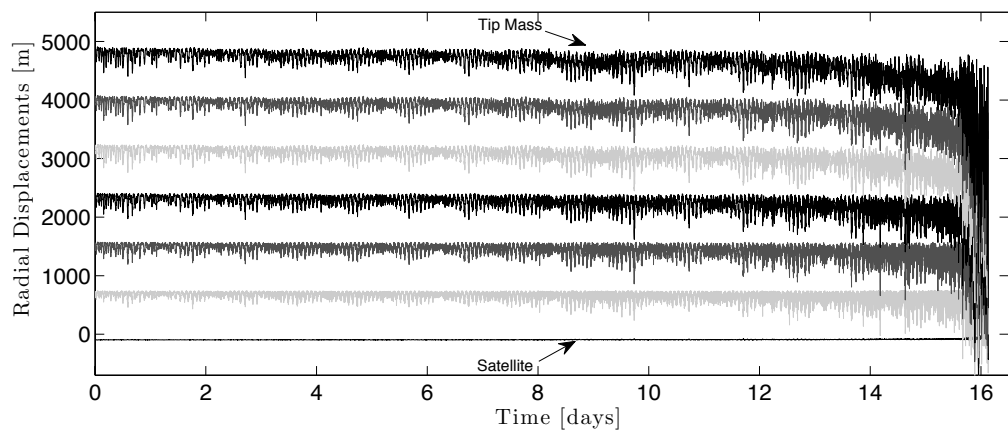


Figure 7.44: Radial displacements - only damper

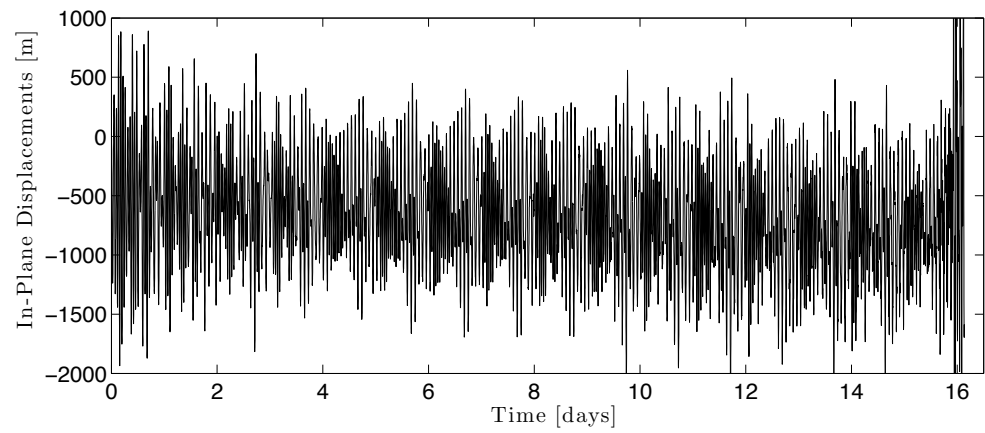


Figure 7.45: In-plane displacements - only inert damper

tether and the damping mechanism, whose coefficient has been chose in proximity of the optimum value. The reentry is faster, approximately 27days, and the dynamics is much smoother and less affected by skip-rope motion, as we can see comparing the maximum deflection of Fig. 7.43 and Fig. 7.52. This simulation has been done for an equatorial orbit, that is better for the stability of the

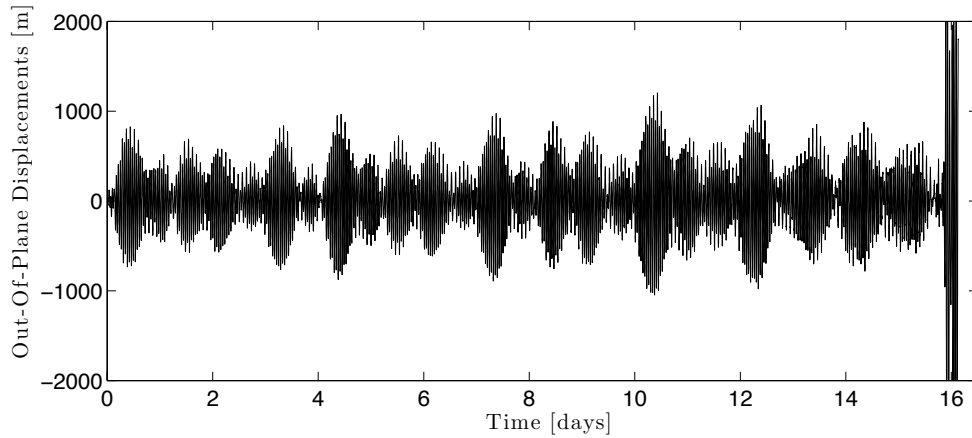


Figure 7.46: Out-of-plane displacements - only inert damper

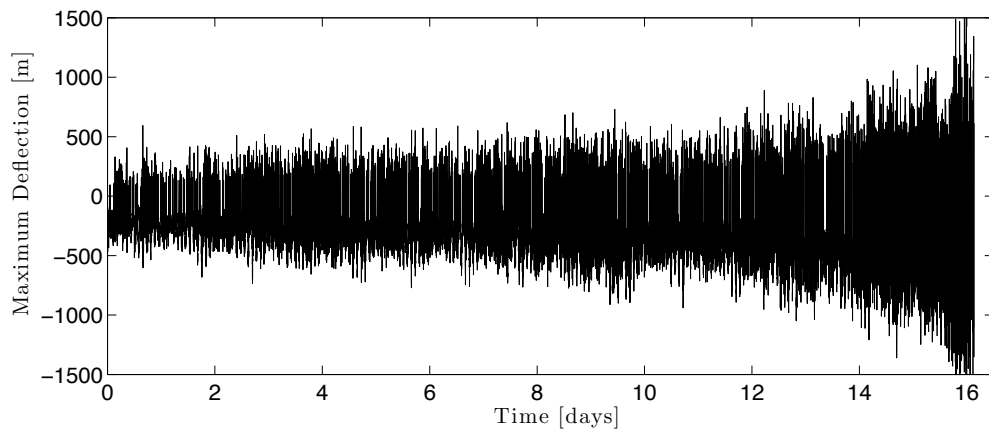


Figure 7.47: Maximum lateral deflection - only inert damper

tethered system than a high inclined orbit, because the Lorentz force maintains a little component along the  $z$ -axis (w.r.t. synodic reference frame) and so out-of-plane motion is less excited.

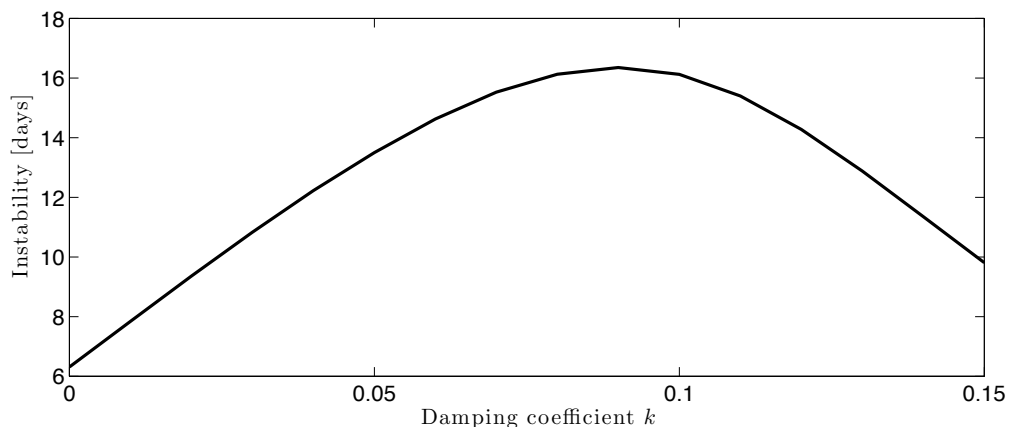


Figure 7.48: Instability versus damping coefficient

As the orbital inclination increases the skip-rope motion becomes more severe and dangerous,

but the damping mechanism helps to dissipate part of the energy accumulated by the wire and maintain the satellite stable. Figures 7.53 report the mean tension and electric current along the wire during the deorbiting and its electric resistance. As already said, tension is a very critical aspect to take into account for the safety of the mission, because it drives the design of the tether geometry. In the simulation the maximum tension, due to the skip rope motion, reaches peaks about 5N.

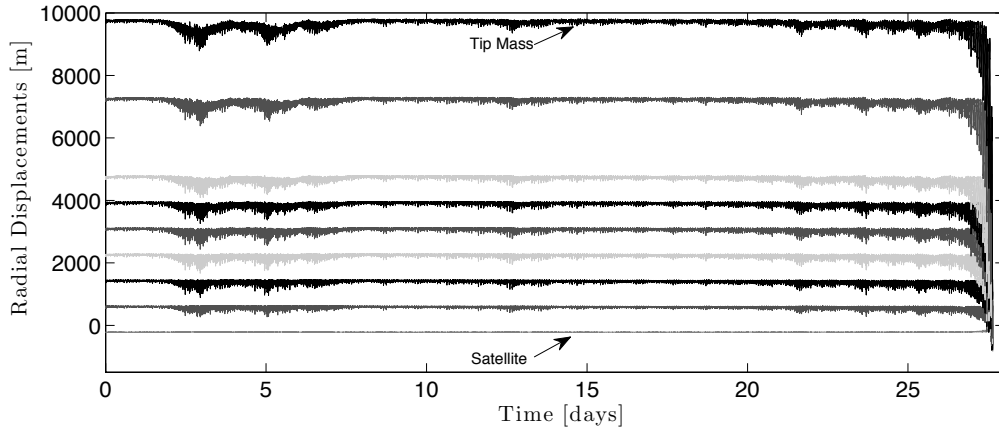


Figure 7.49: Radial displacements - hybrid system

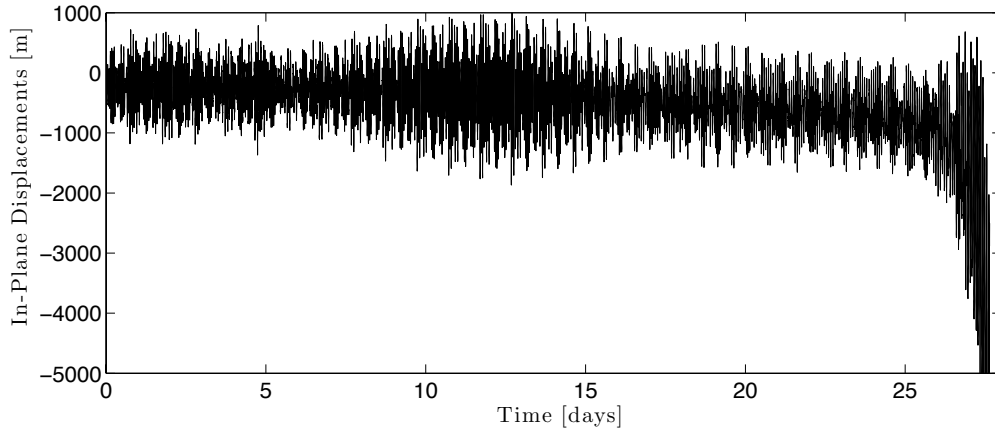


Figure 7.50: In-plane displacements - hybrid system

To conclude this section, Fig. 7.54 shows that the skip rope motion can be noted already in the 2-Bars model. When the flexibility of the wire is introduced and no control is mounted, the two bars (here considered of the same length) tend to move more and more rapidly [70][72]. The skip rope affects the dynamics of the two portions of wire causing very large oscillations bringing the system into instability in very short time.

### Damping Mechanism Design

In literature there are several solutions for passive damping mechanism. They can be divided in two main categories: elastic-damping elements and dampers. In the first group we find pneumatic, hydraulic, electromagnetic and electrodynamic mechanism, and elasto-damping materials. Elasto-damping materials are those that have relatively low elastic moduli, allowing large deforma-

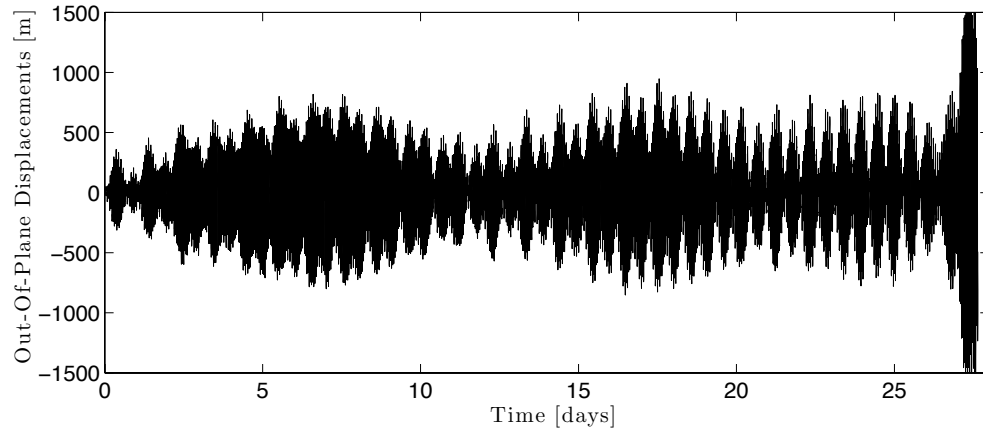


Figure 7.51: Out-of-plane displacements - hybrid system

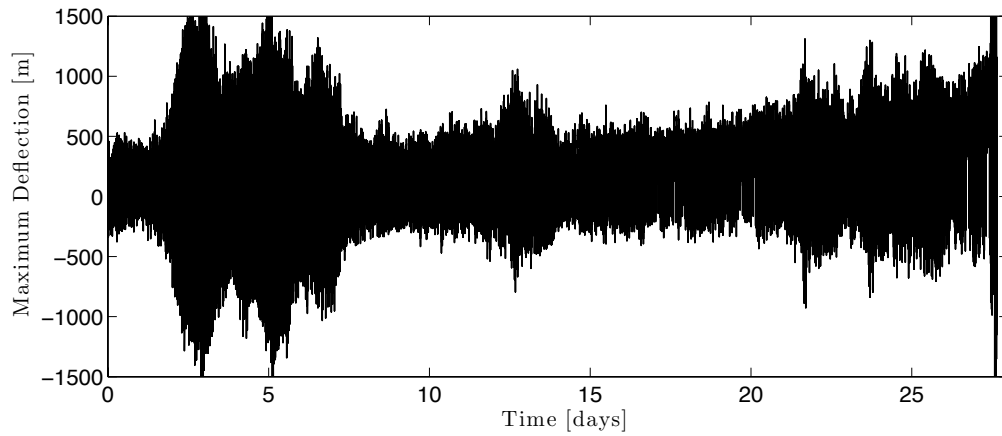


Figure 7.52: Maximum lateral deflection - hybrid system

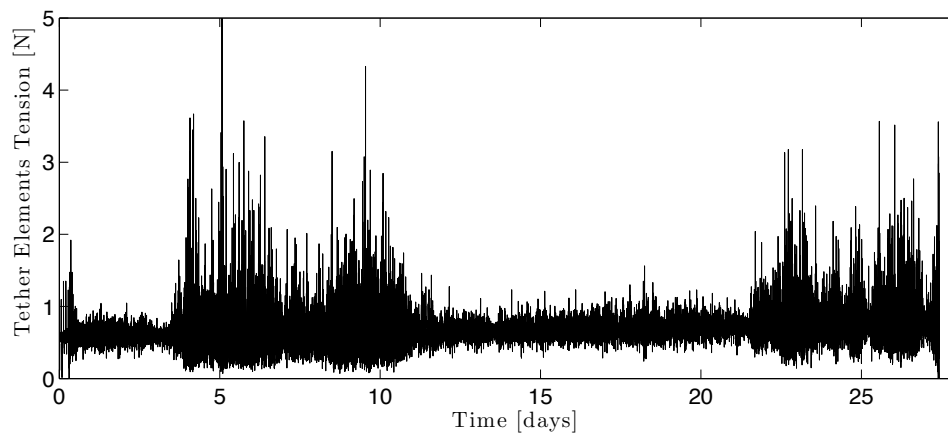


Figure 7.53: Average tension along the tether - hybrid system

tions, and exhibiting relatively high-energy dissipation under solicitations. These materials includes high-damping metals, 3-D meshed or knitted fibrous materials, elastometers (rubbers) and some plastics.

In the latter group there is only energy dissipation without elastic deformation, and encompasses

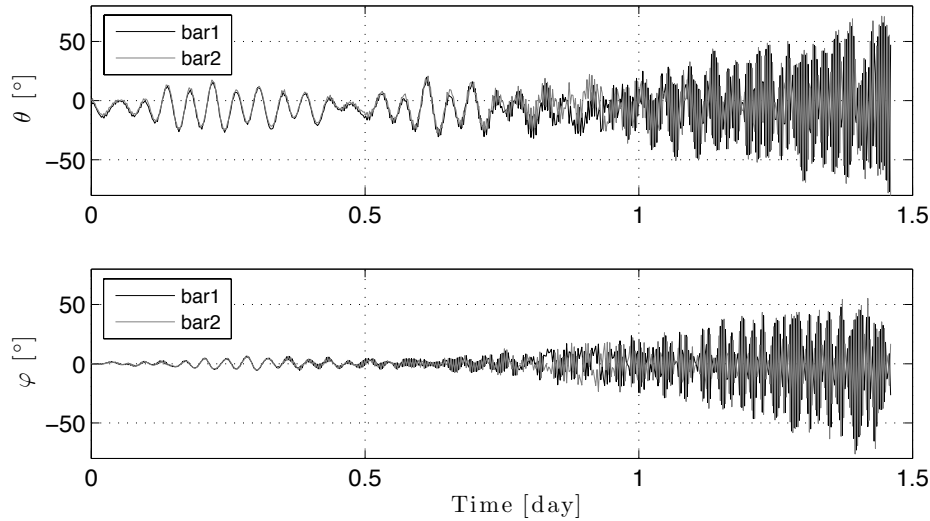


Figure 7.54: Skip rope motion in the 2-Bars model

fluid (viscous) dampers, dry (Coulomb) friction damper and electromagnetic.

Viscous dampers are based on the relative motion between two surface. The damping force is proportional to the velocity of relative sliding between the surface by the viscous coefficient. Dry friction dampers rely on the same idea, but using non-lubrified surfaces. Usually, to guarantee good performance the materials are obtained by sintering from metal and ceramic powder. At last electromagnetic dampers utilize the interaction between a magnetic field (usually from strong permanent magnets) and eddy currents induced in a sold (short-circuited) conductor moving inside the magnetic field. In this case the resistance force is proportional to the velocity of the conductor respect to the magnets.

These are some possible solutions we want to better investigate in order to understand the best for our mechanism. As it has been seen from simulations the damping is really important for two main reasons: it subtracts continuously energy to libration motion and provide stabilization to skip-rope motion. In fact the hybrid system described before is the only to guarantee the complete reentry till high inclinations where the out-of-plane motion is much more critical for the stability, and the damper lets to accelerate the reentry time.

Up to now we thought two main mechanical solutions to realize this mechanism. The former uses a rigid *fishing rode* connecting the wire with the satellite see Fig. 7.39. Such an element has two degrees of freedom respect to the satellite and, thanks to some hinges, it can rotate along two axes. We neglect the third rotation, that could happen respect the longitudinal axis, because no so important for our aim. Hence the friction in the hinges dissipates a little of energy at every oscillations, letting to subtract it from the attitude dynamics of the spacecraft. Then the effectiveness of the damper and stability of the tether are increased by the additional gravity gradient force/torque provided by the inert tether.

The latter foresees to connect the tether to the satellite by means a set of springs and dampers that dissipate energy, see Fig. 7.55. This solution is easier to realize and integrate in the deployer, but the only authority of control is given by the friction coefficient of the dampers, instead by using the fishing rode we can change both the friction at the hinges and the length of the rod to increase the stability. If the displacements of the attachment point are quite wide it can reach higher velocity

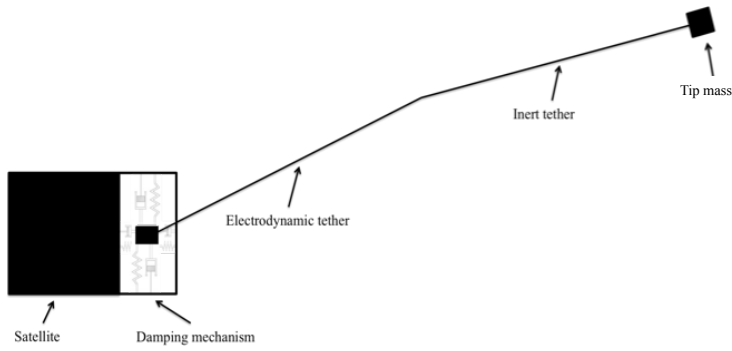


Figure 7.55: Spring-damper with moveable attachment damping mechanism

and so dissipate a major amount of energy. But we have to consider that this point must stay inside a limited range, whose width depends on the stiffness of the springs. So a good design is necessary to find the optimal trade-off. It is important to highlight that the spring-damper mechanism works only along the in-plane and out-of-plane directions, there is already energy dissipation along the longitudinal direction of the tether due to its internal viscosity.

## Results

In this last part we report numerical results obtained with the orbital simulator for some specific cases. Parametric simulations have been run in order to show the capabilities of EDT system to deorbit a satellite by using the extensible flexible model. Specifically, the results show the complete reentry always from an altitude of 1000km for various orbital inclinations. The following pictures show the results varying the orbital inclination from  $0^\circ$  to  $75^\circ$  and considering several configuration of the tape/wire: two different conductive lengths (3 and 5 km) and width (1 and 2 cm) while the tape thickness is equal to  $30\mu\text{m}$ . In Fig. 7.56 a 500kg mass was assumed for the satellite and a conservative 20 kg for the tip mass. As already said the tip mass is also important for stability (see Fig. 7.2) because it helps maintaining the center of mass of the whole system sufficiently close to the electrodynamic center of pressure. For each configuration we assumed an inert tether length equal to the electrodynamic portion in order to double the gravity gradient force and quadruple the torque.

At low inclinations all the configurations work very well and provide fast reentries for both short and long tethered systems: for the shorter 3km long wire the deorbiting time is approximately two months and half. As expected, at high inclination the decay time becomes longer for short tethers but it continues to be rather short for the 5km long wires. For example at  $75^\circ$  inclination, with a 3km long and 1cm wide tape the deorbiting takes approximately 170 days to complete, and with a 5km long and 2 cm wide tape it takes about 70 days.

Instead, Fig. 7.57 depicts the 1000kg case, mounting a tether 1cm wide and  $50\mu\text{m}$  thick. The results are interesting because doubling the mass of the satellite the reentry time should double, too. But if we properly augment also the thickness of the tether then the collection area will remain more or less the same, while the electric resistance decrease a lot, but so the time required for the maneuver doesn't change so much with respect to the previous case.

In particular till  $30^\circ$  the deorbiting takes less than three months, but as the orbital inclination increases the required time augments rapidly, exploding in the 3km case. In fact already for incli-

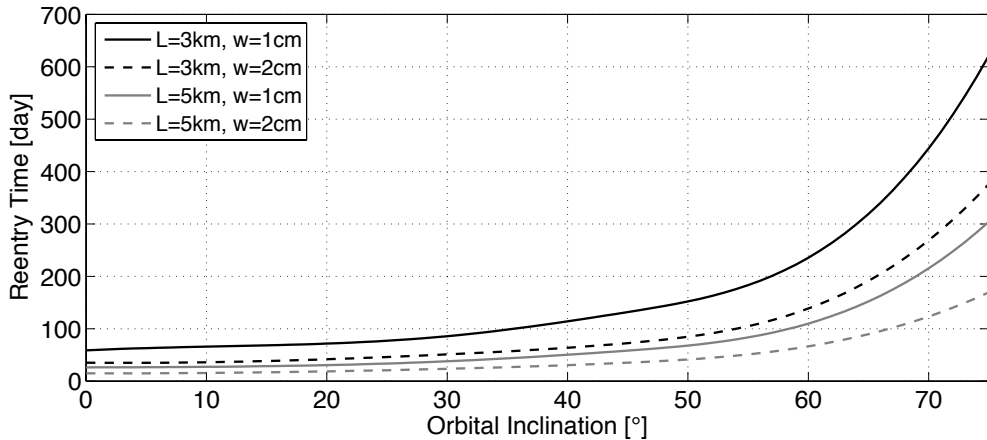


Figure 7.56: Reentry time for different configurations of tether size: mass satellite  $m_{sat}=500\text{kg}$

nation higher than  $65^\circ$  the decay maneuvers takes more than a year, and this can be dangerous for exposition to the space environment and, hence the risk of space debris impact.

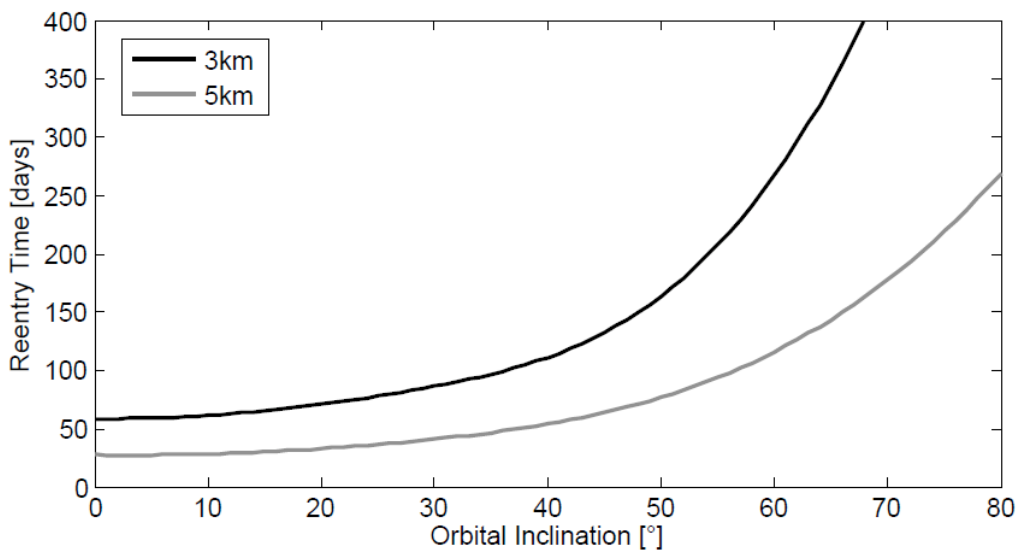


Figure 7.57: Reentry time for different configurations of tether size: mass satellite  $m_{sat}=1000\text{kg}$

Another interesting aspect to investigate is how the reentry time changes varying the initial orbital altitude. In fact, the relation is non-linear since performance depends on the electron density of the ionosphere, which has a peak at low altitudes (300-400 km), and then decreases with increasing altitude. Figures 7.58-7.60 clarify this trend: at low altitudes the reentry is very fast while, for high LEO, the deorbiting takes longer, yet still comparatively fast, because the electron population decreases with altitude.

The main advantage of an EDT system is that it is a propellantless device and so, even if the deorbit starts from high altitudes, the mass of the system does not change. The figures show the time required to complete the manoeuvre, that indeed is longer than by using chemical thrusters but, requiring only a few months, is much smaller than the 25 year time indicated in the guidelines. Electrodynamic systems are a long way ahead in terms of performance than any neutral drag

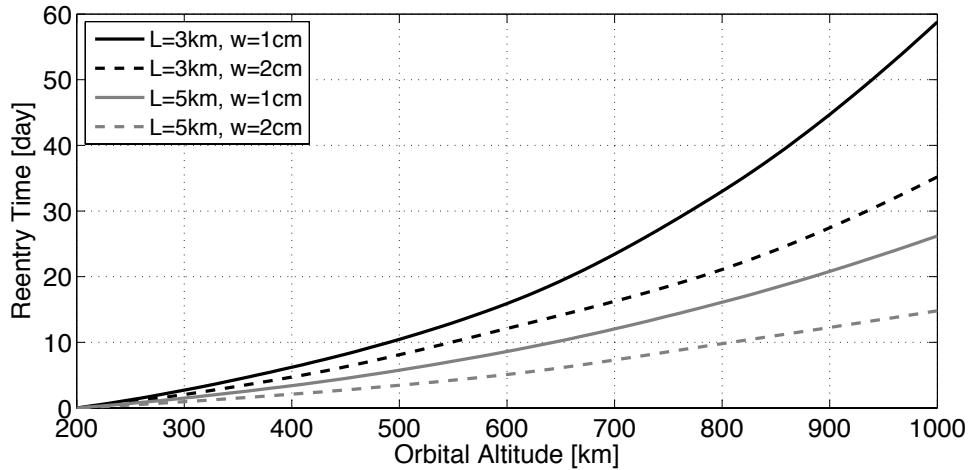
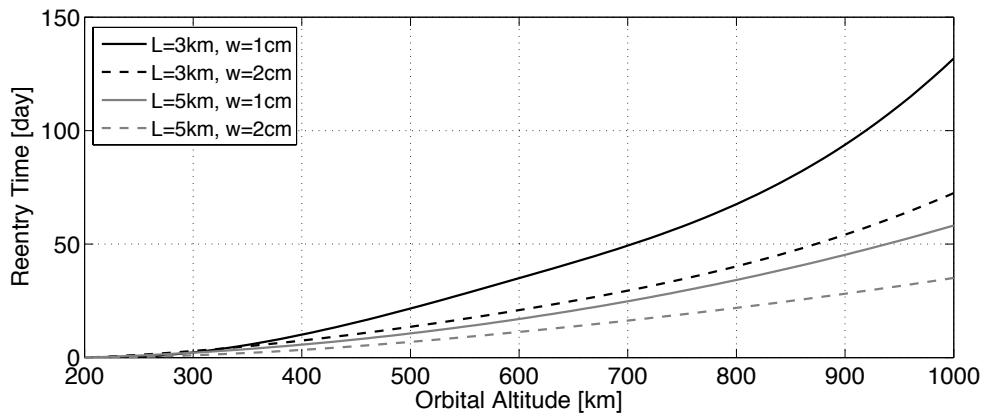
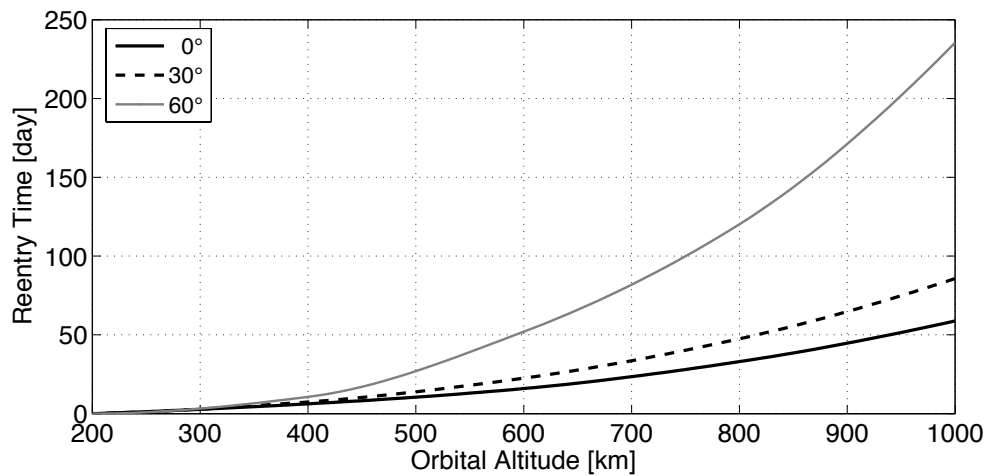
Figure 7.58: Reentry time as a function of altitude: orbital inclination  $0^\circ$ Figure 7.59: Reentry time as a function of altitude: orbital inclination  $60^\circ$ 

Figure 7.60: Reentry time as a function of altitude: ED length = IN length = 3 km, width = 1 cm

augmentation devices that are only effective at very low altitudes. Moreover, the electrodynamic system saves fuel when compared to thrusting systems and increasingly so for satellites that are

heavy and operating in high LEO. EDT systems are competitive on the basis of mass savings, when compared to chemical thrusters, for deorbiting satellites operating between 700-1500 km of altitude, while the neutral drag augmentation devices are ineffectual in that altitude range. Moreover, the mass savings increases as a function of altitude and spacecraft mass, while the time for reentry is always much shorter than the duration specified in the guidelines. The propellantless characteristic and the ability to produce sizeable Lorentz forces make these devices very interesting for deorbiting spacecraft at the end of life.

### Jason Mission

Jason-3 is an oceanographic mission, involving a quadripartite collaboration between the two meteorological organizations Eumetsat and NOAA, CNES and NASA, and will allow the continuity of high precision ocean topography measurements beyond TOPEX/Poseidon, Jason-1 and Jason-2, which are now operational in orbit. Jason 3 will offer the same ocean measurement accuracy as Jason 2, including near coastal zones, as well as lakes and rivers.

The satellite will be placed in the same orbit as Jason-2, at an altitude of 1336 kilometres with an inclination of 66 degrees, to provide virtually blanket coverage of all ice-free ocean surfaces. Its weight at launch is 553 kg. Its launch is expected for mid 2013 for a mission life of 3 years.

The orbital simulator has been used to simulate the reentry of Jason at the end of the mission by means of an electrodynamic tether. It is a critical case for such solution, because the initial orbital altitude is very high and the electron density low. Moreover the orbital inclination is very high, too, so the motional electric field component along the wire becomes little, and this means low electric current. The values of each parameter of the whole system are reported in the following table.

$m_{sat}$	$m_B$	$w$	$h$	$L_{ED}$	$L_{IN}$
500kg	20kg	1cm	100 $\mu$ m	5km	10km

Table 7.4: Jason mission: tethered system configuration

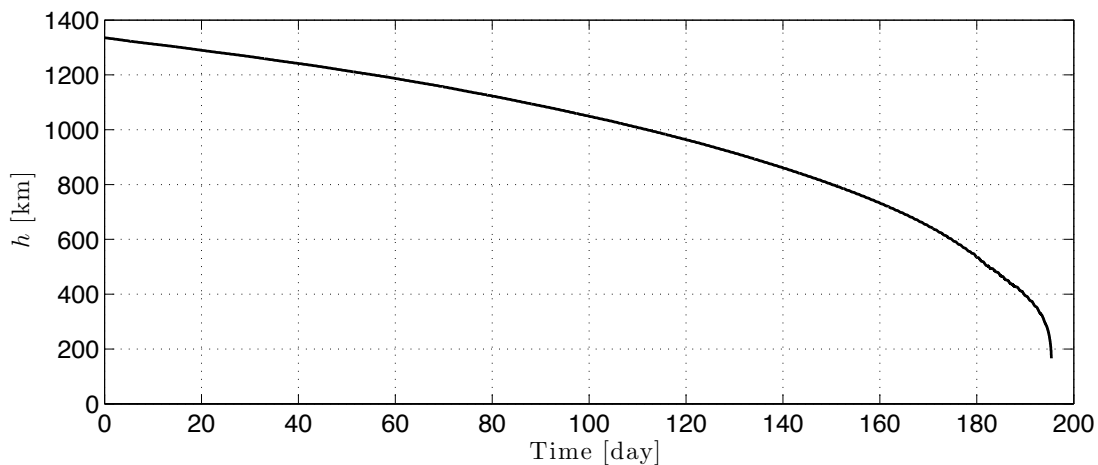


Figure 7.61: Jason mission: orbital altitude

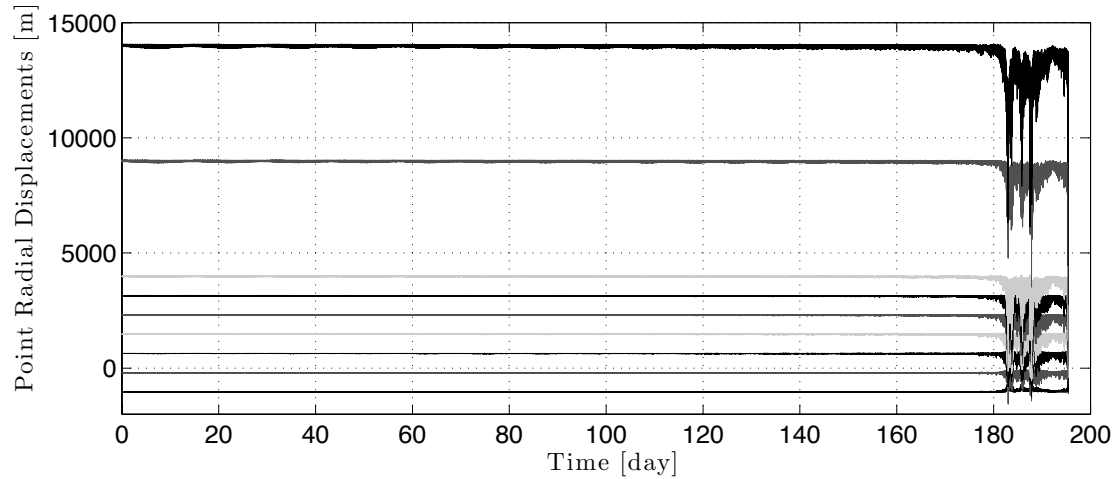


Figure 7.62: Jason mission: radial displacements of the lump masses

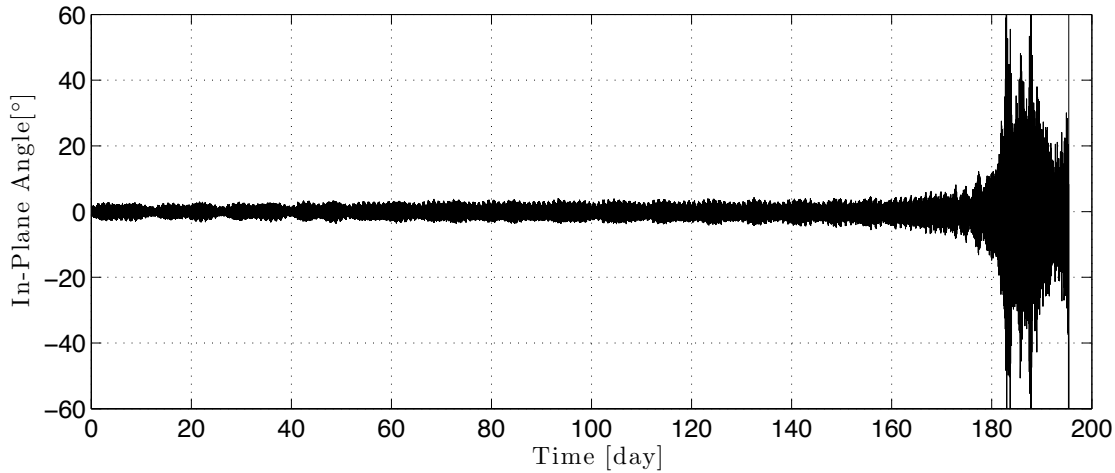


Figure 7.63: Jason mission: in-plane angle

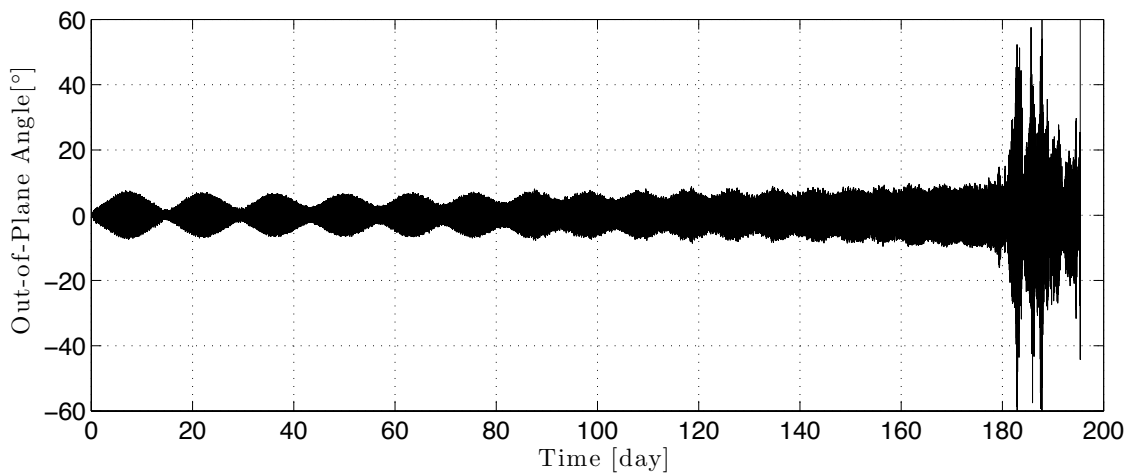


Figure 7.64: Jason mission: out-of-plane angle

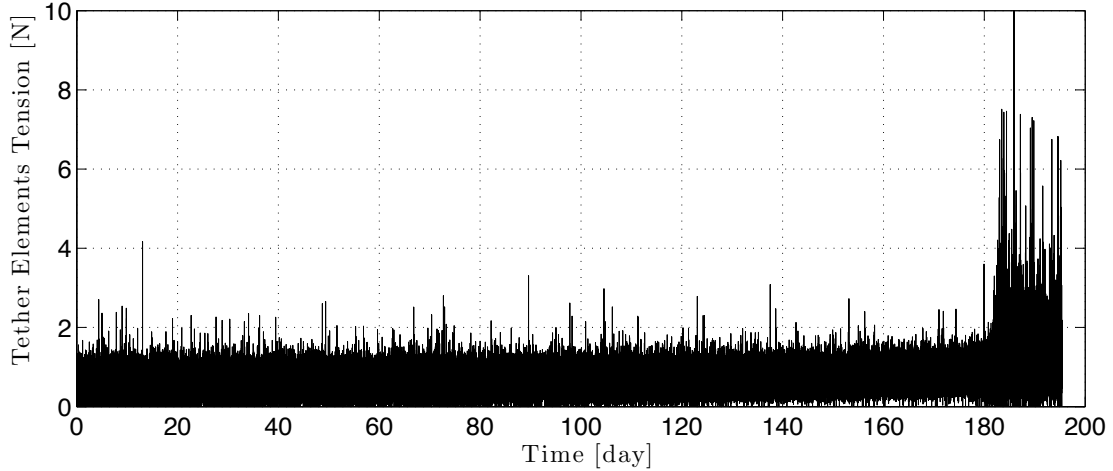


Figure 7.65: Jason mission: mean tension along the wire

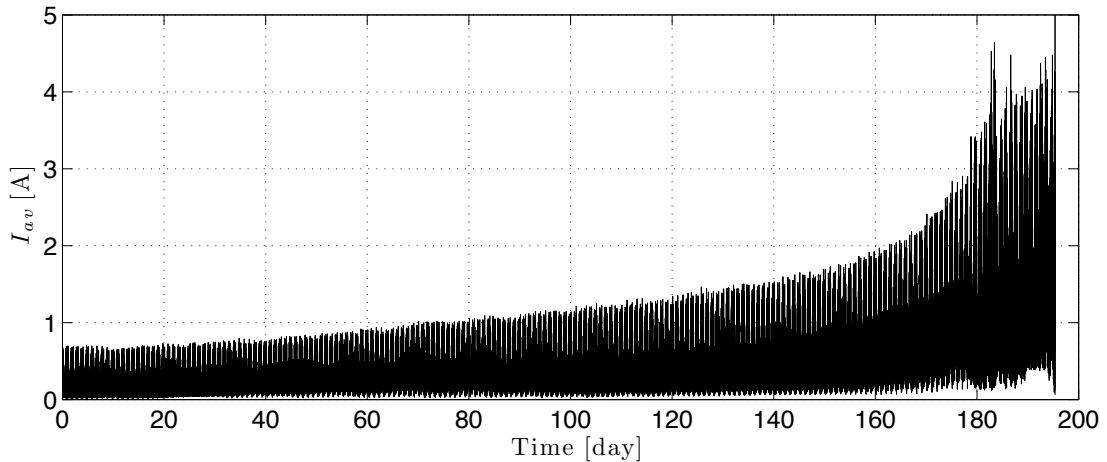


Figure 7.66: Jason mission: electric current

Figures 7.61-7.67 illustrate the results of the simulation. Even if the tether used is long and thick the maneuvers requires more than six months to reenter. In particular the satellite need 110 days to arrive at an altitude under 1000km. That's why the electron density at high quotes is very low and the electric current (see 7.66) doesn't overcome 1A in the sunlight region. At last Fig. 7.67 shows the variation of the orbital inclination and eccentricity. The inclination changes because perturbed by the out-of-plane component of the Lorentz force, which tends to increase it.

### Attitude of the Spacecraft

Another important aspect to consider is the attitude of the satellite, that is perturbed by the tension  $Y$  along the wire. In fact the tether is fixed to the deployer, which is displaced respect to the center of mass of the spacecraft, so the tension acts on it in two ways: the former lets it orbits around the Earth with the same angular velocity of the whole tethered system, while the latter generates a torque  $M_Y$  that affects the stability of its attitude.

In order to include also this dynamics, other two reference system are here defined. The orbital reference frame has the  $y$ -axis in the opposite direction to the angular momentum of the orbit, the

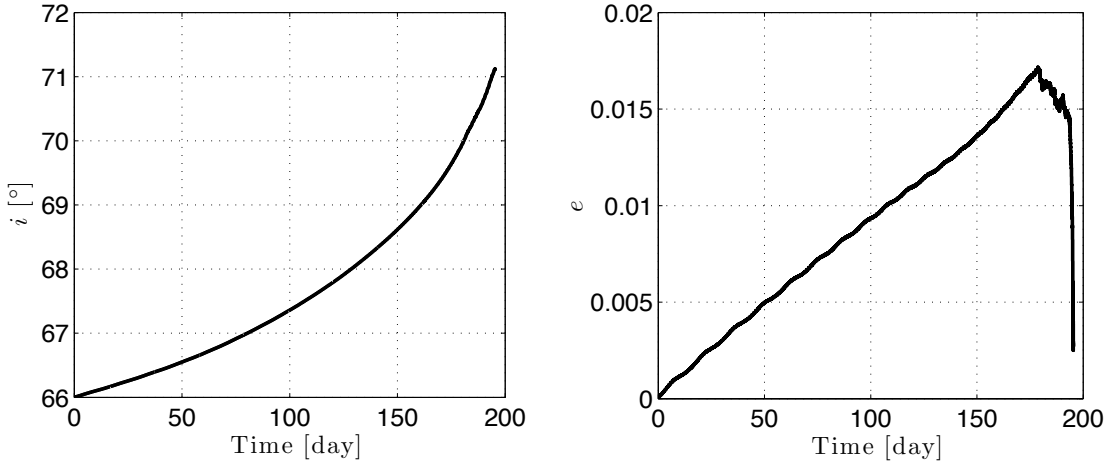


Figure 7.67: Jason mission: variations of the orbital inclinations and eccentricity during the deorbiting

$z$ -axis along the local vertical, and the  $x$ -axis to close the tern. The rotation matrix from the synodic reference frame to the orbital one is:

$$[R]_S^O = \begin{bmatrix} 0 & 1 & 0 \\ 0 & 0 & -1 \\ -1 & 0 & 0 \end{bmatrix}$$

Instead the satellite body reference frame can be evaluated introducing the Euler's angle  $\gamma$ ,  $\vartheta$  and  $\psi$ . They define three rotations that let to arrive from the orbital reference frame at the satellite body one. The sequence used is the 3→2→1: three rotations  $\psi$ ,  $\vartheta$  and  $\gamma$  around  $z$ ,  $y$  and  $x$ , respectively.

$$\begin{aligned} [R]_\psi &= \begin{bmatrix} \cos \psi & \sin \psi & 0 \\ -\sin \psi & \cos \psi & 0 \\ 0 & 0 & 1 \end{bmatrix} \\ [R]_\vartheta &= \begin{bmatrix} \cos \vartheta & 0 & -\sin \vartheta \\ 0 & 0 & 1 \\ \sin \vartheta & 0 & \cos \vartheta \end{bmatrix} \\ [R]_\gamma &= \begin{bmatrix} 1 & 0 & 0 \\ 0 & \cos \gamma & \sin \gamma \\ 0 & -\sin \gamma & \cos \gamma \end{bmatrix} \end{aligned}$$

So the rotation matrix from  $[R]_O^{BSC}$  will be:

$$[R]_O^{BSC} = [R]_\gamma [R]_\vartheta [R]_\psi$$

$$[R]_O^{BSC} = \begin{bmatrix} \cos \psi \cos \vartheta & \cos \vartheta \sin \psi & -\sin \vartheta \\ -\cos \gamma \sin \psi + \cos \psi \sin \vartheta \sin \gamma & \cos \psi \cos \gamma + \sin \psi \sin \vartheta \sin \gamma & \cos \vartheta \sin \gamma \\ \cos \psi \cos \gamma \sin \vartheta + \sin \psi \sin \gamma & \cos \gamma \sin \psi \sin \vartheta - \cos \psi \sin \gamma & \cos \vartheta \cos \gamma \end{bmatrix}$$

Supposing that the body reference frame chosen is the maximum inertia one, the angular momentum of the satellite  $\vec{H}_{sat}$  is expressed by:

$$\vec{H} = [I] \vec{H}_{SC} = \begin{pmatrix} I_x \omega_{SC_x} \\ I_y \omega_{SC_y} \\ I_z \omega_{SC_z} \end{pmatrix}$$

and its variation due to the external perturbations is given by:

$$\vec{H}_{sat} - \vec{\omega}_{SC} \times \vec{H}_{sat} = \vec{M}_{gr} + \vec{M}_Y \quad (7.24)$$

that provide the Euler's equations:

$$\begin{cases} I_x \dot{\omega}_{SC_x} + I_y I_z (\omega_{SC_z} - \omega_{SC_y}) &= M_{gr_x} + M_{Y_x} \\ I_y \dot{\omega}_{SC_y} + I_x I_z (\omega_{SC_x} - \omega_{SC_z}) &= M_{gr_y} + M_{Y_y} \\ I_z \dot{\omega}_{SC_z} + I_x I_y (\omega_{SC_y} - \omega_{SC_x}) &= M_{gr_z} + M_{Y_z} \end{cases} \quad (7.25)$$

where  $\vec{\omega}_{SC}$  is:

$$\vec{\omega}_{SC} = \begin{pmatrix} \omega_{SC_x} \\ \omega_{SC_y} \\ \omega_{SC_z} \end{pmatrix} = \begin{pmatrix} \dot{\gamma} - \dot{\psi} \sin \vartheta - \omega_{orb} \sin \vartheta \\ \dot{\vartheta} \cos \gamma + (\dot{\psi} + \omega_{orb}) \cos \vartheta \sin \gamma \\ (\dot{\psi} + \omega_{orb}) \cos \vartheta \cos \gamma - \dot{\vartheta} \sin \gamma \end{pmatrix}$$

The torques  $\vec{M}_{gr}$  and  $\vec{M}_Y$  are:

$$\vec{M}_{gr} = 3\omega_{orb}^2 \begin{pmatrix} (I_z - I_y) \cos \gamma \sin \gamma \cos \vartheta^2 \\ (I_z - I_x) \cos \vartheta \sin \vartheta \cos \gamma \\ (I_x - I_y) \cos \vartheta \sin \vartheta \sin \gamma \end{pmatrix}$$

$$\vec{M}_{tens} = \vec{d} \times \vec{Y}$$

while  $\vec{d}$  is the vector from the barycenter of satellite to the deployer, where the tension acts.

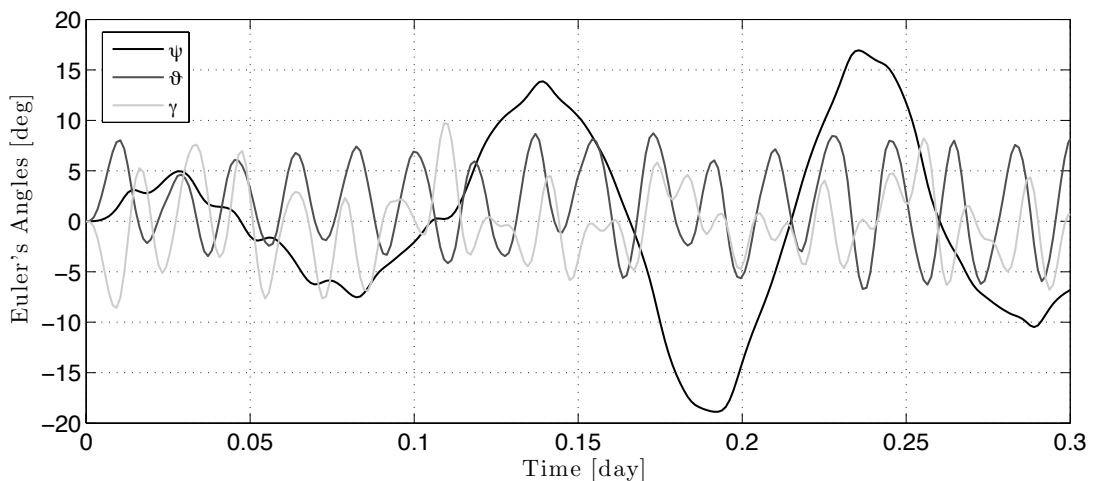


Figure 7.68: Satellite attitude described by Euler's angles

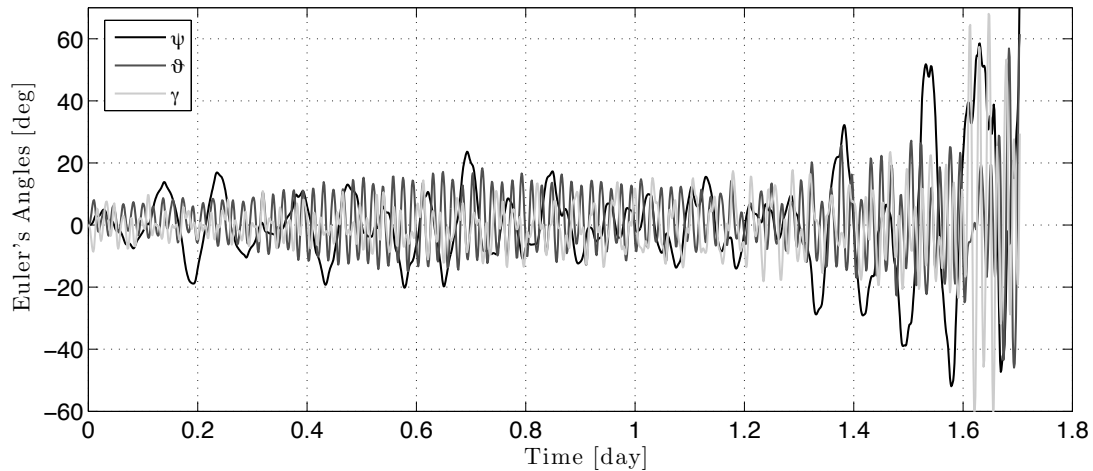


Figure 7.69: Uncontrolled satellite attitude

Figure 7.68 shows an example of attitude dynamics, where the motion of the three angles is reported. The  $\psi$  angle is the more perturbed, and describes larger oscillations at lower frequency than  $\vartheta$  and  $\gamma$ .

Without any control the attitude goes quickly into instability since the gravity gradient torque is not sufficient to compensate the disturbing action of the tension, hence provoking the rotation of the satellite around its center of mass (see Fig. 7.69). So the control system must be maintained active also during the deorbiting in order to assure stabilization and avoid the risk that tether is cut touching the surface of the satellite.

# Chapter 8

## Deployment Strategies

Tether deployment is a very critical issue, because on it depends the success of the mission, and electrodynamic deorbiting. Deploying a relatively-wide tape tether will require the development of a specialized deployer design which in turn establishes the maximum velocity and acceleration that the deployer can sustain.

### 8.1 Deployment strategies

Deployment strategies are determined by orbital conditions and the state of the tether system at the end of the maneuver. A librating deployment is most suitable for a system that has to end up aligned with the local vertical. Conversely, a spinning deployment is the natural choice for a system that needs to spin after deployment is complete. A librating deployment requires a relatively strong gravity gradient (e.g., in LEO with relatively long tethers) to keep the tether straight and bound to librate (or stay aligned) with the local vertical. Gravity gradient is not an issue for spinning deployments because centrifugal forces provide the tether tension.

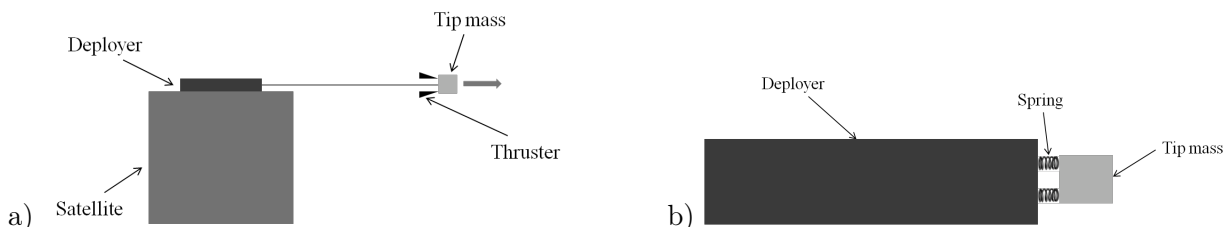


Figure 8.1: Librating deployment: a) ejection by thruster, b) ejection by springs

Tether deployments in flight missions have thus far taken place in Low Earth Orbit (LEO) and utilized the librating-deployment strategy. In a librating deployment there are no significant centrifugal forces (due to spin) and the tether tension may need to be increased in the early stages of deployment or even throughout deployment by, for example, a thruster firing along the tether line. Alternatively, one can reduce the time spent at short tether length by ejecting the tip mass at relatively high speed and very low tension in close-to-free-flying conditions and slowing the velocity down later on.

In a spinning deployment, centrifugal forces generated by the spin provide the tether tension to facilitate the extraction of the tether from the deployer. A spinning deployment is usually faster than a librating deployment because there are no limits imposed on the tether exit velocity by librational stability considerations. Spinning deployments have not been tested in space yet but

they have been studied by several authors (see for example [41][59][62][63][79]) and their realization is expected to be rather straight forward.

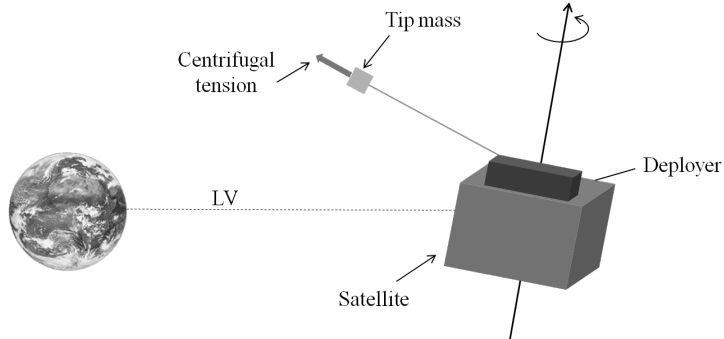


Figure 8.2: Spinning deployment

The BETs system is planned for deorbiting satellites with a wide range of masses. A spinning deployment will require the mother satellite to follow the rotation of system, not only during deployment but also afterwards, that is throughout deorbiting, as the spin rate will change over time. While it is conceivable, although not desirable, that the satellite spin is controlled during the relatively short deployment, we can not expect that the satellite will be controlling its spin throughout deorbit to follow the changing spin rate of the tether system. This consideration is especially compelling for heavy satellites with large moments of inertia. For light satellites with small moments of inertia, we can envision that the spinning tether system could apply enough torque, through its attachment point offset from the satellite center of mass, to drive the satellite spin to follow that of the tether system. A hanging system will have a broader range of utilizations, although spinning systems can not be ruled out for very light systems. We will focus on deployment for hanging systems in what follows.

Deployment of tethered systems is carried out by utilizing stationary (passive) or reeling (active) deployers. When designed properly, a stationary deployer is lighter and simpler than a reeling deployer. Active deployers must be used for systems that need to be retrieved (e.g., TSS missions), for systems in which the tether length must be shortened during the mission or in cases where the tether has a geometry not suitable for being spooled into a stationary spool to be unravelled. In many other cases, a passive deployer is well suited for deploying the tether and keeping the tether length constant. Stationary deployers were used successfully for the SEDS and PMG missions, which utilized cylindrical tethers.

The other distinguishing factor for deployers is the mechanics. Active deployers can utilize a drum and a leveling mechanism (if necessary) to reel out the tether. Passive deployers use a stationary spool whereby the tether unravels from the spool along the spool's axis. This type of deployers (e.g., the SEDS deployer) cannot retrieve the tether but they are very simple and light. Moreover, in a stationary spool the only moving mass is the exiting portion of the tether mass and, consequently, the tether can tolerate sudden accelerations without incurring high tensions. On the contrary, in a reeling deployer the whole moment of inertia of the drum and spool come into play when the tether speed changes and strong tensions are unavoidable following strong accelerations. This consideration implies that a spring ejection system that imparts a strong initial acceleration is not suitable in conjunction with a reeling deployer but it is suitable for a stationary-spool deployer.

## 8.2 Past Flight Experience

Let us look at some of the control strategies utilized for deployment in past tether missions. The NASA/ASI TSS missions (TSS-1 in 1992 and TSS-1R in 1996), which deployed from the space Shuttle, used a velocity control technique that was well-suited for the motorized deployer of those missions (see 8.3). In this case, the tether exit-velocity was controlled to follow a deployment trajectory computed before the flight. The deployment trajectory (velocity vs. time) was designed to provide a small-amplitude libration about LV at end of a deployment maneuver that lasted about 6 hours to unravel a 20-km-long tether system.

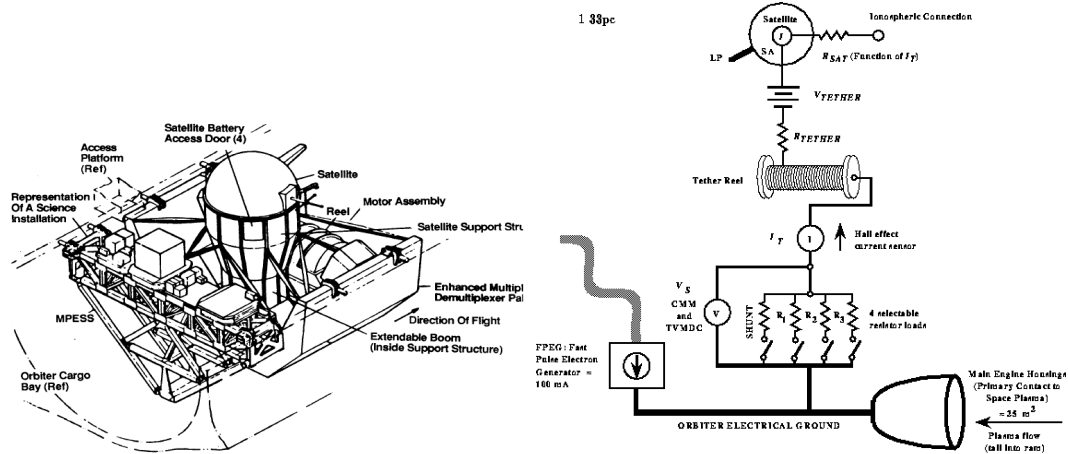


Figure 8.3: TSS missions

The NASA SEDS missions (SEDS-I in 1993 and SEDS-II in 1994) also deployed (non-conductive) tethers of 20-km length each from the second stage of a Delta rocket left in orbit. The two SEDS missions had very different deployment requirements. SEDS-I needed to reach the widest possible amplitude at end of deployment and utilized the back swing to provide a  $\Delta V$  to deorbit the tip mass that was separated from the tether at the crossing of LV. SEDS-I simply ejected the tip mass with the desired velocity vector and then applied an open-loop brake control to reduce the exit speed at the end of deployment.

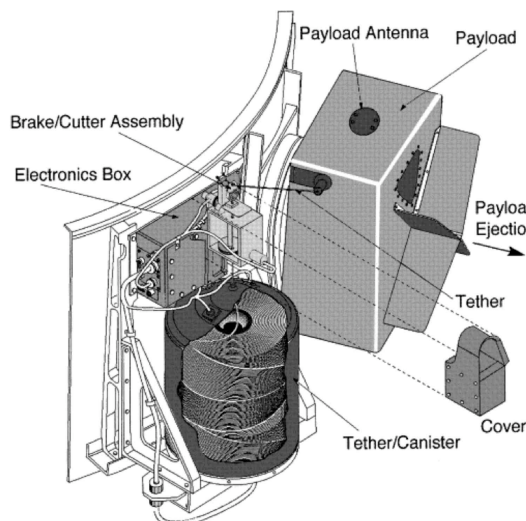


Figure 8.4: SEDS missions

SEDS-II mission was designed for testing a quick and accurate deployment with a small-amplitude libration at the end of the maneuver. Deployment took 1 hour and 15 minutes to deploy a 20-km-long tether and attained a maximum libration amplitude of less than  $4^\circ$ . The controller utilized an ideal pre-computed deployment trajectory capable of providing the desired deployment time and small-amplitude librations. The SEDS deployer was a passive deployer that could not control the exit velocity directly but had a (very non-linear) brake that could increase or decrease the tether exit friction. The non-linearity of the brake was eliminated by using the technique of input-output linearization, that is, at the ideal deployment trajectory (length and velocity vs. time) was associated an ideal braking profile (number of brake turns vs. time). A linear feedback loop was then used to adjust the ideal brake profile as a function of the departure of the actual deployment (length and velocity) from the ideal deployment profile. The strategy proved to be very robust to changes in the frictional characteristic of the brake and the deployment strategy worked very well in flight.

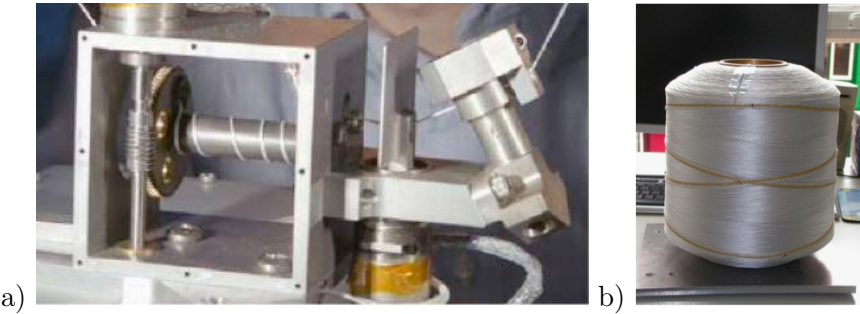


Figure 8.5: SEDS missions: a) brake mechanism, b) tether spool

The ESA Young Engineers Space mission (YES2) deployed a 32 km of non-conductive tether in 2010. The goal of the YES2 mission was like the one of SEDS-I that is to provide the necessary  $\Delta V$  to the tip mass to make it reenter the atmosphere. The difference between the two missions was that the tip mass of YES2 was a reentry capsule to be retrieved on the ground after reentry. YES2 utilized a modified design of the SEDS deployer and a new type of control law. The control strategy was aimed at maximizing the amplitude of the system at the end of deployment. The control law used a two-stage technique with a smaller-amplitude swing at a short tether length and a large-amplitude swing at the end of the second phase. This strategy was aimed at making the deployment robust and timing accurately the crossing of the local vertical during the back swing of the tether in order to provide a small foot print of the reentry capsule. The system did deploy more than 30 km of tether, that is the longest structure deployed in space, but the deployment resulted to be rather inaccurate and unfortunately the reentry capsule could not be located on the surface of the Earth.

At last Fig. 8.6 - 8.7 provide a brief list of all the tethered mission flown in up to now.

### 8.3 Deployment study plan

The tradeoff analysis and prototyping conducted at DLR-Bremen (see next section 8.4) concluded that a non-motorized reeling deployer is well suited for a 1-3 cm wide tape like the tapes planned for BETs. In case of a tape, a reeling system (see for example [46]) is preferable to a stationary spool because the relatively-wide tape could be twisted while exiting along the axis of the stationary spool and is likely to produce high friction or even to cause jamming. Consequently, we focused on

Year	Mission	Main	Typ	Objective	Technology	Length	Results	Remark	Ref.
1966	Gemini-11	NASA	D	Mechanical link between Gemini and Athena. Artificial gravity (Tethered capsules set in rotation), Gravity gradient stabilization	15-m tether between capsules	15m	Successful deployment and stable rotation Stable swing, Local vertical	LEO, Spin stable 0.15 rpm, Manne with manual control, 0.00015g (Artificial)	NASA 1967
1966	Gemini-12				30-m tether between capsules Tethered capsules set in rotation	(0.036) 0.04km			NASA 1967
1980	TPE-1 (K-9M-69)	ISAS	ED	Plasma interaction and VHF wave generation	Conductive tether	0.04 of 0.4km	Partial deployment	Suborbital	Sasaki 1987
1981	TPE-2 (S520-2)	ISAS	ED	Plasma interaction and VHF wave generation	Conductive tether	0.07 of 0.4km	Partial deployment	Suborbital	Sasaki 1987
1983	Charge-1	NASA / ISAS	ED	Plasma interaction and VHF wave generation	conducting tether, Cold gas assisted	0.418km	Partial deployment	Suborbital	Sasaki 1988
1985	Charge-2					0.426km	Full deployment		
1986	Space Shuttle Challenger disaster								
1988	ECHO-7	ESA	ED	Magnetic field aligned	Electrons and ions 30eV to 30KeV	unknown	unknown	Suborbital	
1989	Oedipus-A	CSA	ED	Ionospheric science EDI/Plasma Physics	9.58m conducting tether, spinning, spin rate 0.7 rpm, Spool type reel, Teflon coated stranded tin-copper wire of 0.85mm diameter , Cold gas assisted, Passive reel,	0.959 km	Successful EM coupling between conducting tether ends through tether-guided wave modes Obtained data on behavior of tethered system as large double electrostatic probe	Suborbital	Tyc 1995 Vigneron 1997
1992	Charge-2B	NASA/ISAS	ED	Plasma interaction and VHF wave generation	400m conducting tether, Cold gas assisted	0.4km	Full deployment	Suborbital	Sasaki 1994 Raitt 1995
1992	TSS-1	NASA	ED	Electrodynamic Shuttle missions.	20-km insulated conducting tether to study plasma-electrodynanic processes and tether orbital dynamics, Active reel deployment, Controlled retrieval of tether,	0.268 of 19.6 km	Tether deployment stopped after 0.260 km, deployer jammed due to the too-long bolt Demonstrated stable dynamics of short tethered system	LEO	Dobrowolny 1994
1993	SEDS-1	NASA	D	Momentum Exchange	0.75mm Spectra 1000 tether (750+ N) 8 strands of fibers into a hollow braid, Winding (* Criss-cross, *Cone), Mechanical brake + spool, Tensionmeter (0.15-7.5 N), "Barbar pole" brake, passive damping, a thread tie-down, Simulator (Beadsim)	20km	Successful, Controlled stable deployment of tether, Demonstrated deorbit of payload, Downward deployment, Rebound well damping (40 N), 20-km nonconducting tether and released it into suborbital trajectory,	LEO	Carroll 1993 AIAA 93-4764
1993	PMG (Plasma Motor Generator)	NASA	ED	Power and thrust,	500-m insulated conducting tether, Hollow cathode contactors at both ends, Conductive insulated tether, passive spool	0.5km	Demonstrated ED boost and generator mode operation 7 hrs experiment piggyback on Delta,	LEO	McCoy 1995
1994	SEDS-2	NASA	D	20-km tether to study dynamics and survivability	Downward deployment, Local vertical stable, Rate feedback braking	19.7km	Successful, controlled deployment of tether with minimal swing, Tether severed after 3 days in space, SEDS-2 probably cut by debris after mission completion,	LEO	Carroll 1995,1

Figure 8.6: Tethered missions - I part

1995	OEDIPUS-C	CSA	ED	Plasma Physics	Dynamic data during flight arc compared with pre-flight simulation	1.174km	Obtained data on plane and shear waves in ionospheric plasma, 1.174-m conducting tether, spinning.	Suborbital
1996	TSS-IR	NASA	ED	Power generation, Plasma Physics	20-km insulated conducting tether to study plasma-electrodynamic processes and tether orbital dynamics, Reel system, protruding bolt	19.6km Severed	Electrodynamic performance exceeded existing theories, Demonstrated ampere-level current, – Flaw in insulation allowed high-voltage arc to cut tether prior to full deployment Tether broken after science success	LEO Gilchrist 1998
1996	TIPS	NRL	D	Study survival and stability,	• Deployed 4-km nonconducting tether to study dynamics and survivability	4km	Successful deployment. Tether survived over 10 years on orbit, Cut after 1 decade in orbit, Mechanical, passive spool,	LEO Barndt 1998
1997	YES	ESA	D	Rotation, re-entry Accurate re-entry of a scientific capsule	Mechanical, double-strand tether, brake + spool	0km <sup>35</sup> Not deployed	GTO. Not deployed due to unsafe orbit.	LEO Knijff 1999, II
1998	ATEX	NRL	D	Stability & control	Tape tether deployed with pinch rollers Mechanical, tape, reel, Active stability and control demonstrator	0.022km(6) Not deployed	Deployment method "pushing on a rope" resulted in unexpected dynamics Deployed only 22 meters before experiment terminated, S/W stopped deployment	LEO Zedl 1998
2000	METS		ED	Thrust (Mir station)	Bare conductive tape/mechanical, passive reel	(5)km	Cancelled as Mir was deorbited	LEO Levin 2007
2000	Picosats 2/23	NASA	D	Formation	• 2 picosats connected by 30-m gold strand tether	0.03km	Demonstrated tethered formation flight	LEO
2001	Picosats 7/8	NASA	D	Formation	2 picosats connected by 30-m tether	0.03km	+ Demonstrated tethered formation flight	LEO
2002	MEPSI-1	NASA	D	Formation	2 picosats linked by ~15-m tether deployed from Shuttle	0.03km	+ Tethered formation flight	LEO
2003	Space shuttle Columbia disaster							
2005	ProSEIDS	NASA	ED	Thrust	Bare conductive, brake + spool	(13.1)km Cancelled for ISS safety	Bare conductive tether small, closely packed cross section of wires,	LEO Johnson 2003
2006	MEPSI-2	NASA	ED	Formation	2 picosats linked by 15-m tether deployed from Shuttle		Tethered formation flight of nanosats with propulsion and control wheels	LEO
2007	MAST	NASA	D	Study tether survivability, scientific capsule	3 tethered picosats to study tether survivability in orbital debris environment, Multi-line "Hoytether" plus inspactor crawler	0.001? of 1.0km	Satellite separation initiated but the actual length of the tether deployed is unknown. Minimal deployment, Problem with release mechanism resulted in minimal tether deployment	LEO Hoyt 2003
2007	YES-2	ESA	D	Momentum Exchange, Accurate re-entry of a scientific capsule	Deployed payload on 30-km nonconductive tether and released into suborbital trajectory	31.7km	Tether deployed over 30 km, Full two-stage deployment, Mechanical, brake + spool Overdeployed, controlling computer experienced resets during deployment, Re-entry capsule status is unknown,	LEO Knijff 2009, I, II
2009	AeroCube-3	NASA	D	Formation	Deployed from Minotaur on TacSat-3 launch a 2 picosats linked by 61-m tether	0.061km	+ Tethered formation flight with tether reel and tether cutter	LEO
2010	T-REX	ISAS/JAXA	ED	Conductive bare tether tape fast deployment,	• Sounding rocket experiment • 300-m bare tape tether	0.136km	+ Tether deployed to 130-m Suborbital, passive folded, Successfully deployed, video	Suborbital Fujii 2010

Figure 8.7: Tethered mission - II part

developing control strategies that are suitable for non-motorized reeling deployers.

A non-motorized deployer is quite similar to a stationary deployer from the point of view of control strategy because the reeling velocity cannot be controlled directly (through the motor) but rather it must be controlled by changing the friction. Consequently, a control law that tracks the ideal deployment profile through a linear feedback that depends on the departure of the actual profile from the desired one is a valid strategy to follow.

The ideal deployment trajectory is derived by solving a non-linear, time-variable boundary value problem in which initial conditions are fixed and the accelerating force is provided by the in-line thrusters (with a constant level of low thrust) and the gravity gradient. The goal of the control law is to minimize the libration amplitude at the end of deployment in a given time and provide a small final velocity.

The ideal trajectory is strongly dependent upon the tether length and the deployment time. We will, therefore, derive two different ideal deployment profiles that are applicable to two different tether lengths that are representative of two typical configurations of the BETs system

## 8.4 Deployer

The determination of a passive deployment strategy for a conductive tape tether is a critical points, since no mission used this configuration in the past. In deorbiting maneuvers retrieval is no required, so the deployment doesn't need not to be motorized. So we are looking for a passive and as simple as possible mechanism, that satisfies the requirements for a safe deployment. Several concepts have been analyzed before choosing the best one. A brief summary is here reported highlighting advantages and disadvantages for each configuration.

### 8.4.1 Concept1

In the first concept, the reel and the tether are together fixed in a box (see Fig. 8.9), which contains the whole deployment mechanism and is mounted inside or sideways on a satellite. The latch of the box serves as end mass. The loose tether end is attached to that latch. If the deploy mechanism is released, the latch is pushed away and unreels the tether.

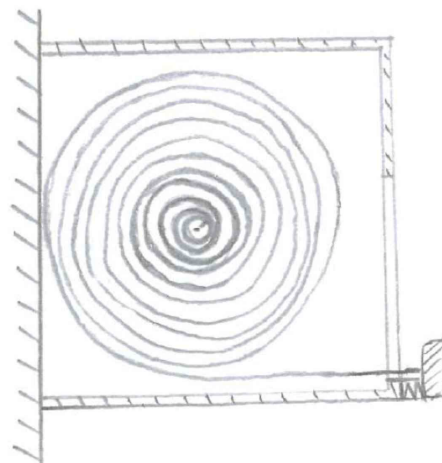


Figure 8.8: Deployment concept n° 1

For fixation of the latch to the box, heating wires are mounted between the latch and the box. To activate the deploy mechanism, the heating wire are heated up and burn the melting wires when

the release signal is set.

The advantage of this concept is the simple handling which goes quite easy for reeling and unreeling. Furthermore there is no twisting effect of the tether during deployment and the tether deploys steady what means there are no discontinuities to be expected in the deployment behavior.

The biggest disadvantage in this concept is that all layers of the tether are laid upon each other in a single plane, so with increasing tether length the diameter of the reel increases. If the tether reaches a certain length this concept becomes hardly useable for space applications.

#### 8.4.2 Concept2

The tether is reeled up on an individual reel. The package, formed by the reel and tether combined, is putted into a box (Fig. 8.9). On the bottom of the box there are several springs which give a pretension to the tether, when the box is closed. On the other side of the box there is an hatch, which is fixed to it by a hinge and a melting wire. When such a wire is burnt by a heater, the hatch can open letting the tether go out and activates the deployment maneuver.

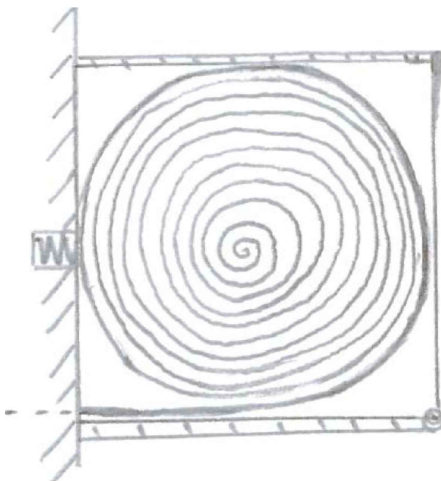


Figure 8.9: Deployment concept n° 2

When the box is opened the tether reel is pushed outside by the springs, which remain in the box. Because one end of the tether is fixed to the box, the reel unfolds itself when it is pushed outside the box. In this case the reel with the tether serves as end mass for the tether deployment. The advantage of this concept is the handling which goes quite easy for reeling and unreeling. Furthermore there is no twisting effect of the tether during deployment and the tether deploys steady what means there are no discontinuities to be expected in the deployment behavior.

The biggest disadvantage in this concept is that all layers of the tether are laid upon each other in a single plane, so with increasing tether length the diameter of the reel increases. If the tether reaches a certain length this concept becomes hardly useable for space applications.

#### 8.4.3 Concept3

A cylindrical shaped pole is mounted to a round plate which serves as a socket and contains the electronics, mechanism-control and hollow cathode. The pole is not rotateable and the tether is reeled on the pole in multiple layers. This can be done in multiple reel layers or spiral wise like a thread reel. The tether is deployed in axis direction of the pole.

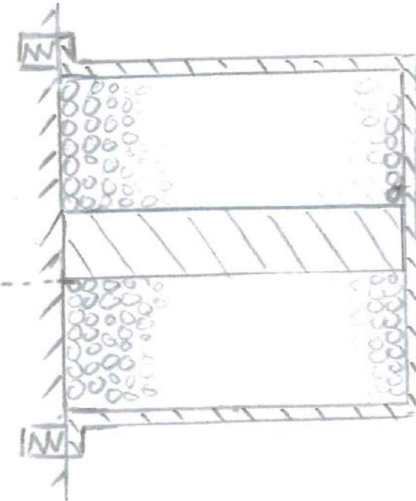


Figure 8.10: Deployment concept n° 3

The reeled tether is surrounded by a housing which is attached to the socket by melting wires, which works as a release mechanism. The wires run through a heating wire which melts them when the deployment mechanism is activated. Between socket and housing, several springs are mounted which push the housing away when the mechanism is activated and the housing is accelerated away from the spacecraft. In this way, the housing serves as an end mass and pulls the tether off from the pole, the other tether end is attached to the housing.

This configuration has the advantage that the tether volume is better arranged than in concept n°1 and becomes more compact so that the tethers transportability improves. In addition to that, there are no moving parts in this concept necessary which reduces the complexity and increases the reliability.

One of the disadvantages which could occur is the fact that the pole, where the tether is reeled up, is not rotate able which could create a higher friction related resistance for the tether deployment. Since the tether is unreeled in direction of the pole axis and every tether winding has to overcome the edge of the pole, the possibility of getting stuck or damaging the tether is given when passing by the pole end. The tether could tangle up on the pole and stop the unreeling process.

#### 8.4.4 Concept4

This concept is similar to the previous one, but instead of a cylindrical shaped pole there is a cone shaped pole mounted to a round plate which serves as socket and contains the electronics, mechanism-control and hollow cathode. The cone is not rotating and the tether is reeled up on the cone in multiple layers. This can be done in multiple reel layers or spiral wise like a thread reel. The tether is deployed in axis direction of the cone.

Comparing it with previous configuration n°3, this one is easier to deploy, since the tether doesn't have to overcome the edge of a pole and even the friction is reduced due to the fact that the tether immediately lifts off from any touching parts like the remaining tether layers or the cone pole. This concept has, like the n°3, the advantage that the tether volume is better arranged than in concepts n°1 and n°2, so the system can be realized in a more compacted way so that the tethers volume improves. In addition there are no necessary moving parts, and so it reduces the complexity and increases the reliability.

The main disadvantage is the reeling process: it's more difficult to reel a tether up on a cone than

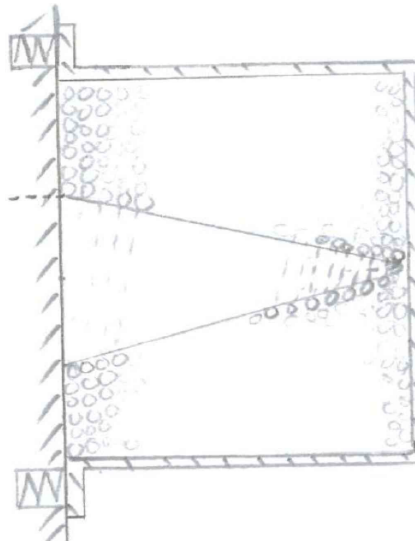


Figure 8.11: Deployment concept n° 4

on a cylindrical shaped pole due to the fact that the tether has the tendency to glide off the cone.

#### 8.4.5 Concept5

The tether is folded in a single plane in the box shaped tether storage container, that has the same width as the tether itself and has an open on the satellite facing side. The folding starts at the ground of the container and ends at the opening. The open part of the box is fixed by the release mechanism to the base of the deployment mechanism, which includes the electronics for the release mechanism and the separation springs. The base is mounted on the spacecraft side wall. In case of the deployment the whole tether box is used as end mass and deployed into open space. When the release mechanism is activated, the container is unlocked and accelerated away from the spacecraft.

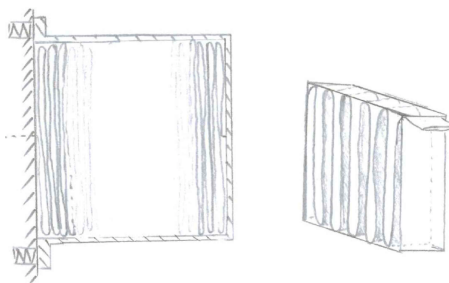


Figure 8.12: Deployment concept n° 5

The main advantage is that it allows a rack construction and can be integrated simply in a spacecraft. In addition to that, for the deployment a very low force is required.

The disadvantage in this case is that with increasing tether length, the tether box becomes a very long and thin box and according from a certain tether length unusable for space applications.

#### 8.4.6 Concept6

The tether is folded in a square shaped box in multiple layers. To increase the packaging density, the whole volume in a single layer is filled completely with the folded tether before the next layer starts.

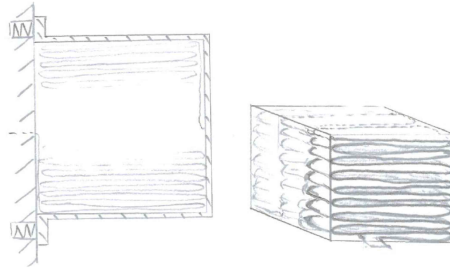


Figure 8.13: Deployment concept n° 6

The folding direction is based on the stacked layers perpendicular to the deploy direction. The storage container is connected to the base of the deployment mechanism. The electronic and the release mechanism, as well as the separation springs are positioned in the base. The base is mounted on the space craft itself. To deploy the tether, the release mechanism unlocks the separation springs and they accelerate the whole tether box away from the container. The tether is still partly located inside the box and deployed by the remaining inertia mass impulse, stored in the accelerated end mass.

The advantage is that the ground area of the tether box is rectangular and therefore independent from the tether length. Further this concept do not need any moving parts, therefore the mechanical complexity is low.

The disadvantage is the high complexity of the folding procedure and the attacking jerk impulse when a new tether layer starts to deploy and the tether folding needs to be pulled out of its storage position. This could end in an early stop of the deployment process because the stored inertia mass impulse is very fast removed.

#### 8.4.7 Concept7

In this last concept the tether is reeled in a cylindrical shaped tether storage container. The reeling begins at the wall of the tether box and is continued until the middle of the box. At this point, the next stacked layer is going to be started. The tether box is used as an end mass and the tether is connected to it at the top site.

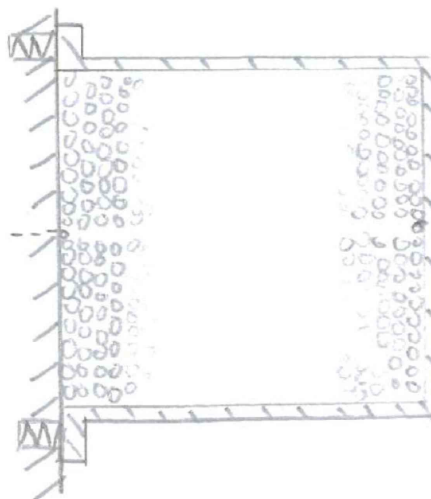


Figure 8.14: Deployment concept n° 7

The other side of the tether is attached to the base plate, which is equipped with the separation

mechanism made of launch locks and separation springs to accelerate the end mass away from the satellite. The connection between the tether container and the base is realized with the release mechanism. For the deployment, the release mechanism unlocks the tether box and the separation springs, so the end mass is accelerated away from the spacecraft.

The advantages are that the tether is only positioned in the tether box and no other component is needed to carry the tether. This results in a low complexity of the deployment mechanism. The disadvantages of this concept are that, as a result of the wounded tether, there is free space between the tether layers left. So the compaction and the used storage capacity are suboptimal and maximum space exploitation is not possible. Furthermore the handling complexity of wounding the tether is difficult.

#### 8.4.8 Comparison

To make a final selection of the tested deployment concepts, some weighting criteria must be established in order to allow a comparable evaluation of all the different concepts:

**Complexity:** to analyse the overall difficulty to realize the concept. This point is massively influenced by the number of parts, mechanisms and moveable parts that could get stuck. All tested concepts were passive systems, so the overall complexity of the systems is already pretty low. But to keep the tethers in place during launch and operation of the spacecraft at least some actuator systems are needed. At this point a good concept design can keep the requirements of the actuators quite low and the reliability high;

**Handling:** to describe the tether handling during the accomplished tether storage tests. The handling is split into the following:

- *preparation:* evaluates the handling during the preparation for the tests. The main focus is how easy the tether can be stored in each concept.
- *deployment:* investigates the reliability of the deployment itself. Key aspects of this weighting factor are the maximum pull force and the smoothness of deployment;

**Tether twisting:** to avoid uncontrollable movement of the de-orbiting mechanism and the satellite itself it is important to reduce implemented vibrations and frequencies coming from the de-orbiting mechanism during deployment. It has shown up during the tests that twisted tethers have a high perturbation and stuck potential when trying to de-twist during deployment;

**Entanglement risk:** is very important for the deployment behaviour of the tether. With a higher risk that the tether entangled also the risks of a failure increases. Therefore the entanglement of the tether during the beginning of the deployment, for example, that the tether entangle in a part of the satellite, or the possibility that the tether entangled into each other should be avoided;

**Volume:** deorbiting system should keep its influence on the overall satellite system as small as possible. A small volume and mass will increase the acceptance of an end-of-life deorbiting system from the satellite customer site. The mass itself is not an individual weighting factor. The differences of the individual systems are not big due to the fact that all concepts are passively deploying and the tether length does not vary.

very good	good	neutral	bad	very bad
++	+	0	-	--

Concept	n°1	n°2	n°3	n°4	n°5	n°6	n°7
Complexity	+	+	0	0	+	+	+
Handling Preparation	+	+	0	-	-	--	0
Handling deployment	+	++	0	0	+	+	+
Tether twisting	++	++	--	--	+	+	--
Entanglement risk	++	++	0	-	+	+	-
Volume in cm <sup>3</sup>	412.8	412.8	310	390	1190	805	612.6

Table 8.1: Concepts Comparison

The best evaluated concept, and therefore selected for its study and implementation, is concept n°1. The tether is unreeled without any twisting of the tether and therefore the entanglement risk is very low so that a failure of the deployment caused by the deployment process is nearly completely avoid. The next important design criteria is the complexity of the whole deployment mechanism including the release mechanism. In this case the complexity is low, because the whole mechanism has only three components: the tether storage box, the release mechanism, including the interfaces to the power supply and to the data handling, and the tether reel with the tether. Moreover this configuration has the big advantage, respect to concept n°2, that lets to mount a control mechanism to drive the deployment.

The only drawback in this concept is that with increasing tether length, regarding to a full scale mission with a tether length of 10 km the reeled tether becomes a large disc. But if the whole length will be reel on a number of reels with the same storage capacity the large disc can be avoid. That means that for the deployment of the 10km tether the several tether discs will be deployed into space after each other.

#### 8.4.9 Enginnering Model

The concept n° 1 has been studied and translated in engineering terms. Figure 8.15 shows the overall system of the deployer. The blue box is the outer shell of the whole mechanism and can also be used a mounting interface between the deployment mechanism and the main spacecraft. The tether reel colored grey is mounted on a reel axis placed in the middle of the box. The relative motion of the reel with respect to the box is let by two bearings. Their choice is a very critical point, because mechanical bearings can have high internal friction that affects the deployment operation. The endmass on the front of the box will be released with the help of a thruster mounted on the the tip mass itself in order to facilitate the deployment of the tether. The tether is mounted with screws on the reel as well as on the endmass. A brake meccanism (in green) acts directly on the reel to control and regulate its angular velocity, and so the deployment of the wire. Figure 8.16 shows how it works. The slip ring path is directly mounted to the tether reel. The slip ring contact springs are placed close to the reel axis. This small distance is needed to be capable to remove the slip ring contacts with a threaded rod. This threaded rod is equipped on a stepping motor. To remove the contact spring the motor will be switched on and move the T shaped remover to the end of the threaded rod.

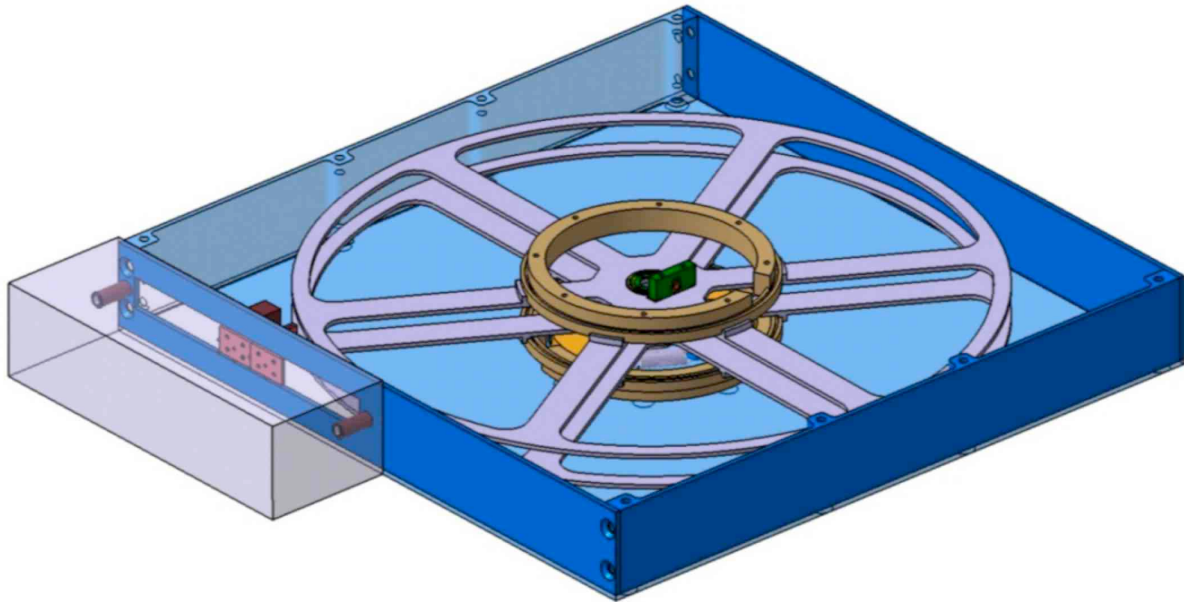


Figure 8.15: CAD model of the deployer

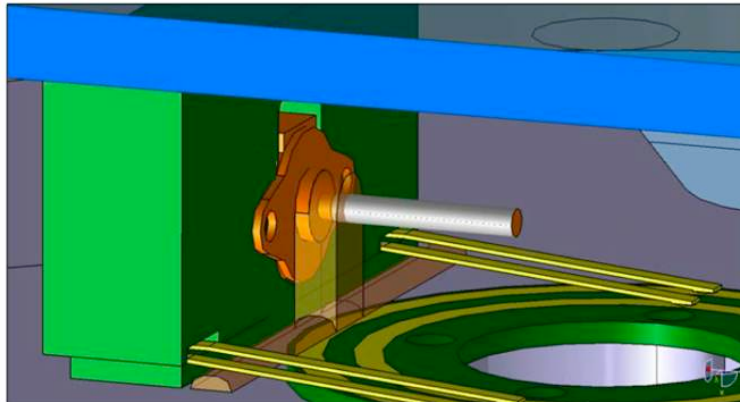


Figure 8.16: CAD model of the brake mechanism

## 8.5 Deployment Equations

In order to investigate the dynamics of the wire during the deployment we consider it as rigid, and so the dumbbell model can be adopted to study it [26]-[29][54]-[57]. This assumption is good for two reasons:

- during such an operation the tether is kept taut by the tension due to the friction mechanism and the thrust force mounted at the other end to facilitate the release of the end mass and drive the deployment itself;
- deployment is very fast if compared with the other typical phenomena highlighted in the section 5.2, and the eigen-frequencies have no time to be excited by external forces.

The dynamics of the wire during the deployment can be evaluated writing the Lagrangian function of the tethered system, which is the sum of the kinetic energy and the potential of all conservative

forces affecting the motion. Thus we can draw the equations deriving it choosing as generalized coordinated the length and the libration angles. To evaluate kinetic and potential terms we use the synodic reference system for defining the position along the system and, then, integrate the expressions obtained. To simplify the calculation we assume that mass of the satellite is much bigger than the tip mass, so the barycenter of the whole system is inside the satellite itself. The position of the point  $x$  and its velocity  $v$  can be written as:

$$\vec{x} = l \begin{bmatrix} \cos \theta \cos \varphi \\ \sin \theta \cos \varphi \\ \sin \varphi \end{bmatrix} \quad (8.1)$$

$$\vec{v} = \dot{l} \begin{bmatrix} \cos \theta \cos \varphi \\ \sin \theta \cos \varphi \\ \sin \varphi \end{bmatrix} + \omega_{orb} l \begin{bmatrix} \sin \theta \cos \varphi (1 - \dot{\theta}) - \cos \theta \sin \varphi \dot{\varphi} \\ \cos \theta \cos \varphi (\dot{\theta} - 1) - \sin \theta \sin \varphi \dot{\varphi} \\ \cos \varphi \dot{\varphi} \end{bmatrix} \quad (8.2)$$

where  $\theta$  and  $\varphi$  are the libration angles in the adimensional form and  $\omega_{orb}$  the orbital velocity. We can introduce the potential factors of the gravitational attraction of the Earth and the apparent forces due to the non-Galilean nature of the orbital frame:

$$dV_g = \frac{\mu}{r} \left[ 1 - \frac{\vec{x} \cdot \vec{s}_1}{r} + \frac{3}{2} \left( \frac{\vec{x} \cdot \vec{s}_1}{r} \right)^2 - \frac{1}{2} \frac{\vec{x} \cdot \vec{x}}{r} + o \left( \frac{\vec{x} \cdot \vec{x}}{r} \right)^3 \right] dm \quad (8.3)$$

$$dV_g = \left[ \vec{\gamma}x - \frac{1}{2} \left( \vec{\Omega} \cdot \vec{x} \right)^2 - \vec{\Omega} \cdot (\vec{x} \times \vec{v}) \right] dm \quad (8.4)$$

where  $\gamma$  is the acceleration of the origin of the orbital frame, and  $r$  the orbital radius.

$$\begin{aligned} \vec{\gamma} &= -\omega_{orb}^2 r \vec{s}_1 \\ \vec{\Omega} &= \omega_{orb}^2 \vec{s}_3 \\ \mu &= \omega_{orb}^2 r^3 \end{aligned}$$

The total potential energy is given by the sum of the two terms, and can be separated in the contributions due to the tether and the tip mass:

$$E_P = \int_0^L dV_g + \int_0^L dV_i = E_{P_{tether}} + E_{P_{m_B}} \quad (8.5)$$

$$E_{P_{tether}} = -\frac{1}{12} \rho \omega_{orb}^2 l^3 \cos^2 \varphi \left( 5 + 3 \cos 2\theta + 4\dot{\theta} \right)$$

$$E_{P_{m_B}} = -\frac{1}{4} \omega_{orb}^2 l^2 \cos^2 \varphi \left( 5 + 3 \cos 2\theta + 4\dot{\theta} \right)$$

$$E_P = -\frac{1}{6} (3m_B + \rho l) \omega_{orb}^2 l^2 \cos^2 \varphi \left( 1 + 3 \cos^2 \theta + 2\dot{\theta} \right) \quad (8.6)$$

where  $\rho$  is the linear density of the wire.

In the same way we can evaluate the kinetic energy:

$$E_P = \frac{1}{2} \int_0^L \rho \vec{v} \cdot \vec{v} dl = E_{K_{tether}} + E_{K_{m_B}} \quad (8.7)$$

$$E_{K_{tether}} = \frac{1}{6} \rho l \left[ 3\dot{l}^2 + \omega_{orb}^2 l^2 \left( \cos^2 \varphi (2\dot{\theta} - 1)^2 + \dot{\varphi}^2 \right) \right]$$

$$E_{K_{tether}} = \frac{1}{2}m_B \left[ 3\dot{l}^2 + \omega_{orb}^2 l^2 \left( \cos^2 \varphi (2\dot{\theta} - 1)^2 + \dot{\varphi}^2 \right) \right]$$

$$E_K = \frac{1}{6} (3m_B + \rho l) \left[ 3\dot{l}^2 + \omega_{orb}^2 l^2 \left( \cos^2 \varphi (2\dot{\theta} - 1)^2 + \dot{\varphi}^2 \right) \right] \quad (8.8)$$

So the Lagrangian function can finally calculate:

$$L = E_K - E_P$$

The equations of the deployment are determined by deriving the lagrangian function choosing as generalized coordinates the in-plane and out-of-plane libration and the tether length deployed, and as independent variable the time:

$$\begin{cases} \partial_t \partial_{\dot{\theta}} - \partial_{\theta} L = 0 \\ \partial_t \partial_{\dot{\varphi}} - \partial_{\varphi} L = 0 \\ \partial_t \partial_{\dot{l}} - \partial_l L = 0 \end{cases}$$

$$\ddot{\theta} = -3 \cos \theta \sin \theta - 3 \frac{\dot{l} (2m_B + \rho l) (1 + \dot{\theta})}{l (3m_B + \rho l)} + 2 \tan \varphi (1 + \dot{\theta}) \dot{\varphi} \quad (8.9)$$

$$\ddot{\varphi} = -\cos \varphi \sin \varphi (1 + 3 \cos^2 \theta + \dot{\theta} (2 + \dot{\theta})) - 3 \frac{\dot{l} (2m_B + \rho l)}{l (3m_B + \rho l)} \dot{\varphi} \quad (8.10)$$

$$\ddot{l} = -\frac{1}{2} \frac{\rho \dot{l}^2}{m_B + \rho l} + \frac{\omega_{orb}^2 l (2m_B + \rho l) (1 + 3 \cos^2 \theta + \dot{\theta} (2 + \dot{\theta}))}{2 (m_B + \rho l)} \quad (8.11)$$

In the Eqs. 8.9-8.10 the  $\dot{l}$  term compares: it represents a positive damping term when  $\dot{l}$  is positive, while it becomes a destabilizing factor when it is negative, is that during retrieve operations. In Eq. 8.11  $\rho l^2$  describes the mass flux: the distribution of the mass changes bringing the tether itself from inside the deployer to outside.

If we consider also the electrodynamic interaction (from an electrical point of view, it's better to keep always closed the circuit, so a little current can flow along the tether during the deployment affecting the maneuver):

$$\begin{cases} \partial_t \partial_{\dot{\theta}} - \partial_{\theta} L = M_{\theta} \\ \partial_t \partial_{\dot{\varphi}} - \partial_{\varphi} L = M_{\varphi} \\ \partial_t \partial_{\dot{l}} - \partial_l L = 0 \end{cases}$$

where  $M_{\theta}$  and  $M_{\varphi}$  are the generalized torques.

$$M_{\theta} = J_1 (B_y \cos^2 \varphi + (B_x \cos \theta + B_z \sin \theta) \cos \varphi \sin \varphi)$$

$$M_{\varphi} = J_1 (B_z \cos \theta - B_x \sin \theta)$$

And the equations of the libration become:

$$\ddot{\theta} = -3 \cos \theta \sin \theta - 3 \frac{\dot{l} (2m_B + \rho l) (1 + \dot{\theta})}{l (3m_B + \rho l)} + 2 \tan \varphi (1 + \dot{\theta}) \dot{\varphi} + \frac{J_1 (B_y \cos^2 \varphi + (B_x \cos \theta + B_z \sin \theta) \cos \varphi \sin \varphi)}{I_s \cos \varphi} \quad (8.12)$$

$$\ddot{\varphi} = -\cos \varphi \sin \varphi \left( 1 + 3 \cos^2 \theta + \dot{\theta} (2 + \dot{\theta}) \right) - 3 \frac{\dot{l}}{l} \frac{2m_B + \rho l}{3m_B + \rho l} \dot{\varphi} + \frac{J_1 (B_z \cos \theta - B_x \sin \theta)}{I_s} \quad (8.13)$$

Without any control it is not possible to realize a good deployment bringing the tether to be aligned along the local vertical, and so, minimizing the libration angles, in particular the in-plane one. In order to maintain the whole system as simple as possible (and so more competitive) the deployment can be controlled only by means a tension force along it, which regulates the variation of the tether length. A brake mechanism is mounted inside the deployer to apply the right tension necessary to satisfy the operation.

So the equation of the tether acceleration  $\ddot{l}$  must include such a term:

$$\ddot{l} = -\frac{T_{brake} + \frac{1}{2}\rho l^2}{m_B + \rho l} + \frac{\omega_{orb}^2 l (2m_B + \rho l) \left( 1 + 3 \cos^2 \theta + \dot{\theta} (2 + \dot{\theta}) \right)}{2(m_B + \rho l)} \quad (8.14)$$

where  $T_{brake}$  represents the tension along the wire due to the brake mechanism.

To guarantee the success of the maneuver, also a thruster is placed in the tip mass to help the exit of the wire, mostly at the beginning, where the gravity gradient acceleration is low and can be overcome by the internal friction of the mechanism.

$$\ddot{l} = \frac{T_{thruster} - T_{brake} - \frac{1}{2}\rho l^2}{m_B + \rho l} + \frac{\omega_{orb}^2 l (2m_B + \rho l) \left( 1 + 3 \cos^2 \theta + \dot{\theta} (2 + \dot{\theta}) \right)}{2(m_B + \rho l)} \quad (8.15)$$

The thrust force acts directly on the end mass pushing it far from the satellite and can be model as:

$$T = \dot{m}_{prop} I_{sp} g_0$$

where  $m_{prop}$  is the propellant mass,  $I_{sp}$  the specific impulse of the thruster and  $g_0$  the Earth's gravity acceleration.

The brake mechanism acts directly on the deployer limiting the acceleration  $\ddot{l}$ , but it has to do it following an optimal profile in order to minimize the final libration and velocity. In fact also the deployment must arrive at the end with  $\dot{l}$  near to zero in order to avoid elastic deformation of the wire, and so wide longitudinal oscillations.

## 8.6 Optimal Profile

The brake is a fundamental aspect of the mechanism, in fact without any control authority it's impossible to deploy correctly the tether, because it starts to rotate around the satellite, as shown in Figs. 8.17-8.19.

Moreover the tether goes out too fastly reaching the goal length at high velocity. This is another critical point, because the longitudinal kinetic energy in excess transform itself in elastic deformation energy, provoking strong recalling force still when the tether is taut, then the tension disappears since the wire can't bear pressure force and the tip mass tends to go towards the satellite. The gravity gradient force is little and so it requires a lot of time to bring back the wire and the tip mass towards the configuration aligned to the local vertical. In the following simulations such effect

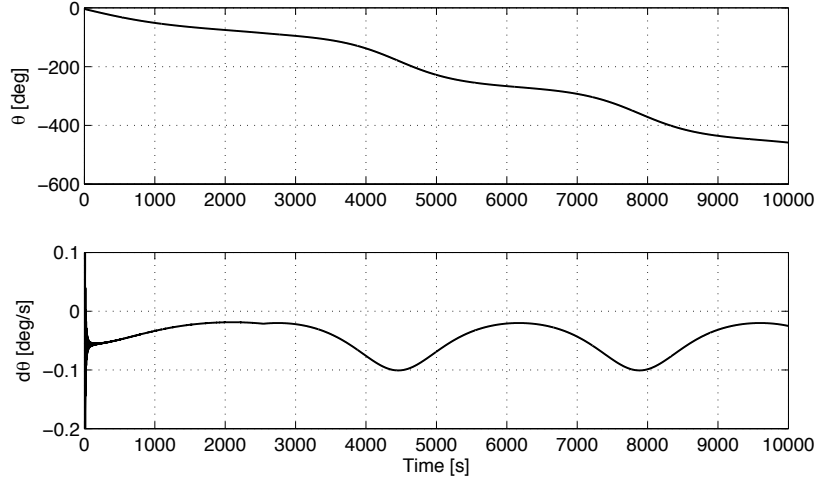


Figure 8.17: Uncontrolled mechanism: in-plane angle

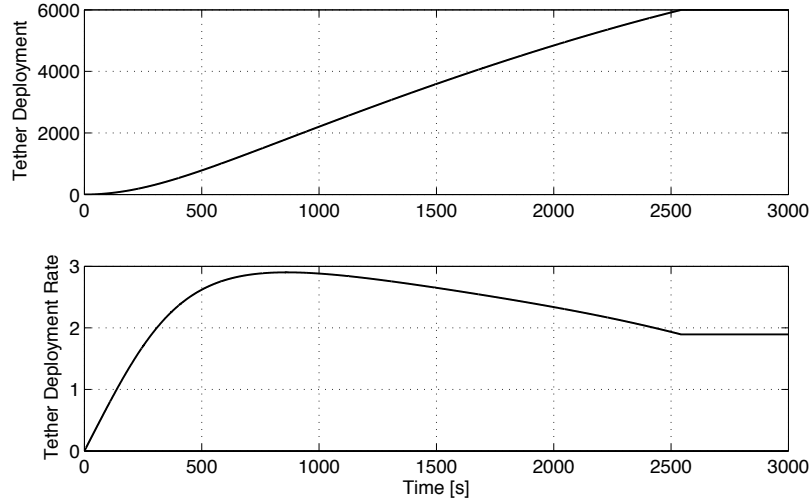


Figure 8.18: Uncontrolled mechanism: deployment

is not considered because we want to arrive at end of the deployment with final velocity very close to zero. But just to show what happens in such a situation Fig. 8.20 illustrates an example for a 2km long tether. The oscillations are slowly damped by the internal viscosity of the wire.

The optimal profile is that particular combination of friction action that lets to arrive at the end of the deployment with the minimum libration. Such a profile can be evaluated by means of an optimization algorithm, which has been written including the set of differential equations before drawn. The equations are integrated varying the tension along the wire till to arrive to the best solution that brings the tether as close as possible to the local vertical.

The aim is to obtain the trend of  $l$ ,  $\dot{l}$ ,  $\theta$ ,  $\dot{\theta}$ ,  $\varphi$  and  $\dot{\varphi}$  as a function of time, in order to use them as reference trajectory during the real operations for building a feedback input to control the brake.

### 8.6.1 Optimization

The tension profile must be optimized in order to arrive at the end of the operation satisfying these requirements:

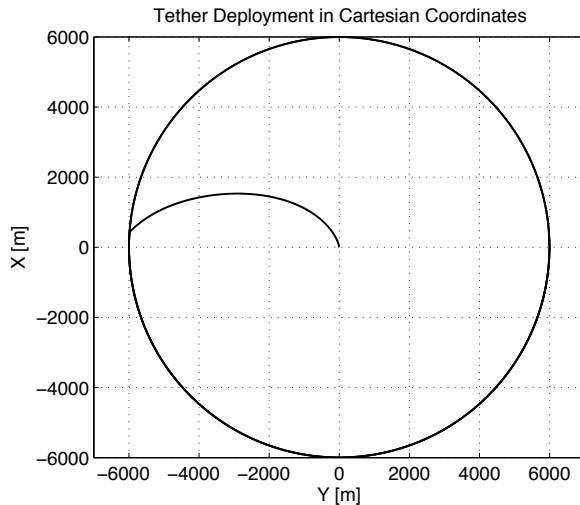


Figure 8.19: Uncontrolled mechanism: deployment in cartesian coordinates

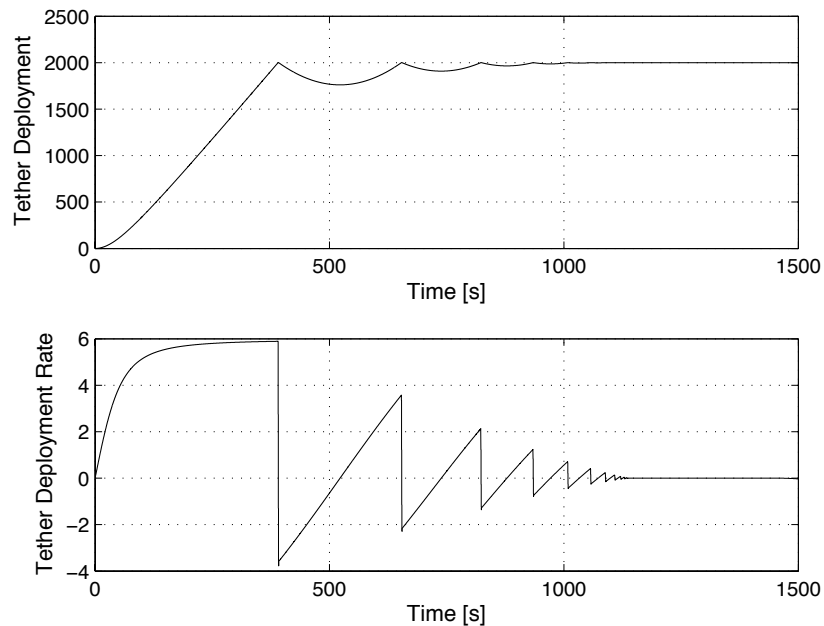


Figure 8.20: Uncontrolled mechanism: longitudinal oscillations

- the whole tether must be deployed
- final velocity close to zero
- final minimum libration

It is a boundary values problem, whose solution, obtained by numerical techniques, provides the reference trajectory and control input brake that steers the system along the desired path. To reach the goal we can follow two different ways: the former searches directly the best combination of the tension that satisfies the previous requirements; instead the latter evaluates the velocity profile, and at last from Eq. 8.15 draws the tension one.

Both methods fix some switch points where the variable of interest is evaluated, and then approximate it interpolating such values to obtain the whole profile. The operation must start at

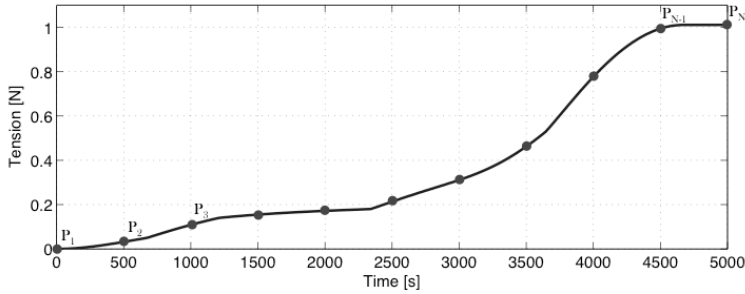


Figure 8.21: Switch points used to calculate the optimal profile of the tension along the tether

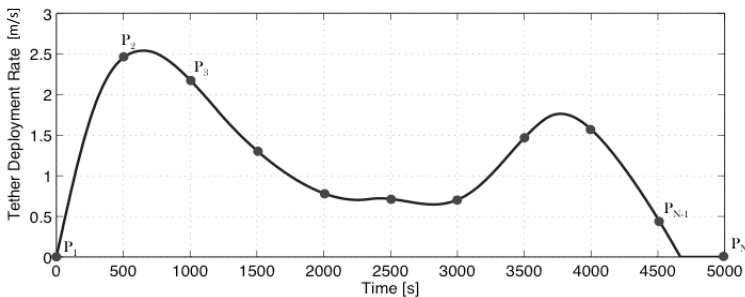


Figure 8.22: Switch points used to calculate the optimal profile of the velocity  $\dot{l}$  [m/s]

low friction to guarantee the release of the tip mass and the increase of velocity, that starts from zero, then the brake action grows up gradually till to stop the wire when it reaches the desired length. Figures 8.21-8.22 give an idea about the algorithm:  $P_N$  switch points are defined and changed by the algorithm. In order to vary them in the right way and arrive to the optimal solution a cost function  $F$  must be defined:

$$\begin{aligned} F = & C_1 (l_{end} - l_{goal})^2 + C_2 (\dot{l}_{end} - \dot{l}_{goal})^2 \\ & + C_3 (\theta_{end} - \theta_{goal})^2 + C_4 (\dot{\theta}_{end} - \dot{\theta}_{goal})^2 \\ & + C_5 (\varphi_{end} - \varphi_{goal})^2 + C_6 (\dot{\varphi}_{end} - \dot{\varphi}_{goal})^2 \end{aligned} \quad (8.16)$$

Such a function estimates the committed error respect to ideal case, where  $l_{goal}$  is the objective length, while the other variables ( $\dot{l}_{goal}$ ,  $\theta_{goal}$ ,  $\dot{\theta}_{goal}$ ,  $\varphi_{goal}$  and  $\dot{\varphi}_{goal}$ ) must be close to zero.  $F$  is a continuous function so it will have at least a minimum that the algorithm has to find.

The code used for the deployment analysis has been written in MATLAB environment and utilizes the function *fminsearch* to find the minimum of  $F$ . This routine is a direct search method that does not use numerical or analytic gradients, but the Nelder-Mead simplex algorithm [65]. This technique can minimize an objective function in a many-dimensional space approximating a local optimum of a problem with  $N$  variables when the objective function varies smoothly and is unimodal. Given an initial value of the switch points, the code returns the profile looked for.

It is a long process that usually requires a lot of iterations to conclude, since each time it has to integrate the set of equations 8.12-8.13-8.15.

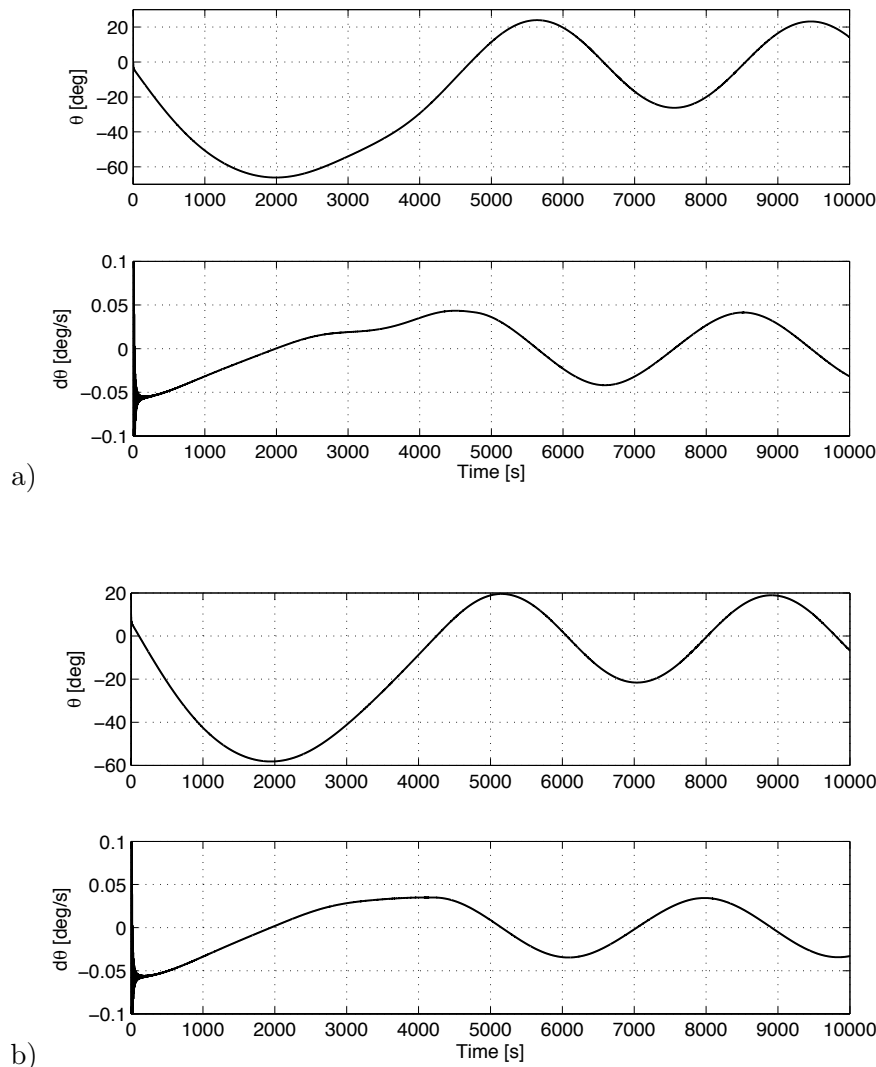
Actually the cost function  $F$  has several local minima, so it needs to be helped choosing appropriately the initial conditions, otherwise the algorithm converges to another solution that is not the best. Moreover the profiles of the velocity and acceleration are other critical aspects to take into account. The maximum acceleration must be limited, and profile of the velocity must stay far from the zero in the middle of the deployment, because even if the thruster remains active till the end of the

operation the internal friction can block the rotation of the reel.

### 8.6.2 Results

In this part we show some results obtained with our algorithm. In the previous chapter 7 we highlighted the importance to mount an inert portion after the electrodynamic one. So, that's why, in our simulations, we studied directly configurations including the no-conductive element, that must be deployed too. For the sake of simplicity we assumed that the transversal section and the linear density is the same of the electrodynamic part. The geometry of the tether considered is:

- total length: 3+3km and 5+5km;
- width: 2cm
- thickness: 50 $\mu$ m



The tip mass at end of the wire is 20kg, and an average current about 0.1A is supposed to flow along it. The deployer, like every mechanical components, has an internal friction, that is not always so easy to estimate since it depends on a lot of terms (like lubrication, temperature,...). In the code a constant tension term  $T_0$ , due to the internal friction, is introduced in the equations and set equal to 0.1N. At last the satellite is supposed to orbit in an equatorial circular orbit at an altitude

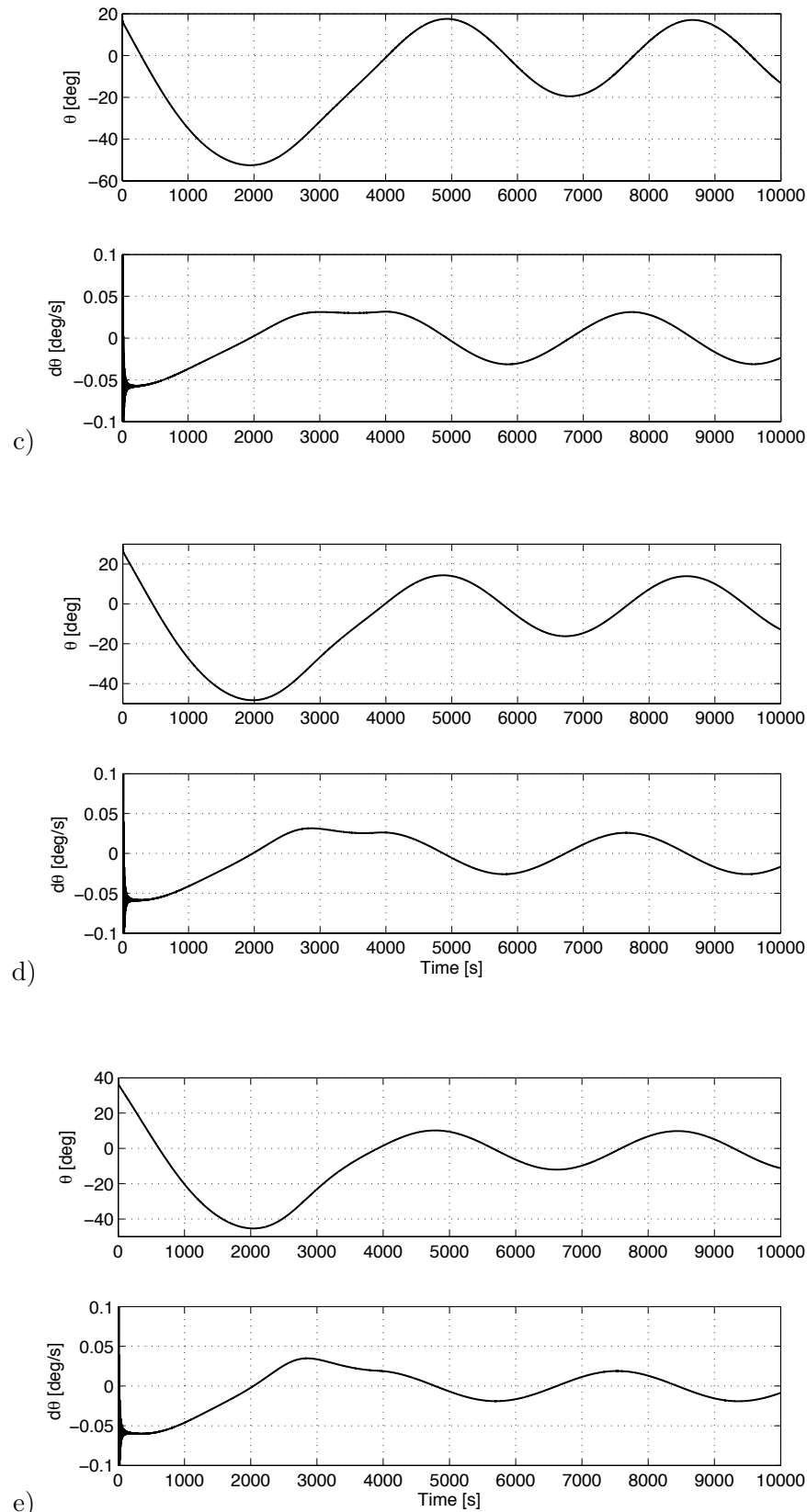
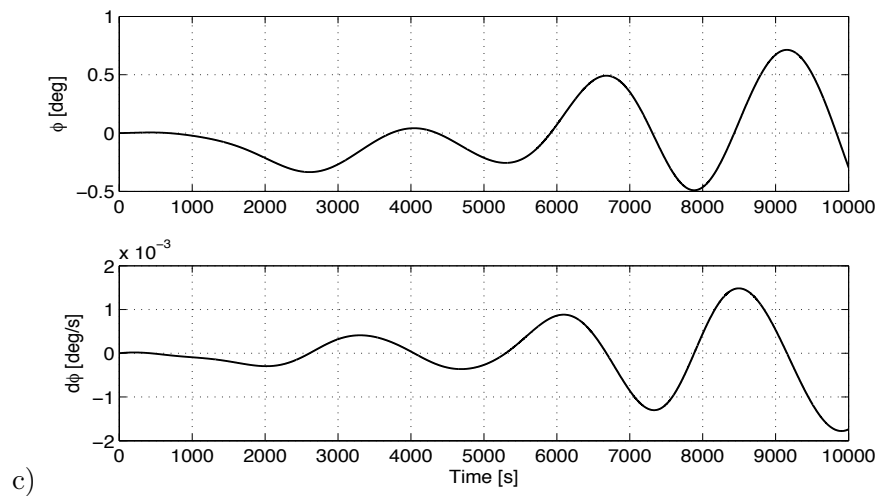
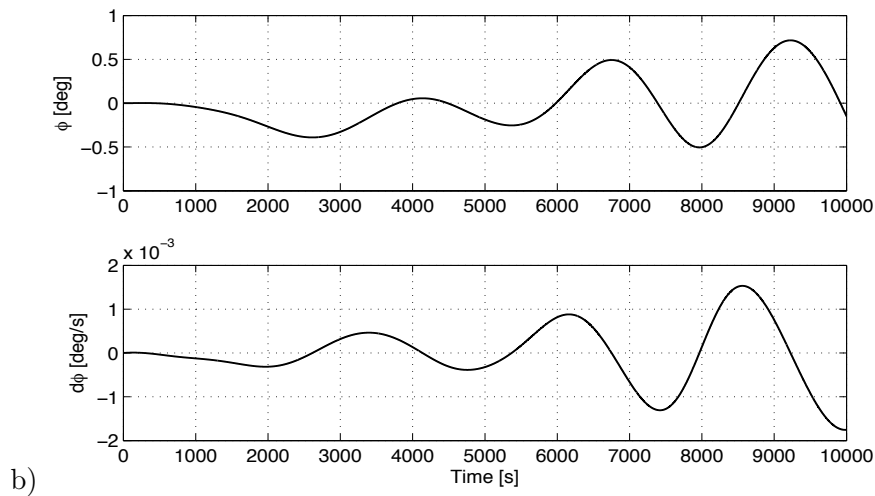
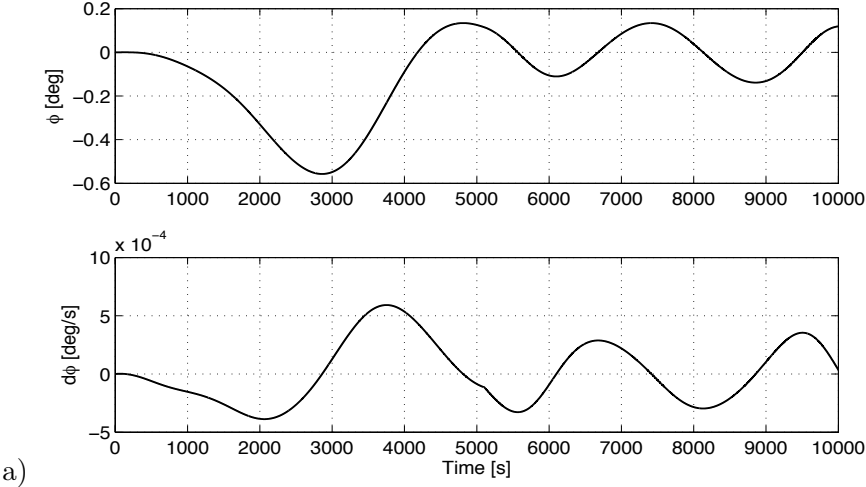


Figure 8.23: In-Plane libration starting with: a)  $\theta_0=0^\circ$ , b)  $\theta_0=10^\circ$ , c)  $\theta_0=20^\circ$ , d)  $\theta_0=30^\circ$ , e)  $\theta_0=40^\circ$ ,  $L_{tot} = 6\text{km}$ ,  $w = 2\text{cm}$

of 1000km, where the orbital angular velocity is  $9.9625 \times 10^{-4}$  rad/s.

The following Figs. 8.23-8.27 represents the deployment of a 6km long tether with different initial



in-plane angle ( $\theta_0=0, 10, 20, 30, 40^\circ$ ), while the other variables are so set:  $\dot{\theta}_0=0$ ,  $\varphi_0=0$ ,  $\dot{\varphi}_0=0$ ,  $l_0=0.1$ ,  $\dot{l}_0=0$ . The pictures show the in-plane and out-plane libration, the tether length deployed and its velocity, the deployment in synodic coordinates, and at last the tension profile necessary for the

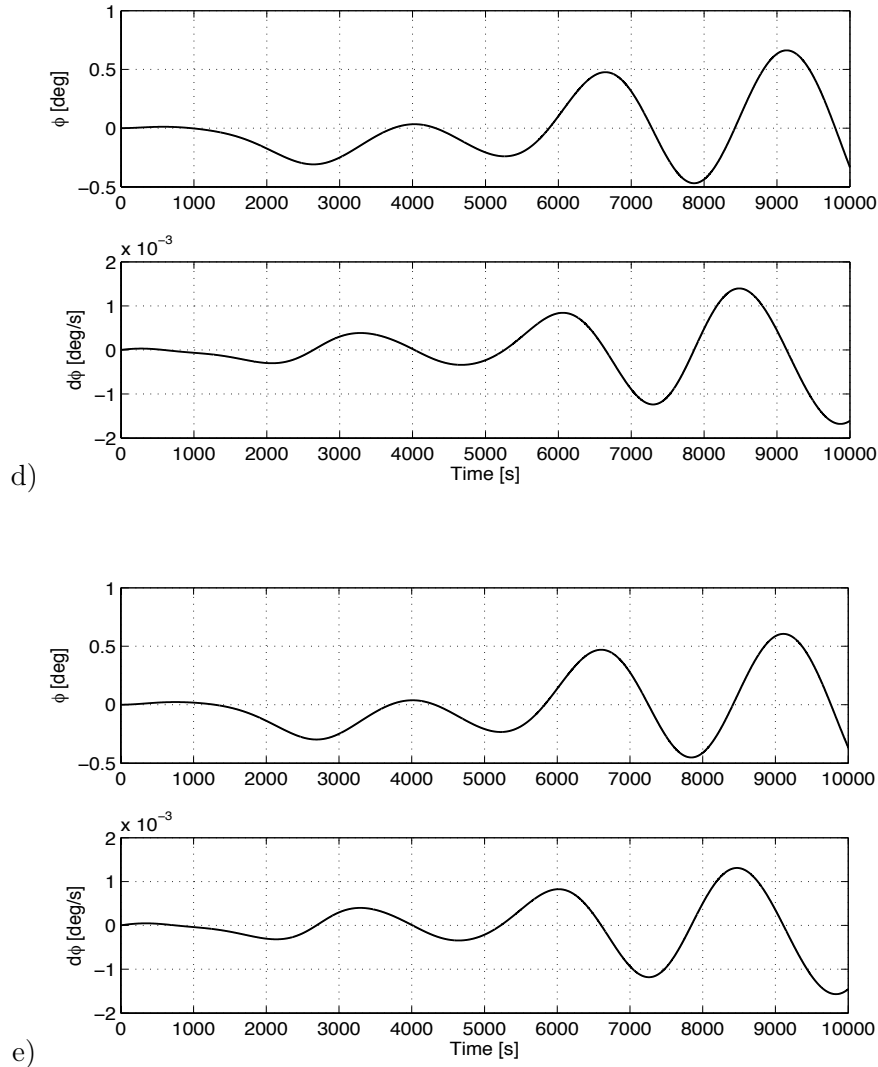
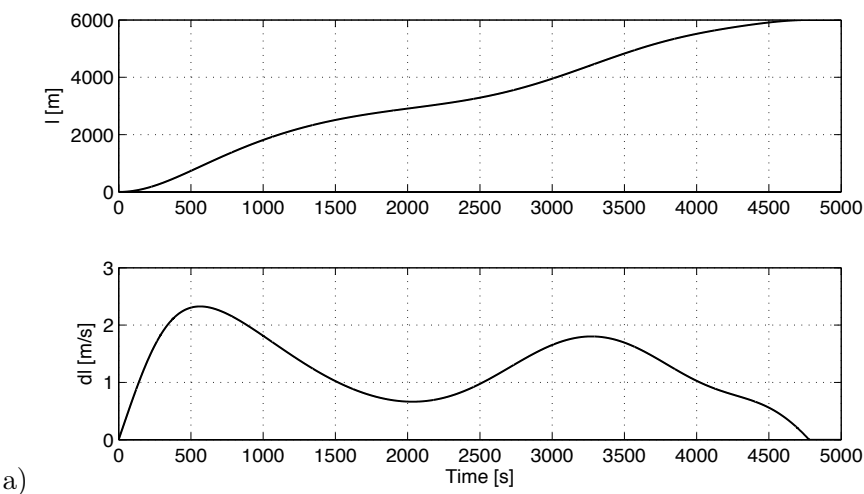
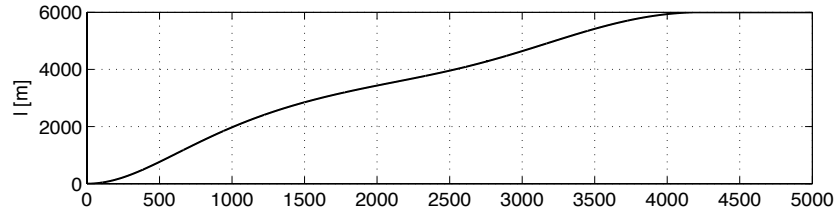


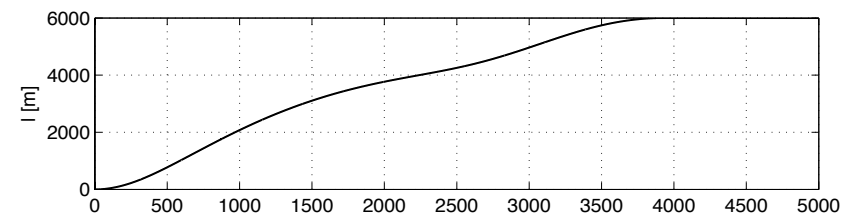
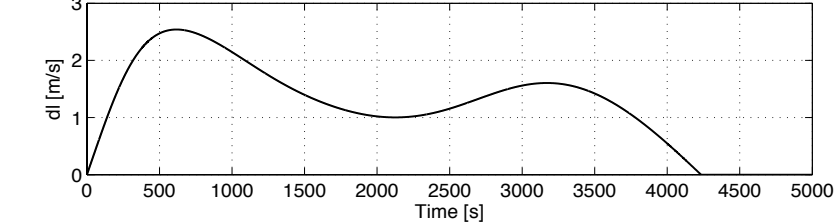
Figure 8.24: Out-of-plane libration starting with: a)  $\theta_0=0^\circ$ , b)  $\theta_0=10^\circ$ , c)  $\theta_0=20^\circ$ , d)  $\theta_0=30^\circ$ , e)  $\theta_0=40^\circ$ ,  $L_{tot} = 6\text{km}$ ,  $w = 2\text{cm}$



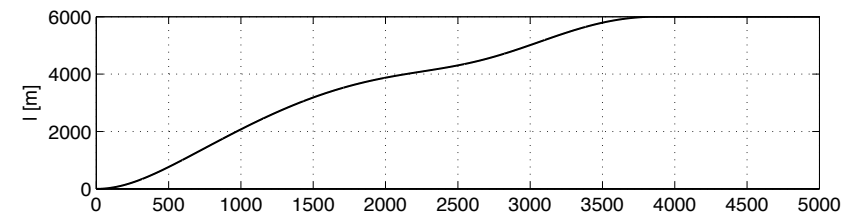
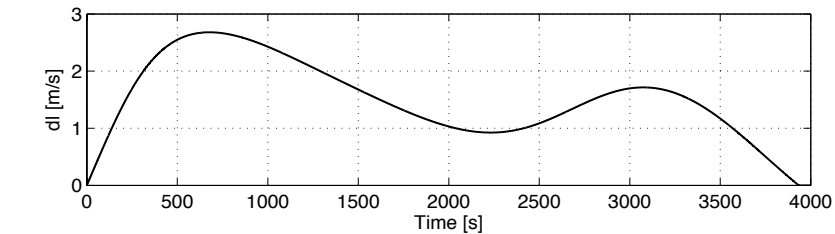
control. The tether initially deploys at low friction and tends to go in the direction opposite to the orbital motion because affected by Coriolis terms. Then the brake starts to control the operation



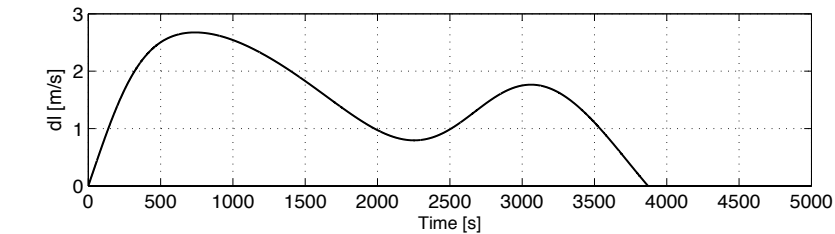
b)



c)



d)



and the in-plane angle reaches a minimum beyond which it oscillates with small amplitude around the equilibrium position with the electrodynamic force. Instead the out-of-plane angle remains small and doesn't affect a lot the deployment. The velocity  $\dot{l}$  is always positive, that means the wire is not

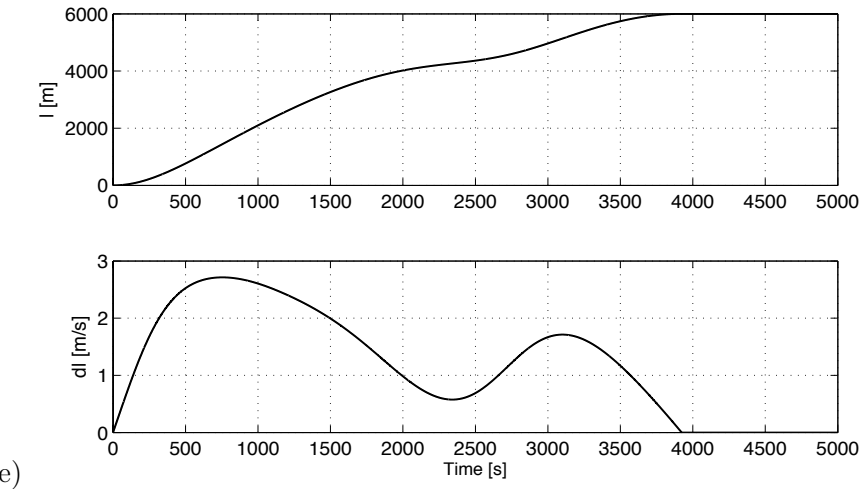
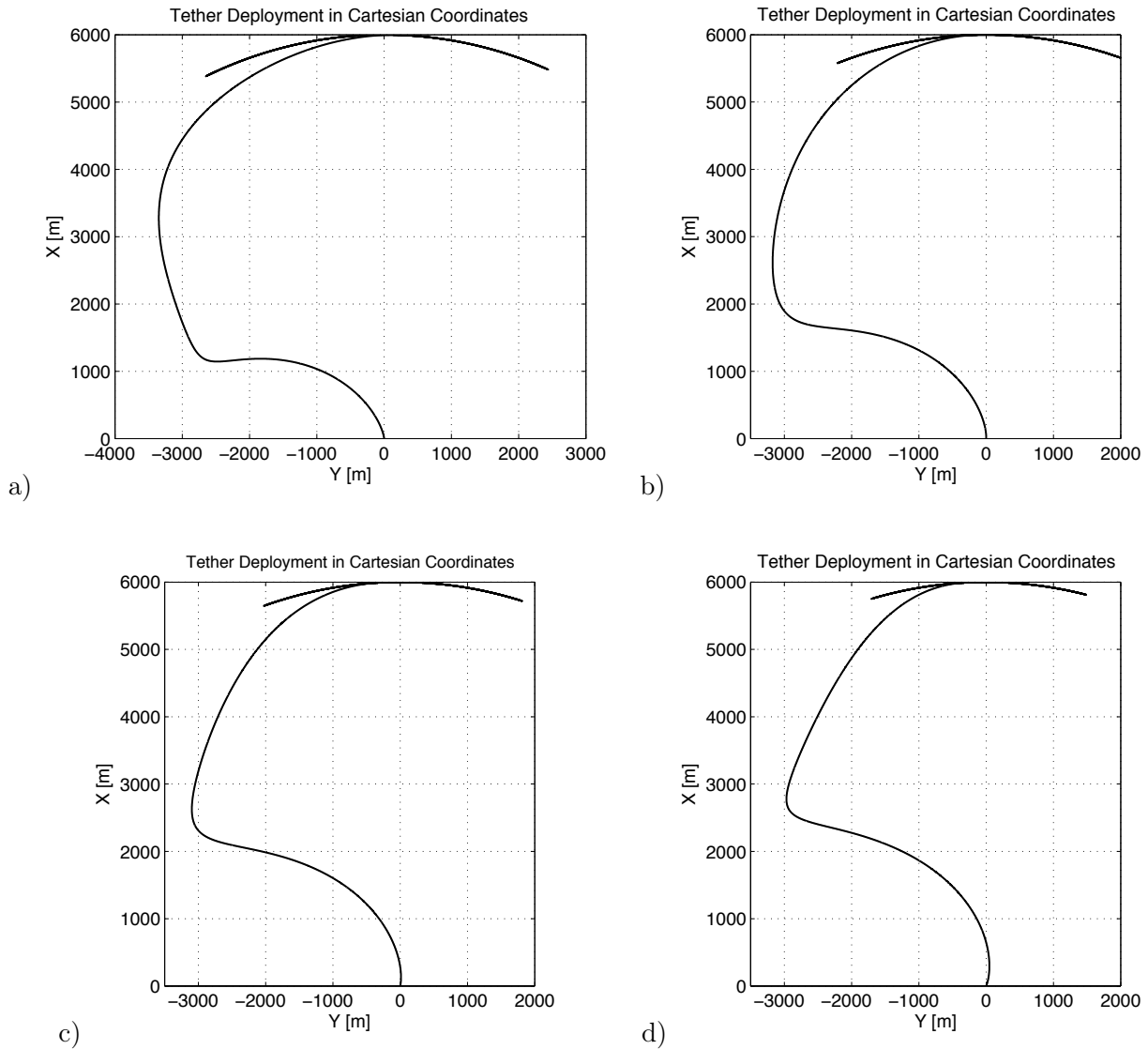


Figure 8.25: Tether Deployment starting with: a)  $\theta_0=0^\circ$ , b)  $\theta_0=10^\circ$ , c)  $\theta_0=20^\circ$ , d)  $\theta_0=30^\circ$ , e)  $\theta_0=40^\circ$ ,  $L_{tot} = 6\text{km}$ ,  $w = 2\text{cm}$



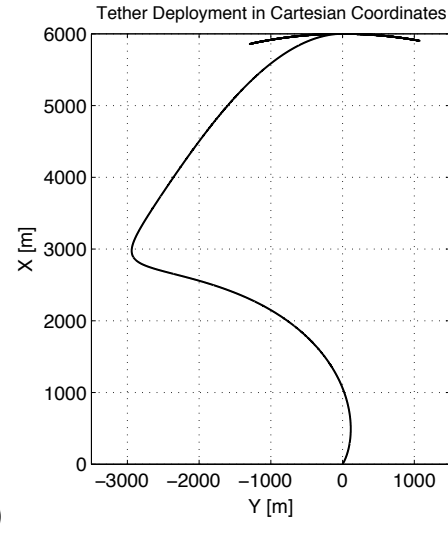
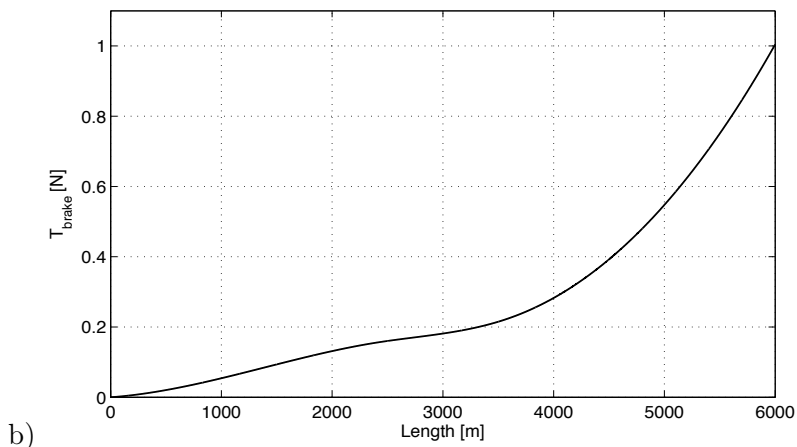
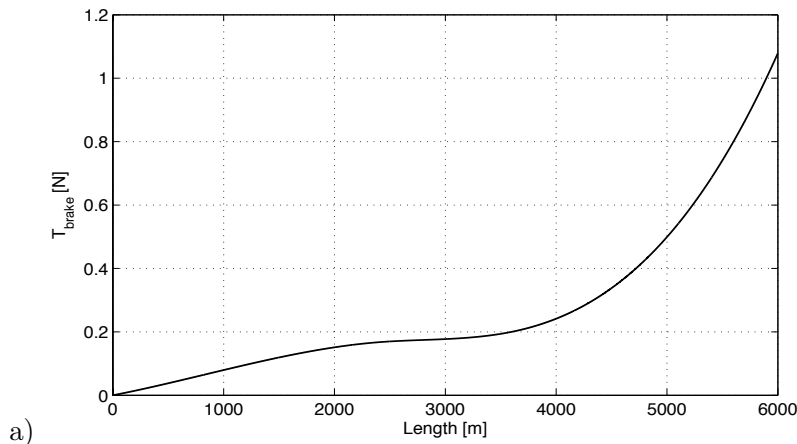


Figure 8.26: Deployment in Cartesian coordinates starting with: a)  $\theta_0=0^\circ$ , b)  $\theta_0=10^\circ$ , c)  $\theta_0=20^\circ$ , d)  $\theta_0=30^\circ$ , e)  $\theta_0=40^\circ$ ,  $L_{tot} = 6km$ ,  $w = 2cm$



retrieved. It reaches a first maximum, then it slows down, because the in-plane angle goes towards the minimum and the tension increases. So it reaches a second maximum for going, successively, to

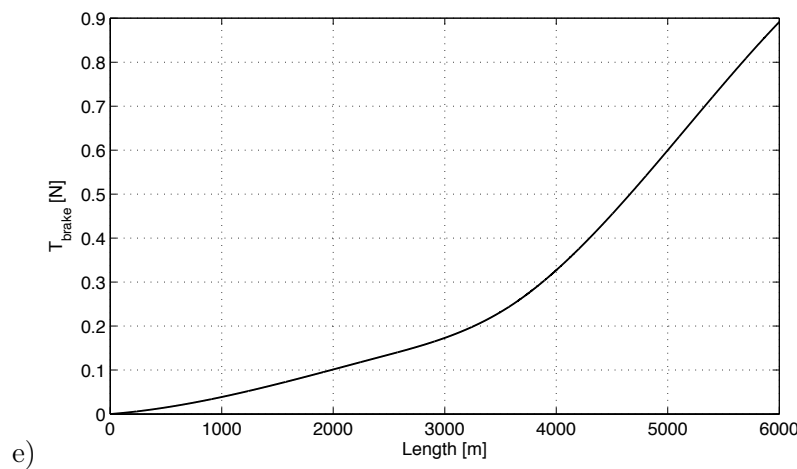
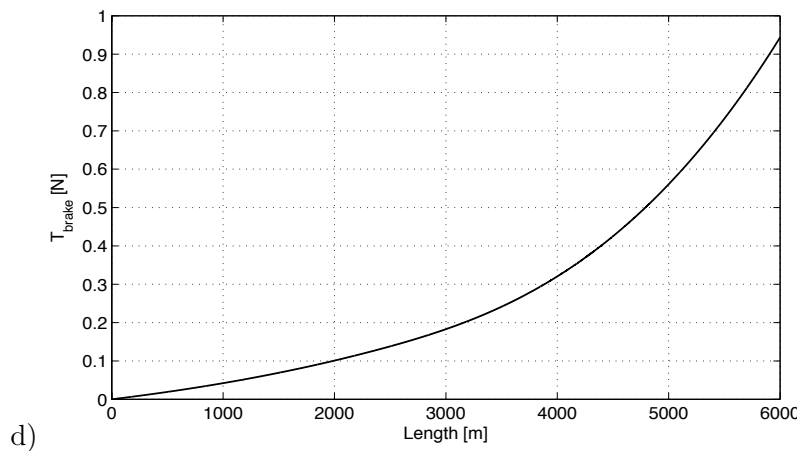
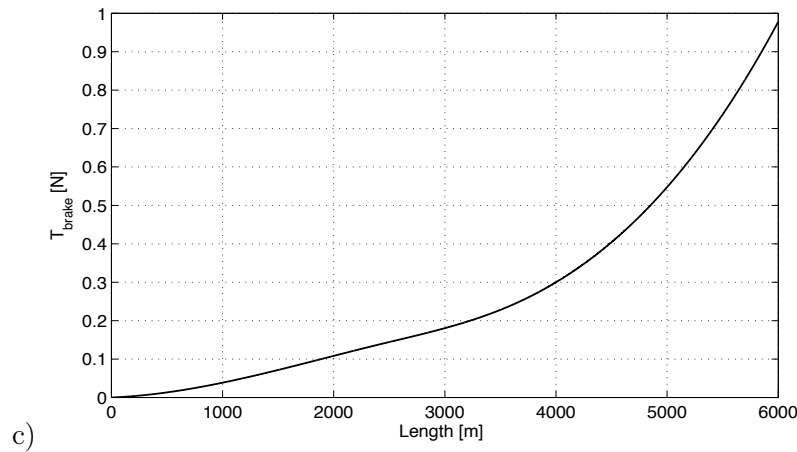


Figure 8.27: Tension along the wire evaluated by means of optimization algorithm, starting with:  
a)  $\theta_0=0^\circ$ , b)  $\theta_0=10^\circ$ , c)  $\theta_0=20^\circ$ , d)  $\theta_0=30^\circ$ , e)  $\theta_0=40^\circ$ ,  $L_{\text{tot}}=6\text{km}$ ,  $w=2\text{cm}$

zero when the goal length is got.

If the deployment begins with an initial angle in the direction of the orbital motion, then we can help the in-plane dynamics, because the minimum becomes less critical and the final oscillation is

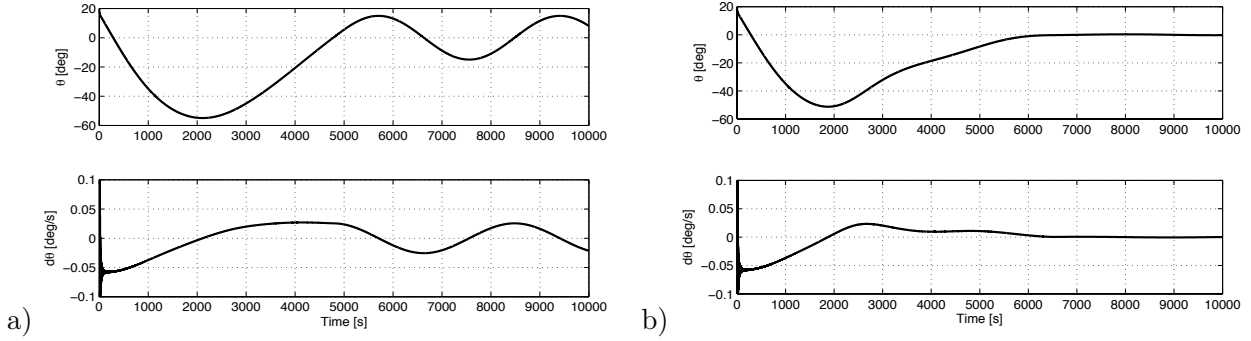


Figure 8.28: In-plane angle starting with  $\theta_0=20^\circ$ ,  $L_{tot}=10\text{km}$ ,  $w=2\text{cm}$ : a)  $T_{deployment} \approx 4750\text{s}$ , b)  $T_{deployment} \approx 6500\text{s}$

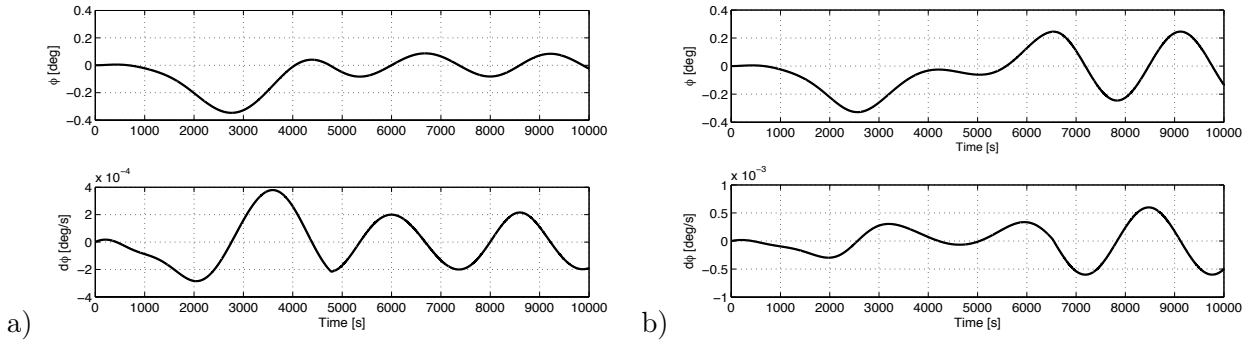


Figure 8.29: Out-of-plane angle starting with  $\theta_0=20^\circ$ ,  $L_{tot}=10\text{km}$ ,  $w=2\text{cm}$ : a)  $T_{deployment} \approx 4750\text{s}$ , b)  $T_{deployment} \approx 6500\text{s}$

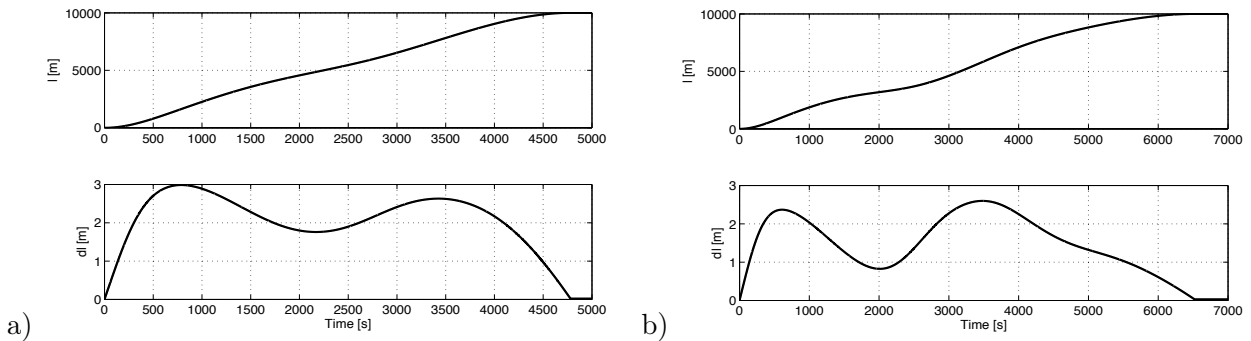


Figure 8.30: Tether Deployment starting with  $\theta_0=20^\circ$ ,  $L_{tot}=10\text{km}$ ,  $w=2\text{cm}$ : a)  $T_{deployment} \approx 4750\text{s}$ , b)  $T_{deployment} \approx 6500\text{s}$

less wide. When the deployment starts with a positive in-plane angle it's possible to provide an initial component of the acceleration  $\ddot{l}$  along the  $y$ -axis that tries to maintain the tip mass in the satellite's wake. In fact two masses orbiting at the same angular velocity  $\omega_{orb}$ , but at diverse heights, have different orbital velocity. In particular the upper part requires a higher value to compensate the distance. So if we increase the component of  $\ddot{l}$  along  $y$  the adding component resulting in  $\dot{l}_y$  tries

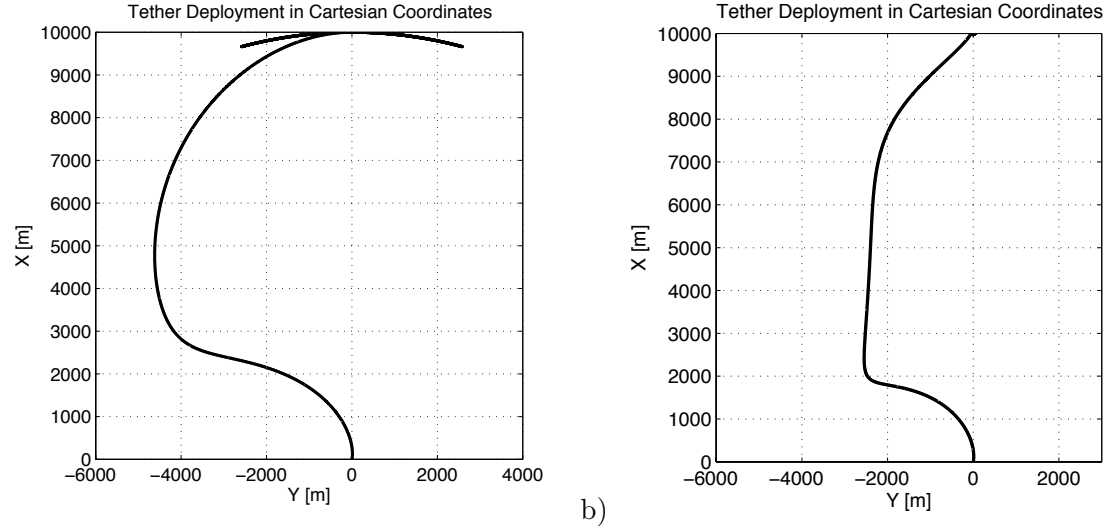


Figure 8.31: Deployment in Cartesian coordinates starting with  $\theta_0=20^\circ$ ,  $L_{tot}=10\text{km}$ ,  $w=2\text{cm}$ : a)  $T_{deployment} \approx 4750\text{s}$ , b)  $T_{deployment} \approx 6500\text{s}$

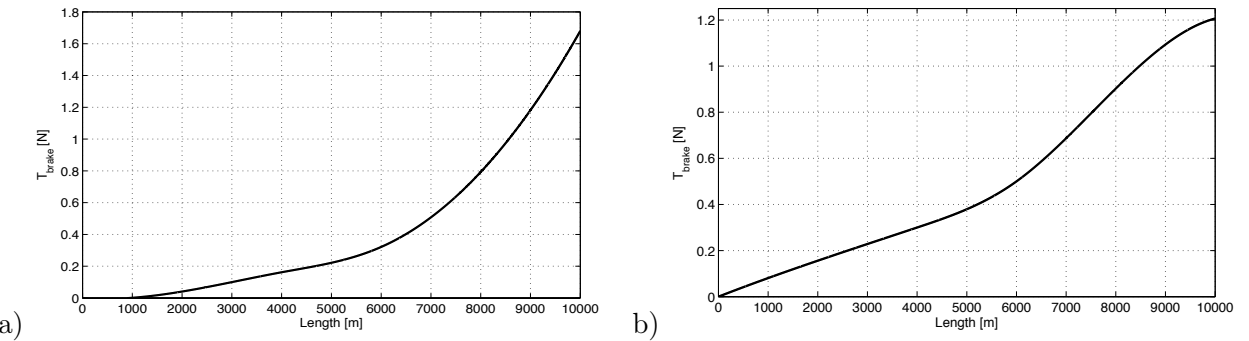


Figure 8.32: Tension along the wire evaluated by means of optimization algorithm, starting with  $\theta_0=20^\circ$ ,  $L_{tot}=10\text{km}$ ,  $w=2\text{cm}$ : a)  $T_{deployment} \approx 4750\text{s}$ , b)  $T_{deployment} \approx 6500\text{s}$

to maintain the libration closer to the local vertical.

At last Figs. 8.27 illustrate the tension profile for each case. It is an increasing function with the time (and so with the tether length), but the switch points must be well evaluated in order to guarantee a successful deployment.

Instead Figs. 8.28-8.32 portray the case of a 10km long tether. It is another interesting configuration, useful for heavy satellite, where longer wires are required to quicken the deorbiting maneuver. We considered the same initial conditions defined before, with an initial in-plane angle equal to  $20^\circ$ . The algorithm found two interesting profiles, which correspond to two different minima of  $F$ : the former is faster ( $T_{deployment} \approx 4750\text{s}$ ), with a final in-plane oscillation about  $15^\circ$  (see the picture on the left in Fig. 8.28); while the latter requires more time ( $T_{deployment} \approx 6500\text{s}$ ), but lets to arrive at the end of deployment with a maximum libration within  $2^\circ$  (on the right in Fig. 8.28).

## 8.7 Control-Brake Strategy

The optimal profile of the friction is the nominal control of the brake that steers the tether along the reference trajectory ( $l_{ref}, \dot{l}_{ref}, \theta_{ref}, \dot{\theta}_{ref}, \varphi_{ref}, \dot{\varphi}_{ref}$ ).

Up to now the deployer has been studied from a mechanical point of view. In this part we want to investigate how to control the deployment following the trajectories just obtained. A new concept for the brake device has been introduced (see Fig. 8.16), acting directly on the reel, instead on the tether as done in previous missions, as for example SEDS II. The following pictures represent a multibody description of the deployer. It has been realized with SIMPACK, a software for the multibody dynamics. Two disks (the magenta elements) mounted on the cylinder (in blue) hold the tether, which is wound around the cylinder itself. The rotational motion of the disks is guaranteed by the bearings (in green), whose internal parts are fixed to the external box (here hidden for the sake of clarity) of the deployer, attached to the satellite. Instead the brake is constituted by a system of two thin bars that can touch the rotating plate slowing down the angular velocity of the reel.

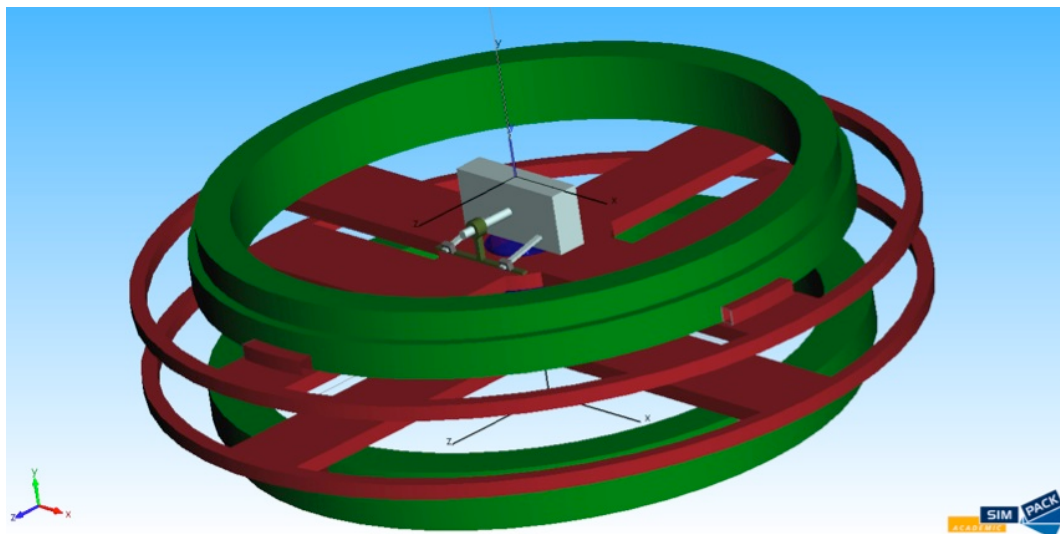


Figure 8.33: Multibody model of the deployer

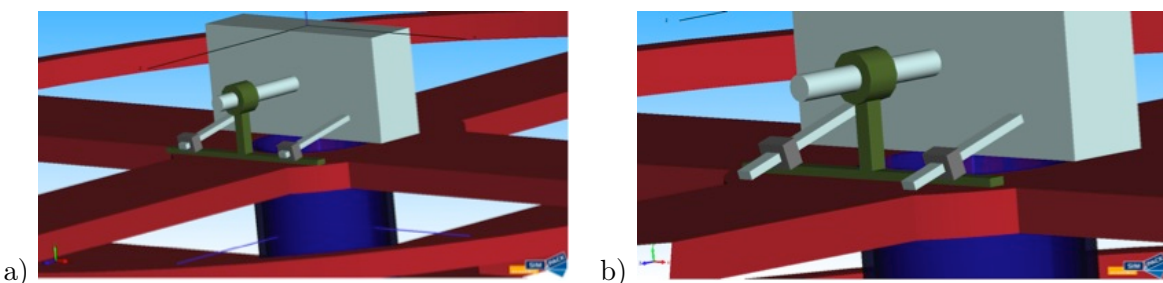


Figure 8.34: Brake mechanism controlled by the stepper motor: a) no contact with the disk, b) contact with the disk and so friction force

The two bars are fixed to the external box of the deployer, so they don't rotate with the reel, and have just only one degree of freedom. They are hinged at one extremity in order to let the contact with the plate at the other one.

Figures 8.33-8.34 provide a representation of the mechanism, realized in this multibody environment. The two bars are constrained to a transversal element that can move back and forth since forced by a stepper motor. As consequence of transversal motion the two bars rotate at the hinge

moving up and down the free extremities, which go in contact with the disk of the reel. The magnitude of the friction force is directly proportional to the normal pressure exercised by the rods on the surface through the friction coefficient. The control has been implemented by means of a co-simulation: the rotation of the reel inside the deployer and brake mechanism are simulated in SIMPACK, instead the comparison of the tether dynamics with the reference trajectory and the feedback force to control the stepper motor are made in SIMULINK.

Figure 8.35 describes the interface realized in SIMULINK to include SIMPACK. It is easy to note how some outputs of SIMULINK are used as input for SIMPACK and viceversa. The reel needs to know the acceleration the tether exits with, in order to deduce the torque applied. The brake system wants the control force to apply for moving the transversal element, and so the two bars. Instead SIMULINK requires the effective friction force affecting the disk and the rotational velocity of the reel in order to obtain the real dynamics of the tether and so the libration, too. At last the trajectory followed is compared with the reference one for creating a feedback force proportional to the errors  $\Delta l$  and  $\Delta \dot{l}$ .

With this strategy it is not possible to apply directly the tension force calculated by the optimization algorithm, but only indirectly by means the contact force. Therefore SIMULINK needs in input the friction torque generated by the brake in order to translate it into a tension along the wire and understand if the device is following the reference one or not. Hence the co-simulation works in this ways

- the reference trajectory, previously evaluated by MATLAB, must be loaded;
- the real motion, is computed, by the Dynamics block (see Fig. 8.36) inside the SIMULINK interface, and sampled in order to simulate the behavior of the sensors, that provide the information every  $\Delta t_{sampling}$ . The block includes also the equation of orbital motion to evaluate the magnetic field and so the electrodynamic torque direction (the electric circuit is maintained closed and a little current is supposed to flow), and the consume of propellant due to the thruster; moreover the block can take into account the disalignment of thruster with respect to the tether due to the attitude dynamics of the tip mass, which can oscillate generating a little torque disturbing in particular the in-plane angle;
- the acceleration  $\ddot{l}$  is translated into a torque for the reel and the feedback force to control the brake is built. Then both are sent to SIMPACK as input;
- the motion of the reel is simulated inside SIMPACK through a multibody system having the same inertial properties. The input torque moves the reel, which makes the tether going out. Then the rotation velocity is measured and given in input to *Dynamics* block to evaluate the length deployed  $l$  and its velocity  $\dot{l}$ ;
- always inside SIMPACK the input force is used to move the brake and to control the motion of the tether. The friction force is measured, translated into a tension along the wire and sent in input to *Dynamics* block to compare it with the reference one;
- at last the feedback force is computed comparing the reference trajectories with those obtained from the numerical model.

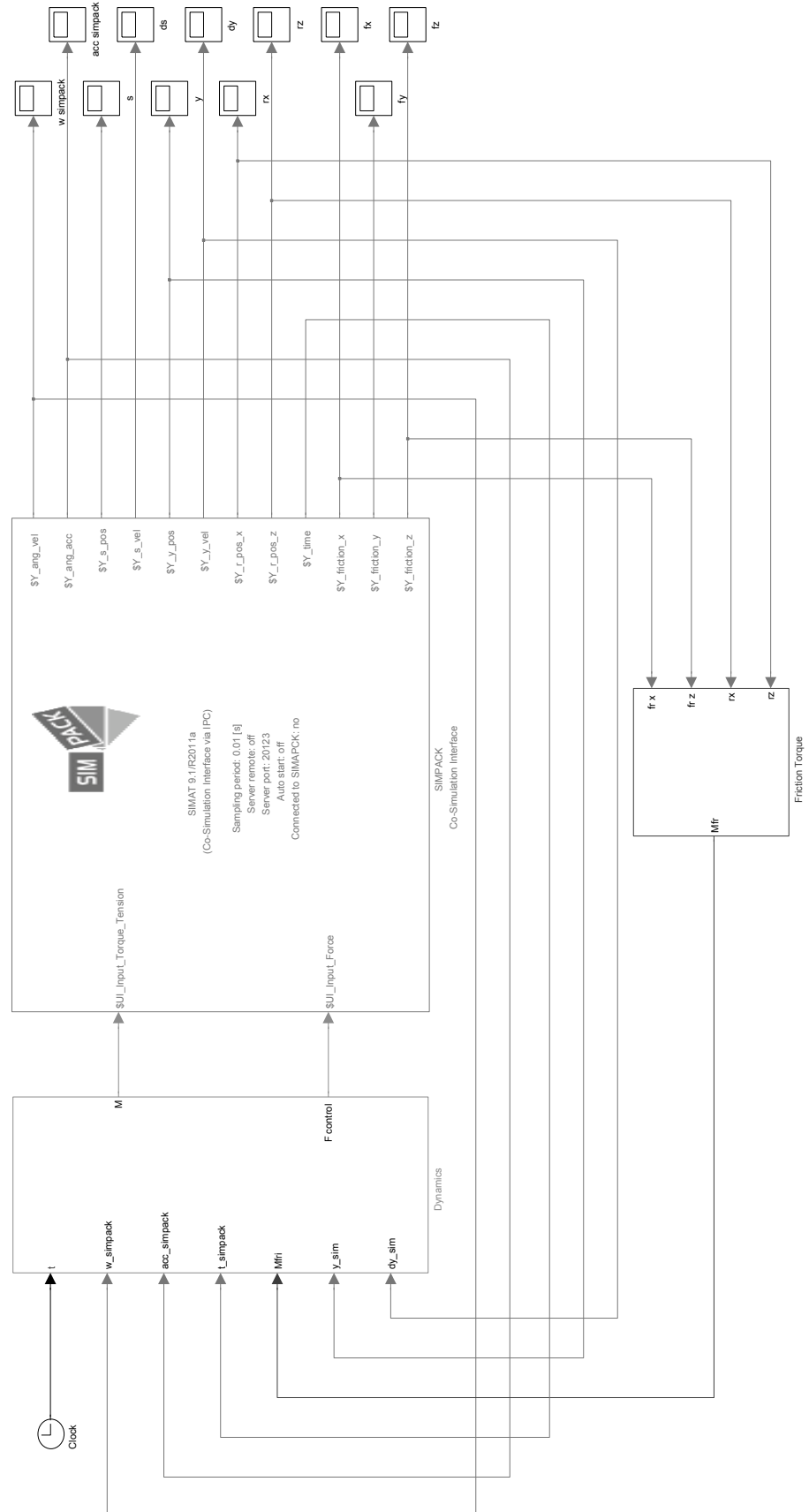


Figure 8.35: SIMULINK-SIMPACK interface

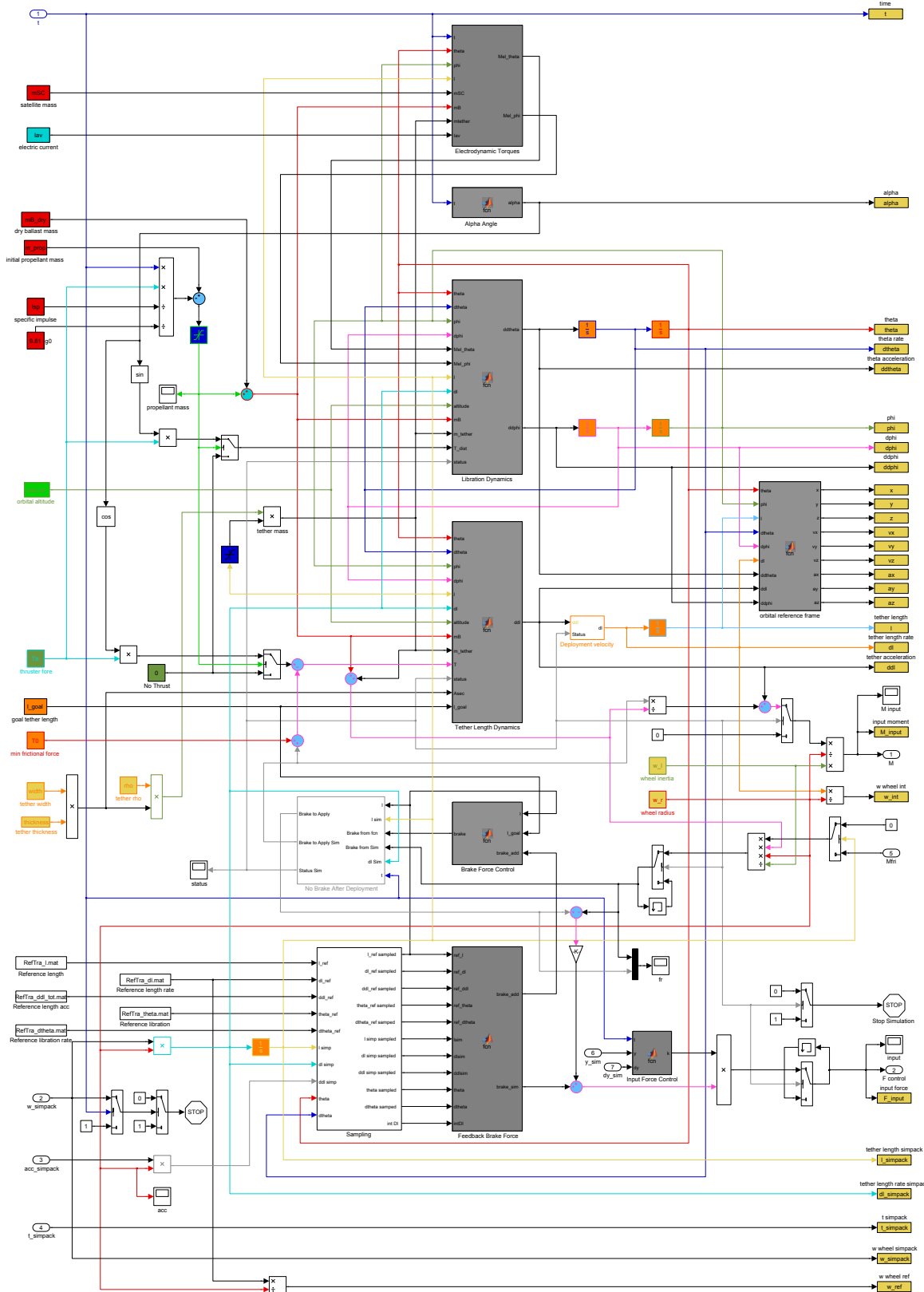


Figure 8.36: SIMULINK dynamics block

## Results

The control system has been tested through some simulations in order to see if the tether follows the desired trajectory giving in input the right initial conditions. Successively we studied the behavior

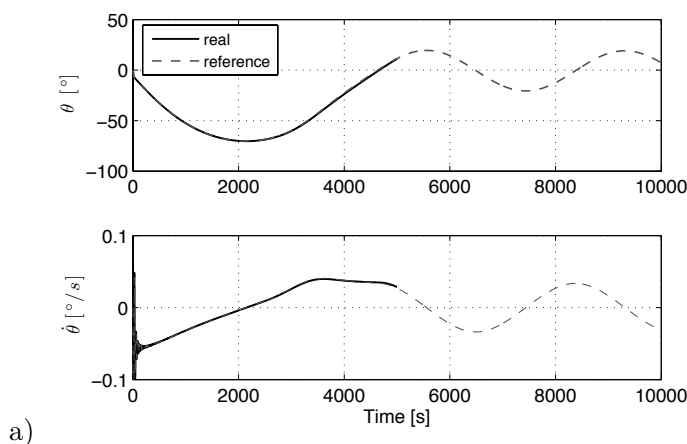
of the brake when there are some initial errors or different conditions respect to those foreseen, in order to see if it can correct such effects or not.

For this campaign of simulations the case of 6km long tether and  $\theta_0=0^\circ$  has been considered as reference trajectory. Figure 8.37 represents the ideal situation where the deployment starts in the same initial conditions foreseen. The brake works very well, and both the librations and the tether deployment (in black in the pictures) follow the reference profiles (in grey) with little and limited errors. If the deployment begins with an initial velocity different from zero ( $\dot{l}_0=0.5\text{m/s}$  in Fig. 8.38) the libration will be affected by this error. Moreover in the SIMULINK Dynamics block we supposed to start the control only after a  $\Delta t=30\text{s}$  (see the zoom of the velocity trend in Fig. 8.38c) in order to be sure that the brake doesn't stop it in the first meters. The brake can well correct the errors about the velocity, but not those introduced into the libration. Furthermore it changes a lot since the feedback input is created as a function of  $\Delta l$  and  $\dot{\Delta l}$  errors. Figure 8.39 illustrates the case where the initially in-plane angle ( $\theta_0=10^\circ$ ) is different from the reference one. As said before, the control can solve very well errors about  $l$  and  $\dot{l}$ , but not about the libration.

The internal friction  $T_0$  of the deployer is one of the most critical point, because very difficult to evaluate accurately, since depends on a lot of parameters. For obtaining the reference profile we supposed it is 0.1N. Now we want to understand what happens if in the real case it is bigger or littler than that value.

In the following graphs we assumed a 20% error, less ( $T_0=0.08\text{N}$ ) in Fig. 8.40, and more ( $T_0=1.2\text{N}$ ) in Fig. 8.41.

The first case is easier to solve because it is just necessary to ask to the brake to work harder, and augment the friction between the two surfaces. In fact the deployment is very close to the reference one. Instead the other case is more critical, because the deployer can't subtract the additional friction or accelerate the reel. Therefore the control starts to work in delay, only when tension along the wire required by the reference profile is higher than the internal friction of the mechanism. This kind of error can be solved supposing to work with a stronger thruster that compensate the increase of the internal friction, but this means a higher consume of propellant and more mass. So an accurate evaluation of the mechanism friction, which depends mainly on the bearings, is necessary in order to improve the control, too.



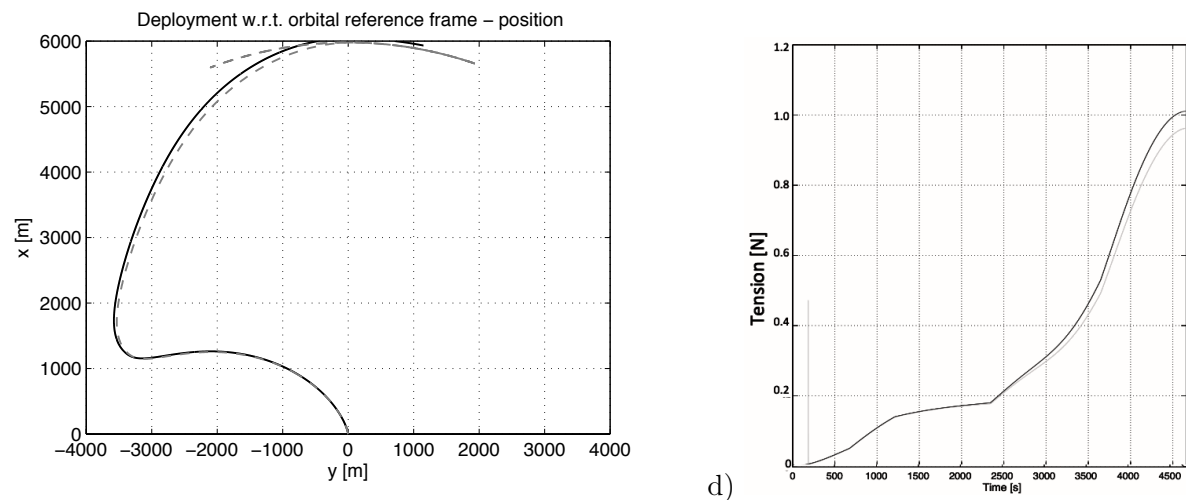
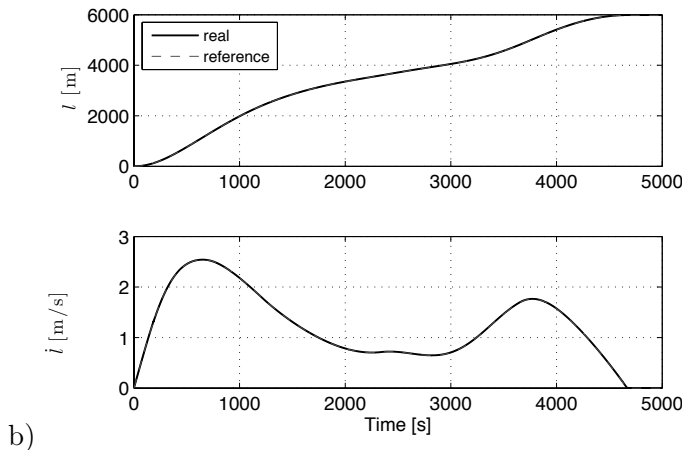
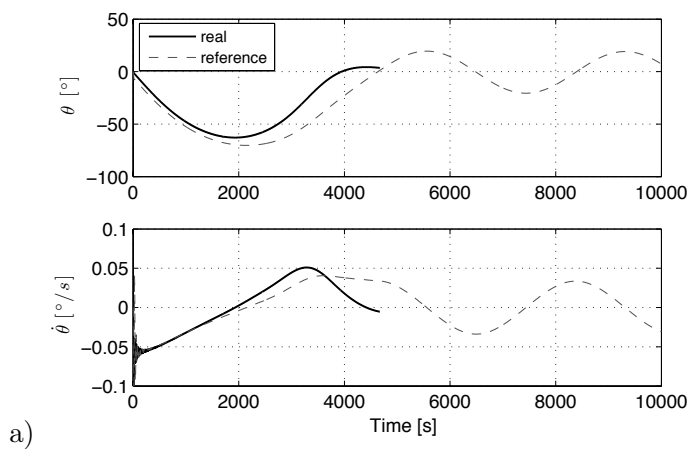
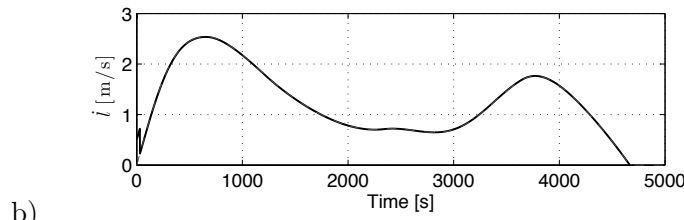
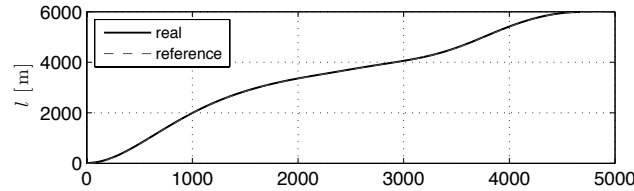
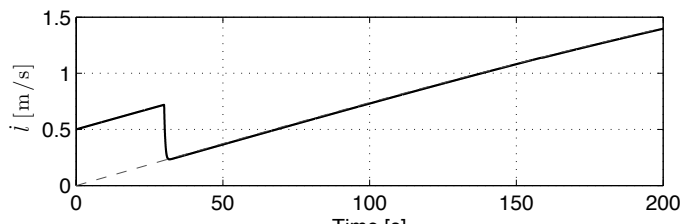


Figure 8.37: Controlled deployment with ( $\theta_0=0^\circ$ ,  $\dot{\theta}_0=0^\circ/s$ ,  $\varphi_0=0^\circ$ ,  $\dot{\varphi}_0=0^\circ/s$ ,  $l_0=0.1\text{m}$ ,  $\dot{l}_0=0\text{m/s}$ ,  $T_0=0.1\text{N}$ ) initial conditions: a) in-plane libration, b) tether deployment, c) tether deployment in Cartesian coordinates, d) tension along the wire: in black the reference one, in gray that generated by the brake mechanism

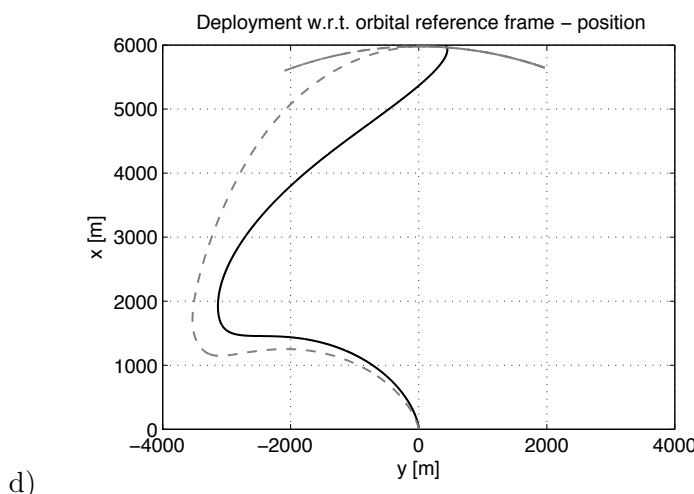




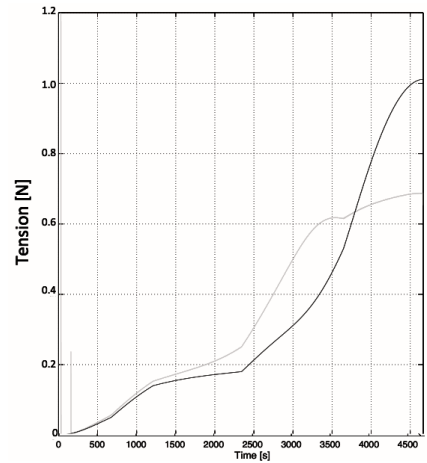
b)



c)



d)



e)

Figure 8.38: Controlled deployment with  $(\theta_0=0^\circ, \dot{\theta}_0=0^\circ/s, \varphi_0=0^\circ, \dot{\varphi}_0=0^\circ/s, l_0=0.1\text{m}, \dot{l}_0=0.5\text{m/s}, T_0=0.1\text{N})$  initial conditions: a) in-plane libration, b) tether deployment, c) zoom of the velocity  $\dot{l}$ , d) tether deployment in Cartesian coordinates, e) tension along the wire: in black the reference one, in gray that generated by the brake mechanism

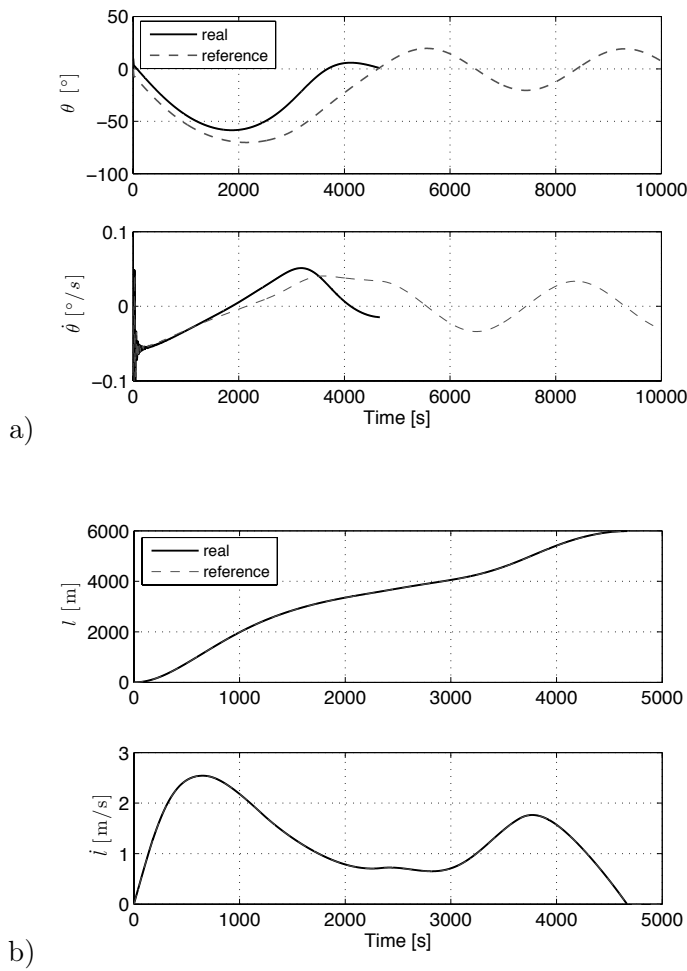


Figure 8.39: Controlled deployment with ( $\theta_0=10^\circ$ ,  $\dot{\theta}_0=0^\circ/s$ ,  $\varphi_0=0^\circ$ ,  $\dot{\varphi}_0=0^\circ/s$ ,  $l_0=0.1m$ ,  $\dot{l}_0=0m/s$ ,  $T_0=0.1N$ ) initial conditions: a) in-plane libration, b) tether deployment, c) tether deployment in Cartesian coordinates, d) tension along the wire: in black the reference one, in gray that generated by the brake mechanism

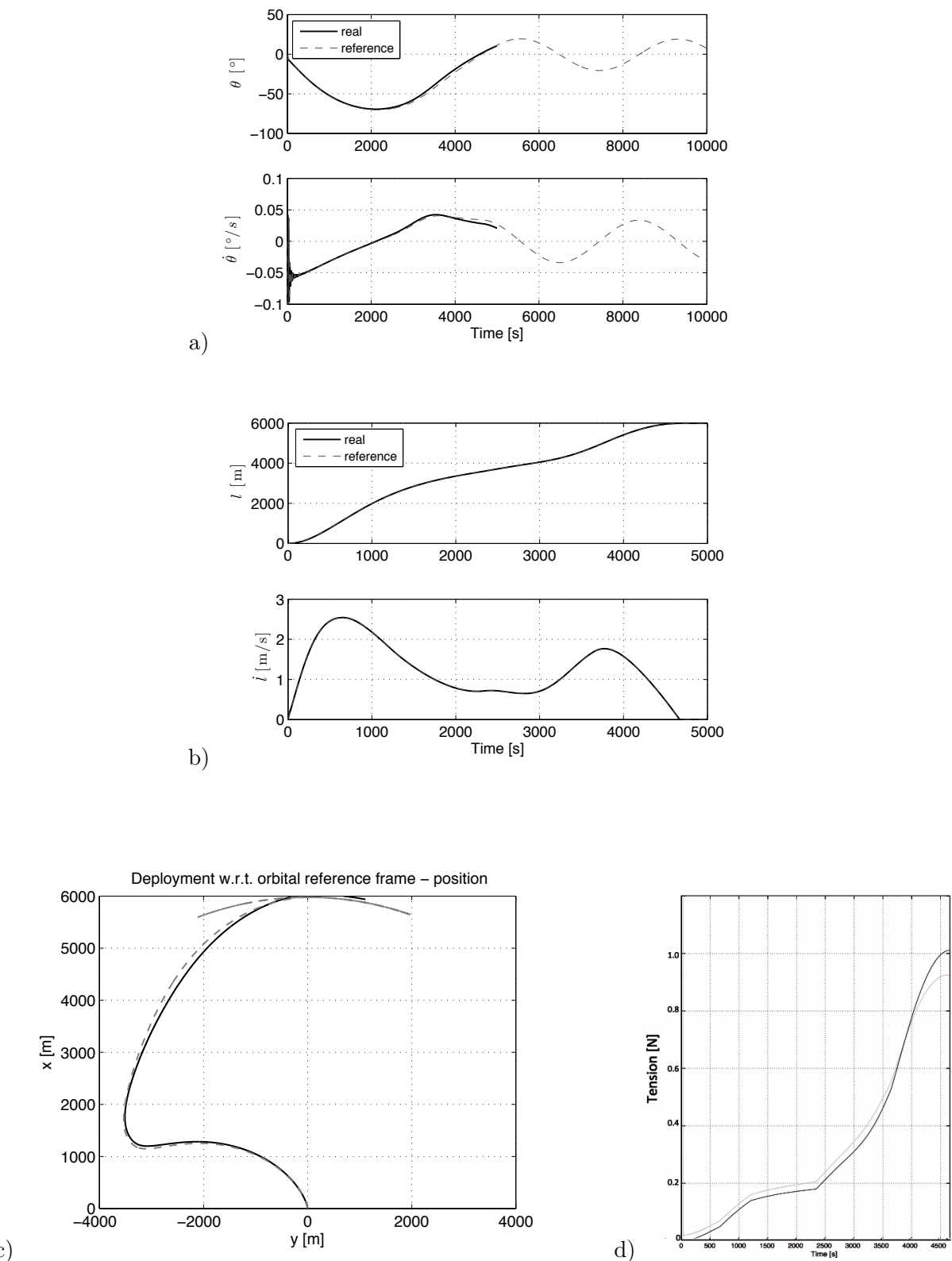


Figure 8.40: Controlled deployment with ( $\theta_0=0^\circ$ ,  $\dot{\theta}_0=0^\circ/s$ ,  $\varphi_0=0^\circ$ ,  $\dot{\varphi}_0=0^\circ/s$ ,  $l_0=0.1m$ ,  $\dot{l}_0=0m/s$ ,  $T_0=0.08N$ ) initial conditions: a) in-plane libration, b) tether deployment, c) tether deployment in Cartesian coordinates, d) tension along the wire: in black the reference one, in gray that generated by the brake mechanism

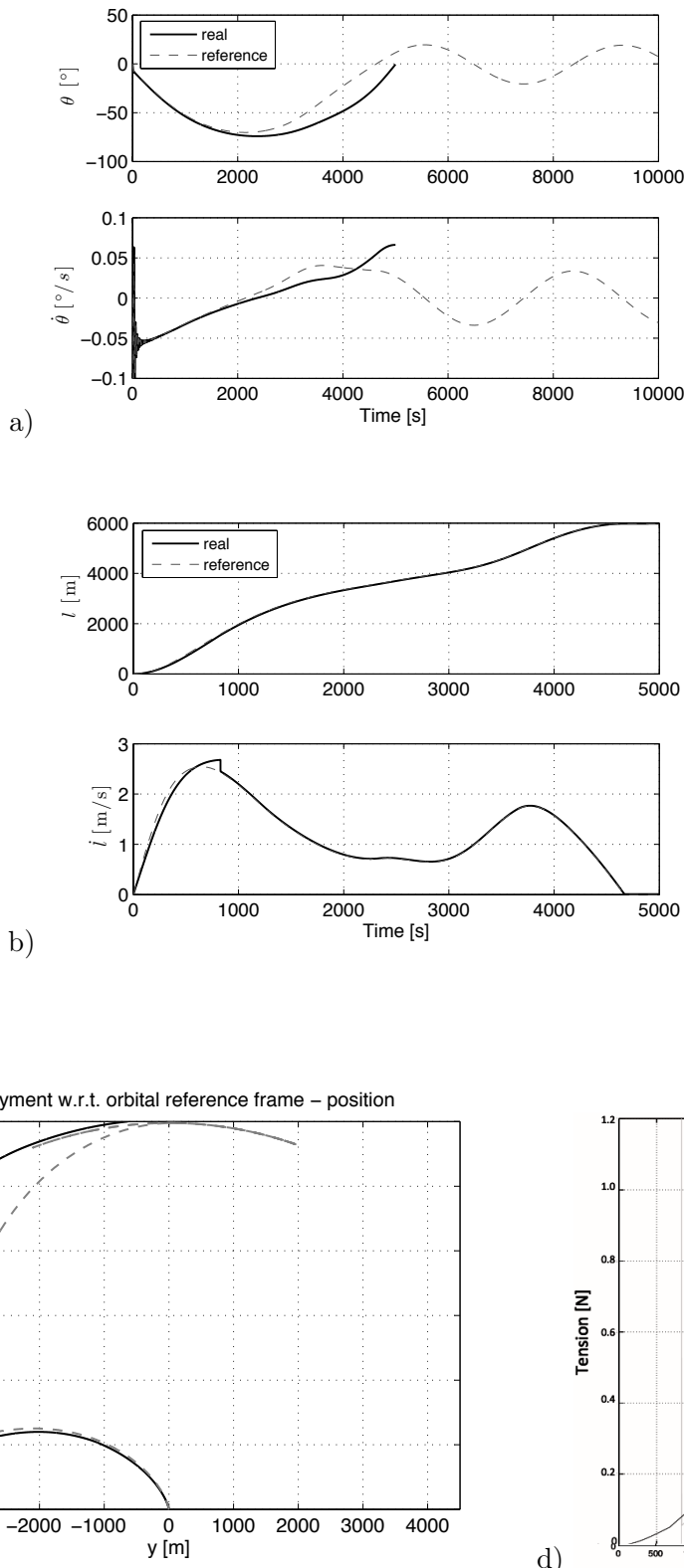


Figure 8.41: Controlled deployment with ( $\theta_0=0^\circ$ ,  $\dot{\theta}_0=0^\circ/\text{s}$ ,  $\varphi_0=0^\circ$ ,  $\dot{\varphi}_0=0^\circ/\text{s}$ ,  $l_0=0.1\text{m}$ ,  $\dot{l}_0=0\text{m/s}$ ,  $T_0=0.12\text{N}$ ) initial conditions: a) in-plane libration, b) tether deployment, c) tether deployment in Cartesian coordinates, d) tension along the wire: in black the reference one, in gray that generated by the brake mechanism

# Chapter 9

## Conclusion

An EDT satellite is a very complex system comprising a lot of features (electrons collection and expulsion by means of cathode, attitude dynamics, deployment, electronics, survival to debris collision,...). The dynamics of the wire has been studied by using several models including all the main forces, torques and features affecting it. Different approaches have been used to simulate the dynamics, thermodynamics and electrodynamics of a bare tethered satellite operating in Earth's orbit. At the beginning the rigid dumbbell model has been utilized to investigate its performance and the main frequencies with spectral analysis. Then the flexible wire model has been adopted to study in detail the effects of the lateral bending on the stability.

The simulator utilizes up-to-date environmental routines for magnetic field, ionosphere, atmosphere and gravity field, and it has been used to simulate the full dynamics of a tethered system during deorbiting of satellites at end of life. Reentry times are rather short when using few-kilometer-long bare tethers that can collect efficiently electrons from the environment to flow intense electric currents along the wire, as we can see from analytical expressions. But mounting longer wire, the increase of the performance occurs to the detriment of the attitude stability.

Without any control the EDT system goes rapidly into instability. The simple dumbbell model has been used for the parametric analysis of the dynamics and to highlight the key parameters affecting the response of an uncontrolled system. In particular the following key parameters have an influence on the system dynamics: the size of the tether (length, width and thickness), the reduced system mass, the orbital parameters (inclination, eccentricity and altitude), and the environment condition (solar activity).

In the past several control strategies have been presented to control the libration dynamics. Each one has been analyzed in order to understand if it can be really used for BETs. These techniques mainly concern on the self-balanced condition, the control of the current or, under very specific assumptions, on the possibility to insert the librational dynamics of the tethered system along a periodic profile. The first technique wants to annul the electrodynamic torque by means of a precise choice of each part forming the tethered system. Instead periodic orbits strategy tries to insert the in-plane and out-of-plane coupled motion into a closed loop in the phase space. In this way the total energy accumulated after a whole oscillation is zero. At last the current control technique opens and closes the circuit as a function of the libration dynamics. When the energy associated with the oscillation of the wire overcomes a fixed threshold the algorithm control turns on the electric current only when the Lorentz force is opposite to the libration. While the third concept is more realistic and easier to obtain (even if limited by electric arches), the other two are much more restricted, in particular periodic orbits exist only in ideal cases with periodic repeating environmental conditions. So a new promising solution has been proposed: a damping mechanism is introduced in the system

for dissipating the energy in excess. In this way it's possible to maintain the system stable all along the decay maneuvers and assure rapid reentry times, because the system always works at the highest performances without dead moments, like happens for the on-off control. This strategy has been studied by means of all the developed codes. The dumbbell, two and three bars models provide very interesting results, but when the also the longitudinal dynamics is included by adopting the lump masses approach we can see that the damper alone is not sufficient to guarantee the stability. However, if it integrated with an inert portion of wire to insert after the conductive one, which increases the gravity gradient torque, then it will assure a rapid and safe reentry.

At last parametric simulations highlights that a tethered system work very well at low inclinations, while the deorbiting becomes more and more long approaching to the polar orbits. This is due to a double geometrical factor: first the component of electromotional field along the tether decreases, and second the main component of Lorentz force becomes the out-of-plane, that doesn't provide drag, but just a variation of the orbital inclinations and more instability. So at low inclinations the reentry is very fast, just few weeks, while at higher ones becomes longer, and tether with better performances are preferable, as seen for the Jason mission scenario.

During the operative life of the satellite the tether must be kept inside a box, wound on a spool. At end of the mission it will deployed for starting the deorbiting. A brief summary on the deployment strategy utilized or proposed in the past has been described in order to find practical solutions that can be used also with a tape tether. Several concepts have been investigated in order to find out the best solution. The analysis highlighted that a reeling system is preferable to a stationary spool because the relatively-wide tape could be twisted while exiting along the axis of the stationary spool and is likely to produce high friction or even to cause jamming. So a non-motorized reeling deployer is well suited for a 1-3 cm wide tape like those planned for BETs. This kind of deployer is quite similar to a stationary one from the point of view of control strategy because the reeling velocity cannot be controlled directly (through a motor) but rather it must be controlled by changing the friction (produced by a brake mechanism).

The first objective was to identify some reference profiles to follow in order to arrive at the end of the deployment satisfying all the requirements. For this reason an optimization code has been written to derive deployment profiles for the case of 6km and 10km tethers, which are representative for the project. In each configuration, half wire is used for the inert portion of the tether that is necessary to provide stability to the attitude motion of the whole system during deorbiting. Some interesting trajectories have been calculated, which guarantee deployment up to the goal length and small final libration amplitudes.

Finally the brake system mounted inside the deployer has been included and simulated to control the tether during deployment. Further cases have been analyzed to demonstrate the capabilities of the control law to provide a successful deployment in the presence of errors or different conditions respect to the foreseen ones.

# Bibliography

## Papers/Reports/Books

- [1] Ahedo, E., and Sanmartín, J. R., “Analysis of Bare-Tether Systems for Deorbiting Low-Earth-Orbit Satellites”, *Journal of Spacecraft and Rockets*, Vol. 39, No. 2, pp. 198-205, March-April 2002.
- [2] Allais, E., and Bergamaschi, S., “Dynamics of Tethered Satellites Two Alternative Concepts for Retrieval”, *Journal of Italian Association of Theoretical and Applied Mechanics*, pp. 103-111, June 1979.
- [3] Battin, R. H., “An Introduction to the Mathematics and Methods of Astrodynamics”, *AIAA Education Series*, Washington, DC, 1987.
- [4] Beletskii, V. V., and Levin, E. M., “Dynamics of the Space Tether System”, *Advances in the Astronautical Sciences*, Vol. 83, 1993.
- [5] Bergamaschi, S., Bonon, F. and Legnami, M., “Spectral Analysis of Tethered Satellite System-Mission 1 Vibrations”, *Journal of Guidance Control and Dynamics*, Vol. 18, No. 3, pp. 618-624, May-June 1995.
- [6] Biesbroek, R. G. J., and Crellin, E. B., “On the Validity of a Simple Bead-Model for Tethered Systems”, 50<sup>th</sup> International Astronautical Congress, Amsterdam, 1999.
- [7] Bilitza, D., “International Reference Ionosphere 2000”, *Radio Science*, Vol. 36, No. 2, pp. 261-275, 2001.
- [8] Bombardelli C., Lorenzini E., Curreli D., Sanjurjo-Rivo M., Lucas F. R., Pelaez J., Scheeres D. J., Lara M., “Io Exploration with Electrodynamic Tethers”, AIAA/AAS Astrodynamics Specialist 2008 Conference, 18-21 August 2008, Honolulu, Hawaii, USA.
- [9] Bombardelli, C., Peláez, J., and Sanjurjo, M., “Asymptotic Solution for the Current Profile of Passive Bare Electrodynamic Tethers”, *Journal of Propulsion and Power*, Vol. 26, No. 6, pp. 1291-1304, November-December 2010.
- [10] Bombardelli, “Power Denisty of a Bare Electrodynamic Tether Generator”, *Journal of Propulsion and Power*, Vol. 28, No. 3, pp. 664-668, May-June 2012.
- [11] Bortolami, S. B., Lorenzini, E. C., Rupp, C. C., and Angrilli, F., “Control Law for the Deployment of SEDS - II”, AAS/AIAA Astrodynamics Conference, Victoria, pp. 733-748, 16-19 August 1993.

- [12] Bruno, L. I. C., Ulivieri, C., and Vannaroni, G., "Satellite De-Orbiting by Means of Electrodynamic Tethers Part 2: System Configuration and Performance", *Acta Astronautica*, Vol. 50, No. 7, pp. 407-416, 2002.
- [13] Carroll, J. A., "SEDS Deployer Design and Flight Performance", Paper WSEDS-A-1 at the 4th International Conference on Tethers In Space, Washington DC, April 1995.
- [14] Chapel, J. D., and Grosserode, P., "Precession and Circularization of Elliptical Space-Tether Motion", AIAA Guidance, Navigation and Control Conference, Monterey, CA, pp. 147-156, August 9-11, 1993.
- [15] Cleghorn, G. et al., "Orbital Debris: a Technical Assessment", National Academy Press, Washington, 1995.
- [16] Colombo, G., et al., "Skyhook Report", Smithsonian Astrophysical Observatory, Cambridge, MA, 1974.
- [17] Corsi, J., and Iess, L., "Stability and control of electrodynamic tethers for de-orbiting applications", *Acta Astronautica*, Vol. 48, pp. 491-501, March 2001.
- [18] Cosmo, M., Lorenzini, E. C., Vetrella, S., and Moccia, A., "Transient Dynamics of the Tether Elevator/Crawler System", AIAA/AAS Astrodynamics Conference, Minneapolis, Minnesota, 15-17 August 1988.
- [19] Cosmo, M., and Lorenzini, E. C., "Electrodynamic Tethers in space handbook", Special Report under Grant NAG8-1160 Third Edition, NASA Marshall Space Flight Center, Dec. 1997.
- [20] Dobrowolny, M., Vannaroni, G., and De Venuto, F., "Electrodynamic deorbiting of LEO satellites", *Il Nuovo Cimento*, Vol. 23, No. 1, pp. 85-105, January-February 2000.
- [21] Dobrowolny, M., "Lateral Oscillations of an Electrodynamic Tether", *Journal of the Astronautical Sciences*, Vol. 50, No. 2, pp. 125-147, 2002.
- [22] Ellis, J. R., and Hall, C. D., "Model Development and Code Verification for Simulation of Electrodynamic Tether System", *Journal of Guidance Control and Dynamics*, Vol. 32, No. 6, pp. 1713-1722, November-December 2009.
- [23] Estes, R. D., and Sanmartín, J. R., "Cylindrical Langmuir probes beyond the orbital-motion-limited regime", *Physics of Plasmas*, Vol. 7, pp. 4320-4325, October 2000.
- [24] Estes, R. D., Sanmartín, J. R., and Martínez-Sánchez, "Performance of Bare-Tether Systems Under Varying Magnetic and Plasma Conditions", *Journal of Spacecraft and Rockets*, Vol. 37, No. 2, pp. 197-204, March-April 2000.
- [25] Estes, R. D., Lorenzini, E. C., Sanmartín, J. R., Peláez, J., Martínez- Sánchez, M., Johnson, C. L., and Vas, I. E., "Bare Tethers for Electrodynamic Spacecraft Propulsion", *Journal of Spacecraft and Rockets*, Vol. 37, No. 2, pp. 205-211, March-April 2000.
- [26] Fujii, H. A., and Uchiyama, K., "Mission Function Control of Tethered Subsatellite Deployment/Retrieval: In-Plane and Out-of-Plane Motion", *Journal of Guidance Control and Dynamics*, Vol. 14, No. 2, pp. 471-473, March-April 1991.

- [27] Fujii, H. A., and Uchiyama, K., "Deployment/Retrieval Control of a Tethered Subsatellite under Aerodynamic Effect of Atmosphere", *The Journal of the Astronautical Science*, Vol. 40, No. 2, pp. 171-188, March-April 1992.
- [28] Fujii, H. A., and Anazawa, S., "Deployment/Retrieval Control of Tethered Subsatellite Through an Optimal Path", *Journal of Guidance Control and Dynamics*, Vol. 17, No. 6, pp. 1292-1298, November-December 1994.
- [29] Fujii, H. A., Miyahara, Y., and Ichiki, W., "Optimal Trajectories for Deployment/Retrieval of Tethered Subsatellite", International Symposium on Space Technology and Science, 20<sup>th</sup>, Gifu, Japan, pp. 390-395, 19-25 May 1996.
- [30] Fujii, H. A., and Ichiki, W., "Nonlinear Dynamics of the Tethered Subsatellite System in the Station Keeping Phase", *Journal of Guidance Control and Dynamics*, Vol. 20, No. 2, pp. 403-406, March-April 1997.
- [31] Fujii, H. A., Ichiki, W., Suda, S., and Watanabe, T. R., "Chaos Analysis on Librational Control of Gravity-Gradient Satellite in Elliptic Orbit", *Journal of Guidance Control and Dynamics*, Vol. 23, No. 1, pp. 145-146, 2000.
- [32] Fujii, H. A., Watanabe, T., Kojima, H., Oyama, K., et al., "Sounding Rocket Experiment of Bare Electrodynamic Tether System", *Acta Astronautica*, Vol. 64, pp. 313-324, 2009.
- [33] Fujii, H. A., Watanabe, Sahara, H., T., Kojima, H., Takeara, S., and al., "Space Demonstration of Bare Electrodynamic Tape-Tether Technology on the Sounding Rocket S520-25", AIAA Guidance Navigation and Control Conference, Portland, Oregon, 8-11 August 2011.
- [34] Farquhar, R., "Tether Stabilization at a Collinear Libration Point", *Journal of the Astronautical Sciences*, Vol. 49, No. 1, 2001.
- [35] Hover, F. S., "Simulation of Stiff Massless Tethers", *Elsevier Science*, Vol. 24, No. 8, pp. 765-783, 1997.
- [36] Iess, L., Bruno, C., Ulivieri, C., Ponzi, U., Parisse, M., Laneve, G., Vannaroni, G., Dobrowolny, M., Venuto, F. D., Bertotti, B., and Anselmo, L., "Satellite De-Orbiting by Means of Electrodynamic Tethers Part 1: General Concepts and Requirements", *Acta Astronautica*, Vol. 50, No. 7, pp. 399-406, 2002.
- [37] Iñarrea, M., and Peláez, J., "Libration Control of Electrodynamic Tethers Using the Extended Time-Delayed Autosynchronization Method", *Journal of Guidance Control and Dynamics*, Vol. 33, No. 3, pp. 923-933, May-June 2010.
- [38] Ishige, Y., Kawamoto, S., and Kibe, S., "Study on Electrodynamic Tether System for Space Debris Removal", *Acta Astronautica*, Vol. 55, pp. 917-929, August 2004.
- [39] Kalantzis, S., Modi, V. J., and Pradhan, S., "Dynamics and Control of Multibody Tethered Systems", *Acta Astronautica*, Vol. 42, No. 9, pp. 503-517, 1998.
- [40] Kawamoto, S., Makida, T., Sasaki, F., Okawa, Y., and Nishida, S., "Precise Numerical Simulations of Electrodynamic Tethers for an Active Debris Removal System", *Acta Astronautica*, Vol. 59, pp. 139-148, 2006.

- [41] Kim, M. and Hall, C. D., "Control of a Rotating Variable-Length Tethered System", 13th AAS/AIAA Space Flight Mechanics Meeting, Ponce, Puerto Rico, February 9-13, 2003.
- [42] Kojima H., Iwasaki, M., Fujii, H. A., Blanksby, C., and Trivailo, P., "Nonlinear Control of Librational Motion of Tethered Satellites in Elliptic Orbits", *Journal of Guidance Control and Dynamics*, Vol. 27, No. 2, pp. 229-239, March-April 2004.
- [43] Kojima H., and Sugimoto, T., "Stability analysis of in-plane and out-of-plane periodic motions of electrodynamic tether system in inclined elliptic orbit", *Acta Astronautica*, Vol. 65, pp. 477-488, 2009.
- [44] Kokubun, K., and Fujii, H. A., "Deployment/Retrieval Control of a Tethered Subsatellite under Aerodynamic Effect of Tether Elasticity", *Journal of Guidance Control and Dynamics*, Vol. 19, No. 1, pp. 84-90, January-February 1996.
- [45] Kokubun, K., Anazawa, S., and Fujii, H. A., "Real-TIME Optimal State Feedback Control for Tethered Subsatellite System", *Journal of Guidance Control and Dynamics*, Vol. 19, No. 4, pp. 972-974, July-August 1996.
- [46] Koss, S., "Tether Deployment Mechanism for the Advanced Tether Experiment (ATEx)", Proceedings of 7<sup>th</sup> European Space Mechanism and Tribology Symposium, ESTEC, Noordwijk, 1-3 October 1997.
- [47] Kruijff, M., and Van Der Heide, E. J., "Qualification and In-Flight Demonstration of a European Tether Deployment System on YES2", *Acta Astronautica*, Vol. 64, No. 9-10, pp. 882-905, May-June 2009.
- [48] Lanoix, E. L. M., Misra, A. K., Modi, V. J., and Tyc, G., "Effect of Electrodynamic Forces on the Orbital Dynamics of Tethered Satellites", *Journal of Guidance Control and Dynamics*, Vol. 28, No. 6, pp. 1309-1315, November-December 2005.
- [49] Lara, M., and Peláez, J., "On the Numerical Continuation of Periodic Orbits: An Intrinsic, 3-Dimensional, Differential, Predictor-Corrector Algorithm", *Astronomy and Astrophysics*, Vol. 389, No. 2, pp. 692-701, July II, 2002.
- [50] Larsen, M. B., and Blanke, M., "Nonlinear Control of Electrodynamic Tether in Equatorial or Somewhat Inclined Orbits", Mediterranean Conference on Control and Automation, Athens, July 27-29, 2007.
- [51] Leamy, M. J., Noor, A. K., and Wasfy, T. M., "Dynamics Simulation of a Tethered Satellite Using Finite Elements and Fuzzy Sets", *Computer Methods in Applied Mechanics and Engineering*, Vol. 190, pp. 4847-4870, 2001.
- [52] Leamy, M. J., Noor, A. K., and Wasfy, T. M., "Sensitivity Analysis of Bare-Wire Space Tether Systems", *Computer Methods in Applied Mechanics and Engineering*, Vol. 190, pp. 5495-5503, 2001.
- [53] Liangdong, L., "Effect of Tether Flexibility on the Tethered Shuttle Subsatellite Stability and Control", PSN-NASA-AIDAA Second International Conference on Tethers in Space, Venice, 4-8 October 1987.

- [54] Cosmo, M., Lorenzini, E. C., Vetrella, S., and Moccia, A., "Dynamics and Control of the Tether Elevator/Crawler System", *Journal of Guidance Control and Dynamics*, Vol. 12, No. 3, pp. 404-411, May-June 1988.
- [55] Lorenzini, E. C., Bortolami, S. B., Rupp, C. C., and Angrilli, F., "Control and Flight Performance of Tethered Satellite Small Expendable Deployment System - II", *Journal of Guidance Control and Dynamics*, Vol. 19, No. 5, pp. 1148-1156, September-October 1996.
- [56] Lorenzini, E. C., Welzyn, K., and Cosmo, M. L., "Expected Deployment Dynamics of ProSEDS", Joint Propulsion Conference and Exhibit, Alabama, July 2003.
- [57] Lorenzini, E. C., Estes, R. D., Cosmo, M. L., Sanmartín, J., Peláez, J., and Ruiz, M., "The Propulsive Small Expendable Deployer System (PROSEDS)", Technical Report, December 2003.
- [58] Mankala, K. K., and Agrawal, S. K., "Equilibrium to Equilibrium Maneuvers of Rigid Electrodynamic Tethers"
- [59] Matunaga, S., Mori, O., Nakaya, K., Iai, M., Omagari, K., Yabe, H., et al. "New Spinning Deployment Method of Large Thin Membranes with Tether Control", 54th Congress of the International Astronautical Federation, Bremen, Germany, September 29 - October 3, 2003.
- [60] Menon, C., Kruijff, M., and Vavouliotis, A., "Design and Testing of a Space Mechanism for Tether Deployment", *Journal of Spacecraft and Rockets*, Vol. 44, No. 4, pp. 927-939, July-August 2007.
- [61] Misra, A. K., and Modi, V. J., "A Survey on the Dynamics and Control of Tethered Satellite Systems", *Advances in the Astronautical Sciences*, Vol. 62, pp. 667-719, 1987.
- [62] Nakaya, K., Iai, M., Omagari, K., Yabe, H., and Matunaga, S., "Formation Deployment Control for Spinning Tethered Formation Flying-Simulations and Ground Experiments", AIAA Guidance, Navigation, and Control Conference and Exhibit, AIAA 2004-4896, Providence, Aug.16-19 2004.
- [63] Nakaya, K., Iai, M., Mori, O., and Matunaga, S., "On Formation Deployment For Spinning Tethered Formation Flying and Experimental Demonstration", Proceedings of the 18<sup>th</sup> International Symposium on Space Flight Dynamics, ESA SP-548, Munich, Germany, pp. 531- 536, 11-15 October 2004.
- [64] NASA, "Orbital Debris Program Office", United Nations, New York, Sales No. E.99.I.17, ISBN 92-1-100813-1, 1999.
- [65] Nelder, J. A., and Mead, R., "A Simplex Method for Function Minimization", Computer Journal, Vol. 7, pp. 308-313, 1965.
- [66] Netzer, E., and Kane, T. R., "Electrodynamic Forces in Tethered Satellite System. Part I: System Control", *IEEE Transaction on Aerospace and Electronic Systems*, Vol. 30, No. 4, pp. 1031-1038, October 1994.
- [67] Netzer, E., and Kane, T. R., "Electrodynamic Forces in Tethered Satellite System. Part II: Orbit Transfer", *IEEE Transaction on Aerospace and Electronic Systems*, Vol. 30, No. 4, pp. 1039-1043, October 1994.

- [68] Ohtsuka, T., "Nonlinear Optimal Feedback Control for Deployment/Retrieval of a Tethered Satellite", *Transactions of the Japan Society for Aeronautical and Space Sciences*, Vol. 43, No. 142, pp. 165-173, 2001.
- [69] Pasca, M., and Lorenzini, E. C., "Two Analytical Models for the Analysis of a Tethered Satellite System in Atmosphere", *Meccanica*, Vol. 32, No. 4, pp. 263-277, 1997.
- [70] Peláez, J., Lorenzini, E. C., López-Rebollar, O., and Ruiz, M., "A New Kind of Dynamic Instability in Electrodynamic Tethers", *The Journal of the Astronautical Sciences*, Vol. 48, No. 4, pp. 449-476, October-December 2000.
- [71] Peláez, J., López-Rebollar, O., Lara, M., and Ahedo, E., "Dynamic Stability of a Bare Tether as a Deorbiting Device", *Advances in the Astronautical Sciences*, Vol. 112, No. 2, pp. 1257-1274, 2002.
- [72] Peláez, J., Ruiz, M., López-Rebollar, O., Lorenzini, E. C., and Cosmo, M. L., "Two Bar Model for Two Bar Model for the Dynamics and Stability of Electrodynamic Tethers", *Journal of Guidance Control and Dynamics*, Vol. 25, No. 6, pp. 1125-1135, November-December 2002.
- [73] Peláez, J., and Lara, M., "Periodic Solutions in Electrodynamic Tethers on Inclined Orbit", *Journal of Guidance Control and Dynamics*, Vol. 26, No. 3, pp. 395-406, May-June 2003.
- [74] Peláez, J., Sanjurjo, M., and Fontdecaba, J., "Satellite Deorbiting Using a Self Balanced Electrodynamic Tether", 55<sup>th</sup> International Astronautical Congress, Vancouver, Canada, 2004.
- [75] Peláez, J., and Lorenzini, E. C., "Libration Control of Electrodynamic Tethers in Inclined Orbit", *Journal of Guidance Control and Dynamics*, Vol. 28, No. 2, pp. 269-279, March-April 2005.
- [76] Peláez, J., and Andrés, Y. N., "Dynamic Stability of Electrodynamic Tethers in Inclined Elliptical Orbits", *Journal of Guidance Control and Dynamics*, Vol. 28, No. 4, pp. 611-622, July-August 2005.
- [77] Peláez, J., and Sanjurjo, M., "Generator Regime of Self-Balanced Electrodynamic Tethers", *Journal of Spacecraft and Rockets*, Vol. 43, No. 6, pp. 1359-1369, November-December 2006.
- [78] Pradhan, S., Modi, V. J., and Misra, A. K., "Tether-Platform Coupled Control", *Acta Astronautica*, Vol. 44, No. 5, pp. 243-256, 1999.
- [79] Quadrelli, M., "Modeling and Dynamics Analysis of Tethered Formations for Space Interferometry", AAS/AIAA Spaceflight Mechanics Meeting, Santa Barbara, CA, February 11-14, 2001.
- [80] Roithmayr, C. M., "Contributions of Spherical Harmonics to Magnetic and Gravitational Fields", Langley Research Center, Hampton, Virginia, NASA/TM-213007, 2004.
- [81] Ruiz, M., López-Rebollar, O., Lorenzini, E., and Pelaez, J., "Modal Analysis of the Stability of Periodic Solutions in Electrodynamic Tethers", *Advances in the Astronautical Sciences*, Vol. 109, No. 2, pp. 1553-1570, 2001.
- [82] Samanta Roy, R. I., Hastings, D. E., and Ahedo, E., "System Analysis of Electrodynamic Tethers", *Journal of Spacecraft and Rocket*, Vol. 29, No. 3, pp. 415-424, May-June 1992.

## BIBLIOGRAPHY

---

- [83] Sanjurjo, M. R., "Self Balanced Bare Electrodynamic Tethers. Space Debris Mitigation and other Applications", PhD Thesis, 2009.
- [84] Sanjurjo, M. R., and Peláez, J., "Energy Analysis of Bare Electrodynamic Tethers", *Journal of Propulsion and Power*, Vol. 27, No. 1, January-February 2011
- [85] Sanmartín, J., Martínez-Sánchez, M., and Ahedo, E., "Bare Wire Anodes for Electrodynamic Tethers", *Journal of Propulsion and Power*, Vol. 9, No. 3, pp. 353-360, May-June 1993.
- [86] Sanmartín, J., Martínez-Sánchez, M., and Ahedo, E., "The Orbital-Motion-Limited Regime of Cylindrical Langmuir Probes", *Physics of Plasma*, Vol. 6, No. 1, pp. 395-405, January 1999.
- [87] Sanmartín, J. R., and Estes, R. D., "Magnetic Self-Field on Bare-Tether Current Collection", 2001ESASP.476..531S
- [88] Sanmartín, J. R., Ahedo, E., Conde, L., Peláez, J., and Ruiz, M., "Short Electrodynamic Tethers", Spacecraft Charging Technology, Proceedings of the 7<sup>th</sup> International Conference, ESTEC, Noordwijk, the Netherlands, pp. 581-585, 23-27 April 2001.
- [89] Sanmartín, J. R., Charro, M., Bramanti, C., and Bombardelli, C., "Electrodynamic Tether Microsats at the Giant Planets", Ariadna Study/05/3203, ESA.
- [90] Sanmartín, J. R., "A Review of Electrodynamic Tethers for Science Applications", *Plasma Sources Science Technology*, Vol. 19, 2010.
- [91] Sanmartín, J., Lorenzini, E. C., and Martínez-Sánchez, M., "Electrodynamic Tether Applications and Constraints", *Journal of Spacecraft and Rocket*, Vol. 47, No. 3, pp. 442-456, May-June 2010.
- [92] Sanmartin, J. R., Khan, S. B., Bombardelli, C., Lorenzini, E. C., Colombatti, G., Zanutto, D. et al., "Propellantless Deorbiting of Space Debris by Bare Electrodynamics Tethers", 62<sup>nd</sup> International Astronautical Congress, Cape Town, South Africa, October 2011.
- [93] Sanmartin, J. R., Khan, S. B., Bombardelli, C., Lorenzini, E. C., Colombatti, G., Zanutto, D. et al., "An Universal System to De-Orbit Satellites at the End of Life", *Journal of Space Technology and Science*, Japanese Rocket Society, Vol. 26, No. 1, pp. 21-32, 2012.
- [94] Sanyal, A. K., Shen, J., and McClamroch, N. H., "Dynamics and Control of an Elastic Dumbbell Spacecraft in a Central Gravitational Field", Proceedings of the 42<sup>nd</sup> IEEE Conference on Decision and Control, Hawaii, pp. 2798-2803, December 2003.
- [95] Servin, M., and Lacoursière, C., "Massless Cable for Real-Time Simulation", *Computer Graphics Forum*, Vol. 26, No. 2, pp. 172-184, 2006.
- [96] Sidorenko, V. V., and Celletti, A., "A Spring-Mass Model of Tethered Satellite Systems: Properties of Planar Periodic Motions", *Celestial Mechanics*, Vol. 107, pp. 209-231, 2010.
- [97] Somenzi, L., Iess, L., and Peláez, J., "Linear Stability Analysis of Flexible Electrodynamic Tethers", *American Astronautical Society*, Paper AAS03-539, 2003.
- [98] Steindl, A., and Troger, H., "Optimal Control of Deployment of a Tethered Subsatellite", *Non-linear Dynamics*, Vol. 31, pp. 257-274, 2003.

- [99] Steiner, W., Zemann, J., Steindl, A., and Troger, H., "Numerical Study of Large Amplitude Oscillations of a Two-Satellite Continuous Tether System With a Varying Length", *Acta Astronautica*, Vol. 35, No. 9, pp. 607-621, 1995.
- [100] Takeichi, N., Natori, M. C., and Okuzumi, N., "In-Plane/out-of-Plane Librations of a Tethered System in Elliptical Orbits", *Transactions of the Japan Society for Aeronautical and Space Sciences*, Vol. 43, No. 142, pp. 196-202, February 2001.
- [101] Takeichi, N., "Practical Operation Strategy for Deorbit of an Electrodynamic Tethered System", *Journal of Spacecraft and Rockets*, Vol. 43, No. 6, pp. 1283-1288, November-December 2006.
- [102] Thompson, D. C., Bonifazi, C., Gilchrist, E. G., Williams, S. D., Raitt, W. J., Lebreto, J. P., Burke, W. J., Stone, N. H., and Wright, K. H., "The current-voltage characteristics of a large probe in low Earth orbit: TSS-1R results", *Geophysical Research Letters*, Vol. 25, No. 4, pp. 413-416, February 1998.
- [103] Vallado, D., and McClain, W. D., "Fundamentals of astrodynamics and applications", Space Technology Library, Kluwer Academic Publishers, Second Edition, 2004
- [104] Van de Heijning, S., and Zandbergen, B., "Testing of a Tether Deployment System Using a Cold Gas Thruster", 56<sup>th</sup> International Astronautical Congress, 2005.
- [105] Vestroni, F., Luongo, A., and Pasca, M., "Stability and Control of Transversal Oscillations of a Tethered Satellite System", *Applied Mathematics and Computation*, Vol. 70, pp. 343-360, 1995.
- [106] Xianrem, K., Dafu, X., and Jun, L., "Dynamics of Electrodynamic Tether Deorbiting System for LEO Satellites", 3<sup>rd</sup> International Symposium on Systems and Control in Aeronautics and Astronautics (ISSCAA), Harbin, pp. 550-555, 8-10 June 2010.
- [107] Yamaigiwa, Y., Hiragi, E., and Kishimoto, T., "Dynamic Behavior of Electrodynamic Tether Deorbit System on Elliptical Orbit and Its Control by Lorentz Force", *Aerospace Science and Technology*, Vol. 9, pp. 366-373, 2005.
- [108] Williams, P., Watanabe, T., Blanksby, C., Trivalio, P., and Fujii, H. A. "Libration Control of Flexible Tethers Using Electromagnetic Forces and Movable Attachment", *Journal of Guidance Control and Dynamics*, Vol. 27, No. 5, pp. 882-897, September-October 2004.
- [109] Williams, P., "Deployment/Retrieval Optimization for Flexible Tethered Satellite Systems", *Nonlinear Dynamics*, Vol. 52, pp. 159-179, 2008.
- [110] Williams, P., Hyslop, A., Stelzer, M., and Kruijff, M., "YES2 Optimal Trajectories in Presence of Eccentricity and Aerodynamic Drag", *Acta Astronautica*, Vol. 64, pp. 745-769, 2009.
- [111] Williams, P., "Libration Control of Electrodynamic Tethers Using Predictive Control with Time-Delayed Feedback", *Journal of Guidance Control and Dynamics*, Vol. 32, No. 4, pp. 1254-1268, July-August 2009.
- [112] Williams, P., "Dynamic Multibody Modeling for Tethered Space Elevators", *Acta Astronautica*, Vol. 65, pp. 399-422, 2009.

## BIBLIOGRAPHY

---

- [113] Zanutto, D., Colombatti, G., and Lorenzini, E. C., “Electrodynamic Tethers for Deorbiting Maneuvers”, *3<sup>rd</sup> CEAS Air&Space Conference - 21<sup>st</sup> AIDAA Congress*, Venice, Italy, 24-28 October 2011.
- [114] Zanutto, D., Lorenzini, E. C., Mantellato, R., Colombatti, G., and Sanchez, A., “Orbital Debris Mitigation Through Deorbiting With Passive Electrodynamic Drag”, *63<sup>rd</sup> International Astronautical Congress*, Naples, Italy, 1-5 October 2012.

## Websites

- [115] <http://ccmc.gsfc.nasa.gov/modelweb/>



# Ringraziamenti

Eccoci qua, ormai alla fine di questo lungo percorso universitario! Beh... che dire dopo triennale, specialistica e dottorato?

In realtà una domanda mi gira per la testa: tornando indietro lo rifarei? Mi iscriverei nuovamente ad ingegneria???

Ma immagino che la risposta sarebbe sì!!! Nonostante la mole di studio, le difficoltà e le nottate sui libri prima degli esami, non mi pento della mia scelta e uscendo dal liceo mi iscriverei ancora qui! Per questo devo ringraziare tutti i professori, quelli bravi e pignoli, e quelli più “incasinati”, quelli buoni e quelli ... un po' meno, perché non mi hanno insegnato solo un corso di laurea, ma mi hanno mostrato la passione per ogni singola materia.

Di persone da ringraziare ce ne sono tante e vorrei partire dai miei genitori, Rino e Antonella. Senza il loro amore, aiuto e appoggio, in questo momento non starei sicuramente finendo di scrivere questa tesi.

I miei fratelli Fabio e Marco, perché ci sono stati, ci sono e so che ci saranno sempre per me, e io per loro.

I miei nonni Guido e Anna, perché figure importantissime nella mia vita. Nonno mi manchi ...

La vecchia compagnia (Concordia e dintorni) e gli amici nuovi conosciuti a Padova, per tutti i momenti di allegria e di svago, le serate, gli spritz, i caffè alle macchinette, e le cazzate sparate assieme.

E naturalmente, at last but not least, Ilaria, per ogni singolo momento passato insieme, e perché da quanto c'è lei tutto ha un senso ... ti amo da morire

Denis Zanutto